TURBULENCE MODULATION IN NON-UNIFORM AND UNSTEADY CLAY SUSPENSION FLOWS

M.G.W. (Marijke) DE VET

UNIVERSITY OF **Hull**

Front cover: clay suspension flow as it exits the experimental range. July 2021

Turbulence modulation in non-uniform and unsteady clay suspension flows

M.G.W. (Marijke) DE VET

Examiners	*Supervisors*
Dr Lawrence AMY (external)	Dr Robert M. DORRELL
Dr Rebecca WILLIAMS (internal)	Dr Roberto FERNÁNDEZ
Dr Jonathan DEAN (chair)	Dr Jaco H. BAAS
	Prof. William D. MCCAFFREY
	Prof. Daniel R. PARSONS

Submitted in accordance with the requirements for the degree of Doctor of Philosophy

UNIVERSITY OF Hull

ENERGY AND ENVIRONMENT INSTITUTE
University of Hull
Hull
HU6 7RX
United Kingdom

September, 2022

De deur zit vaker dan me lief is al bij voorbaat dicht.
Maar een deur is geen deur als hij niet nog open kan:
eerst op een kiertje, en geleidelijk aan steeds meer.

Dilara Bilgiç

CONTENTS

ABSTRACT

Cohesive sediment is common within natural environments, such as rivers, estuaries, shallow seas and deep oceans. High-magnitude, low-frequency events, such as storms, floods, and post-wildfire erosion, which occur more often due to climate change, can enhance the cohesive sediment supply to rivers. The higher sediment transport rates can have major impacts on water quality and aquatic ecosystems, including fish habitats, and also on channel morphology. Further, subaqueous sediment gravity currents are among the volumetrically most important sediment transport processes on Earth.

In contrast to non-cohesive sediments, suspended cohesive sediment particles may form larger particles, or flocs, when the distance between the particles is sufficiently small. Networks of flocs in the flow, i.e., clay gels, enhance viscosity and yield stress, and thus are a key control on flow turbulence. Research into steady, uniform clay flows indicates a close interaction between turbulent and cohesive forces, controlling the dynamic structure of clay flows.

Subaqueous sediment gravity currents can be classified into different flow types, similar to a clay flow classification scheme of open-channel flows. On one side of the spectrum, turbidity currents are relatively dilute flows, in which the particles are supported by the upward component of fluid turbulence; correlated to turbulent flows with characteristics of a turbulent, wall-bounded shear flow for open-channel flows. On the other side of the spectrum, debris or mud flows have limited internal turbulence and cohesive sediment provides grain support through yield strength; correlated to an almost fully suppressed turbulence in quasi-laminar plug flows for open-channel flows. Transitional flows bridge the gap between turbidity currents, i.e. turbulent flows, and debris flows, i.e. quasi-laminar plug flow. These transitional flow types contain transient turbulent behaviour.

The transitional flow properties of clay-laden flow are based on steady, uniform open-channel flow. However, open-channel flows and gravity currents are naturally non-uniform, i.e. varying in space, or unsteady, i.e. varying in time. The formation of bonds between cohesive sediment particles is a time-dependent (thixotropic) process and, therefore, clay-laden flows need time to adjust to spatial or temporal variations in flow velocity. Despite clay being the most abundant sediment type on earth, the present knowledge on turbulent dynamics of non-uniform or unsteady clay-laden flows remains limited, whereas it directly influences the sediment transport capacity.

To research the influence of suspended cohesive clay on changing flow dynamics under non-uniform flow conditions, new experiments were conducted using decelerating and accelerating clay suspension open-channel flows in a recirculating flume. The flows transition between clay flow types, with different degrees of turbulence enhancement and attenuation as the flow adapts to the change in velocity. The experimental results show that decelerating clay suspension flows have a longer adaptation time than accelerating clay suspension flows, which is potentially correlated to the formation of clay bonds in decelerating flows requiring more time than the breakage of clay bonds in accelerating flows. This hysteresis is more pronounced for higher concentration decelerating flows that pass through a larger variety of flow phases of turbulence enhancement and attenuation.

To research the adaptation time of clay suspension flows to unsteady flow conditions, new experiments were conducted using unsteady clay suspension open-channel flows. The flow velocity was adjusted with increments of 0.1 m/s after which the adaptation time to reach the equilibrium conditions was quantified. The experimental results show that accelerating, strongly turbulence attenuated, clay flows require more time than weakly or non-turbulence attenuated clay

flows due to the time required for turbulence to penetrate the plug flow in order to break the clay bonds. Relative to turbulent flows, the adaptation time of decelerating flows is reduced as the flow evolves through clay flow types as the increase in clay concentration allows for a higher frequency of inter-particle collision. Adaptation time is then increased again with stronger turbulence attenuated flows as the increasingly dominant cohesive forces reduce inter-particle collision and consequently the formation of clay bonds takes longer.

To research the evolvement of non-uniform clay-laden gravity currents, new experiments with constant-flux flows in a submerged flume were conducted. Based on velocity measurements three different flow types are identified with increasing turbulence attenuation: a) turbidity current, b) turbulent plug flow and c) transitional plug flow. The combination of balance between turbulent and cohesive forces and the formation of clay bonds determines the evolvement of a gravity current. For low clay concentrations, entrainment of ambient water and the additional turbulence developed at the upper interface penetrates into the gravity current preventing the formation of clay bonds. Consequently, the gravity current evolves towards a more turbulent flow condition. For high clay concentrations, entrainment and turbulence generation remains in the outer region allowing the formation of clay bonds in the inner region. Consequently, the gravity current evolved towards a less turbulent flow condition as a plug flow develops in the inner region towards the bed.

Turbulent flow dynamics have a direct influence on sediment erosion, transport and deposition patterns. Research into non-uniform and unsteady clay suspension flows indicates a complex interplay in cohesive and turbulent forces as the flow adapts to changes in velocity, which likely affects erosional and depositional processes in a variety of fluvial and submarine settings.

GLOSSARY

A glossary of the main terms is provided for clarification of definitions used within this research.

Cohesive sediment	Sediment containing predominantly clay- and silt-sized fractions of clay-type minerals, containing the electromagnetic properties of which cause the sediment to bind together.
Debris flow	A debris flow is a sediment flow with plastic rheology and laminar state in which matrix strength predominate over turbulence grain support.
Gravity current	A gravity current is a flow of one fluid within another caused by the density difference between the fluids. The difference in specific weight provides the driving force. This research focuses on subaqueous sedimentary gravity currents where the difference in specific weight is due to suspended sediment.
Non-uniform flow	The flow is non-uniform when the flow velocity changes from point to point at any given instant of time. In this research flow non-uniformity is defined as streamwise changes in depth-averaged velocity in space (along the flume).
Plug flow	Plug flow is an idealized flow of fluids in which all particles in a given cross-section have identical velocity and direction in motion, and consequently without mixing between different heights in the flow. Within clay-laden flows, as within this research, a plug flow refers to a quasi-plug flow. The quasi-plug flow is characterised by a low velocity gradient, which correlates with low turbulence intensity. Note, plug flow is also used within the definitions of clay flow types of open-channel flows and gravity currents, where it should read in conjunction of the clay flow type.
Steady flow	The flow is steady when the flow velocity at a point does not change with time. In this research flow steadiness is defined as constant streamwise depth-averaged velocity in time.
Turbidity current	A turbidity current is a sediment flow with Newtonian rheology and turbulent state in which turbulence provides the main particle support.
Uniform flow	The flow is uniform when the flow velocity at a given instant of time is the same in both magnitude and direction at all points in the flow. In this research flow uniformity is defined as constant streamwise depth-averaged velocity in space (along the flume).
Unsteady flow	The flow is unsteady when the flow velocity at a point does change with time. In this research flow unsteadiness is defined varying streamwise depth-averaged velocity in time.

Clay flow types in open-channel flows, with increasing clay concentration:

TF - Turbulent Flow

Turbulent flow has a logarithmic vertical velocity profile with an associated decrease in turbulence intensity away from the bed.

TETF - Turbulence-Enhanced Transitional Flow

In turbulence-enhanced transitional flow, velocity decreases and turbulence intensity increases with increasing clay concentration across the entire flow depth, while retaining the logarithmic relationship with flow height.

LTPF - Lower Transitional Plug Flow

Lower transitional plug flow contains decreasing near-bed velocity, combined with increasing near-bed turbulence and decreasing turbulence in the outer flow with initial plug flow development.

UTPF - Upper Transitional Plug Flow

As clay concentration increases within the upper transitional plug flow, the plug-flow region gradually grows to its maximum thickness, near-bed velocity continues to decrease, and turbulence intensity rapidly decreases.

QLPF - Quasi-Laminar Plug Flow

The quasi-laminar plug flow is characterized by a laminar plug flow region moving on a thin shear layer. The shear layer has a steep velocity gradient and usually possesses some residual turbulence.

Clay flow types in gravity current (identified in experiments of Chapter 4)

Turbidity current

A turbidity current is a gravity current, which shows no plug flow within the downstream velocity profile and is fully turbulent.

Turbulent plug flow

A turbulent plug flow is a gravity current, which does contain a plug flow within the downstream velocity profile, but the measured velocity fluctuations are fully turbulent.

Transitional plug flow

A transitional plug flow is a gravity current, which does contain a plug flow within the downstream velocity profile and shows attenuation of higher frequency velocity fluctuations.

1

INTRODUCTION

Cohesive sediment occurs commonly in a wide range of natural environments, such as rivers, estuaries, shallow seas and deep oceans (Whitehouse et al., 2000; Flemming, 2002; Winterwerp and Van Kesteren, 2004), and industrial settings (Ackers et al., 2001). Cohesive sediment predominantly contains clay- and silt-sized fractions of clay-type materials, which contain electromagnetic properties allowing the sediment to bind together. The majority of flows should contain mud, composed of water, clay minerals, sand, silt and organic matter (Whitehouse et al., 2000; Mehta, 2013), since mud is one of the most common sediment types within natural environments (Flemming, 2002; Schindler et al., 2015). The supply of cohesive sediment to these environments can be increased by high-magnitude, low-frequency events, such as landslides, floods, hill slope failure, storms and post-wildfire erosion (Swanson, 1981; Sankey et al., 2017), which occur more often due to climate change (Geertsema et al., 2006; Reneau et al., 2007; Barbero et al., 2015). Further, cohesive sediment is common in submarine gravity currents, such as turbidity currents, hybrid events, mass transport events and associated deposits (Talling et al., 2012). Sediment gravity currents are volumetrically one of the most important sediment transport processes on our planet, frequently transporting cohesive sediment in high concentrations (Kneller and Buckee, 2000; Talling et al., 2012). The increases in sediment transport due to climate change can have major impacts on water quality and aquatic ecosystems, including fish habitats (Bilotta and Brazier, 2008; Ji, 2017; Parsapour-Moghaddam et al., 2019), and also on channel morphology (Smith et al., 2011). The capability to predict the movement of cohesive sediment is crucial in understanding the distribution of pollutants, such as heavy metals which can be absorbed onto clay or silt particles (Whitehouse et al., 2000; Best et al., 2022). High-concentrated clay-laden flows could also transport and bury macro- or microplastics across environments (Pohl et al., 2020b; Zhong and Peng, 2021).

High suspended cohesive sediment concentrations modify flow dynamics by either enhancing (Best et al., 1997; Baas and Best, 2002) or dampening turbulence (Bagnold, 1954; Wang and Larsen, 1994), influencing sediment transport rates and erosion and deposition patterns (Partheniades, 1965; Mehta et al., 1989). Cohesive clay particles may form larger particles, or flocs, when the distance between the particles is sufficiently small (van Olphen, 1977; Winterwerp and Van Kesteren, 2004). Networks of flocs in the flow, i.e., clay gels, enhance viscosity and yield stress, and thus are a key control on flow turbulence (Baas and Best, 2002). The flow properties due to suspended sediment have been determined for steady uniform flow conditions. Where uniform flow refers to a constant streamwise depth-averaged velocity in space and steady flow refers to a constant streamwise depth-averaged velocity in time. However, flows are naturally non-uniform and/or unsteady, i.e. varying in space and/or time, due to for example geometry changes (bed slope,

1

river width) (Yang et al., 2006; Emadzadeh et al., 2010), tidal variations (Leeder, 2011; Uncles and Mitchell, 2017), flood hydrographs (Karimaee Tabarestani and Zarrati, 2015; Fielding et al., 2018; Mrokowska and Rowiński, 2019) and sediment gravity currents naturally evolve both in space and time depending on the boundary conditions (Kneller, 1995; Mulder and Alexander, 2001; Felix and Peakall, 2006; Talling et al., 2007; Kane and Pontén, 2012). Despite the regular occurrence, the dynamics of these clay-laden non-uniform and/or unsteady flows are poorly understood, whereas understanding this is pivotal. Erosion, transport and deposition of sediment, including development and stability of bedforms (Baas and Best, 2008; Baas et al., 2016*b*) and hybrid event beds (Haughton et al., 2009; Talling et al., 2012), depends on the magnitude and distribution of flow turbulence (Dorrell et al., 2018). Variations in turbulence directly affects the transport capacity and deposition and erosion patterns (Whitehouse et al., 2000; Dorrell and Hogg, 2012; Moody et al., 2013), but the understanding of turbulent-laminar transitions in non-uniform and unsteady clay-laden flows remain poorly understood.

The stickiness of muddy sediment classifies cohesive sediment (Whitehouse et al., 2000). The movement of cohesive sediment is closely related to flow hydrodynamics (Section 1.1) as well as the material properties (Section 1.2). The combination of flow properties and suspended sediment concentration has significant influence on the flow type (Winterwerp and Van Kesteren, 2004), with turbulent flow and laminar flow as the two end members. Transitional flows bridge the gap between laminar and turbulent flow with different degrees in turbulence enhancement and / or attenuation (Wang and Plate, 1996; Baas et al., 2009, Section 1.3). This thesis aims to further develop the knowledge of non-uniform and unsteady clay-laden flows (Section 1.5) for both open-channel flows (Chapters 2, 3) and gravity currents (Chapter 4).

1.1. HYDRODYNAMICS

The movement of sediment depends on the hydrodynamic forcing. Hydrodynamic flows are generally turbulent, characterised by their ability to transport and mix fluid (Pope, 2000). Laminar flow is used as a term for flow conditions when the fluid flows in parallel layers with no disruption between them (White, 2016) and energy losses are low due to the absence of flow mixing. Within turbulent flow, liquid particles move in irregular paths resulting in irreversible mixing of the fluid (Chaudhry, 2008). The ratio between inertial and viscous forces defines if the flow is laminar or turbulent, indicated by the Reynolds number (Tennekes and Lumley, 1972). Viscous forces resist deformation of a fluid and inertial forces represent resistance of the fluid mass to acceleration (Leeder, 2011, Section 1.2.5).

$$Re = \frac{UL}{v} \tag{1.1}$$

where Re is the Reynolds number, U is the characteristic flow scale, velocity, L the characteristic length scale, commonly hydraulic depth or radius, and v is the kinematic viscosity of the liquid (Section 1.2.5). The flow is classified as laminar when viscous forces dominate, but no universal Reynolds number can be defined as it is influenced by individual molecular properties of the fluid (Chow, 1959; Tennekes and Lumley, 1972; Novopashin and Muriel, 2002; Chaudhry, 2008; Massey and Ward-Smith, 2012).

1.1.1. TURBULENT LENGTH SCALES

In turbulent flow, fluid moves in random patterns referred to as eddies (Tennekes and Lumley, 1972). The largest size range of eddies are in the order of the flow scale, set for example by flow depth (Section 1.1) and the smallest are referred to as Kolmogorov micro-scales (Tennekes and Lumley, 1972). Large eddies are unstable and break up, transferring their energy to smaller eddies by inviscid processes, a process referred to as energy cascade (Pope, 2000). This process continues until the Kolmogorov scale, where energy is dissipated to thermal energy by viscous effects due

to molecular viscosity (Andersson et al., 2011). The large eddies, affected by the boundary conditions of the flow, are anisotropic and contain the highest energy content, which contributes most to the turbulent transport (Tennekes and Lumley, 1972; Pope, 2000, Figure 1.1). The small-scale turbulent motions are often assumed to be statistically isotropic and universal, i.e. similar in every high-Reynolds number turbulent flow (Pope, 2000; Biferale and Procaccia, 2005). These small-scale, Kolmogorov, motions are determined by the energy-dissipation rate, ϵ, and the viscosity, v, (Pope, 2000; Kaneda et al., 2003; Iyer et al., 2020).

$$
\begin{aligned}
\text{Length:} &\quad \eta = (v^3/\epsilon)^{1/4} \\
\text{Time:} &\quad \tau_\eta = (v/\epsilon)^{1/2} \quad (1.2) \\
\text{Velocity:} &\quad u_\eta = (v\epsilon)^{1/4}
\end{aligned}
$$

where v is the viscosity, ϵ rate of dissipation and η, τ_η and u_η the Kolmogorov scales of length, time and velocity respectively. By definition Kolmogorov's length and velocity scale give a Reynolds number equal to 1 (Pope, 2000). The ratio of the smallest (η) and the largest (L) scale decreases with the Reynolds number (Re) of the flow according to:

$$
\frac{\eta}{L} = Re^{-3/4} \tag{1.3}
$$

The higher the Reynolds number, the higher the range of turbulent length scales. At the inertial (sub)range, between the large and the small scales, turbulent motion is governed by a high Reynolds number (advection dominates) and is not directly affected by viscosity. The rate of dissipation is scaled to the energy distribution as (Pope, 2000; Monin and Yaglom, 2013, Figure 1.1):

$$
E(\kappa) = \alpha \epsilon^{2/3} \kappa^{-5/3} \tag{1.4}
$$

where $E(\kappa)$ is the energy spectrum, α is a universal constant, ϵ the rate of dissipation and κ the wave number, which is a reciprocal length scale. Turbulence needs a continuous supply of energy to make up for the viscous losses (Tennekes and Lumley, 1972; Davidson, 2015). Shear in the mean flow is a common source of energy for turbulent velocity fluctuations (Tennekes and Lumley, 1972; Monin and Yaglom, 2013; Buaria et al., 2019).
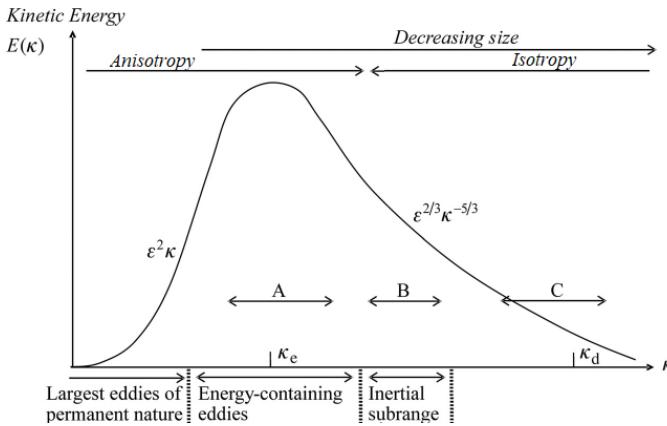
Figure 1.1: Energy distribution of turbulent kinetic energy over the range of length scales. A: large energy-containing eddies, which interact with and extract energy from the mean flow. The energy is transferred to smaller scaled into region B. B: inertial subrange, where turbulent kinetic energy is neither produced nor dissipated. C: dissipative region of turbulent kinetic energy into heat. Eddies in this region are isotropic and scales are given by the Kolmogorov scales. Adapted from Andersson et al. (2011).

1.1.2. TURBULENT SHEAR STRESS

Characterising turbulence as superimposed on the principal motion, Reynolds decomposition separates turbulent fluctuations (u') from the mean flow ($\overline{u}$) (Tennekes and Lumley, 1972; Massey and Ward-Smith, 2012).

$$u = \overline{u} + u' \tag{1.5}$$

where u is the velocity signal. The contribution of the turbulent motion to the mean stress (τ_t) can be described as (Tennekes and Lumley, 1972; Pope, 2000), with v' the turbulent fluctuations of the vertical velocity:

$$\tau_t = -\rho \overline{u'v'} \tag{1.6}$$

The Reynold stress defines the turbulent shear stresses across a shear plane parallel to the mean flow direction. The total shear stress (τ_{tot}) is a function of the gradient of the time-averaged stream wise velocity (τ_l) and the random fluctuations of the stream-wise component and vertical components of velocity (τ_t). These represent two mechanisms of momentum transfer within a moving fluid: molecular momentum transfer due to viscosity at microscale and momentum transfer due to turbulent fluctuations at macroscale (Schlichting and Gersten, 2016, Figure 1.2).

$$\tau_{tot} = \tau_l + \tau_t = \mu \frac{\partial \overline{u}}{\partial z} - \rho \overline{u'v'} \tag{1.7}$$

where μ is the dynamic viscosity, related to the kinematic viscosity with the density of the fluid, i.e. $v = \mu/\rho$ (Andersson et al., 2011; Davidson, 2015) and z height above the bed.
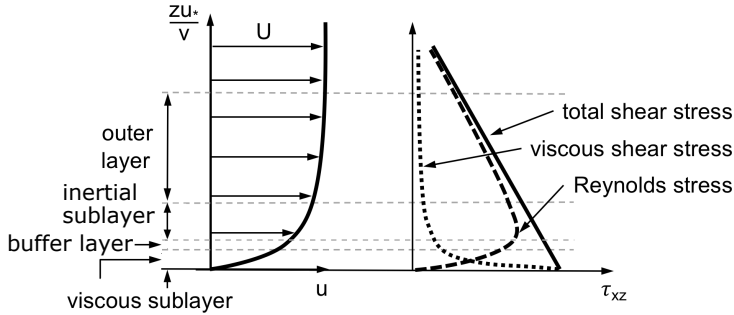
Figure 1.2: Shear stress distribution correlated to the velocity profile in open-channel flow. Adapted from (Pope, 2000; Schlichting and Gersten, 2016).

1.1.3. VELOCITY PROFILE

The velocity profile can be divided into two sections, the boundary layer and the outer flow. The wall region or boundary layer is dominated by the boundary conditions at the wall and the outer layer is influenced by the whole flow geometry where the effects of friction are negligible (Schlichting and Gersten, 2016). The wall enforces the no-slip condition; the fluid has zero velocity relative to the boundary. Above the boundary, the stream-wise velocity gradually increases with height above the bed and asymptotically approaches the free-stream value at some distance from the bed. The no-slip condition results in large velocity gradients perpendicular to the wall (Tennekes and Lumley, 1972). The boundary layer (δ) is defined as the distance from the boundary surface to the point where $u = 0.995u_e$, with u_e the velocity in the outer layer (Schlichting and Gersten, 2016).

The wall region or inner layer is divided into three sublayers: the viscous sublayer ($z^+ < 5$) where viscous shear stresses dominate, the buffer or transition layer ($5 < z^+ < 30$) where both

viscous and turbulent shear stresses are important and the inertial sublayer ($z^+ > 30$), which is dominated by turbulent shear stresses (Tennekes and Lumley, 1972, Figure 1.2). Velocity u and height y are commonly made dimensionless with the shear velocity (u_*) and viscosity (v), referred to as wall coordinates.

$$u^+ = \frac{u}{u_*} \qquad z^+ = \frac{z u_*}{v} \tag{1.8}$$

The friction or shear velocity is a fundamental velocity scale widely used to normalize mean velocity and turbulence for comparison. The direct determination of the friction velocity within experiments or in the field includes a high degree of difficulty (Chauhan et al., 2007; Hutchins and Choi, 2002). Various indirect methods exist to determine the friction velocity, among others the Reynolds shear stress distribution, the log law applied on the mean velocity distribution and the water level slope ($u_* = \sqrt{ghS}$) (Nezu and Nakagawa, 1993; Nezu et al., 1997; Kneller, 2003); where g is the gravitational acceleration, h flow depth and S is the bed slope.

Within the viscous sublayer ($z^+ < 5$), the velocity profile is linear (Equation 1.9) and within the inertial sub-layer, the velocity profile is logarithmic (Equation 1.10).

$$u^+ = z^+ \tag{1.9}$$

$$u^+ = \frac{1}{\kappa} ln\left(\frac{z}{z_0}\right) \tag{1.10}$$

where κ is the von Karman constant generally around or equal to 0.41 (Clauser, 1954; Nezu and Nakagawa, 1993; Pope, 2000; Chauhan et al., 2007; Segalini et al., 2013) and z_0 the roughness length depending on the roughness of the bed. A wall is considered smooth when roughness elements with height k_s, i.e. the Nikuradse roughness (Soulsby, 1997), are submerged in the viscous sub-layer (Van Rijn, 2011). When the roughness elements are larger and penetrate into the buffer layer or further, flow separation behind the elements dominates the momentum transfer. Intermediate or transitional roughness is referred to when the momentum transfer is affected by both the viscosity and by flow separation. For a rough wall ($k_s = 2.5d_{50}$), there are no changes in the velocity profile at the outer region. In the inner region, turbulent wakes are formed responsible for inviscid drag on the surface (Tennekes and Lumley, 1972). In the velocity profile, the Nikuradse roughness length, z_0, varies from hydrodynamically smooth ($z_0 = v/(9u_*)$) via transitional ($z_0 = v/(9u_*) + k_s/30$) to rough ($z_0 = k_s/30$) (Schlichting and Gersten, 2016).

The boundary layer inner region is described by a logarithmic profile by von Karman (Law of the wall). In the outer layer ($z^+ > 50$) the velocity profile can deviate from the log law, also referred to as defect layer (Pope, 2000). Coles (1956) combined these two analytical descriptions into one formula known as the law of the wake.

$$U = \frac{u_*}{\kappa} ln\left(\frac{z}{z_0}\right) + \frac{2\Pi u_*}{\kappa} sin^2\left(\frac{\pi}{2} \frac{z}{\delta}\right) \tag{1.11}$$

where δ is the thickness of the boundary layer and Π the wake strength parameter. The wake function, which is the second part of Equation 1.11, describes the velocity profile in the outer region of turbulent boundary layers (Coles, 1956). The law of the wake is particular useful for the velocity distribution in transitional flow conditions (Baas et al., 2009, Section 1.3). Coles (1956) was the first author to express the boundary layer as wake function added to the description of the inner layer, several authors followed with adjustments of the wake function (Finley et al., 1966; Lewkowicz, 1982; Sandham, 1991; Chauhan et al., 2007).

1

1.2. SEDIMENT PROPERTIES

Cohesive clay minerals, when suspended in water, have a surface charge that enables electrostatic forces of attraction between individual particles (Section 1.2.2), leading to the formation of clay flocs and gels (Yong and Warkentin, 1975; van Olphen, 1977; Whitehouse et al., 2000, Section 1.2.3). These material properties (Section 1.2.4) influence the turbulence within the flow and the sediment transport rate of open-channel flows (Wang and Plate, 1996; Partheniades, 2009; Baas et al., 2009) and gravity currents (Mulder and Alexander, 2001; Talling et al., 2012).

1.2.1. CLAY STRUCTURE

Clay minerals can be grouped according to their crystal structure and stacking sequence of various layers (van Olphen, 1977; Bergaya and Lagaly, 2013*b*; Adamis et al., 2005; Partheniades, 2009, Section 1.2.4). Each layer is a combination of tetrahedrically arranged silica sheets and octahedrically arranged aluminium or magnesium sheets (Figure 1.3). Numerous layers of stacked units may form one clay particle (Bergaya and Lagaly, 2013*b*; Wypych, 2015; Shaikh et al., 2017). Tetrahedral units, four oxygen atoms arranged in tetrahedron shape around a silicon atom, are combined in a sheet structure referred to as silica or tetrahedral sheet. The second building block consists of six oxygens having the configuration of an octahedron enclosing an aluminium or magnesium atom (van Olphen, 1977; Bergaya and Lagaly, 2013*a*). Tetrahedral and octahedral sheets can combine by sharing oxygen atoms (Partheniades, 2009). The fourth oxygen atom protruding from the silica sheet is then shared with the octahedral sheet. In 1:1 clay minerals, sharing of oxygen atoms occurs between one silica sheet and one octahedral sheet. 2:1 clay minerals contain one octahedral sheet with two silica sheets, one on each side (van Olphen, 1977; Bergaya and Lagaly, 2013*a*, Section 1.2.4). Cleavage parallel to the layers is relatively easy, which explains the flaky, plate-shaped shape of clay particles (van Olphen, 1977; Bergaya and Lagaly, 2013*b*).
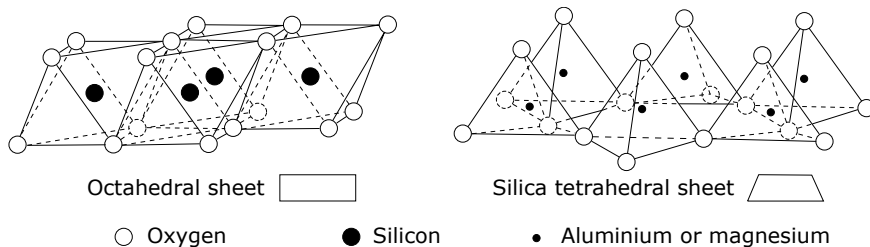
Figure 1.3: Structure of tetrahedrically arranged silica sheets and octahedrically arranged aluminium or magnesium sheets (Winterwerp and Van Kesteren, 2004).

1.2.2. PARTICLE BONDING

Bonding between clay particles can be separated into two general categories: (1) interatomic or primary bonds and (2) secondary bonds (van Olphen, 1977; Adamis et al., 2005; Partheniades, 2009; Shaikh et al., 2017). The stronger primary bonds hold the atoms and molecules of any matter together, which depend on the atomic structure of the matter itself. Two types of primary bonds, electrovalent or ionic and covalent bonds, influence the formation of flocs (Partheniades, 2009; Bergaya and Lagaly, 2013*a*). Ionic bonds are developed by the electrostatic attraction of elements with opposite electric charges. With covalent bonds, one or more bonding electrons are shared among a number of atoms, which occurs in combining tetrahedral and octahedral sheets (Nasser and James, 2006; Bergaya and Lagaly, 2013*a*, Section 1.2.1).

Weaker secondary bonds act between material particles. The strongest secondary bond is a hydrogen bond, where a hydrogen atom is attracted to an electronegative atom such as oxygen (Partheniades, 2009; Delgado et al., 2007), found between attached layers of clay (Section 1.2.1).

Electric charges are not distributed symmetrically creating dipoles with oppositely charged ends which may be attracted by other differently oriented molecules. These attractive van der Waal forces decrease rapidly with distance and are the primary mechanism for flocculation (Coussot, 1997; Partheniades, 2009, Section 1.2.3).

Within the clay layers, some silicon or aluminium atoms are replaced by atoms of lower positive valence resulting in an excess of a negative charge, which is compensated by the adsorption of cations to maintain electroneutrality, referred to as isomorphous substitution (Partheniades, 2009). These cations, such as Ca^{++} and K^+, are retained in an exchangeable state and can be replaced by other cations (Coussot, 1997; van Olphen, 1977; Bergaya and Lagaly, 2013b). The quantity of these exchangeable cations is referred to as cation exchange capacity (CEC), measured in milliequivalents per 100 g of clay mineral [meq/100 g] (Yong and Warkentin, 1975). The cohesion is greater with higher CEC resulting in higher potential of individual clay particles to form aggregates or flocs in water (Adamis et al., 2005; Wypych, 2015; Shaikh et al., 2017; Section 1.2.3).

The exchangeable cations may slightly diffuse in water, forming an electric double layer around clay particles (Mitchell et al., 2005; Hunter, 2013, Figure 1.4). The double layer consists of two layers; the inner Stern layer and a cloud of particles referred to as the outer diffuse layer (Bergaya and Lagaly, 2013a; Shaikh et al., 2017). The Stern layer consists of cations attracted to the negative surface charge of the particle. Ions in the diffuse layer are sparsely dispersed and their concentration gradually decreases with increasing distance from the particle (van Olphen, 1977; Hunter, 2013; Bergaya and Lagaly, 2013a). A layer of surrounding fluid remains attached to the particle. The slipping plane (shear plane) is the interface between this immobile fluid near the particle surface and the free-flowing ambient fluid (Shaikh et al., 2017). The ζ-potential is a measure of electric potential at the slipping plane (Kaszuba et al., 2010; Hunter, 2013; Shaikh et al., 2017, Figure 1.4), depending on pH, cation concentration and valence (Winterwerp and Van Kesteren, 2004). Sodium Adsorption Ratio (SAR) is a measure for the relative concentration of Na^+, Ca^{++} and Mg^{++} (Whitehouse et al., 2000) and reflects on the thickness of the double layer (Winterwerp and Van Kesteren, 2004; Hunter, 2013). Together with the charge density of clay surfaces, which depends on cation exchange capacity (CEC) and specific surface area (SSA), SAR is a useful parameter to quantify the effects of cations in the surrounding water on the mechanical properties of a sediment, like shear strength, permeability and erodibility (Winterwerp and Van Kesteren, 2004; Mehta and McAnally, 2008).

In the DVLO theory, developed by and named after Derjaguin and Landau (1941) and extended by Verwey et al. (1948), colloid stability is determined by the potential energy of the particles, which is a balance between potential energy of attractive van der Waals forces and potential energy of the repulsive electric double layer (Hunter, 2013; Wypych, 2015; Shaikh et al., 2017, Figure 1.5). If the net force between two particles is repulsive or attractive depends on cation concentration and particle distance (Winterwerp and Van Kesteren, 2004; Mehta and McAnally, 2008, Figure 1.5). If cation concentration is low, the suspension is stable meaning the repulsive forces are sufficient to maintain particles far from each other (Coussot, 1997; Hunter, 2013). If cation concentration is high, van der Waals forces dominate and particles aggregate. Particles have to overcome an energy barrier before flocculation is possible, which is a local minimum in the net force (Winterwerp and Van Kesteren, 2004; Partheniades, 2009), caused by the balance between attractive and repulsive forces. In high electrolyte concentrations and reduced length of the double layer, two particles will be subjected to an attractive force as soon as they come sufficiently close to each other, and flocculation will take place (Partheniades, 2009; Hunter, 2013). Next to van der Waals electrostatic forces (Syvitski et al., 1995; Mehta and McAnally, 2008), clay particles can also be held together by organic matter (Furukawa et al., 2014; Asmala et al., 2014; Ye et al., 2020).
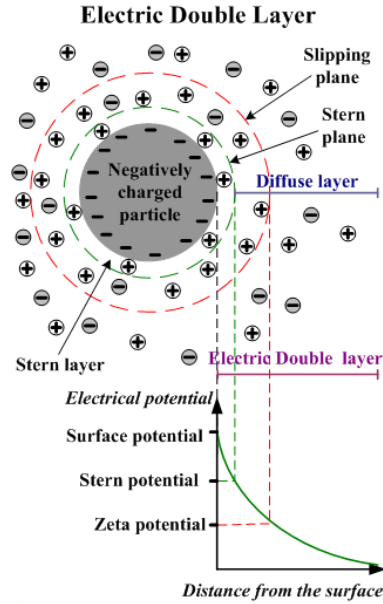
Figure 1.4: Electric double layer (Mitchell et al., 2005).
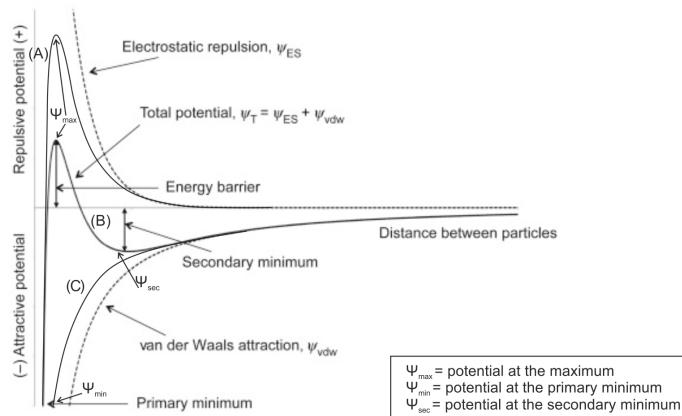
Figure 1.5: Schematic diagram of net and gross attractive repulsive force between clay particles including various potential energy of particles depending on concentration: (A) Low concentration (C) High concentration. Adapted from Gelardi and Flatt (2016).

1.2.3. FLOCCULATION

The most characteristic property of cohesive sediment is that it can form flocs when the sediment is brought in contact with a fluid. Flocs contain an open structure formed by a large number of clay particles and a high water content (Huang, 1993; Khelifa and Hill, 2006; Xu and Dong, 2017; Spencer et al., 2022). Flocs may join together to form higher order aggregates depending on suspended sediment concentration (Jiang and Logan, 1991; Barany et al., 2009; Sun et al., 2016;

Spencer et al., 2021, Figure 1.6). Krone (1963) proposed a conceptual model of floc structure, where compact flocs of primary grains with strong bonds are referred to as zero order aggregates. With the increase of order of aggregates, there is a discontinuous increase in the percentage of voids, fewer contact points and consequently lower aggregate strength (Partheniades, 2009). The effective density (bulk density minus water density) of flocs generally decreases as the flocs grow in size (Klimpel and Hogg, 1986), but their settling velocity increases (Dyer and Manning, 1999; Spearman and Manning, 2017).

Above a critical volume fraction, the gelling point might be reached resulting in the formation of a space-filling network structure of particle bonds referred to as a gel (van Olphen, 1977; Winterwerp and Van Kesteren, 2004; Genovese, 2012). These space-filling networks results in elastic gel-like behaviour influencing the flow properties of clay suspension flows (Baas et al., 2009; Partheniades, 2009, Section 1.3) and an apparent yield stress (Toorman, 1997, Section 1.2.5). A gel can already form at low clay concentrations of 2% volume (Coussot, 1997; Whitehouse et al., 2000; Winterwerp, 2002; McAnally et al., 2007) and at higher concentrations (2% to 11%) it progressively can support larger grains, such as sand or silt (Hampton, 1975; Torfs et al., 1996; Marr et al., 2001; Amy et al., 2006; Sumner et al., 2009; Baas et al., 2011). The formation of bonds between cohesive particles is a time-dependent (thixotropic) process (Peterfi, 1927; Freundlich, 1935; Mitchell, 1960; Ren et al., 2021, Section 1.2.5). For example, an applied shear stress (i.e. accelerating flow) breaks the bonds within clay particles (McAnally and Mehta, 2000; Partheniades, 2009; Cuthbertson et al., 2010). After the increased shear, the flow attempts to adjust itself to the new situation and local ions in the double layer will redistribute (Zhang et al., 2017). After enough time a new equilibrium is formed with a balance between attractive and repulsive forces. Thixotropy is a process of reorientation and rearrangement of particles, changes of adsorbed water structure and redistribution of ions, which allows flocculation (Skempton and Northey, 1952; Ren et al., 2021). Thixotropy has various implications on temporal variations of clay bonds for sediment flows (Manning and Dyer, 1999; Gratiot and Manning, 2004), but how this affects non-uniform or unsteady clay-laden open-channel flows or gravity currents remains unknown.
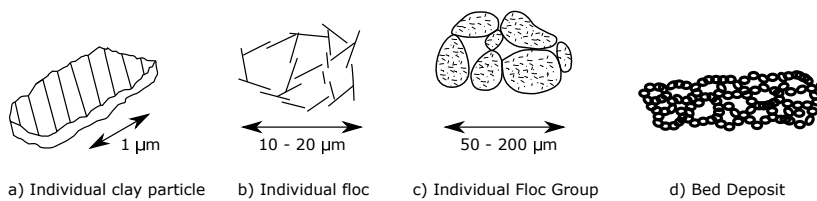
Figure 1.6: Sizes of clay particles, flocs and floc groups (McDowell and O'connor, 1977).

In suspension, particles are subjected to forces due to gravity, inertia, mean flow, turbulence fluctuations, and collisions with other particles in suspension (Mehta and McAnally, 2008) influencing the flocculation in flowing water (Figure 1.7). The complex interplay of fluid shear and suspended sediment concentration results in continuous particle aggregation and aggregate breakup (Lick et al., 1993; Manning and Dyer, 1999; Mietta et al., 2009; Safak et al., 2013; Lamb et al., 2020). Flocculation occurs when a collision brings two particles close enough together for attractive forces to overcome repulsive forces (Mehta and McAnally, 2008). As aggregation occurs, the floc might grow large enough to settle to become part of the bed. If fluid forces and collisions exceed floc strength the floc might break into smaller parts and repeat the process.
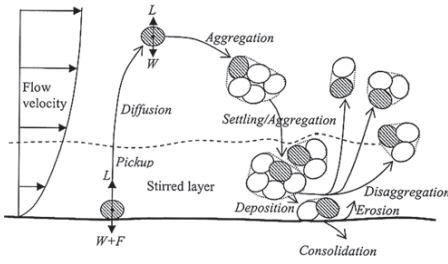
Figure 1.7: Schematic drawing showing transport and aggregation of cohesive sediment particles or flocs (Mehta and McAnally, 2008).
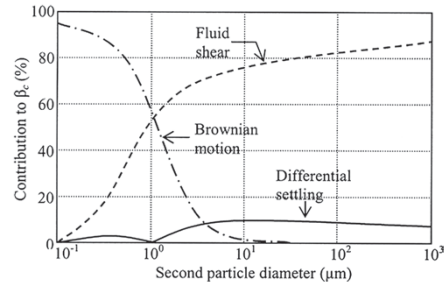
Figure 1.8: Simulated relative contributions to the collision frequency (β_c) for typical water column conditions between two particles. First particle diameter is 1 μm (Mehta and McAnally, 2008).

Three primary processes govern flocculation; Brownian motion, velocity gradients and differential settling (Krone, 1962, Winterwerp and Van Kesteren, 2004, Partheniades, 2009). Brownian motion, caused by thermal activity of the water molecules, cause particles to collide, resulting in the formation of aggregates (Levich, 1962). As Brownian motion depends on thermal motion of fluid molecules, it depends on the temperature. Generally, Brownian motion affects small particles and in moving water velocity gradient and collision frequency have a larger influence on flocculation than Brownian motion, i.e. aggregation due to Brownian motion is negligible (McCave, 1984; van Leussen, 1994; McAnally and Mehta, 2000; Partheniades, 2009, Figure 1.8). Differences in settling velocity cause collision between particles, referred to as differential settling (Soulsby, 1997; Mehta and McAnally, 2008; Spearman and Manning, 2017). Velocity gradient or shear rate causes particles to collide and form flocs, but on the other hand, it may disrupt the flocs, causing floc break-up (Dyer, 1988; McAnally and Mehta, 2000; Winterwerp, 2002; Partheniades, 2009; Cuthbertson et al., 2010). The resistance to breakup or disaggregation is referred to as floc strength and depends on cohesion, size, orientation of particles within the floc and to a lesser extent on salinity and pH (van Olphen, 1977; Adamis et al., 2005; Mehta and McAnally, 2008; Yu et al., 2013; Ren et al., 2021). The relative importance of these mechanisms depends on the natural situation (Dyer, 1988; Manning and Dyer, 1999; Mietta et al., 2009) and the location in the flow, e.g near the bed, shear stresses are stronger increasing the chance of deflocculation (McCave and Hall, 2006; Mehta and McAnally, 2008; Safak et al., 2013; Schlichting and Gersten, 2016).

1.2.4. CLAY TYPE
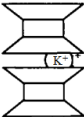
The most common clay minerals with their characteristic parameters are summarized in Table 1.1. Kaolinite is a weakly cohesive clay mineral with a low specific surface area (SSA) and low cation exchange capacity (CEC) (Winterwerp and Van Kesteren, 2004) and classified as a 1:1 layer clay (van Olphen, 1977; Bergaya and Lagaly, 2013b). Kaolinite originates from weathering of often feldspar-rich rocks and is common in humid tropics (Adamis et al., 2005; Shaikh et al., 2017).

Montmorillonite, part of the smectite group (Adamis et al., 2005), on the other hand is a stronger clay and results from weathering of volcanic rocks (Yong and Warkentin, 1975; Shaikh et al., 2017). Montmorillonite, a 2:1 layer clay, is a swelling clay because when in contact with water, water molecules penetrate in between the layers increasing the volume (van Olphen, 1977; Karimi and Salem, 2011). Cations at the interlayer can be exchanged with cations in the ambient water, resulting in a larger SSA and CEC than kaolinite and illite (next paragraph). Particles remain relatively thin due to the low bonding strength between the layers (Winterwerp and Van Kesteren, 2004). Bentonite is composed of a mixture of smectite clay minerals of which montmorillonite is the most common (Karimi and Salem, 2011; Shaikh et al., 2017).

Illite is a 2:1 layer clay where the negative charge is counterbalanced by K^+-ions between the layers (Meunier and Velde, 2004; Winterwerp and Van Kesteren, 2004) and does not experience interlayer swelling with water (van Olphen, 1977). As water does not penetrate in between the layers, only the ions at the external surfaces are exchangeable, decreasing the CEC compared to montmorillonite but also limiting the number of layers when potassium is not sufficiently available (Winterwerp and Van Kesteren, 2004), resulting in thinner crystalline particles than kaolinite (Meunier and Velde, 2004; Bergaya and Lagaly, 2013*b*).

Chlorite is structurally related to the 2:1 layer clays (van Olphen, 1977). The clay mineral consists of two tetrahedral sheets with one aluminium octahedral sheet (gibbsite octahedra) bonded by a magnesium octahedral sheet (brucite interlayer) (Winterwerp and Van Kesteren, 2004).

Table 1.1: Properties most common clay minerals (Mehta and McAnally, 2008; Partheniades, 2009; Winterwerp and Van Kesteren, 2004)

Clay mineral	General thickness [nm]	Specific Surface Area SSA [m^2/g]	Cation Exchange Capacity CEC [$meq/100g$]	Structure (Section 1.2.1)
Kaolinite	100	10-20	3-15	
Montmorillonite (incl. Bentonite)	2	700-800	80-150	
Illite	20	65-100	10-40	
Chlorite	30	70-90	24-35	

1.2.5. RHEOLOGICAL PROPERTIES

Rheological properties of clay suspensions include two main parameters: viscosity, η and yield stress, τ_y (Ghezzehei and Or, 2001; Massey and Ward-Smith, 2012; Nguyen et al., 2018). Viscosity is a quantitative measure of a fluid's resistance to flow (Massey and Ward-Smith, 2012) and yield stress is defined as the minimum shear stress required to initiate a flow, which within clay suspension flows is a measure of strength of the attractive interparticle forces between clay particles (Au and Leong, 2013; Lin et al., 2016). The correlation between stress against rate of shear determines the rheological properties (Takahashi, 2014; Figure 1.9). In shear thickening flow, also referred to as dilatant, the fluid increases its resistance with increasing strain rate. In shear thinning flow or pseudo-plastic flow, the dynamic viscosity increases as the rate of shear increases. In a Bingham plastic a minimum driving shear stress, the yield stress, is required before deformation after which the shear stress increases linearly with increasing shear rate (Massey and Ward-Smith, 2012; Takahashi, 2014; White, 2016). The Herschel-Bulkley model combines a yield stress with shear thinning. For the nonlinear curves, the slope at any point is called the apparent viscosity (White, 2016).
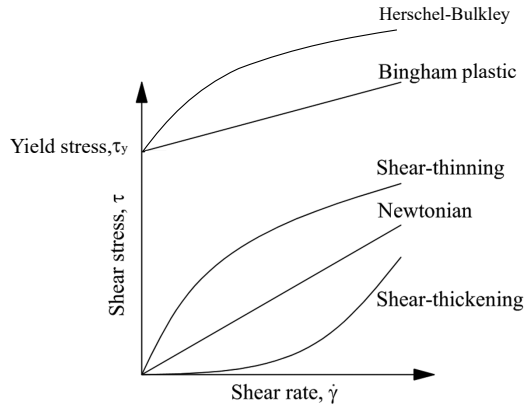
Figure 1.9: Rheological behaviour of viscous materials, stress versus strain rate. Modified after (Massey and Ward-Smith, 2012; White, 2016).

Several aspects influence the yield stress and apparent viscosity of clay-laden flows, including sediment type (cohesive or non-cohesive) due to particle interaction, clay type (Adamis et al., 2005; Yu et al., 2013), volumetric concentration (Wan, 1982; Laxton and Berg, 2006), fresh or salt water, flow velocity and thixotropic behaviour (Einstein, 1906; Richardson and Zaki, 1954; Coussot, 1997). The influence of clay concentration, for kaolinite clay, can be roughly divided into three sections, low concentrations where the behaviour is linear ($\phi < 15\%$), non-linear behaviour at intermediate concentrations ($15\% < \phi < 42\%$) and shear-thinning at high concentrations ($\phi > 42\%$) (Beazley, 1972; Zhu et al., 2017), where ϕ [−] is the volumetric concentration. Nguyen et al. (2018) suggest that the Bingham model is suitable for when the clay to water content ratio is <1 and Hershel-Bulkley for when the clay to water content ratio is ≥ 1.

Einstein (1906) proposed a correlation between viscosity of turbid water and clear water based on the suspended concentration.

$$\mu_e = \mu(1 + 2.5\phi) \tag{1.12}$$

where μ_e is the effective viscosity and μ the viscosity of clear water. The correlation of Einstein (1906) is valid for dilute suspensions ($\phi < 2\%$) of non-interacting spheres or ellipsoids, i.e. non-cohesive sediment. The rate of influence of particles on neighbouring particles increases as the sediment concentration increases and therefore often a multinomial correlation is used, of which higher orders can be neglected (Russel et al., 1989; Wan and Wang, 1994).

$$\mu_e = \mu(1 + k_1\phi + k_2\phi^2 + O(\phi^3)) \tag{1.13}$$

Values for k_1 have been found to be around 2.5, but literature suggest a large range for k_2 values, varying from 7.6 (Batchelor, 1972) to 14.1 (Pabst, 2004; Mueller et al., 2010), depending on flow conditions. The effective viscosity exhibits a steeper increase with concentration with a high degree of anisometry (e.g. plate shape clay particles, Section 1.2.4) than suspensions with isometric or spherical particles (Gregorova et al., 2009). Due to large amount of factors influencing the yield stress and effective viscosity, numerous empirical models exist in literature (Wan, 1982; Krieger, 1972; Adamis et al., 2005; Yu et al., 2013; Spearman, 2017).

Thixotropy, described as a phenomenon of reversible changes of colloidal solutions from fluid conditions to an elastic solid-like gel (Peterfi, 1927; Freundlich, 1935; Mitchell, 1960; Ren et al., 2021, Section 1.2.3), and shear-thinning behaviour of mud (Barnes, 1997; Sun and Huang, 2015) influences the kinematics of flow behaviour in clay-laden flows (Skempton and Northey, 1952; Evans and Ryan, 2005; Hu et al., 2017). Shear thinning behaviour enables the viscosity to increase

with a reduction in flow velocity, i.e. shear rate, while maintaining the clay concentration, which enables the development of a network of cohesive bonds between clay particles (Coussot, 1997; Baas et al., 2009; Talling et al., 2013, Section 1.3). The reduction in velocity and the increased viscosity both results in a reduction of Reynolds number (Equation 1.1), in a transient mode due to the thixotropic processes (Skempton and Northey, 1952). However, the rate at which the clay-laden flows adjust to the changes in velocity remains unknown.

1.3. Transitional flows

With increasing clay concentration flow properties change from Newtonian to non-Newtonian (Wang and Plate, 1996, Section 1.2.5). Relatively small percentages of clay can enhance or dampen fluid turbulence and result in transitional flow conditions. Baas et al. (2009) defined a clay flow classification scheme, consisting of five different flow types in order of increasing clay concentration: turbulent flow (TF), turbulence-enhanced transitional flow (TETF), lower transitional plug flow (LTPF), upper transitional plug flow (UTPF), and quasi-laminar plug flow (QLPF) (Figure 1.10). The dynamic properties of clay-laden flows are strongly dependent on the clay concentration and turbulence properties (Baas et al., 2009, Section 1.1.2).

Subaqueous sediment gravity currents vary in their sediment concentration that correlates with their particle support mechanism (Haughton et al., 2009; Talling et al., 2012; Pickering and Hiscott, 2015). On one side of the spectrum, turbidity currents are relatively dilute flows, in which the particles are supported by the upward component of fluid turbulence (Mulder and Alexander, 2001; Leeder, 2011); correlated to TF flows based on the classification of Baas et al. (2009). On the other side of the spectrum, debris or mud flows have limited internal turbulence and cohesive sediment provides the grain support through yield strength (Middleton and Hampton, 1973; Mulder and Alexander, 2001). The cohesive strength resists the admixture of water into the flow, maintaining the coherence of the body (Mulder and Alexander, 2001); equivalent to QLPF flows based on the classification of Baas et al. (2009). Transitional flows bridge the gap between turbidity currents, i.e. turbulent flows, and debris flows, i.e. quasi-laminar plug flow. These transitional flows contain various degrees of turbulence enhancement or attenuation (Wang and Plate, 1996; Baas et al., 2009; Sumner et al., 2009).

For non-cohesive sediment gravity currents, turbidity currents can be subdivided into low-density turbidity currents and high-density turbidity currents. The point of transition between low and high density is a contentious issue (Kuenen, 1950; Kuenen and Migliorini, 1950; Kuenen, 1951; Lowe, 1982; Talling et al., 2012). Fluid turbulence is the main particle support in low-density turbidity currents, whereas other processes, such as grain-to-grain interactions, development of excess pore pressure and hindered settling, play a role in supporting sediment within high-density turbidity currents (Lowe, 1982; Talling et al., 2012). This division into low- and high-density turbidity currents is complex to apply to clay-laden gravity currents as the behaviour of cohesive sediment is fundamentally different from that of non-cohesive sediment (Whitehouse et al., 2000; Winterwerp and Van Kesteren, 2004; Talling et al., 2012). This thesis focuses on clay-laden open-channel flows and gravity current, in which the used terminology follows the interpretation of transitional, turbulence-modulated flow behaviour.
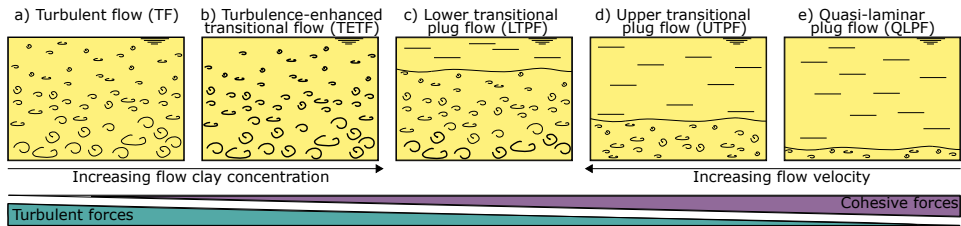
1

Figure 1.10: Schematic model of the balance between cohesive and turbulent forces that determines the behaviour of turbulent, transitional and laminar clay-laden flows, divided into five different types after the classification scheme of Baas et al. (2009). Modified after Baas and Best (2002).

In open-channel flows, TF has a logarithmic vertical velocity profile (Nezu and Nakagawa, 1993, Section 1.1.3, Figure 1.10a) with an associated decrease in turbulence intensity away from the bed. In this flow type, turbulent fluctuations are strong enough to prevent the clay from forming cohesive bonds (Baas et al., 2011).

The velocity of turbulence-enhanced transitional flows progressively diminishes, in particular close to the base of the flow, which is caused by a drag reduction in the boundary layer. Over the full flow depth, TETF exhibits a progressive increase in turbulence intensity over the full flow depth, whilst the logarithmic velocity profile is maintained (Figure 1.10b).

With increasing clay concentration, cohesive forces outbalance turbulent forces near the flow surface where the shear stress is lowest and clay particles establish a network of electrostatic bonds. Baas and Best (2002) suggested that the formation of cohesive electrostatic bonds between clay particles prevent the upward dispersion of turbulent eddies. This results in a plug flow region, which is virtually free of turbulence. A large gradient of turbulent intensity is noticeable between the base of the flow, a basal layer of high velocity gradient, and the top of the flow, a plug flow region which has low, or no, vertical gradients in downstream velocity (Figure 1.10c, Baas and Best, 2002; Baas et al., 2011). Vorticity, in the form of Kelvin-Helmholtz instabilities, penetrates upwards into the flow from the shear layer, whilst gradually dissipating (Baas et al., 2011), resulting in a saw-tooth signal in the downstream velocity (Baas and Best, 2002).

The plug flow region expands downwards as clay concentration increases, changing flow conditions from LTPF to UTPF (Figure 1.10d). The maximum turbulence moves away from the bed, showing similar reduction in near-wall velocity gradient and growth of viscous sublayer as found in drag-reducing flows (Best and Leeder, 1993; Li and Gust, 2000), where a decrease in shear stress in the viscous sublayer is found (Toms, 1949; Virk, 1975; Gust, 1976; Best and Leeder, 1993; Li and Gust, 2000). UTPF flows comprise decreased near bed velocities and reduced turbulence intensity. The velocity profile for LTPF and UTPF is best described by Coles wake function (Baas et al., 2009, Section 1.1.3).

If the clay concentration increases further, clay particles form a gel, increasing the effective viscosity of the flow and suppressing most of the turbulence (Baas et al., 2011, Section 1.2.5). The yield stress within most of the flow is high enough to prevent any turbulence from breaking up the electrostatic bonds between clay particles (Baas et al., 2009). In quasi-laminar plug flows the turbulence is fully suppressed apart from minor residual turbulence near the base of the flow within a thin shear layer (Figure 1.10e).

Research has focussed frequently on the two end members of the flow spectrum, turbidity current and debris flow (Lowe, 1982), but the dynamic structure of transitional clay flows is more complex than the existing conceptual models portray (Baas et al., 2009; Haughton et al., 2009; Hermidas et al., 2018). The transitional flow types that bridge the gap between turbidity current and debris flow are currently poorly understood. Gravity currents are difficult to observe and measure in

nature (Xu et al., 2004; Talling et al., 2015; Heijnen et al., 2020) and the behaviour of cohesive gravity currents is critically influenced by suspended clay (Baas et al., 2009; Baker et al., 2017; Hermidas et al., 2018). Based on flow visualisation in experiments, a turbidity current, generally with a low density, is fully turbulent, whereas a debris flow, generally with a high density, moves as a coherent mass without significant deformation (Mohrig and Marr, 2003; Felix and Peakall, 2006; Baker et al., 2017). The key distinction is the mode of transport, turbulence within a turbidity current and matrix strength or grain-to-grain interaction (cohesion), in debris flows (Mulder and Alexander, 2001; Kneller and Buckee, 2000; Haughton et al., 2009). Hermidas et al. (2018) defined transitional flow properties for gravity currents based on the division of three layers: free shear layer, boundary layer and plug flow layer. However, insufficient turbulence data were presented to ascribe the flows to a specific transitional flow category of Baas et al. (2009).

It should be noted that due to the complex interplay of cohesive and turbulent forces, no single concentration value should be used as a general discriminator of clay flow types for either open-channel flows or gravity currents, although previously suggested for distinguishing turbidity currents from debris flows (Middleton, 1993; Shanmugam, 2000; Mulder and Alexander, 2001; Pickering and Hiscott, 2015).
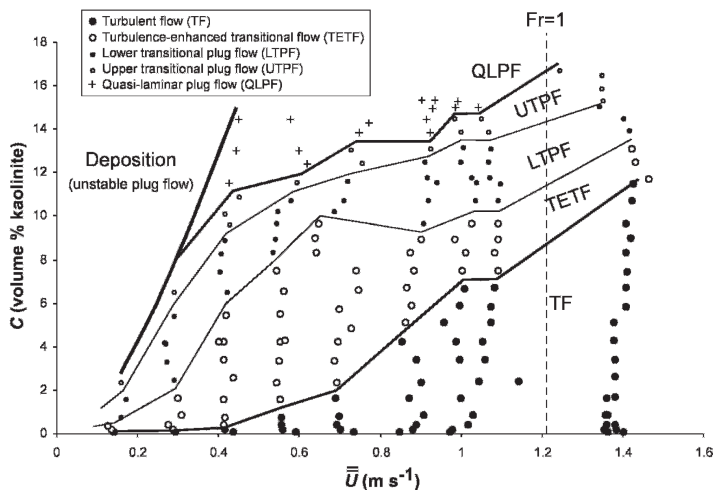
Figure 1.11: Phase diagram as a function of depth-averaged flow velocity, $\overline{\overline{U}}$, and depth-averaged clay concentration, C, for kaolinite flows moving over a flat, smooth, fixed boundary (Baas et al., 2009).

Flow velocity and clay concentration are the principal physical parameters that control the dynamics of clay flows (Figure 1.11). In general, at higher velocities, the turbulence intensity is higher and flows are more able to prevent flocculation and gelling. However, turbulence modulation depends on multiple factors in natural flows, including fluid shear, bed surface roughness (Section 1.1.3), flow velocity, mixture with non-cohesive sediment and characteristics of the clay such as clay type (Section 1.2.4) and concentration (Baas and Best, 2002, Section 1.2.5). A hydraulically rough boundary instead of a smooth boundary results in a comparable correlation between turbulent and cohesive forces, but excludes TETF-type flows (Baas and Best, 2009). Bentonite is a clay mineral that attains higher viscosities at lower volumetric concentrations within a flow than kaolinite and therefore lower concentrations are needed to form transitional flow conditions (Baas et al., 2016a, Section 1.2.4). Natural flows typically transport mixtures of cohesive, non-cohesive and organic material, for which the relative fraction of clay or biological cohesion can significantly influence the flow behaviour (Paterson et al., 1990; Malarkey et al., 2015; Takahashi, 2014; Parsons

1

et al., 2016; Shakeel et al., 2019). In addition, salinity enhances cohesion by aiding flocculation compared to fresh water (Di Maio, 1996; Li and Gust, 2000; Laxton and Berg, 2006; Rinaldi and Clariá Jr, 2016). Baas et al. (2009) defined transitional flow properties for open-channel flows, but transitional flows occur frequently in subaqueous gravity currents as well. The stability regimes are expected to vary for gravity currents from those of open-channel flows (Baas et al., 2009), because turbulence at the upper flow boundary in gravity currents is stronger than near the free surface of hydrodynamically equivalent open-channel flows (Mulder and Alexander, 2001; Leeder, 2011; Hermidas et al., 2018; Wells and Dorrell, 2021). However, to date the balance between turbulent and cohesive forces identified for open-channel flows are used to understand turbulent-laminar transitions in gravity currents and related deposits (Sumner et al., 2009; Baker and Baas, 2020; Peakall et al., 2020; Baas et al., 2021).

The flow dynamics for clay-laden flow have been determined for uniform, steady flow conditions, i.e flows that do not change in time nor in space. The phase diagram (Figure 1.11) suggests that if a flow is non-uniform or unsteady there are regions within the clay concentrations versus velocity space where transitions within flow types occur. Despite flows being non-uniform or unsteady in nature, these transitions within clay flow types are poorly understood. It is expected that the thixotropic process influences the varying flow conditions, but the exact influence remains unknown (Section 1.2.3) for both open-channel flows and gravity currents.

1.4. EXPERIMENTAL DESIGN

Predicting the nature of sediment transport and deposition from open-channel flows or gravity currents relies on a detailed understanding of fluid dynamics (Soulsby, 1997; Whitehouse et al., 2000). However, research on the internal structure of clay-laden flows is limited due to the challenges of data acquisition in opaque, high-concentrated flows. Especially for gravity currents, there is an added challenge due to the difficulty of observing these flow types in nature, due to their relatively inaccessible location, often unpredictable occurrence and ability of the flow to severely damage instruments in place (Talling et al., 2013; Azpiroz-Zabala et al., 2017). For physical experiments, the only technique currently available for velocity measurements in high-concentrated flows is Ultrasonic Velocity Profiler (UVP) (Best et al., 2001; Baas and Best, 2002). Other frequently used measurement equipment, for example, acoustic doppler velocimeter (ADV) or particle image velocimetry (PIV) measurements, are unable to measure in clay-laden flows (Poelma et al., 2006; Tropea et al., 2007; Linne et al., 2009; Aberle et al., 2017; Thomas et al., 2017) and consequently, previous research has focused on conceptual models based on visualisation with a lack of quantitative support (Kneller and Buckee, 2000; Mohrig and Marr, 2003; Nogueira et al., 2013; Baker et al., 2017) or relied on the use of a saline solution to generate density excess (Simpson, 1997; Kneller and Buckee, 2000).

The development of Ultrasonic Velocity Profilers (UVPs) allows the collection of velocity measurements within opaque sediment-laden suspensions, which can enhance the understanding of fluid turbulence within these high-concentrated flows (Takeda, 1991; Best et al., 2001). Albeit, UVPs are designed to work along a single beam (Met-Flow, 2002) and consequently, the clay flow classification scheme defined by Baas et al. (2009) is based upon streamwise velocity measurements. In physical experiments, the profiler can be installed facing upstream in the flow direction to measure the horizontal component of flow velocity (Chapter 2). This allows accurate measurements of the horizontal flow component, but only at 1 measurement height in the flow, i.e. at the height of the installation of the profiler. To collect velocity measurements at multiple heights within the flow, the UVP can be placed under an angle of 30 up to 45° relative to the vertical (Tropea, 1983; Lhermitte and Lemmin, 1994; Pedocchi and García, 2012, Chapter 3). In this method, the vertical velocity is assumed to be zero in order to convert the measurements to a streamwise velocity profile.

To measure the flow velocity, UVPs uses the doppler shift which relies on use of pulsed echosound echography wherein an ultrasound pulse is emitted along a measuring line from profiles, and the same profiler receives the echo reflected from the surface of small particles supended within the flow (Takeda, 1991; Best et al., 2001). A short emission of ultrasound is transmitted after which an UVP switches to receiving mode. Part of the ultrasound energy scatters if it hits a small particle, which the UVP is able to detect in the receiving mode (Met-Flow, 2002). These small particles can be suspended sediment (e.g. clay particles) within the flow or additional seeding if the concentration of suspended sediment is low. The Doppler shift frequency is determined from several repeated ultrasound pulses, which is used to determine the flow velocity (Met-Flow, 2002):

$$U = \frac{f_d c}{2 f_0} \tag{1.14}$$

where U is the flow velocity, f_d the Doppler shift, c the sound velocity in liquid (1480 m/s) and f_0 the transmitting frequency.

1.5. Research objective and thesis outline

In a flow, cohesive clay particles may form larger particles, or flocs, when the distance between the particles is sufficiently small (van Olphen, 1977; Winterwerp and Van Kesteren, 2004, Section 1.2). Networks of flocs in the flow, i.e., clay gels, enhance viscosity and yield stress, and thus are a key control on flow turbulence (Baas and Best, 2002, Section 1.2.5). Research into steady, uniform clay flows indicates a close interaction between turbulent and cohesive forces, controlling the dynamic structure of clay flows (Baas and Best, 2002; Baas et al., 2009, Section 1.3). As the clay concentration increases, it becomes increasingly difficult to break the cohesive bonds between particles, resulting in the formation of a pervasive network of permanently interlinked clay particles; turbulent energy is dissipated by the high effective viscosity, and the flow becomes laminar. Conversely, the electrostatic bonds between the clay particles can be broken in regions of high shear (Section 1.2.3). Thus, an increase in turbulence generation in the flows by, for example, an increasing flow velocity has the potential to break bonds between the clay particles and reduce the flow viscosity (Partheniades, 2009). This shifting balance between turbulent and cohesive forces regulates the dynamic structure of cohesive flows (Baas et al., 2009, Section 1.3).

Natural flows commonly transport high concentrations of cohesive sediment. Transient turbulent behaviour has been recognized in a wide range of environmental flow. For example: at the Dutch shoreface and shelf in the North Sea, near Noordwijk, reductions in bed load transport are found at locations with high mud contents. These high mud concentrations might have damped the turbulence and therefore decreased the bed load transport rate (Kleinhans and Grasmeijer, 2006). Mud-rich sandstone deposits that are likely deposited by flow that became transitional between turbidity currents and debris flows, for example in the Oligocene flysch of the East Carpathians, Romania (Sylvester and Lowe, 2004) or in the Lower Cretaceous Britannia Formation, UK North Sea (Lowe and Guy, 2000; R. Lowe et al., 2003). Diffusely laminated silt and muds in fjord-marine deposits in Trondheimsfjorden near the outlet of the Nidelva River were possible formed by fluctuating transitional flows (Hansen et al., 2011). Nonetheless, the likelihood of occurrence of transitional flow conditions in natural environments, transitional flow properties to date have not been measured within field campaigns. Natural clay flows are opaque and consequently difficult to study or image. Additionally, gravity currents are unpredictable, difficult to observe and measure in nature as these flows are strong enough to damage the measurement equipment (Xu et al., 2004; Talling et al., 2015; Heijnen et al., 2020). The lack of field flow measurements means that a lot of aspects of transitional flow conditions remain unknown, whereas the have large implications on the sediment transport rates in rivers, estuaries, oceans and location and type of sedimentary deposits. Only with the development of Ultrasonic Velocity Profiler (UVP), it became possible to

1

reveal the complex internal dynamics of clay-laden flows with high concentrations in laboratory experiments (Best et al., 2001; Baas and Best, 2002).

The transitional clay flow properties are based on flume experiments of steady, uniform clay flows (Baas et al., 2009, Section 1.3). However, flows are naturally non-uniform (varying in space) or unsteady (varying in time). The effect of clay on non-uniform or unsteady flow is essential for understanding sediment-laden flow dynamics. The formation of bonds between cohesive sediment particles is a time-dependent (thixotropic) process (Section 1.2.3) and, therefore, cohesive sediment-laden flows need time to adjust to spatial variations in flow velocity. However, the changing balance between turbulent and cohesive forces in clay-laden flows under non-uniform or unsteady conditions is poorly understood. Understanding this balance is pivotal, as erosion, transport, and deposition of sediment depend on the magnitude and distribution of flow turbulence (Dorrell et al., 2018), especially as high-concentration clay-laden flows occur more frequently due to climate change (Barbero et al., 2015). Spatio-temporal increases and decreases in turbulence directly affect the transport capacity and deposition and erosion patterns (Dorrell and Hogg, 2012; Moody et al., 2013). Therefore, the main objective of the research is to:

Understand turbulence modulation in non-uniform and unsteady clay suspension flows.

To achieve the overall objective, the following research questions will be answered in the chapters of this thesis.

1. *How are non-uniform, i.e. spatially accelerating and decelerating, flows influenced by suspended cohesive sediment?*

The transitional flow properties that are based on the shifting balance between turbulent and cohesive forces have been identified for uniform open-channel flows (Section 1.3). However, flows are naturally non-uniform. For example, the geometry of channels and bedform properties contain variations in flow depth, width or bed slopes enforcing changes in velocity. The dynamics of these non-uniform open-channel clay suspension flows are poorly understood. However, magnitude and distribution of flow turbulence directly influence sediment transport capacity. Therefore, an increased understanding of the influence of cohesive sediment on non-uniform flow conditions is needed. Chapter 2 details experimental results on the flow structure of clay-laden flows, isolating spatial deceleration and acceleration in open-channel flows.

2. *What is the adaptation time of transitional flows to velocity changes?*

The formation or breakage of bonds between cohesive sediment particles contains time-dependent processes (Section 1.2.5) influencing the adaptation of turbulent, transitional and laminar flows to non-uniform open-channel flows (Chapter 2). However, flows are naturally unsteady, with tides or floods as classical examples. Changes in velocity, e.g. non-uniform or unsteady flow, are expected to influence the adaptation of clay-laden flows, but the adaptation time of clay-laden flows to temporal varying flow velocities remains unknown. Currently, it is unknown if the adaptation to velocity changes due to geometry (non-uniform, spatial variations, Chapter 2) or time (unsteady, temporal variations, Chapter 3) have similar or different time and length scales. The temporal scales of turbulent-laminar transitions in naturally unsteady flows

remain unknown, but are key for understanding sediment-laden flow dynamics and directly affects sediment transport capacity. An increased understanding of the influence of cohesive sediment on unsteady flow conditions is needed. Chapter 3 details experimental results on the flow structure of clay-laden flows, isolating temporal deceleration and acceleration in open-channel flows.

  3. *How do the flow dynamics of non-uniform clay-laden gravity currents evolve?*

Gravity currents are naturally non-uniform and continuously evolve as they move downstream. To date, the balance between turbulent and cohesive forces identified for open-channel flows is used to understand turbulent-laminar transitions in gravity currents. However, gravity currents are fundamentally different from open-channel flows as gravity currents are driven by the action of gravity on the density difference between the particle-fluid mixture and the ambient fluid. Consequently, the stability regime of Baas et al. (2009) might not be suitable for gravity currents and the adaptation to non-uniform conditions might be different than in open-channel flows (Chapter 2). Gravity currents are major agents of sediment transport in seas and oceans and the turbulence dynamics modified by suspended clay have direct influence on the sediment transport and deposits. Consequently, an increased understanding of the influence of cohesive sediment on non-uniform gravity currents is needed. Chapter 4 details experimental results on the flow structure of clay-laden gravity currents.

  Finally, Chapter 5 summarizes the main findings of this thesis and discusses their broader implications.

2

TURBULENCE MODULATION IN NON-UNIFORM OPEN-CHANNEL CLAY SUSPENSION FLOWS

Cohesive properties of clay promote the formation of clay flocs and gels and relatively small suspended clay concentrations can enhance or suppress turbulence in a flow. Flows are naturally non-uniform, varying in space and time, yet the dynamics of non-uniform open-channel clay suspension flows are poorly understood. To research the influence of suspended cohesive clay on changing flow dynamics under non-uniform flow conditions, new experiments were conducted using decelerating and accelerating clay suspension open-channel flows in a recirculating flume. The flows transition between clay flow types, with different degrees of turbulence enhancement and attenuation as the flow adapts to the change in velocity. The experimental results show that decelerating clay suspension flows have a longer adaptation time than accelerating clay suspension flows. The formation of bonds between cohesive sediment particles is a time-dependent process and establishing clay bonds, as in the decelerating flows, requires more time than breaking them, as in the accelerating flows. These different adaptation time scales and associated clay flow type transitions are likely to affect erosional and depositional processes in a variety of fluvial and submarine settings.

2.1. INTRODUCTION

Cohesive sediment-laden flows are important in a wide range of natural environments, such as rivers, estuaries, shallow seas and deep oceans (Whitehouse et al., 2000; Winterwerp and Van Kesteren, 2004), and in industrial settings (Ackers et al., 2001). For example, cohesive sediment supply to rivers can be increased by high-magnitude, low-frequency events, such as storms, floods and post-wildfire erosion (Swanson, 1981; Sankey et al., 2017), which occur more often because of climate change (Geertsema et al., 2006; Reneau et al., 2007; Barbero et al., 2015). Further, cohesive sediment is common in submarine gravity currents, such as turbidity currents and mass transport events and associated deposits, such as hybrid event beds (Talling et al., 2012). The increases in sediment transport can have major impacts on water quality and aquatic ecosystems, including fish habitats, and also on channel morphology (Smith et al., 2011). High suspended sediment concentrations modify flow dynamics by either enhancing (Best et al., 1997) or dampening turbulence (Bagnold, 1954; Wang and Larsen, 1994), influencing sediment transport rates and erosion and deposition patterns (Mehta et al., 1989; Partheniades, 1965). These processes can be enhanced by the presence of cohesive sediment in suspension due to the cohesive properties promoting flocculation (Baas and Best, 2002; Section 1.2). Baas et al. (2009) defined a clay flow classification scheme, consisting of five different flow types in order of increasing clay concentration: turbulent flow (TF), turbulence-enhanced transitional flow (TETF), lower transitional plug flow (LTPF), upper transitional plug flow (UTPF), and quasi-laminar plug flow (QLPF) (Figure 1.10, Section 1.3).

Flows are naturally non-uniform. The geometry of channels and bedform properties result in variations in flow depth and width or bed slopes, which can enforce changes in velocity. Non-uniform flow within experimental settings can be achieved by different methods including converging or diverging the flume width or using positive or negative longitudinal bed slopes. Previous research often uses a sloping bed where the spatial variation in the flow depth forces the flow to accelerate or decelerate (Cardoso et al., 1991; Kironoto and Graf, 1995; Nezu et al., 1997). The inner region of non-uniform flow can be described by the law of the wall (Section 1.1.3), but within the outer region, systematic deviations occur. The velocity profile of decelerating flow gets more slender and falls above the log-law (Kironoto and Graf, 1995; Nezu et al., 1997). Accelerating flows tend to have a fuller velocity profile and fall below the log law (Cardoso et al., 1991). In the near-bed region accelerating flows contain larger velocity gradients than decelerating flows (Figure 2.1a,b, Song and Chiew, 2001).
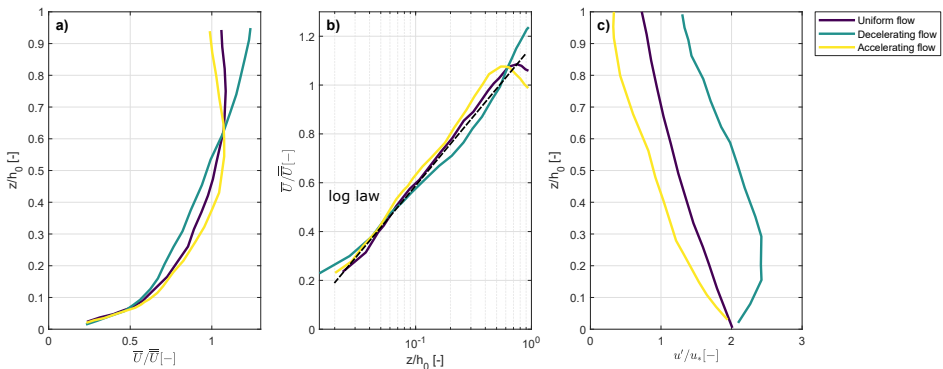
Figure 2.1: a) Vertical profiles of time-averaged velocity ($\overline{U}$) normalised by depth-averaged velocity ($\overline{\overline{U}}$); b) Normalised velocity profiles on a logarithmic scale; c) Vertical profile of turbulence intensity (u'/u_*) for uniform and non-uniform flow. Modified after Kironoto and Graf (1995).

Based on flume experiments, non-uniform flow forced by a change in width or change in bed slope contain comparable velocity and turbulence intensity profiles (Kironoto and Graf, 1995; Yang et al., 2006; Emadzadeh et al., 2010). Explanation of these profiles is based on a change in bed slope, which is a more common method in previous research. Changing the bed slope produces a spatial variation in flow depth in the flow direction, forcing the flow to accelerate or decelerate. In a gradually varied flow, the pressure distribution follows the hydrostatic distribution (Chaudhry, 2008). A positive pressure gradient (decelerating flow), results in an increasing shear near the bed and a negative pressure gradient (accelerating flow) results in a decreasing shear compared to uniform flow (Kironoto and Graf, 1995; Emadzadeh et al., 2010). Correlated to an increase in the pressure gradient, increasing the slope to force changes in velocity results in an increase in Reynolds stresses for decelerating flow and a decrease for accelerating flow (Emadzadeh et al., 2010). In uniform flows, the vertical velocity is zero. However, in decelerating flow, the vertical velocity can be positive or upwards as the water depth increases and negative in accelerating flow with decreasing water level (Yang et al., 2006). Due to the presence of a vertical velocity, the Reynolds shear stresses deviate from the standard linear distribution (1-y/h) (Yang et al., 2006, Section 1.1.2). The Reynolds shear stresses in decelerating flow are amplified compared to uniform flow and the maximum is found at a certain distance above the bed; the profiles are convex (Cardoso et al., 1991; Song and Chiew, 2001). Whereas in accelerating flow the Reynolds shear stresses are damped and the maximum can be found near the bed; the profiles are concave (Figure 2.1c, Kironoto and Graf, 1995; Song and Graf, 1996). Yang et al. (2006) suggest that a linear correlation can be found if an additional momentum term ($-uv$) is included. Additionally, Nezu et al. (1997) suggest that the Coles' wake parameter is influenced by a vertical velocity, thus resulting in a higher positive value for decelerating flow and a reduced potentially negative value for accelerating flow.

In this chapter, flow non-uniformity is taken to refer to streamwise changes in depth-averaged velocity in space (along the flume). Predicted sediment transport rates, assuming uniform flow, may differ from real-world rates (Wan and Wang, 1994). The effect of clay on streamwise decelerating and accelerating flow is essential for understanding sediment-laden flow dynamics. The formation of bonds between cohesive sediment particles is a time-dependent (thixotropic) process and, therefore, cohesive sediment-laden flows need time to adjust to spatial variations in flow velocity. However, the changing balance between turbulent and cohesive forces in clay-laden flows under non-uniform conditions is poorly understood. Understanding this balance is pivotal, as erosion, transport, and deposition of sediment depend on the magnitude and distribution of flow turbulence (Dorrell et al., 2018). Spatio-temporal increases and decreases in turbulence directly affect the transport capacity and deposition and erosion patterns (Dorrell and Hogg, 2012; Moody et al., 2013).

An increased understanding of the influence of cohesive sediment on non-uniform flow conditions is needed. This chapter details experimental results on the flow structure of clay-laden flows, for the first time isolating the effect of non-uniformity on spatial deceleration and acceleration in open-channel flows. The following research questions are addressed: (1) What are the mean flow and turbulence characteristics of horizontally decelerating and accelerating clay-laden flows? (2) How do non-uniform flows with different suspended clay concentration compare to each other and to uniform clay-laden flows? (3) How much time do decelerating and accelerating flows need to adapt to the changing flow conditions?

2.2. METHODOLOGY

The methodology section is divided into four sections. The experimental setup, involving the description of the flume, equipment location and preparation of the runs is described in Section 2.2.1. The experimental conditions are described in Section 2.2.2. The measurement techniques and instruments used are described in Section 2.2.3 and Section 2.2.4 describes the methods used for the data processing and analysis.

2.2.1. EXPERIMENTAL SETUP

Mixtures of pure kaolinite (Imerys Polwhite-E, $d_{50} = 9 \ \mu m, \rho_s = 2600 \ kg/m^3$, Figure 2.2, Section 1.2.4) and fresh water were circulated through a hydraulic flume by means of a variable-discharge slurry pump (Figure 2.3a). Usage of kaolinite, similar to the material used in the definition of clay flow types (Baas et al., 2009), allows for a more direct comparison between uniform and non-uniform clay-laden open-channel flows. The flume was 10 m long and 0.5 m wide, with a standing water depth, h_0, of 0.15 m.
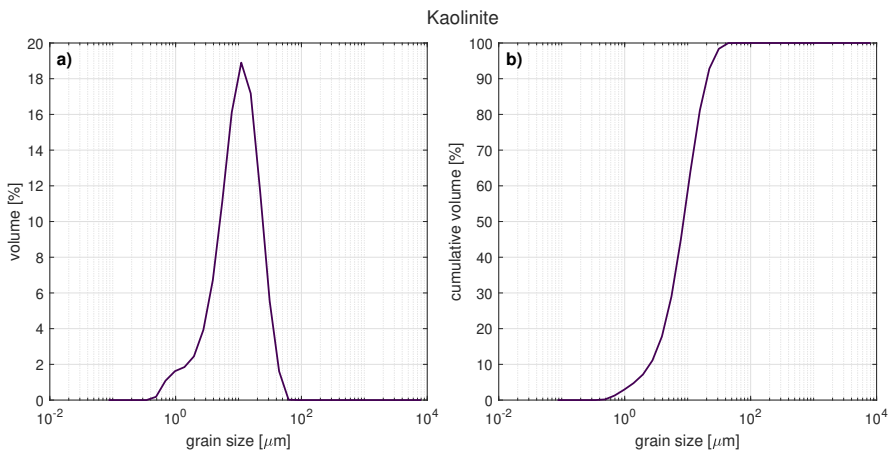
Figure 2.2: a) Grain size distribution kaolinite, b) cumulative grain size.
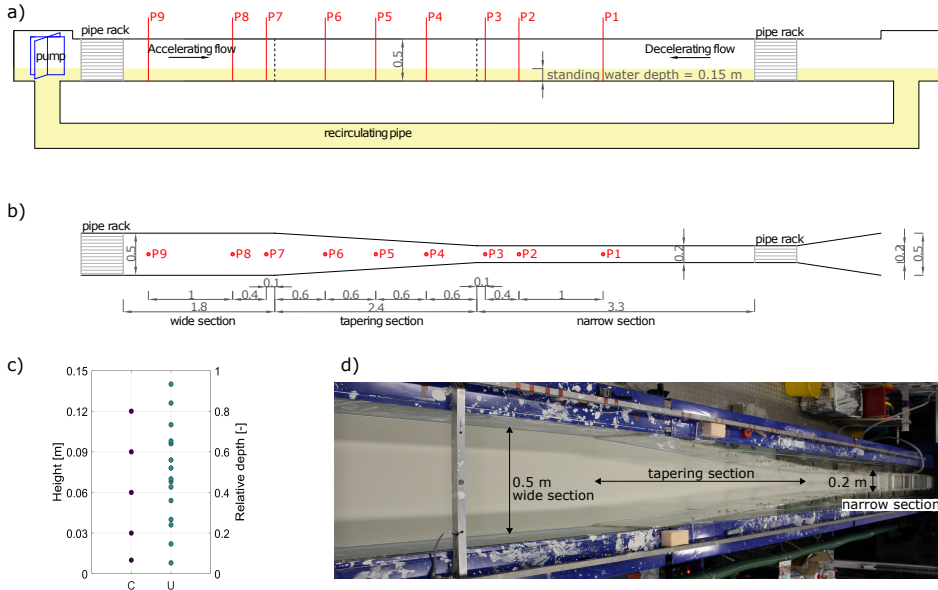
Figure 2.3: a) Side view of the experimental setup, b) top view of the inset channel, with points P indicating measurement locations, c) velocity (U) and sediment concentration (C) measurement positions above the channel bed; relative depth = height / depth, d) photo of the flume setup. All dimensions in meters.

At the upstream end, the flume contained a turbulence-damping grid to straighten the flow. The flow moved over a flat, smooth floor downstream of the turbulence-damping grid. The turbulence-damping grid was made of stacked pipes with the length of the pipes determined by the entrance length, which is the length between the start of the pipe and the point where fully developed flow begins. Within a flow, the shear layer grows in thickness in the flow direction and remains laminar until the Reynolds number exceeds a threshold. The actual value of the critical Reynolds number is strongly dependent on how free from perturbation the outer flow is (Schlichting and Gersten, 2016). Moving downstream in a pipe the thickness of the viscous boundary layer increases until the velocity profiles is parabolic and the flow is fully developed (Figure 2.4). For turbulent flow the entrance length for pipe flows can be defined as (White, 2016):

$$L_e = 4.4Re^{1/6}d \tag{2.1}$$

where L_e is the entrance length, Re the Reynolds number of the flow and d the diameter of the pipes.
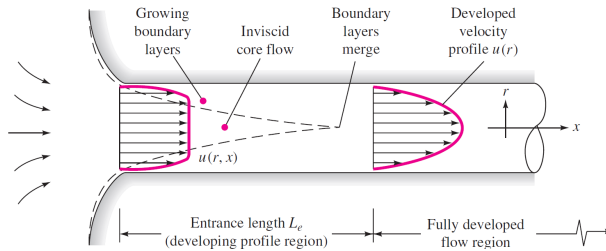
Figure 2.4: Developing velocity profile at entrance of pipe flow (White, 2016).

An inset channel was placed in the flume. It had a 0.2 m wide narrow section and a 2.4 m long tapering section. The inset forced the flow through a narrow to wide transition (decelerating flows) or through a wide to narrow transition (accelerating flows) depending on the flow direction (Figure 2.3b). Thus, in contrast to earlier work in non-tapering flumes (Wang and Plate, 1996; Baas and Best, 2002; Baas et al., 2009), this channel design enabled controlled spatial changes in the flow velocity and turbulence to be measured. Change in width allows the focus on addressing streamwise adaptation of non-uniform clay-laden flow conditions after acceleration or deceleration of the flows. To cover various transitional flow types in the experiments (Section 1.3), the flow velocity needs to be reduced significantly. However, the amount of reduction or accretion is limited by the dimensions of the flume. Reducing the width of the narrow section further than 0.2 m would increase the risk of flow obstruction by the measurement equipment. Based upon the results of Baas et al. (2009), a flow reduction of 2.5 times provided the opportunity to cover a maximum of four flow types depending on the clay concentration.

The flume expansion had a ratio of 1 to 16 to avoid flow separation and recirculation cells. The aspect ratio is based upon the reattachment length occurring at a backward-facing step. The length of the recirculation zone, separated shear layer, depends on the ratio between the boundary layer and the thickness of the step height, parameters of the inflow and channel geometry (Tihon et al., 2012). Previous research suggested different values, but a ratio between reattachment length and step height of 6-8 seemed acceptable (Spazzini et al., 2001; Tihon et al., 2012; Chovet et al., 2017). This ratio is based on turbulent flow and due to the increased viscosity of clay flows and reduced turbulence of transitional flow conditions, a smaller reattachment length is expected for transitional flows containing a plug flow.

Depending on the flow velocity in the flume, the change in flow magnitude can cause a hydraulic jump, which is a natural phenomenon in which supercritical flow is rapidly transformed in subcritical flow with an increased depth (White, 2016). Initial clear water experiments indicated that the highest velocity without a hydraulic jump in the flume is around 0.7 m/s in the narrow section (Figure 2.3b).

2.2.2. Experimental conditions

To assess the influence of flow velocity and clay concentration on turbulent-laminar transitions, experiments were conducted with varying flow velocity and clay concentration for both flow direction, resulting in a total of nine experiments (Table 2.1); control experiments were conducted with clear water. The experimental conditions had been selected based upon the phase diagram of Baas et al. (2009) to cover a range of flow types (Figure 2.5). Clay was soaked in water for a minimum of one day before adding it to the flume, to guarantee that no dry clumps remained. The flume ran for 16 to 20 hours to allow the clay-laden flows to reach equilibrium conditions and allow for any deposition of clay before measurements were taken.

Table 2.1: Overview of experimental runs performed in this study. The labelling of experimental runs is defined using D for decelerating and A for accelerating flows and the depth-averaged clay concentration (C); The variables in the table respond to: C = depth-averaged volumetric concentration; C_m = depth-averaged mass concentration; h_0 = standing water depth; T = water temperature; v_e = effective kinematic viscosity; Measuring point along the flume (Figure 2.3b); $\overline{\overline{U}}$ = depth-averaged velocity; Re = Reynolds number; Fr = Froude number. * deposition was observed at this location.

Experimental run	C [vol %]	C_m [g/L]	h_0 [m]	T [°C]	v_e [$m^2/s \cdot 10^{-6}$]	Measuring point	$\overline{\overline{U}}$ [m/s]	Re [- $\cdot 10^4$]	Fr [-]
				Decelerating flow					
D1-C0.0	0.0	0.0	0.150	16.0	1.00	P1	0.65	9.7	0.54
						P2	0.69	10.3	0.57
						P3	0.71	10.6	0.58

Experimental run	C [vol %]	C_m [g/L]	h_0 [m]	T [°C]	ν_e [$m^2/s \cdot 10^{-6}$]	Measuring point	$\overline{\overline{U}}$ [m/s]	Re [- $\cdot 10^4$]	Fr [-]
						P4	0.59	8.9	0.49
						P5	0.52	7.8	0.43
						P6	0.42	6.2	0.34
						P7	0.34	5.1	0.28
						P8	0.33	4.9	0.27
						P9	0.29	4.3	0.24
D2-C0.0	0.0	0.0	0.158	17.6	1.00	P1	0.46	7.3	0.37
						P2	0.49	7.8	0.40
						P3	0.50	7.9	0.40
						P4	0.44	7.0	0.36
						P5	0.38	5.9	0.30
						P6	0.34	5.4	0.27
						P7	0.30	4.7	0.24
						P8	0.28	4.5	0.23
						P9	0.22	3.5	0.18
D3-C0.9	0.92	63	0.150	18.7	1.06	P1	0.45	6.3	0.37
						P2	0.48	6.7	0.39
						P3	0.46	6.5	0.38
						P4	0.39	5.6	0.32
						P5	0.35	4.9	0.29
						P6	0.33	4.6	0.27
						P7	0.30	4.3	0.25
						P8	0.28	4.0	0.24
						P9*	0.26	3.7	0.21
D4-C1.5	1.47	101	0.150	18.0	1.15	P1	0.60	7.8	0.49
						P2	0.64	8.3	0.52
						P3	0.65	8.5	0.54
						P4	0.56	7.3	0.46
						P5	0.45	6.0	0.37
						P6	0.34	4.5	0.28
						P7	0.34	4.4	0.28
						P8	0.33	4.3	0.27
						P9	0.30	3.9	0.25
D5-C2.7	2.67	180	0.150	18.0	1.41	P1	0.50	5.4	0.42
						P2	0.54	5.8	0.45
						P3	0.55	5.8	0.45
						P4	0.49	5.2	0.40
						P5	0.42	4.5	0.35
						P6	0.32	3.4	0.26
						P7	0.26	2.8	0.22
						P8	0.27	2.9	0.22
						P9	0.28	2.9	0.23
Accelerating flow									
A1-C0.0	0.0	0.0	0.170	17.6	1.00	P1	0.45	7.7	0.35
						P2	0.45	7.6	0.35
						P3	0.44	7.4	0.34
						P4	0.34	5.9	0.27
						P5	0.26	4.4	0.20
						P7	0.16	2.8	0.13
						P8	0.16	2.7	0.12
						P9	0.16	2.8	0.13
A2-C1.4	1.39	94	0.170	18.0	1.13	P1	0.41	6.2	0.32
						P2	0.41	6.2	0.32
						P3	0.41	6.1	0.31
						P5	0.26	3.9	0.20
						P6	0.21	3.2	0.16
						P7*	0.18	2.7	0.14
						P9	0.20	3.0	0.15
A3-C1.5	1.54	105	0.185	18.7	1.16	P1	0.43	6.8	0.32
						P2	0.43	6.9	0.32
						P3	0.42	6.7	0.31
						P4	0.33	5.3	0.25
						P5	0.27	4.3	0.20

2

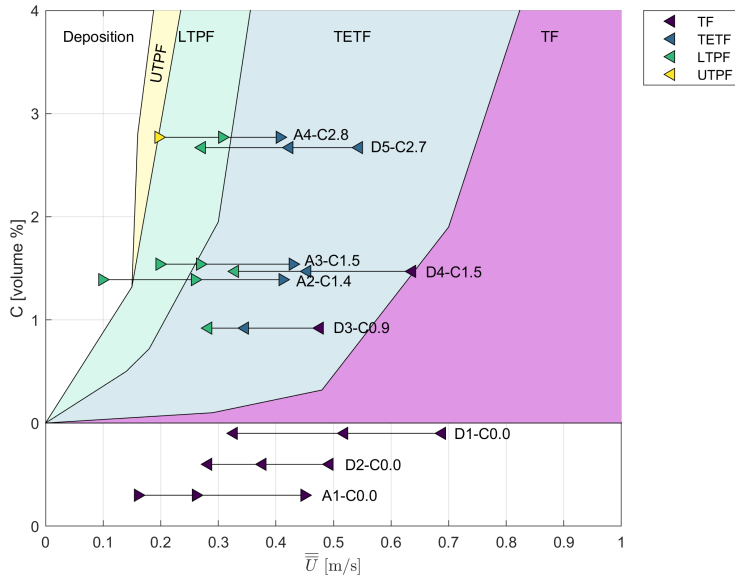| Experimental run	C [vol %]	C_m [g/L]	h_0 [m]	T [°C]	ν_e [$m^2/s \cdot 10^{-6}$]	Measuring point	$\overline{\overline{U}}$ [m/s]	Re [- $\cdot 10^4$]	Fr [-]
A4-C2.8	2.77	182	0.180	18.2	1.43	P6	0.23	3.7	0.17
						P7*	0.17	2.7	0.13
						P8	0.20	3.2	0.15
						P9	0.15	2.3	0.11
						P1	0.41	5.2	0.31
						P2	0.41	5.1	0.31
						P3	0.40	5.0	0.30
						P4	0.33	4.1	0.25
						P5	0.31	3.8	0.23
						P6	0.21	2.6	0.16
						P7*	0.18	2.3	0.14
						P8	0.20	2.5	0.15
						P9	0.19	2.3	0.14

Figure 2.5: Experimental runs over conducted experiments overlaid on results of (Baas et al., 2009).

2.2.3. DATA ACQUISITION

Velocity and clay concentration measurements were collected during the experiments. Velocity measurements were collected at nine locations along the flume to assess the rate of change in flow conditions (Figure 2.3b). The clay concentration was expected to be uniform in the flume during the experiments and therefore only at three locations siphon samples were collected.

SUSPENDED SEDIMENT CONCENTRATION

A vertical rack of siphon tubes was used to collect samples at five different heights in the water column and at three locations for the decelerating (P3, P5, P9) and accelerating (P1, P5, P7) flows (Figure 2.3b, c). To minimize flow disruption a siphon with narrow steel tubing was used (diameter of 2 mm). The steel tubes protruded 65 mm from the front of the rack into the flow and flexible plastic tubing was used to connect the siphon to a peristaltic pump outside the flume. Samples were collected for 2 minutes at five different heights in the flume (Table 2.2) to assess the variations in concentration over the depth (Figure 2.3c). The samples were collected in 60 mL sample pots and were weighed after collection, dried at a temperature of $40°C$ until all water had evaporated, and then weighed again to determine their volumetric clay concentration.

Table 2.2: Measurement height (centrepoint) above the bed (z) of siphon samples to measure the clay concentration

Measurement	z [m]
A	0.01
B	0.03
C	0.06
D	0.09
E	0.12

FLOW VELOCITY

At nine locations along the flume the horizontal component of flow velocity was measured with UVPs (Ultrasonic Velocity Profile) facing upstream (Figure 2.3b) (Takeda, 1991; Best et al., 2001). Six 4 MHz probes were stacked on top of each other with a distance of 14 mm in between their centres. Each UVP had an overall diameter of 13 mm and active diameter of 10 mm, able to measure one projection of a complete flow field (Met-Flow, 2002). The UVPs were directed against the flow direction to measure the streamwise velocity and to reduce the impact of flow obstruction on the measurements. Seeding was added to the flow to increase the amount of suspended material for the ultrasound echo to originate from. Talisman 10 (specific gravity 0.99), pre-sieved to retain the particle size distribution between 20 μm and 100 μm, was used as seeding material (Thomas et al., 2017).

The probe array had been shifted vertically to three different heights to cover the flow depth, resulting in a total of 18 measurement elevations per location (Figure 2.3c). The probes collected velocity data for 500 cycles with a 50 ms delay between probes to avoid measurement interference. The velocity range had been adjusted to the velocity at the different measurement locations to increase the accuracy. Depending on the experimental conditions, these settings result in measurement durations of 174 to 330 s at a temporal resolution of 1.5 to 2.9 Hz. Velocity data was collected between 0.010 m and 0.0559 to 0.0836 m upstream of the probe, at a resolution of 0.00074 m with 50% overlap (Table 2.3). The measurement time is sufficient for statistically significant turbulence characteristics and for determining the mean flow field by averaging out turbulence.

Table 2.3: Settings UVP measurements. TR = Temporal resolution; $D_{upstream}$ = measurement distance upstream from the probe; ΔD = distance resolution; V_{range} = velocity range; ΔV = velocity resolution; X_{data} = distance to the probe head of the data used in the analysis.

2

Experimental run	Measuring point	Duration [s]	TR [Hz]	$D_{upstream}$ [m]	ΔD [m]	V_{range} [m/s]	ΔV [m/s]	X_{data} [m]
Decelerating flow								
D1-C0.0	P1	180	2.78	0.0766	0.00074	1.754	0.0068	0.047
	P2	180	2.78	0.0766	0.00074	1.754	0.0068	0.047
	P3	180	2.78	0.0766	0.00074	1.754	0.0068	0.047
	P4	210	2.38	0.0766	0.00074	1.602	0.0063	0.050
	P5	210	2.38	0.0766	0.00074	1.548	0.0060	0.050
	P6	210	2.38	0.0766	0.00074	1.402	0.0055	0.047
	P7	210	2.38	0.0766	0.00074	1.298	0.0051	0.047
	P8	212	2.38	0.0766	0.00074	1.250	0.0049	0.048
	P9	240	2.08	0.0766	0.00074	1.101	0.0043	0.048
D2-C0.0	P1	212	2.38	0.0836	0.00074	1.250	0.0049	0.047
	P2	213	2.38	0.0836	0.00074	1.250	0.0049	0.048
	P3	212	2.38	0.0836	0.00074	1.250	0.0049	0.048
	P4	240	2.08	0.0836	0.00074	1.149	0.0045	0.047
	P5	240	2.08	0.0836	0.00074	1.101	0.0043	0.047
	P6	270	1.85	0.0836	0.00074	1.000	0.0039	0.048
	P7	270	1.85	0.0836	0.00074	0.900	0.0035	0.048
	P8	270	1.85	0.0836	0.00074	0.900	0.0035	0.047
	P9	273	1.81	0.0836	0.00074	0.851	0.0033	0.043
D3-C0.9	P1	207	2.49	0.0570	0.00074	1.250	0.0049	0.036
	P2	207	2.43	0.0570	0.00074	1.250	0.0049	0.036
	P3	210	2.38	0.0570	0.00074	1.201	0.0047	0.034
	P4	210	2.38	0.0570	0.00074	1.101	0.0043	0.034
	P5	210	2.38	0.0570	0.00074	1.051	0.0041	0.032
	P6	240	2.08	0.0570	0.00074	0.951	0.0037	0.039
	P7	241	2.08	0.0570	0.00074	0.900	0.0035	0.037
	P8	270	1.85	0.0570	0.00074	0.900	0.0035	0.043
	P9	270	1.85	0.0570	0.00074	0.851	0.0033	0.047
D4-C1.5	P1	177	2.87	0.0570	0.00074	1.652	0.0065	0.032
	P2	177	2.83	0.0570	0.00074	1.652	0.0065	0.034
	P3	174	2.87	0.0570	0.00074	1.652	0.0065	0.036
	P4	180	2.77	0.0570	0.00074	1.498	0.0059	0.036
	P5	180	2.78	0.0570	0.00074	1.402	0.0055	0.036
	P6	207	2.38	0.0570	0.00074	1.250	0.0049	0.032
	P7	210	2.38	0.0570	0.00074	1.149	0.0045	0.034
	P8	210	2.38	0.0570	0.00074	1.101	0.0043	0.036
	P9	210	2.38	0.0570	0.00074	1.051	0.0041	0.034
D5-C2.7	P1	174	2.87	0.0559	0.00074	1.652	0.0065	0.028
	P2	177	2.87	0.0559	0.00074	1.652	0.0065	0.028
	P3	174	2.87	0.0559	0.00074	1.652	0.0065	0.028
	P4	180	2.78	0.0559	0.00074	1.498	0.0059	0.030
	P5	180	2.78	0.0559	0.00074	1.402	0.0055	0.032
	P6	180	2.78	0.0559	0.00074	1.298	0.0051	0.030
	P7	183	2.78	0.0559	0.00074	1.250	0.0049	0.023
	P8	210	2.38	0.0559	0.00074	1.201	0.0047	0.026
	P9	210	2.38	0.0559	0.00074	1.201	0.0047	0.029
Accelerating flow								
A1-C0.0	P1	240	2.08	0.0836	0.00074	1.101	0.0043	0.048
	P2	240	2.08	0.0836	0.00074	1.101	0.0043	0.050
	P3	240	2.08	0.0836	0.00074	1.101	0.0043	0.047
	P4	273	1.85	0.0836	0.00074	0.851	0.0033	0.041
	P5	300	1.67	0.0836	0.00074	0.751	0.0029	0.047
	P6	330	1.51	0.0836	0.00074	0.650	0.0025	0.047
	P7	330	1.51	0.0836	0.00074	0.650	0.0025	0.048
	P8	330	1.51	0.0836	0.00074	0.650	0.0025	0.048
	P9	330	1.51	0.0836	0.00074	0.650	0.0025	0.048
A2-C1.4	P1	240	2.08	0.0651	0.00074	1.000	0.0039	0.037
	P2	240	2.08	0.0651	0.00074	1.000	0.0039	0.037
	P3	240	2.08	0.0651	0.00074	1.000	0.0039	0.037

Experimental run	Measuring point	Duration [s]	TR [Hz]	$D_{upstream}$ [m]	ΔD [m]	V_{range} [m/s]	ΔV [m/s]	X_{data} [m]
	P4	270	1.85	0.0651	0.00074	0.799	0.0031	0.041
	P5	300	1.66	0.0651	0.00074	0.751	0.0029	0.036
	P6	300	1.67	0.0651	0.00074	0.751	0.0029	0.041
	P7	330	1.51	0.0651	0.00074	0.699	0.0027	0.043
	P8	330	1.51	0.0651	0.00074	0.699	0.0027	0.047
	P9	330	1.51	0.0651	0.00074	0.699	0.0027	0.047
A3-C1.5	P1	240	2.08	0.0570	0.00074	1.000	0.0039	0.032
	P2	240	2.08	0.0570	0.00074	1.000	0.0039	0.034
	P3	240	2.08	0.0570	0.00074	1.000	0.0039	0.032
	P4	270	1.89	0.0570	0.00074	0.851	0.0033	0.034
	P5	270	1.85	0.0570	0.00074	0.751	0.0029	0.034
	P6	300	1.67	0.0570	0.00074	0.699	0.0027	0.034
	P7	300	1.67	0.0570	0.00074	0.699	0.0027	0.030
	P8	300	1.67	0.0570	0.00074	0.699	0.0027	0.034
	P9	300	1.67	0.0570	0.00074	0.699	0.0027	0.036
A4-C2.8	P1	210	2.38	0.0559	0.00074	1.051	0.0041	0.029
	P2	210	2.38	0.0559	0.00074	1.051	0.0041	0.026
	P3	210	2.38	0.0559	0.00074	1.051	0.0041	0.030
	P4	240	2.08	0.0559	0.00074	1.000	0.0039	0.028
	P5	240	2.08	0.0559	0.00074	0.951	0.0037	0.026
	P6	245	2.08	0.0559	0.00074	0.851	0.0033	0.026
	P7	245	2.08	0.0559	0.00074	0.851	0.0033	0.024
	P8	245	2.08	0.0559	0.00074	0.851	0.0033	0.028
	P9	270	1.85	0.0559	0.00074	0.799	0.0031	0.030

2.2.4. DATA PROCESSING

The UVP data was collected over 128 bins over a set distance away from the probe (Table 2.3). A typical shape of the velocity profile is shown in Figure 2.6a, where the x-axis indicates the distance from the probes in upstream direction. Close to the probe head, the velocity magnitude is reduced due to flow obstruction of the probe array, whilst the accuracy of the velocity data reduces further away from the probes due to a weaker echo signal, resulting in the typical bow-shaped graph. The accuracy of the data depends on the settings of the UVP, velocity and clay concentration in the flume. Therefore, it is not suitable to select a fixed distance from the probe as it will vary per condition, but also per location in the flume. The channels included in the analysis can vary per condition or location but were kept equal at each location to have a constant measurement area over the depth. The area, 11 channels, with the smallest variation in sampled flow velocity was used in the analysis, defined by a relative change in velocity over the distance smaller than 0.01% (Figure 2.6b). The velocity measurements are comparable for the 11 selected channels, but the turbulence intensity can contain larger variations due to the randomness of the measurements. To avoid selecting a channel with relatively high or low turbulence intensity values, out of the 11 selected channels, the channel with turbulence intensity closest to the median of the 11 turbulence intensities was selected. The selected channels used in further analysis were at a distance of 0.03 - 0.05 m, depending on the flow conditions (Table 2.3). The measurements of probe 4, within the stacked UVP array were consistently lower than the measurements of the other probes and therefore the measurements collected by probe 4 are deemed invalid and were excluded from further analysis (Figure 2.7).

2
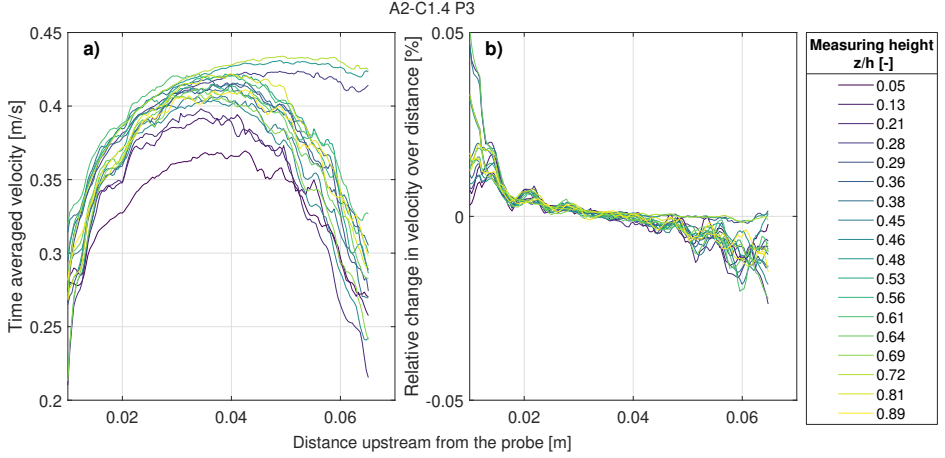
Figure 2.6: a) Time-averaged velocity profile over the distance measured by the UVP probes; b) Relative change of velocity over the distance measured by the UVP probes, for clay-laden accelerating flow A2-C1.4 within the narrow section, P3. For this condition the measurements at a distance of 0.037 m away from the UVP probe is used in the analysis.
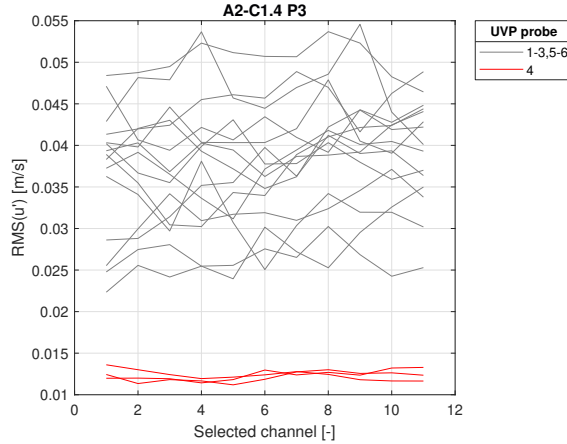
Figure 2.7: Velocity fluctuations over the selected 11 channels of different probes at location P3 for flow A2-C1.4.

Outliers were removed from the velocity signal by eliminating values three standard deviations away from the temporal moving mean over 31 datapoints. Datapoints were excluded where deposition occurs. The temporal mean flow velocity, $\overline{U}$, and its standard deviation, $RMS(u')$, were calculated from the time series of instantaneous velocity data at each measurement height.

$$\overline{U} = \frac{1}{n} \sum_i^n u_i \tag{2.2}$$

$$RMS(u') = \sqrt{\frac{1}{n} \sum_i^n (u_i - \overline{U})^2} \tag{2.3}$$

where n is the number of velocity measurements. A dimensionless measure for turbulence intensity was defined as follows (Baas and Best, 2002):

$$RMS(u')_0 = \frac{RMS(u')}{\overline{U}} \cdot 100 \tag{2.4}$$

Depth-averaged velocity was calculated by integrating the time-averaged velocities over the depth. The integral was numerically evaluated; velocities were set to zero at the bed and velocities at the water surface were assumed to have the same value as the first measurement position below that level.

$$\overline{\overline{U}} = \frac{1}{h_0} \int_0^{h_0} \overline{U} dz \tag{2.5}$$

where h_0 is flow depth and z height above the bed. Depth-averaged turbulence intensity was calculated by integrating the turbulence intensity values over the depth.

$$\overline{RMS(u')_0} = \frac{1}{h_0} \int_0^{h_0} RMS(u')_0 dz \tag{2.6}$$

Outliers within the processed dataset were excluded as follows. Data was identified as an outlier when either the flow velocity, $\overline{U}$, or its standard deviation, $RMS(u')$, was 40% higher or lower than the median value of the six immediately surrounding measurement points from the nearest upstream and downstream locations. Here, the median was used to avoid weighting from outliers. At the outer locations, P1 and P9, the points within the narrow (P2 and P3) or wide (P7 and P8) section were used to include a sufficient number of measurement points in the determination of the median. Near the bed, larger changes in $\overline{U}$ and $RMS(u')$ are likely. Therefore, the lowest measurement elevation was excluded from the outlier analysis. The full measurement location (P1-P9) was deemed invalid if >50% of the data was classified as outliers over the full flow depth. The bed height, z_b, was defined as the height of flume bed, unless potential deposition is observed. Then, the bed height, z_b, was defined as the lowest valid UVP measurement elevation. When the UVP measurements were zero or invalid, there is no flow velocity and consequently at this measurement height it is assumed that deposition occurred. These invalid UVP measurement heights correlated with a measured increase in clay concentration by the siphon samples (Section 2.3.1). To compare the same elevation within different flows, the flows are plotted against normalized height adjusted to the deposit level.

$$\tilde{z} = \frac{z - z_b}{h_0} \tag{2.7}$$

Following Wan (1982), the dynamic viscosity, η, of the suspensions were approximated from the measured suspended sediment concentration.

$$\eta = 0.001 + 0.206\left(\frac{C}{100}\right)^{1.68} \tag{2.8}$$

The effective viscosity of the suspensions has been calculated through the ratio of dynamic viscosity over the density of the clay suspension.

$$\nu_e = \eta / \rho_m \tag{2.9}$$

Where ρ_m is the calculated density of the clay suspension with the density of water adjusted to the temperature according to Huber et al. (2009).

2.3. EXPERIMENTAL OBSERVATIONS

2.3.1. SUSPENDED SEDIMENT CONCENTRATION

The suspended sediment concentrations for the decelerating flows were nearly uniform over the flow depth (Figure 2.8), apart from run D3-C0.9, which contained a higher clay concentration at the lowest sampling point within the wide section of the flume. The suspended sediment concentrations for the accelerating flows were non-uniform along the flume, with higher near-bed sediment concentrations, particularly in the wide section of the flume (Table 2.1). These higher concentrations are within the deposit level of the flows ($\tilde{z} < 0$).
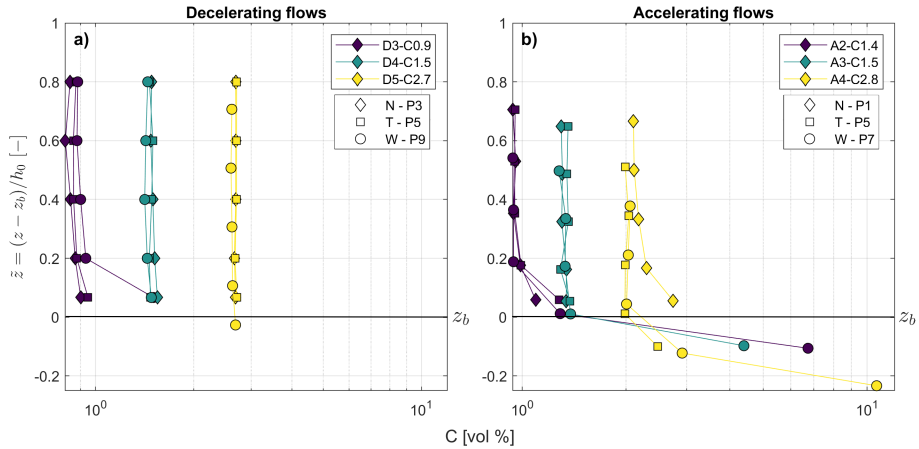

Figure 2.8: Vertical profiles of volumetric sediment concentration against normalised bed height adjusted to deposition (Equation 2.7) for the a) decelerating and b) accelerating clay-laden flows. N, T and W denote narrow, tapering, and wide sections, respectively.

2.3.2. DECELERATING FLOWS

CLEAR WATER FLOWS

Figure 2.9a shows the time-averaged streamwise velocity profiles ($\overline{U}$) and the depth-averaged velocity magnitudes ($\overline{\overline{U}}$) along the flume for the decelerating clear-water flow D1-C0.0. Upstream, in the narrow section of the flume (P1 to P3; Figure 2.3), the depth-averaged velocity shows that the flow is nearly uniform. The velocity decreases progressively as the width of the flume increases (P4 to P6) and continues to decrease more gradually within the wide section of the flume (P7 to P9). At the end of the flume (P9), uniform conditions are established in the lower half of the flow, but they are not fully established in the upper half. Figure 2.9b shows the velocities along the flume for the lower-discharge decelerating flow D2-C0.0 (Table 2.1). The depth-averaged velocities show a comparable pattern to flow D1-C0.0 (Figure 2.9a,b).

Figures 2.9c and 2.9d show the time-averaged streamwise turbulence intensity profiles ($RMS(u')_0$) and the depth-averaged turbulence intensities ($\overline{RMS(u')_0}$) along the flume for D1-C0.0 and D2-C0.0, respectively. The depth-averaged turbulence intensity values of both flows are nearly uniform in the narrow section (P1 to P3). The turbulence intensities decrease away from the bed in the narrow section (Figure 2.9c,d). As the velocity decreases in the widening section (P4 to P6), turbulence intensity increases near the bed, while also progressively increasing upwards in the flow downstream. In both flows, this results in an increase in vertical gradient of turbulence intensity within the widening section followed by a decrease in the vertical gradient in the wide section. The depth-averaged turbulence intensity at P9 is 4.0 times higher than at P2 for D1-C0.0

(Figure 2.9c) and 3.7 times higher for D2-C0.0 (Figure 2.9d), despite the decrease in velocity. Similar increases in turbulence intensity have been observed before (Kironoto and Graf, 1995; Qingyang, 2009). Towards the end of the wide section, at P9, the turbulence intensities remain non-uniform, suggesting that the length of the flume is insufficient to establish equilibrium after the widening section.
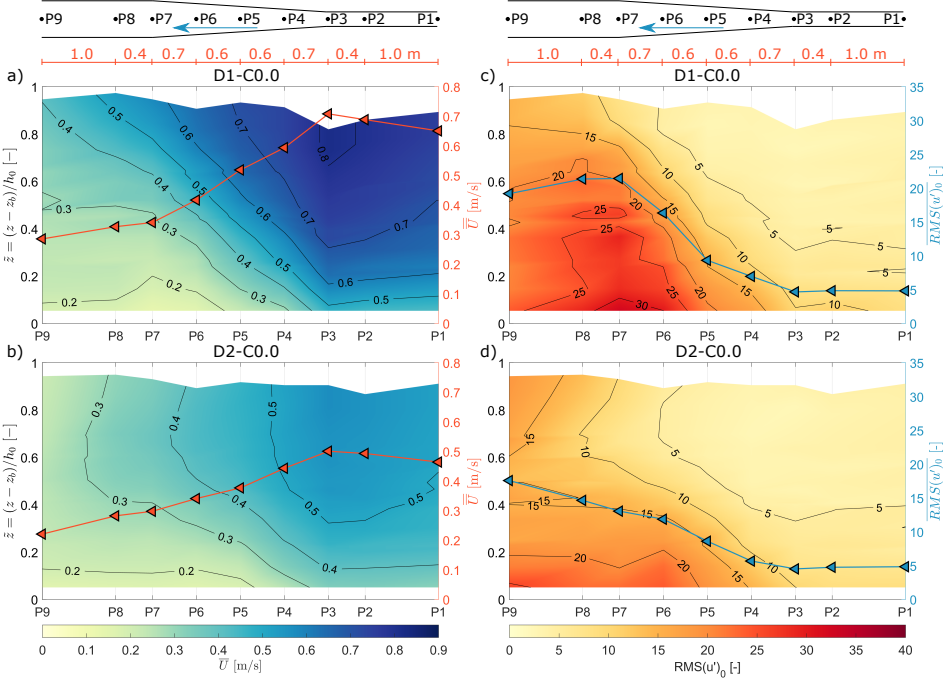

Figure 2.9: Depth-averaged velocity magnitudes ($\overline{\overline{U}}$) and time-averaged streamwise velocity profiles ($\overline{U}$) along the flume for the decelerating clear water flows a) D1-C0.0 and b) D2-C0.0. Depth-averaged turbulence intensities ($\overline{RMS(u')_0}$) and time-averaged streamwise turbulence intensity profiles ($RMS(u')_0$) along the flume for flows c) D1-C0.0 and d) D2-C0.0.

CLAY-LADEN FLOWS

Figures 2.10a, 2.10b and 2.10c show the time-averaged streamwise velocity profiles ($\overline{U}$) and the depth-averaged velocity magnitudes ($\overline{\overline{U}}$) along the flume for the clay-laden decelerating flows D3-C0.9, D4-C1.5 and D5-C2.7, respectively. Figures 2.10d, 2.10e and 2.10f show the time-averaged streamwise turbulence intensity profiles ($RMS(u')_0$) and the depth-averaged turbulence intensities ($\overline{RMS(u')_0}$) along the flume for the same flows. In the narrow section (P1 to P3), the depth-averaged velocities are nearly uniform for each decelerating clay-laden flow. The depth-averaged velocities for each flow decrease along the widening section similarly, albeit with a slightly higher rate of decrease for flow D4-C1.5. Within the wide section (P7 to P9), the depth-averaged velocities are lowest and nearly uniform. At the downstream end of the flume (P9), near uniform conditions are established in the lower half of the flume, but these are not fully established in the upper half.

The depth-averaged turbulence intensity values are nearly uniform in the narrow section (P1 to P3) (Figure 2.10 d, e and f); the turbulence intensities decrease away from the bed. As the velocity decreases in the widening section (P4 to P6), the turbulence intensity increases, initially near the bed, and then progressively higher in the flow downstream. This results in an increase in ver-

tical gradient of turbulence intensity in the widening section followed by a decrease in vertical gradient into the wide section. Towards the end of the wide section, at P9, the turbulence intensity shows a steep vertical gradient for flows D3-C0.9 and D4-C1.5. The turbulence intensity for flow D5-C2.7 remains high between P7 and P9. Despite the decrease in velocity, the depth-averaged turbulence intensity at P9 is 3.6 times higher than at P2 for D3-C0.9, 4.3 times higher for D4-C1.5 and 1.8 times higher for D5-C2.7. Towards the end of the wide section, at P9, the turbulence intensities remain non-uniform, suggesting that the length of the flume is insufficient to establish equilibrium after the widening section.
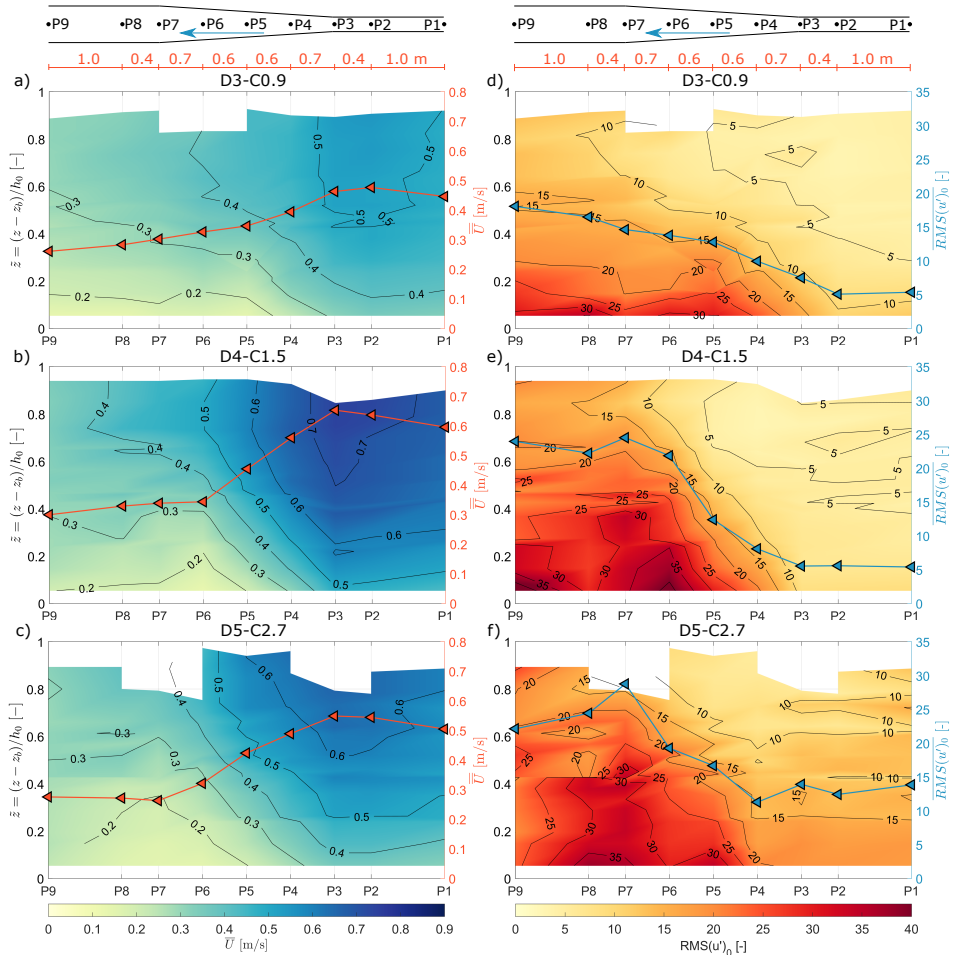
Figure 2.10: Depth-averaged velocity magnitudes ($\overline{\overline{U}}$) and time-averaged streamwise velocity profiles ($\overline{U}$) along the flume for the decelerating clay-laden flows a) D3-C0.9, b) D4-C1.5 and c) D5-C2.7. Depth-averaged turbulence intensities ($\overline{RMS(u')_0}$) and time-averaged streamwise turbulence intensity profiles ($RMS(u')_0$) along the flume for flows d) D3-C0.9, e) D4-C1.5 and f) D5-C2.7.

2.3.3. Accelerating flows

The flow direction was reversed to achieve accelerating conditions, so the flow direction was from left to right, i.e. from P9 to P1 (cf. Figure 2.3a and b).

Clear water flows

Figure 2.11a shows the time-averaged streamwise velocity profile ($\overline{U}$) and the depth-averaged velocity magnitude ($\overline{\overline{U}}$) along the flume for the accelerating clear-water flow A1-C0.0. Upstream, in the wide section of the flume (P9 to P7; Figure 2.3b), the depth-averaged velocity shows that the flow is nearly uniform. The flow accelerates progressively as the width of the flume decreases (P6 to P4) and nearly uniform flow re-establishes within the narrow section (P3 to P1).

Figure 2.11b shows the time-averaged streamwise turbulence intensity profile ($RMS(u')_0$) and the depth-averaged turbulence intensities ($\overline{RMS(u')_0}$) along the flume for flow A1-C0.0. The depth-averaged turbulence intensity values are nearly uniform in the wide section (P9 to P7). The turbulence intensity values decrease as the velocity increases in the narrowing section (P6 to P4) and remain nearly uniform in the narrow section (P3 to P1). The depth-averaged turbulence intensity at P1 is lower by a factor of 0.3 than at P8, despite the increase in velocity. Similar decreases in turbulence intensity have been observed before (Cardoso et al., 1991).

Figure 2.11: Depth-averaged velocity magnitudes ($\overline{\overline{U}}$) and time-averaged streamwise velocity profiles ($\overline{U}$) along the flume for the accelerating clear water flow a) A1-C0.0. Depth-averaged turbulence intensities ($\overline{RMS(u')_0}$) and time-averaged streamwise turbulence intensity profiles ($RMS(u')_0$) along the flume for flow b) A1-C0.0.

Clay-laden flows

Figures 2.12a, 2.12b and 2.12c show the time-averaged streamwise velocity profiles ($\overline{U}$) and the depth-averaged velocity magnitudes ($\overline{\overline{U}}$) along the flume for the clay-laden accelerating flows A2-C1.4, A3-C1.5 and A4-C2.8, respectively. Figures 2.12d, 2.12e and 2.12f show the time-averaged streamwise turbulence intensity profiles ($RMS(u')_0$) and the depth-averaged turbulence intensities ($\overline{RMS(u')_0}$) along the flume for the same flows. Upstream in the wide section (P9 to P7; Figure 2.3b), the depth-averaged velocity shows that the flow is nearly uniform. The flow accelerates progressively as the width of the flume decreases (P6 to P4) and nearly uniform flow re-establishes within the narrow section (P3 to P1).

In the wide section (P9 to P7), where the velocity is low, the depth-averaged turbulence intensities of all three clay flows are higher than in the narrowing and narrow sections, where the velocities are higher (Figure 2.12d, e and f). Towards the base of the flow, the turbulence intensity

shows a steep vertical gradient in the wide section, with especially high turbulence intensity towards the base of flows A2-C1.4 and A3-C1.5. Notably, the turbulence intensity in the bottom half of the flow at P9 and P8 in the wide section of the flume is lower for flow A4-C2.8 (Figure 2.12f) than for flows A2-C1.4 (Figure 2.12d) and A3-C1.5 (Figure 2.12e). The turbulence intensity values are high around P7 for flow A4-C2.8. The depth-averaged turbulence intensity values for all three flows decrease as the velocity increases in the narrowing section (P6 to P4) and remain nearly uniform in the narrow section (P3 to P1). The depth-averaged turbulence intensity at P1 is 0.4 times the intensity at P8 for A2-C1.4, 0.4 times for A3-C1.5 and 0.8 times for A4-C2.8, despite the increase in velocity.
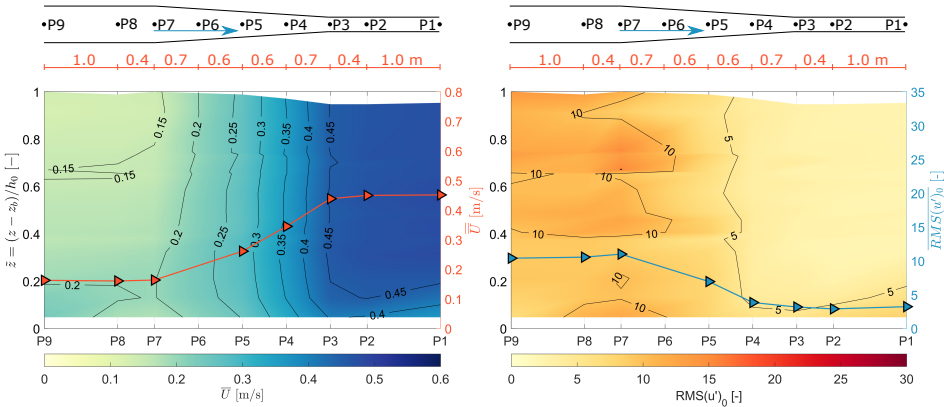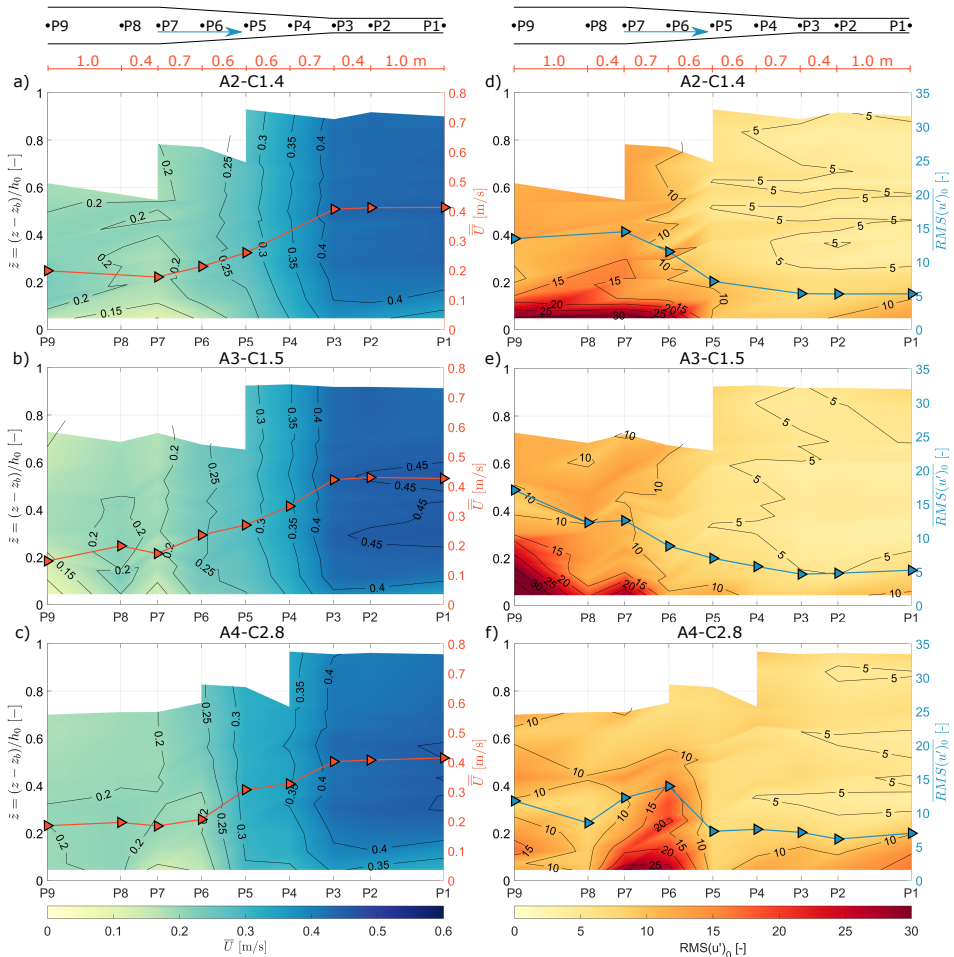

Figure 2.12: Depth-averaged velocity magnitudes ($\overline{\overline{U}}$) and time-averaged streamwise velocity profiles ($\overline{U}$) along the flume for the accelerating clay-laden flows a) A2-C1.4, b) A3-C1.5 and c) A4-C2.8. Depth-averaged turbulence intensities ($\overline{RMS(u')_0}$) and time-averaged streamwise turbulence intensity profiles ($RMS(u')_0$) along the flume for flows d) A2-C1.4, e) A3-C1.5 and f) A4-C2.8.

2.4. DISCUSSION

2.4.1. CLAY FLOW TYPES

DECELERATING FLOWS

Figures 2.13a and 2.13b show the difference in time-averaged streamwise turbulence intensity profiles ($\Delta RMS(u')_0$) and in depth-averaged turbulence intensities ($\overline{\Delta RMS(u')_0}$) along the flume for decelerating flows D3-C0.9 and D5-C2.7 versus flow D2-C0.0. Upstream, in the narrow section (P1 to P3; Figure 2.3b), the turbulence intensity values of flow D3-C0.9 are comparable with the clear-water flow D2-C0.0, i.e., the $\Delta RMS(u')_0$ values are relatively close to zero. This suggests turbulent flow, unaffected by the presence of the suspended clay. As the flow decelerates in the widening section (P4 to P6), the $\Delta RMS(u')_0$ values increase to 10 in the lower half of the flow and to 2.5 in the upper half of the flow. This is typical of turbulence-enhanced transitional flow (Baas et al., 2009); under these conditions the presence of the clay is inferred to cause a thickening of the viscous sublayer and the development of an internal shear layer with associated enhancement of turbulence (Best and Leeder, 1993; Li and Gust, 2000; Baas and Best, 2002). In the wide section (P7 to P9), the $\Delta RMS(u')_0$ values remain above zero in the bottom half of flow D3-C0.9 and they are zero or below zero in the top half of the flow. These negative $\Delta RMS(u')_0$ values suggest the onset of plug development in flow D3-C0.9, i.e., lower transitional plug flow (Baas et al., 2009). Flows D3-C0.9 and D4-C1.4 show comparable $\Delta RMS(u')_0$ patterns (Figures 2.10d and 2.10e), such that the same flow types can be identified.

In the narrow section (P1 to P3), the increased clay concentration in flow D5-C2.7 is inferred to cause the observed positive $\Delta RMS(u')_0$ values. This suggests that flow D5-C2.7 begins as a turbulence-enhanced transitional flow (Figure 2.13b; Baas and Best, 2002). The $\Delta RMS(u')_0$ values progressively increase through the widening section and beyond, suggesting the development of stronger turbulence-enhanced transitional flow (Baas et al., 2009). While the mean velocity profile of flow D5-C2.7 appears reliable, the heterogeneous vertical pattern of $\Delta RMS(u')_0$ above a relative depth of 0.4 at position P9 (Figure 2.13b) may arise from artefacts in the $RMS(u')$ measurements of this flow. This hinders a reliable inference of flow type at this location, but the decrease in $\Delta RMS(u')_0$ below the relative depth of 0.4 between P8 and P9 combined with a decrease in $\Delta RMS(u')_0$ near the top of the flow between P8 and P7 may indicate a change from turbulence-enhanced transitional flow via lower transitional plug flow to upper-transitional plug flow in the wide section (P7 to P9).

Figure 2.13: Difference in depth-averaged turbulence intensities ($\Delta\overline{RMS(u')_0}$) and time-averaged streamwise turbulence intensity profiles ($\Delta RMS(u')_0$) along the flume for decelerating flows a) D3-C0.9 minus D2-C0.0 and b) D5-C2.7 minus D2-C0.0.

ACCELERATING FLOWS

Figures 2.14a and 2.14b show the difference in time-averaged streamwise turbulence intensity profiles ($\Delta RMS(u')_0$) and in depth-averaged turbulence intensities ($\Delta\overline{RMS(u')_0}$) along the flume for accelerating flows A2-C1.4 and A4-C2.8 versus flow A1-C0.0. Upstream, in the wide section and at the start of the narrowing section (P9 to P6), $\Delta RMS(u')_0$ values are relatively close to zero in the upper half of the flow and increase downwards to 15 in the lower half of flow A2-C1.4. The high near-bed $\Delta RMS(u')_0$ values, in combination with the low values in the upper half of the flow, are typical of lower transitional plug flow (Baas et al., 2009). As the flow accelerates through the narrowing section (P6 to P4), the near bed $\Delta RMS(u')_0$ values progressively decrease from 10 to c. 2.5. In the narrow section (P3 to P1), the absolute turbulence intensity values of flow A2-C1.4 are low (Figure 2.12d), but the $\Delta RMS(u')_0$ values are increased to around 2.5. This enhanced turbulence intensity suggests weakly turbulence-enhanced or turbulent flow. Flow A3-C1.5 shows compara-

ble turbulence intensity patterns and values (Figures 2.12d and 2.12e) and similar flow types can be identified.

Upstream, in the wide section (P9 to P8), $\Delta RMS(u')_0$ values are up to 2.5 in the lower half of the flow and down to -2.5 in the upper half for flow A4-C2.8 (Figure 2.14b). This profile suggests upper transitional plug flow, where turbulence enhancement near the bed is lower than for lower transitional plug flows (cf., flow A2-C1.4 in Figure 2.14a). Similar to flow A2-C1.4, $\Delta RMS(u')_0$ values of flow A4-C2.8 between P7 and P6 are relatively close to or below zero in the upper half of the flow and are as high as 15 in the lower half of the flow, suggesting lower transitional plug flow (Figure 2.14b). Between P4 and P1, the depth-averaged $\Delta RMS(u')_0$ values are between 2.5 and 5 and vertical $\Delta RMS(u')_0$ profiles are strictly positive, suggesting turbulence-enhanced transitional flow.
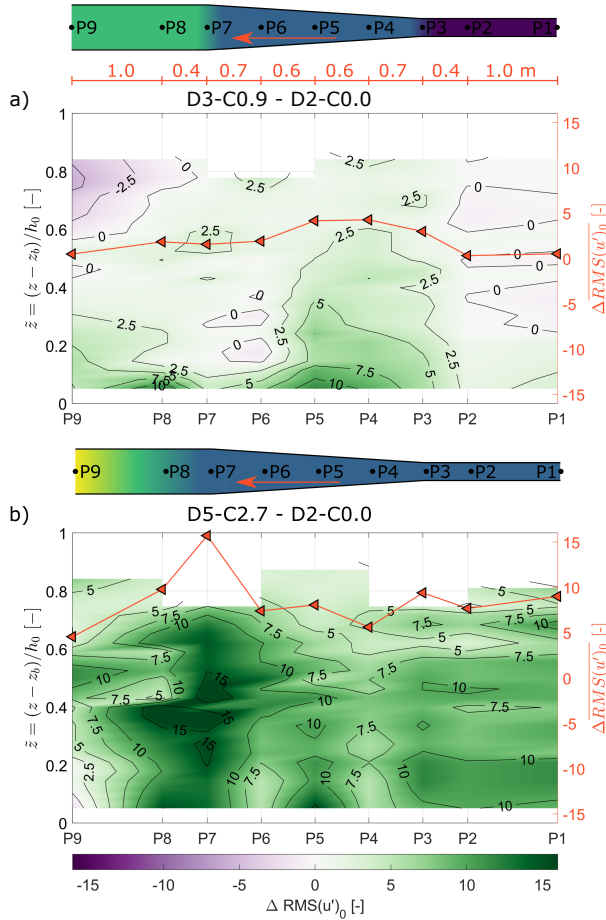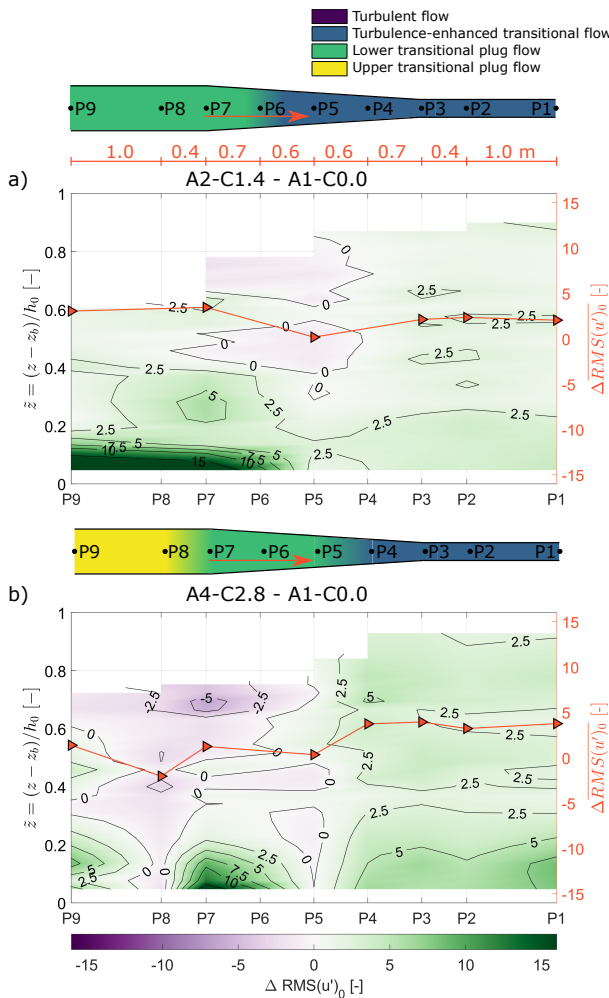

Figure 2.14: Difference in depth-averaged turbulence intensities ($\overline{\Delta RMS(u')}_0$) and time-averaged streamwise turbulence intensity profiles ($\Delta RMS(u')_0$) along the flume for decelerating flows a) A2-C1.4 minus A1-C0.0 and b) A4-C2.8 minus A1-C0.0.

2.4.2. ADAPTATION LENGTH SCALES

The length scales needed by clay flows to adapt to non-uniform conditions can be estimated using the data presented in Figures 2.13 and 2.14. The length scales are based on the identified clay-flow types and the distance between the measurement points at locations where change in velocity is experienced, i.e. these estimations involve length scales downstream of the start of the widening section for the decelerating flows and the narrowing section of the accelerating flows, as well as in the wide section for the decelerating flows and in the narrow section for the accelerating flows. The adaptation length scale in the wide (decelerating flow) or narrow section (accelerating flow) is determined by the distance required to develop (nearly) uniform conditions.

For decelerating flows, the adaptation length scales are determined at the widening section and within the wide section as the flow adapts to the change in velocity. As the flow decelerated at the start of the widening section (P3), flow D3-C0.9 changed from turbulent flow to turbulence-enhanced transitional flow, without a significant adaptation length at this position (Figure 2.13a), i.e. the flow adapted to TETF flow at the next measurement location P4. At a mean depth-averaged flow velocity of 0.43 m/s in between P3 and P4, this results in an adaptation length of 0.7 m (distance between P3 and P4, Figure 2.3b) and adaptation time of 1.6 s (Table 2.4). Throughout the wide section (P7 to P9), the flow adjusted from turbulence-enhanced transitional flow to lower transitional plug flow. Towards the end of the wide section, at P9, $\Delta RMS(u')_0$ remained non-uniform, suggesting that the length of the flume is insufficient to establish uniform conditions after the widening section (Figure 2.13a). Hence, the minimum adaptation length needed to change from turbulence-enhanced flow to lower transitional plug flow was 1.4 m, the full distance between P7 and P9. At the depth-averaged velocity of 0.28 m/s in the wide section, this adaptation length corresponds to a minimum adaptation time of 5.0 s.

Flow D5-C2.7 started to change from a relatively weak to a stronger turbulence-enhanced transitional flow at position P4, i.e., 0.7 m into the widening section (Figure 2.13b), whereas $\overline{\Delta RMS(u')_0}$ started to increase at P3 in flow D2-C0.0, i.e., at the start of the widening section (Figure 2.13a). The maximum adaptation length this high-concentration clay flow needed after starting to experiencing flow widening was therefore 0.7 m (distance between P3 and P4, Figure 2.3b). This is equivalent to an adaptation time of 1.4 s at a mean depth-averaged flow velocity of 0.52 m/s between P3 and P4 (Table 2.1). Flow D5-C2.7 changed from turbulence-enhanced transitional flow via lower transitional plug flow to upper transitional plug flow in the wide section (P7 to P9), without apparently reaching uniform flow conditions (Figure 2.13b). This is equivalent to a minimum adaptation time of 5.2 s at a depth-averaged flow velocity of 0.27 m/s through the 1.4-m long wide section.

Table 2.4: Adaptation time, T, and length, L, scales.

Experimental run	Location	Points	Flow regimes	$\overline{\overline{U}}$ [m/s]	L [m]	T [s]
Decelerating flow						
D3-C0.9	Widening section	P3 to P4	TF to TETF	0.43	0.7	1.6
	Wide section	P7 to P9	TETF to LTPF	0.28	≥1.4	≥5.0
D5-C2.7	Widening section	P3 to P4	weak to strong TETF	0.52	0.7	1.3
	Wide section	P7 to P9	TETF to UTPF	0.27	≥1.4	≥5.2
Accelerating flow						
A2-C1.4	Narrowing section	P6 to P5	LTPF to TETF	0.24	0.6	2.3
	Narrow section	P3	Maintained TETF	NA	0	0
A4-C2.8	Wide section	P8 to P7	UTPF to LTPF	0.19	0.4	2.1
	Narrowing section	P5 to P4	LTPF to TETF	0.32	0.6	1.9
	Narrow section	P3	Maintained TETF	NA	0	0

For accelerating flows, the adaptation length scales are determined at start of the narrowing section and within the narrow section as the flow adapts to the change in velocity. Flow A2-C1.4 changed from lower-transitional plug flow at P6 to turbulence-enhanced transitional flow at P5 within the narrowing section. The distance between P6 and P5 is 0.6 m and with a mean depth-averaged velocity of 0.24 m/s, this results in an adaptation time of 2.3 s. At the start of the narrow section, P3, flow A2-C1.4 established uniform turbulence-enhanced transitional flow (Figure 2.14a) and show no adaptation within the narrow section itself. Hence, within the spatial resolution of the experiments, the adaptation length within the narrow section was at or close to zero.

Flow A4-C2.8 started to change from upper transitional plug flow to lower transitional plug flow just before the narrowing section, from P8 to P7 (distance 0.4 m, Figure 2.3b). This is equivalent to an adaptation time of 2.1 s at a mean depth-averaged flow velocity of 0.19 m/s between P8 and P7 (wide section). Within the narrowing section, P5 to P4, flow A4-C2.8 changed from lower transitional plug flow to turbulence-enhanced transitional flow. Based on the distance between the measurement points P5 and P4 (0.6 m, Figure 2.3b) and the mean depth-averaged flow velocity of 0.32 m/s, this results in an adaptation time of 1.9 s. Flow A4-C2.8 established uniform turbulence-enhanced transitional flow within the narrowing section without additional adaptation within the narrow section. Hence, the change in clay flow type also lacked a significant delay at this location, P3, in the narrow section.

The estimations of adaptation length and time scales show that the decelerating flows generally needed longer to adapt to the imposed non-uniform conditions than the accelerating flows (Table 2.4). The changes within the widening or narrowing section are comparable for decelerating and accelerating flows, albeit some differences also influenced by the distance between the measurement points and flow velocity. The largest adaptation lengths and times were at the end of the widening section in the decelerating flows, where the flows changed from turbulence-enhanced transitional flow to more cohesive lower and upper transitional plug flows. Whereas, the accelerating flows changed from the more cohesive lower transitional plug flow to turbulence-enhanced flow already within the narrowing section. In the narrow section itself, the accelerating flows maintained TETF flow properties with close to zero adaptation time. Flocculation can occur when two clay particles are close enough to each other for attractive forces to overcome repulsive forces (Mehta and McAnally, 2008). Velocity gradients or shear rates can allow clay particles to collide and form flocs, but on the other hand it may disrupt the flocs, causing floc break-up (Dyer, 1988; McAnally and Mehta, 2000; Winterwerp, 2002; Partheniades, 2009; Cuthbertson et al., 2010). The complex interplay of fluid shear and suspended sediment concentration results in continuous particle aggregation and aggregate breakup (Lick et al., 1993; Manning and Dyer, 1999; Mietta et al., 2009; Safak et al., 2013; Lamb et al., 2020). Within these experiments differences are found within adaptation length between decelerating and accelerating flows. These can be explained by the fact that establishing cohesive bonds between clay particles, as in the decelerating flows, potentially requires more time than breaking up these bonds, as in the accelerating flows. Furthermore, it appears to take longer to establish a pervasive network of clay bonds, as in the change from turbulence-enhanced transitional flows to lower and upper transitional plug flow at the end of the widening section in the decelerating flows, than to establish a turbulence-enhanced transitional flow from a turbulent flow by reducing the flow velocity in low-concentration clay flows (e.g., Figure 2.13a). As the flow decelerates, collision between clay particles reduces and it becomes increasingly difficult to form clay bonds. This effect is enhanced when transitional clay flow types with turbulence attenuation start to develop in the wide section of the decelerating flows. Turbulence attenuation further reduces the chances that clay particles become in proximity of each other in order to form clay bonds, which elongates the adaptation length and time scales of decelerating

clay-laden flows. On the other hand, in the accelerating flows, the increase in flow velocity allows break up of clay bonds. Likely, this process is already effective within the narrowing section, allowing for limited or no further adaptation of clay flow types within the narrow section.

2.4.3. WIDER IMPLICATIONS

This research focused on the adaptation of flow dynamics of non-uniform clay-laden flows, but length and time scales of flow adaptation to changing environments are reflected in the depositional product (Dorrell and Hogg, 2012). This study isolates the effect of non-uniformity on spatial deceleration and acceleration in clay-laden open-channel flows and demonstrates that for mud-rich flows such scales differ between decelerating and accelerating regimes, due to the time required to form and break down the cohesive bonds between particles, whose presence affects the flow dynamics. Herein, the formation or breakage of clay bonds are influenced by the shear velocity within a flow, which is controlled by channel hydraulic geometry (e.g. water depth, width or channel slope) (Lamb et al., 2020; Nghiem et al., 2022). Depending on the boundary conditions, this difference in adaptation time likely impacts sedimentation patterns within muddy rivers. For example, after a sediment supply increase following wild-fire related erosion (Reneau et al., 2007; Sankey et al., 2017; Nyman et al., 2020), flow deceleration can occur following for example, a reduction in bed slope or widening of the river channel. The flow deceleration reduces the turbulent forces in the flow and allows the establishment of cohesive bonds between clay particles. The adaptation to stronger turbulence attenuated clay flow types requires time due to the formation of clay bonds and consequently, the deposits associated with the clay flow type form over the adaptation length scale downstream of the location of flow deceleration. In an industrial setting such as downstream of dam flushing or venting events flow acceleration can occur (Antoine et al., 2020), increasing the turbulent forces within the flow, which has the potential to break up bonds between clay particles. This study shows that the adaptation of the clay flow type to a stronger turbulent flow occurs more rapidly and consequently the associated deposits with clay flow type occur near the location of acceleration. Additionally, the different adaptation length and time scales are of particular relevance in interpreting the shape of submarine deposits, such as unconfined submarine lobes (Spychala et al., 2017) and hybrid event beds (Davis et al., 2009; Patacci et al., 2014). It is anticipated that the depositional record of decelerating flows reflects the time scales required to form interparticle bonds, delaying the depositional response to the associated changes in flow conditions. For accelerating flows it is anticipated that changes in deposit properties associated with bond breakage occur more rapidly, such that they are more closely associated with the areas where acceleration occurs.

2.5. CONCLUSION

This research investigated the influence of suspended cohesive clay on changing flow dynamics under non-uniform flow conditions, using decelerating and accelerating open-channel flows in a recirculating flume. These flows may evolve through different clay flow types with different associated degrees of turbulence enhancement and attenuation depending on the clay concentration and whether the flows decelerate or accelerate. Decelerating flows have a longer adaptation time than accelerating flows, as establishing cohesive bonds between clay particles requires more time than breaking the clay bonds. Differences in adaptation time likely influence the distribution and character of deposit within sedimentary environments. The associated deposits with clay flow type of decelerating flows are likely spread over a larger distance than of accelerating flow due to the elongated adaptation time of decelerating flows.

3

FLOW ADAPTATION TO VELOCITY CHANGES IN TRANSITIONAL CLAY SUSPENSION FLOWS

Compared to non-cohesive sediment, small concentrations of cohesive sediment can enhance or suppress turbulence in a flow due to the cohesive properties promoting flocculation. However, these processes take time to fully develop, yet flows naturally vary in time. The dynamics of unsteady open-channel clay suspension flows are poorly understood. To research the adaptation time of clay suspension flows to unsteady flow conditions, new experiments were conducted using unsteady (accelerating and decelerating) clay suspension open-channel flows. The flow velocity was adjusted with increments of 0.1 m/s after which the adaptation time to reach the equilibrium conditions was quantified. The flows transition between clay flow types as the flow adapts to the change in velocity. The experimental results show that accelerating, strongly turbulence attenuated, clay flows require more time than weakly or non turbulence attenuated clay flows due to the time required for turbulence to penetrate the plug flow in order to break the clay bonds. The adaptation time of decelerating clay flows depends on the levels of turbulence attenuation in the flow, correlated to the inter-particle collision between clay particles. Relative to turbulent flows, the adaptation time of decelerating flows is reduced as the flow evolves through clay flow types as the increase in clay concentration allows for a higher frequency of inter-particle collision. Adaptation time is then increased again with stronger turbulence attenuated flows as the increasingly dominant cohesive forces reduce inter-particle collision and consequently the formation of clay bonds takes longer. Depending on the boundary conditions within unsteady flows, these variations in adaptation time can result in hysteresis effects in cohesive strength within flows.

3.1. INTRODUCTION

High concentrations of suspended sediment in fluvial and submarine environments are common due to landslides, floods, hillslope failures, and more recently post-wildfire erosion (Swanson, 1981; Sankey et al., 2017), phenomena that are likely to occur more frequently due to climate change (Geertsema et al., 2006; Reneau et al., 2007; Barbero et al., 2015). Further, cohesive sediment is common in submarine gravity currents, such as turbidity currents and mass transport events and associated deposits, such as hybrid event beds (Talling et al., 2012). Small concentrations of cohesive sediment can enhance or suppress turbulence in a flow due to the cohesive properties promoting flocculation (Baas and Best, 2002, Section 1.2). Baas et al. (2009) developed a phase diagram for quasi-steady cohesive sediment-laden open-channel flow, based on the balance between turbulent and cohesive forces (Figure 1.10, Section 1.3).

The formation or breakage of bonds between cohesive sediment particles is a time-dependent behaviour influencing the adaptation of transitional flows to velocity changes (Winterwerp and Van Kesteren, 2004). Gradually decelerating flows have a longer adaptation time than gradually accelerating flows, as establishing cohesive bonds between clay particles requires more time than breaking the clay bonds. This hysteresis is more pronounced for higher-concentration decelerating flows that change from turbulence-enhanced transitional flow to lower and upper transitional plug flow than for lower-concentration decelerating flows that change from turbulent flow to turbulence-enhanced transitional flow. These results are based on non-uniform flow within experimental settings of converging or diverging the flume width (Chapter 2). However, flows are naturally unsteady. For example, floods in rivers are a classical example of unsteady flows. A typical hydrograph due to flood, snowmelt or rainfall-runoff contains an initial increase in discharge and flow depth followed by a drop in discharge and flow depth (Karimaee Tabarestani and Zarrati, 2015; Fielding et al., 2018; Mrokowska and Rowiński, 2019). Tidal currents within estuaries result in periodic acceleration and deceleration depending on the tidal cycle (Leeder, 2011; Uncles and Mitchell, 2017). Further, gravity currents exhibit unsteady and non-uniform behaviour and may comprise several different flow types and transformations (Talling et al., 2012). Entrainment of water can transform the gravity current from dense to more dilute flow and also from dilute to dense flow as the flow decelerates or by detrainment of water (Meiburg and Kneller, 2010). On the contrary, gravity currents can self-accelerate due to entrainment of sediment from the bed resulting in an increase of velocity and suspended concentration (Sequeiros et al., 2018).

Changes in velocity, e.g. non-uniform or unsteady flow, are expected to influence the adaptation of clay-laden flows, but the adaptation of transitional flows to temporal varying flow velocities remains unknown. Currently it is unknown if the adaptation to velocity changes due to geometry (non-uniform, spatial variations, Chapter 2) or time (unsteady, temporal variations, Chapter 3) have similar or different time and length scales. In this chapter, flow unsteadiness is defined as streamwise changes in depth-averaged velocity in time. The temporal scales of turbulent-laminar transitions in naturally unsteady flows are key for understanding sediment-laden flow dynamics. Understanding the balance between turbulent and cohesive forces in clay-laden flows is pivotal, as erosion, transport, and deposition of sediment depend on the magnitude and distribution of flow turbulence (Dorrell et al., 2018). Spatio-temporal increases and decreases in turbulence directly affect the transport capacity and deposition and erosion patterns (Dorrell and Hogg, 2012; Moody et al., 2013).

An increased understanding of the influence of cohesive sediment on unsteady flow conditions is needed. This chapter details experimental results on the flow structure of clay-laden flows, isolating temporal deceleration and acceleration in open-channel flows. The following research questions are addressed: (1) What are the mean flow and turbulence characteristics of temporal decelerating and accelerating clay-laden flows? (2) How fast do clay-laden flows adapt to temporal velocity changes?

3.2. METHODOLOGY

The methodology section is divided into four sections. The experimental setup, involving the description of the flume, equipment location and preparation of the runs is described in Section 3.2.1. The experimental conditions are described in Section 3.2.2. The measurement techniques and instruments used are described in Section 3.2.3 and Section 3.2.4 describes the methods used for the data processing and analysis.

3.2.1. EXPERIMENTAL SETUP

Mixtures of pure kaolinite (Imerys Polwhite-E, $d_{50} = 9\ \mu m, \rho_s = 2600\ kg/m^3$, Section 2.2.1) and fresh water were circulated through a hydraulic flume by means of a variable-discharge slurry pump (Figure 3.1a). The flume has a flat, smooth floor and was 10 m long, 0.5 m wide and 0.5 m deep in which the standing water depth was kept constant at 0.15 m. For comparison reasons, in these experiments the same clay material and flow depth is used as in Chapter 2. The flow velocity was adjusted with increments of 0.1 m/s, after which the adaptation time to reach the equilibrium conditions was quantified.
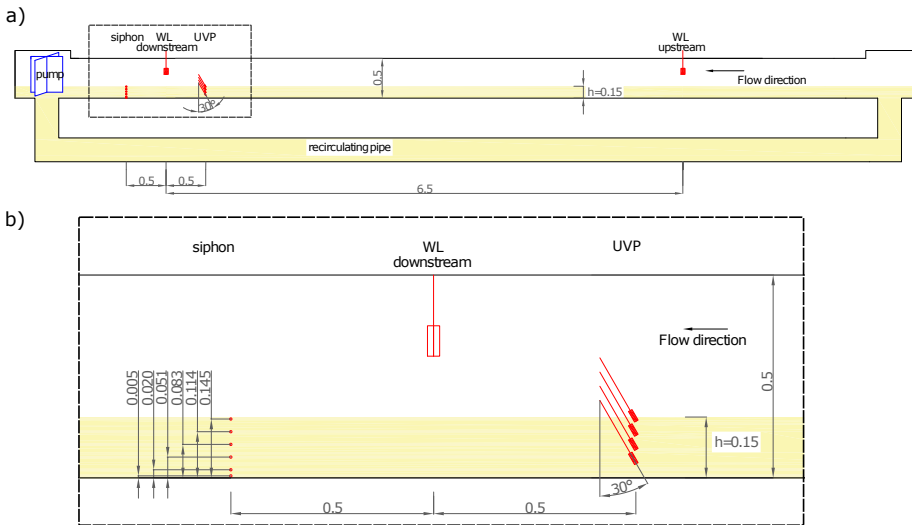
Figure 3.1: a) Side view of experimental setup, b) detailed schematic diagram of installation of equipment. All dimensions in meters.

Kaolinite was soaked in water for minimum a day before adding to the flume to guarantee that no dry clumps would remain. Initially, to stir up all the sediment within the flume, the flume ran for 20 minutes at full speed. Then, to allow the clay-laden flows to reach equilibrium conditions, the flume ran for 1 hour at the required settings for the experiments before conducting the measurements. Once the measurements were started, the flume was left running for 5 minutes at a constant velocity after which a change in velocity was imposed by increasing or decreasing the pump's rotational speed. The measurements were continued for another 20 to 30 minutes to allow the flow to adjust to the new flow condition and reach a constant velocity. Therefore, the total length of the experimental runs was 25 to 35 minutes. Figure 3.2 shows an example of the depth-averaged velocity of an experimental run.

Within the data analysis, the experimental runs were separated into before and after the velocity change. For determination of the velocity before the velocity change, the 5 minutes of measurements before the change of velocity were used within the data analysis. To include only uniform conditions within the determination of the flow conditions, the final 5 minutes of the measurements were used for the determination of the velocity after the velocity change (Figure 3.2).

Figure 3.2: Time series of depth-averaged velocity $(\overline{\overline{u}})$ of an experimental run, A-C8.7-U67, indicating moment of velocity change; Horizontal double-head arrows indicate the 'Before' and 'After' times associated with the flow velocity data used in the analysis; vertical arrows indicate the three times ('Start', 'At velocity change', and 'End') when suspended sediment concentration measurements were collected.

3.2.2. Experimental conditions
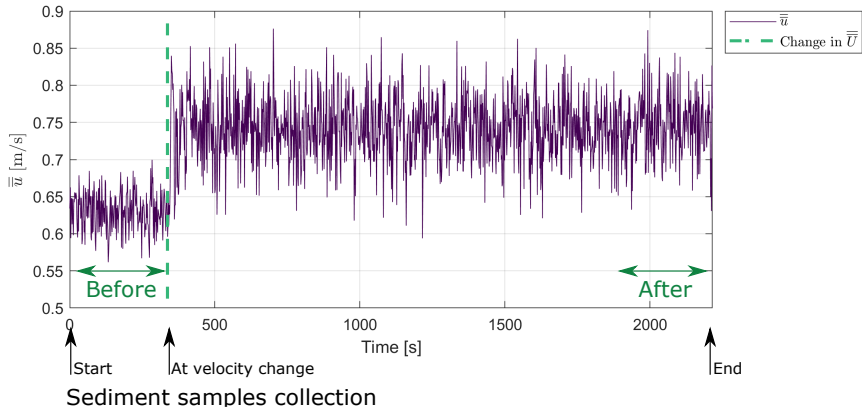
To incorporate the influence of sediment concentration on unsteady flow, different clay concentrations were used (Tables 3.1, 3.2); control experiments were conducted with clear water. The experimental runs were divided into five groups based on the suspended clay concentration; experimental condition CW for clear water, and C1 to C4 for increasing clay concentration.

Table 3.1: Overview of accelerating experimental runs performed in this study. The labelling of experimental runs is defined by the flow rate change (Accelerating (A)) - the depth-averaged clay concentration before velocity change (C) - and an indication of the mean velocity values before and after the imposed velocity change (e.g. U23 = 0.2 m/s to 0.3 m/s); The variables in the table respond to: C = depth-averaged volumetric concentration; C_m = depth-averaged mass concentration; T = fluid temperature; v_e = effective kinematic viscosity; $\overline{\overline{U}}$ = depth-averaged velocity; Re = Reynolds number; Fr = Froude number; h = water depth; Slope = slope of the flume

Experimental run	Moment in flow	C [vol %]	C_m [g/L]	T [°C]	v_e [$m^2/s \cdot 10^{-6}$]	$\overline{\overline{U}}$ [m/s]	Re [- $\cdot 10^4$]	Fr [-]	h [m]	Slope [$\cdot 10^{-3}$]
Experimental condition CW										
A-C0.0-U23	Before	0.0	0.0	17.5	1.00	0.24	3.6	0.20	0.148	0.10
	After	0.0	0.0	17.5	1.00	0.32	4.7	0.26	0.148	0.31
A-C0.0-U34	Before	0.0	0.0	17.5	1.00	0.34	5.0	0.28	0.148	0.31
	After	0.0	0.0	17.5	1.00	0.45	6.6	0.38	0.147	0.45
A-C0.0-U45	Before	0.0	0.0	17.5	1.00	0.35	5.2	0.29	0.147	0.45
	After	0.0	0.0	17.5	1.00	0.48	7.1	0.40	0.148	0.74
A-C0.0-U56	Before	0.0	0.0	17.5	1.00	0.48	7.2	0.40	0.148	0.74
	After	0.0	0.0	17.5	1.00	0.61	8.9	0.51	0.145	0.95
A-C0.0-U67	Before	0.0	0.0	17.5	1.00	0.60	8.8	0.50	0.145	0.95
	After	0.0	0.0	17.5	1.00	0.74	11.0	0.61	0.146	1.38
A-C0.0-U78	Before	0.0	0.0	17.5	1.00	0.72	10.4	0.60	0.146	1.38
	After	0.0	0.0	17.5	1.00	0.83	12.1	0.69	0.149	1.80

Experimental run	Moment in flow	C [vol %]	C_m [g/L]	T [°C]	ν_e [$m^2/s\cdot10^{-6}$]	$\overline{\overline{U}}$ [m/s]	Re [- $\cdot10^4$]	Fr [-]	h [m]	Slope [$\cdot10^{-3}$]
Experimental condition C1										
A-C5.0-U23	Before	5.0	123	17.4	2.18	0.21	1.4	0.17	0.149	0.08
	After	5.0	122	17.4	2.16	0.32	2.2	0.27	0.149	0.30
A-C5.0-U34	Before	5.0	122	17.4	2.16	0.32	2.2	0.27	0.149	0.30
	After	5.4	131	17.4	2.31	0.44	2.8	0.36	0.149	0.37
A-C5.4-U45	Before	5.4	131	17.4	2.31	0.43	2.8	0.36	0.148	0.37
	After	5.5	134	17.4	2.37	0.55	3.4	0.45	0.149	0.72
A-C5.5-U56	Before	5.5	134	17.4	2.37	0.56	3.5	0.46	0.148	0.72
	After	5.6	135	17.4	2.39	0.67	4.1	0.56	0.148	1.00
A-C5.6-U67	Before	5.6	135	17.4	2.39	0.63	3.9	0.52	0.148	1.00
	After	5.6	135	17.4	2.39	0.73	4.5	0.61	0.147	1.35
A-C5.6-U78	Before	5.6	135	17.4	2.39	0.73	4.5	0.61	0.147	1.35
	After	5.6	135	17.4	2.39	0.82	5.0	0.69	0.145	1.85
Experimental condition C2										
A-C8.4-U23	Before	8.4	196	16.9	3.70	0.22	0.9	0.18	0.148	0.16
	After	8.3	194	16.9	3.68	0.32	1.3	0.26	0.148	0.30
A-C8.3-U34	Before	8.3	194	16.9	3.68	0.32	1.3	0.27	0.149	0.30
	After	8.6	199	16.9	3.79	0.43	1.7	0.35	0.149	0.51
A-C8.6-U45	Before	8.6	199	16.9	3.79	0.42	1.6	0.35	0.149	0.51
	After	8.7	201	16.9	3.84	0.52	2.0	0.43	0.148	0.79
A-C8.7-U56	Before	8.7	201	16.9	3.84	0.51	2.0	0.42	0.148	0.79
	After	8.7	202	16.9	3.88	0.61	2.3	0.51	0.147	1.07
A-C8.7-U67	Before	8.7	202	16.9	3.86	0.64	2.4	0.53	0.147	1.07
	After	8.8	203	16.9	3.42	0.74	3.2	0.62	0.147	1.50
A-C8.8-U78	Before	8.8	203	16.9	3.42	0.73	3.1	0.61	0.147	1.50
	After	8.8	203	16.9	3.89	0.84	3.1	0.70	0.145	1.99
Experimental condition C3										
A-C10.7-U23	Before	10.7	241	17.8	4.97	0.25	0.7	0.20	0.149	0.16
	After	11.0	246	17.8	5.10	0.37	1.1	0.31	0.148	0.30
A-C11.0-U34	Before	11.0	246	17.8	5.10	0.37	1.1	0.31	0.148	0.30
	After	11.4	253	17.8	5.33	0.45	1.3	0.38	0.148	0.51
A-C11.4-U45	Before	11.4	253	17.8	5.33	0.45	1.3	0.38	0.148	0.51
	After	11.6	257	17.8	5.45	0.59	1.6	0.49	0.147	0.79
A-C11.6-U56	Before	11.6	257	17.8	5.45	0.59	1.6	0.49	0.147	0.79
	After	11.7	259	17.8	5.52	0.72	1.9	0.60	0.146	1.14
A-C11.7-U67	Before	11.7	259	17.8	5.52	0.71	1.9	0.59	0.146	1.14
	After	11.7	259	17.8	5.53	0.83	2.2	0.70	0.144	1.57
A-C11.7-U78	Before	11.7	259	17.8	5.53	0.83	2.2	0.70	0.144	1.57
	After	11.7	260	17.8	5.53	0.87	2.3	0.72	0.149	1.99
Experimental condition C4										
A-C13.1-U23	Before	13.1	285	17.8	6.37	0.20	0.5	0.17	0.148	0.58
	After	13.5	293	17.8	6.68	0.35	0.8	0.29	0.148	0.79
A-C13.5-U34	Before	13.5	293	17.8	6.68	0.36	0.8	0.30	0.149	0.79
	After	13.6	294	17.8	6.71	0.51	1.1	0.42	0.147	0.86
A-C13.6-U45	Before	13.6	294	17.8	6.71	0.52	1.1	0.43	0.147	0.86
	After	14.0	301	17.8	6.96	0.59	1.2	0.49	0.146	1.00
A-C14.0-U56	Before	14.0	301	17.8	6.96	0.59	1.2	0.50	0.146	1.00
	After	14.5	309	17.8	7.27	0.68	1.4	0.57	0.145	1.07
A-C14.5-U67	Before	14.5	309	17.8	7.27	0.68	1.4	0.57	0.146	1.07
	After	14.7	313	17.8	7.40	0.78	1.5	0.65	0.147	1.50
A-C14.7-U78	Before	14.7	313	17.8	7.40	0.78	1.5	0.65	0.145	1.50
	After	14.7	314	17.8	7.46	0.90	1.8	0.75	0.146	1.99

3

Table 3.2: Overview of decelerating experimental runs performed in this study. The labelling of experimental runs is defined by the flow rate change (Decelerating (D)) - the depth-averaged clay concentration before velocity change (C) - and an indication of the mean velocity values before and after the imposed velocity change (e.g. U32 = 0.3 m/s to 0.2 m/s); The variables in the table respond to: C = depth-averaged volumetric concentration; C_m = depth-averaged mass concentration; T = fluid temperature; v_e = effective kinematic viscosity; $\overline{\overline{U}}$ = depth-averaged velocity; Re = Reynolds number; Fr = Froude number; h = water depth; Slope = slope of the flume

3

Experimental run	Moment in flow	C [vol %]	C_m [g/L]	T [°C]	v_e [$m^2/s \cdot 10^{-6}$]	$\overline{\overline{U}}$ [m/s]	Re [- $\cdot 10^4$]	Fr [-]	h [m]	Slope [$\cdot 10^{-3}$]
Experimental condition CW										
D-C0.0-U32	Before	0.0	0.0	17.5	1.00	0.23	3.4	0.19	0.148	0.31
	After	0.0	0.0	17.5	1.00	0.15	2.2	0.12	0.148	0.26
D-C0.0-U43	Before	0.0	0.0	17.5	1.00	0.36	5.2	0.30	0.146	0.45
	After	0.0	0.0	17.5	1.00	0.23	3.5	0.19	0.148	0.31
D-C0.0-U54	Before	0.0	0.0	17.5	1.00	0.42	6.2	0.35	0.148	0.74
	After	0.0	0.0	17.5	1.00	0.29	4.2	0.24	0.147	0.45
D-C0.0-U65	Before	0.0	0.0	17.5	1.00	0.57	8.2	0.48	0.144	0.95
	After	0.0	0.0	17.5	1.00	0.43	6.4	0.36	0.148	0.74
D-C0.0-U76	Before	0.0	0.0	17.5	1.00	0.72	10.4	0.60	0.146	1.31
	After	0.0	0.0	17.5	1.00	0.58	8.3	0.48	0.144	0.95
D-C0.0-U87	Before	0.0	0.0	17.5	1.00	0.82	12.2	0.68	0.149	1.80
	After	0.0	0.0	17.5	1.00	0.73	10.6	0.61	0.146	1.31
Experimental condition C1										
D-C5.3-U32	Before	5.3	129	17.4	2.27	0.32	2.1	0.27	0.148	0.30
	After	5.0	122	17.4	2.16	0.20	1.4	0.17	0.148	0.08
D-C5.5-U43	Before	5.5	133	17.4	2.36	0.43	2.7	0.36	0.148	0.51
	After	5.3	129	17.4	2.27	0.32	2.1	0.26	0.148	0.30
D-C5.4-U54	Before	5.4	135	17.4	2.39	0.55	3.4	0.45	0.147	0.72
	After	5.6	133	17.4	2.36	0.43	2.7	0.36	0.148	0.51
D-C5.5-U65	Before	5.5	135	17.4	2.38	0.65	4.0	0.55	0.147	1.00
	After	5.5	135	17.4	2.39	0.55	3.4	0.45	0.147	0.72
D-C5.6-U76	Before	5.6	135	17.4	2.39	0.75	4.6	0.62	0.147	1.35
	After	5.6	135	17.4	2.38	0.64	4.0	0.54	0.147	1.00
D-C5.6-U87	Before	5.6	135	17.4	2.39	0.82	4.9	0.68	0.145	1.85
	After	5.6	135	17.4	2.39	0.73	4.5	0.60	0.147	1.35
Experimental condition C2										
D-C8.5-U32	Before	8.5	197	16.9	3.30	0.31	1.4	0.26	0.148	0.30
	After	8.3	194	16.9	3.66	0.22	0.9	0.18	0.148	0.08
D-C8.7-U43	Before	8.7	201	16.9	3.84	0.42	1.6	0.35	0.148	0.51
	After	8.5	197	16.9	3.30	0.31	1.4	0.26	0.148	0.30
D-C8.8-U54	Before	8.8	203	16.9	3.89	0.52	2.0	0.44	0.148	0.79
	After	8.7	201	16.9	3.84	0.42	1.6	0.35	0.148	0.51
D-C8.8-U65	Before	8.8	203	16.9	3.88	0.63	2.4	0.53	0.147	1.14
	After	8.8	202	16.9	3.89	0.53	2.0	0.44	0.148	0.79
D-C8.8-U76	Before	8.8	203	16.9	3.89	0.74	2.8	0.62	0.146	1.50
	After	8.8	203	16.9	3.88	0.53	2.4	0.53	0.147	1.14
D-C8.8-U87	Before	8.8	203	16.9	3.89	0.84	3.1	0.70	0.145	1.99
	After	8.8	203	16.9	3.88	0.73	2.8	0.61	0.146	1.50
Experimental condition C3										
D-C11.5-U32	Before	11.5	256	17.8	5.40	0.36	1.0	0.30	0.148	0.30
	After	11.4	253	17.8	5.33	0.23	0.6	0.19	0.148	0.16
D-C11.6-U43	Before	11.6	258	17.8	5.49	0.48	1.3	0.40	0.148	0.51
	After	11.5	256	17.8	5.40	0.37	1.0	0.31	0.148	0.30
D-C11.7-U54	Before	11.7	259	17.8	5.52	0.59	1.6	0.49	0.147	0.79
	After	11.6	258	17.8	5.49	0.47	1.3	0.39	0.147	0.51
D-C11.7-U65	Before	11.7	260	17.8	5.54	0.73	1.9	0.61	0.145	1.07
	After	11.7	259	17.8	5.52	0.59	1.6	0.49	0.147	0.79
D-C11.7-U76	Before	11.7	260	17.8	5.53	0.83	2.2	0.70	0.144	1.64
	After	11.7	260	17.8	5.54	0.71	1.9	0.59	0.146	1.07
D-C11.7-U87	Before	11.7	260	17.8	5.53	0.87	2.3	0.72	0.149	1.99
	After	11.7	260	17.8	5.53	0.82	2.1	0.69	0.144	1.64

Experimental run	Moment in flow	C [vol %]	C_m [g/L]	T [°C]	v_e [$m^2/s \cdot 10^{-6}$]	$\overline{\overline{U}}$ [m/s]	Re [- $\cdot 10^4$]	Fr [-]	h [m]	Slope [$\cdot 10^{-3}$]
				Experimental condition C4						
D-C14.2-U32	Before	14.2	304	17.8	7.08	0.20	0.7	0.27	0.148	0.79
	After	13.9	300	17.8	6.91	0.32	0.4	0.17	0.149	0.58
D-C14.4-U43	Before	14.4	308	17.8	7.20	0.33	0.9	0.37	0.148	0.86
	After	14.2	304	17.8	7.08	0.44	0.7	0.27	0.148	0.79
D-C14.6-U54	Before	14.6	311	17.8	7.34	0.44	1.1	0.45	0.147	0.93
	After	14.4	308	17.8	7.20	0.55	0.9	0.36	0.148	0.86
D-C14.7-U65	Before	14.7	314	17.8	7.44	0.54	1.3	0.55	0.146	1.07
	After	14.6	311	17.8	7.34	0.65	1.1	0.45	0.148	0.93
D-C14.8-U76	Before	14.8	315	17.8	7.50	0.65	1.5	0.62	0.148	1.50
	After	14.7	314	17.8	7.44	0.75	1.3	0.54	0.146	1.07
D-C14.7-U87	Before	14.7	314	17.8	7.46	0.75	1.8	0.74	0.148	1.99
	After	14.8	315	17.8	7.50	0.89	1.5	0.62	0.148	1.50

3.2.3. DATA ACQUISITION

WATER LEVEL

The water level was measured with two Ultralab ULS Advanced sensors (Figure 3.1A). The water level measurements were collected with a sample rate of 50 Hz. These data were used to compute the water surface slope and verify that flows were parallel to the flume bed, i.e. that flows were uniform. The measurements were also used to determine the temporal mean water depth, h (Equation 3.2).

SUSPENDED SEDIMENT CONCENTRATION

A vertical rack of six 6 mm diameter siphon tubes was used to collect suspension samples through the water column (Table 3.3) downstream of the velocity measurements (Figure 3.1b). The sediment samples were collected at the start time of the velocity measurements, at the moment of the velocity change and at the end of the velocity measurements (Figure 3.2). The sediment samples were weighed with an analytical laboratory scale with a resolution of 0.0001 g and dried to determine their volumetric clay concentration.

Table 3.3: Measurement height (centrepoint) above the bed (z) of siphon samples to measure the clay concentration

Measurement	z [m]
A	0.005
B	0.020
C	0.051
D	0.083
E	0.114
F	0.145

FLOW VELOCITY

The streamwise component of the flow velocity was measured with UVPs (Ultrasonic Velocity Profiler, Section 1.4) facing upstream under an angle of 30° relative to the vertical (Figure 3.1b). Four 1 MHz probes were stacked with a distance of 30 mm between the probes' centres.

The UVPs were installed under an angle of 30° to measure the full velocity profile over the depth. To convert the measurements to a streamwise velocity profile the vertical velocity was assumed to be zero. This assumption was tested by a comparison between velocity measurements of a UVP probe installed under an angle of 30° and a UVP probe installed horizontally facing upstream in streamwise direction at $z = 0.05m$. The combined velocity measurements for two different flow velocities (Test01 and Test02) are shown in Figure 3.3a and b. The time-averaged velocity

$(\overline{U})$ and standard deviation $(RMS(u'))$ of both the vertical UVP and the angled UVP are comparable (Table 3.4) and therefore the assumption of a zero vertical velocity is valid for these experiments. The selected angle (30°) is acceptable in terms of introduced uncertainty on Reynolds stressed (Tropea, 1983).

Table 3.4: Overview of experimental test runs to compare UVPs installed under an angle and horizontally installed UVPs. $\overline{U}$ = time-averaged velocity at $z = 0.05m$; $RMS(u')$ = standard deviation of velocity measurements at $z = 0.05m$; Error between measurements = absolute difference between measurements of angled and horizontal UVP / UVP installed under an angle · 100%

Experimental test run	UVP installed under an angle		UVP installed horizontal		Error between measurements	
	$\overline{U}$ [m/s]	$RMS(u')$ [m/s]	$\overline{U}$ [m/s]	$RMS(u')$ [m/s]	$\overline{U}$ [%]	$RMS(u')$ [%]
Test01	0.46	0.017	0.46	0.017	1.1	0.6
Test02	0.80	0.049	0.78	0.049	3.1	0.7
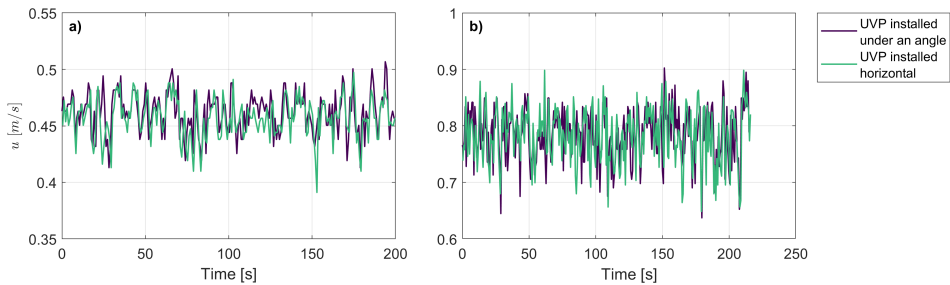
Figure 3.3: Experimental test runs comparing velocity measurements from a UVP probe installed under an angle of 30° against the vertical and a UVP probe installed facing upstream in streamwise direction at $z = 0.05m$. a) Test01; b) Test02.

3.2.4. DATA PROCESSING

DATA CLEANING

Velocity data collected by UVPs and water level measurements collected by Ultralab ULS advanced sensors can contain spurious amplitude spikes that are not part of the genuine signal (Met-Flow, 2002; Goring and Nikora, 2002; Wright and Baas, 2013; Dilling and MacVicar, 2017). To clean the UVP and water level data the following steps were followed:

- Encounter for data wrapping - The velocity range of the UVP settings, displaying the maximum measurable velocity, needed to be selected ahead of the measurements. The velocity step, i.e. the velocity resolution, correlates to the velocity range. Therefore, it is important to select a velocity range that is able to capture the maximum velocity expected in the flow, but not too large to achieve increased detail on the velocity data. If the measured velocity goes up to the upper limit, and further increase of velocity happens, the velocity 'jumps' to the bottom of the graph. The velocity measurements were checked for this potential data wrapping and if it occurred, the data was adjusted accordingly.

  The maximum range of the Ultralab ULS advanced sensors is larger (1.2 m) than the variation in the experiments (0.1 m) and no data wrapping occurs in the water level measurements.

- Delete zero values - For various reasons, UVPs are sometimes unable to measure the velocity properly and when the measurement is 'empty', it is replaced by 'zero' value of velocity.

Generally this occurs when there is a lack of reflecting particles, too weak signal or reflections.

Ultralab ULS advanced sensors always output a measurement value.

- Removal of outliers - Outliers were removed from the velocity signal by eliminating values three standard deviations away from the temporal moving mean over 31 data points.

  Outliers within the water level measurement were deleted by eliminating values two and half standard deviations away from the temporal moving mean over 201 data points. The accuracy of the water level measurements (1 mm) is high and allows a reduction of standard deviations (2.5) compared to UVP measurements (3). The amount of data points included for cleaning the ULS measurements is higher to incorporate a large enough time span, due to the significantly higher measurement frequency of the ULS sensors than the UVP measurements.

- Delete negative values - Within the UVP and water level measurements only positive values are expected and a negative value therefore indicates a bad data point.

- Delete measurement bin with 30% or more bad data points - To enhance the accuracy on determination of the mean flow velocity and turbulence intensity, only measurement bins with enough valid data points are included in further data analysis. The full time series at a measurement bin is excluded from the data analysis if more than 30% of the data points within the time series were excluded by previous steps of cleaning the data.

  The water level measurements only included one measurement bin, for which after processing the data never included more then 30% of invalid data points.

DETERMINATION OF FLOW PARAMETERS

The measured depth-averaged clay concentration was calculated by integrating the suspended sediment samples (c) over the depth, from the lowest measurement at $z_A = 0.05\ m$ to $z_F = 0.145\ m$:

$$C = \frac{1}{z_F - z_A} \int_{z_A}^{z_F} c\,dz \tag{3.1}$$

where z is height above the bed. Without deposition in the experiments, the flume bed is defined as z=0. If potential deposition occurs (Section 3.3.1) z=0 at the height where the velocity measurements reaches zero. The temporal mean water depth, h, was calculated from the time series of instantaneous water level data (wl).

$$h = \frac{1}{k} \sum_{i}^{k} wl_i \tag{3.2}$$

where k is the number of water level measurements. The temporal mean flow velocity, $\overline{U}$, and its standard deviation, $RMS(u')$, were calculated from the time series of instantaneous velocity data at each measurement height (u_i).

$$\overline{U} = \frac{1}{n} \sum_{i}^{n} u_i \tag{3.3}$$

$$RMS(u') = \sqrt{\frac{1}{n} \sum_{i}^{n} (u_i - \overline{U})^2} \tag{3.4}$$

where n is the number of velocity measurements. A dimensionless measure for turbulence intensity proposed by Baas and Best (2002) is used herein:

$$RMS(u')_0 = \frac{RMS(u')}{\overline{U}} \cdot 100 \tag{3.5}$$

The depth-averaged velocity was calculated by curve fitting the Coles wake law (Section 1.1.3) on the time-averaged velocities over the depth using the method of least squares when fitting the data.

$$\overline{\overline{U}} = \frac{1}{h - z_0} \int_{z_0}^{h} \left(\frac{u_*}{\kappa} ln\left(\frac{z}{z_0} \right) + \frac{2\Pi u_*}{\kappa} sin^2\left(\frac{\pi}{2} \frac{z}{\delta} \right) \right) dz \tag{3.6}$$

where $\kappa = 0.41$ is the von Karman constant. Depth-averaged turbulence intensity was calculated by integrating the turbulence intensity values over the depth.

$$\overline{RMS(u')_0} = \frac{1}{h} \int_0^h RMS(u')_0 dz \tag{3.7}$$

The time series of depth-averaged velocity ($\overline{\overline{u}}$) was calculated using a curve fitting procedure based on Coles wake law on the time series of instantaneous velocity data.

$$\overline{\overline{u}} = \frac{1}{h - z_0} \int_{z_0}^{h} \left(\frac{u_*}{\kappa} ln\left(\frac{z}{z_0} \right) + \frac{2\Pi u_*}{\kappa} sin^2\left(\frac{\pi}{2} \frac{z}{\delta} \right) \right) dz \tag{3.8}$$

Froude number was calculated as:

$$Fr = \frac{\overline{\overline{U}}}{\sqrt{gh}} \tag{3.9}$$

Reynolds number was calculated as:

$$Re = \frac{\overline{\overline{U}} h}{\nu_e} \tag{3.10}$$

where g is the gravitational acceleration and ν_e is the effective viscosity with the influence of clay suspension approximated based upon Wan (1982) (Equation 2.8).

FLUME SETTINGS

The hydraulic flume used the pump rotation to adjust the velocity in the flume. For each different clay concentration within these experiments a flow rating curve has been developed. The flow rating curve relates the pump rotation (rpm) to the measured flow velocity within the flume. Both the percentage of pump rotation with respect to the maximum rpm (Figure 3.4a) and slope of the flume (Figure 3.4b) were correlated to the velocity measurements, after which this correlation was used to determine the flume settings for the experimental conditions. Based on Chezy's equation (Equation 3.11), the drag coefficient was calculated for the highest velocity ($C_d = 0.0027$), which was then used to fit through the other measurements to find the correlation between depth-averaged velocity $\overline{\overline{U}}$ and slope of the flume (S). This correlation was used to ensure uniform flow conditions with constant water depth throughout the flume.

$$\overline{\overline{U}} = \sqrt{\frac{gR_h S}{C_D}} \tag{3.11}$$

where R_h is the hydraulic radius and S the slope of the bed.
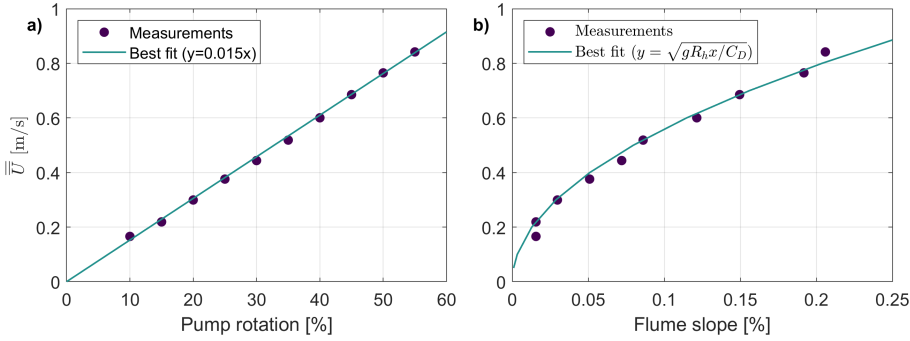
Figure 3.4: a) Correlation between depth-averaged velocity of experimental condition C3 and percentage of pump rotation; b) Correlation between depth-averaged velocity of experimental condition C3 and slope of the flume.

SELECTION OF PROFILES

Distant particles give weaker echo than particles close to the transducer and depending on the concentration within the flow, the signal can be attenuated, reducing the measurement window. To measure the full velocity profile, four 1 MHz probes were installed in a staggered array (Figure 3.1b). 1 MHz probes are used to allow measurements in the high clay concentrations up to 14.7%. The UVPs were directed against the flow direction to measure the streamwise velocity and to reduce the impact of flow obstruction on the measurements. The settings of the UVPs were adjusted to the experimental conditions to increase the data quality. For data analysis, one profile was selected from the four staggered UVP probes. Data attenuation of UVP measurements is indicated by a decrease in velocity correlated with an increase in velocity fluctuations, occurring relatively high up in the flow. Figure 3.5 indicates which profile is selected for further data analysis, based upon the decrease in U and correlating increase in RMS. The data within the selected profile is a combination of the four UVP probes. Both clay concentration and flow velocity influence the height at which data attenuation occurs and for every condition the heights with valid data points are selected. The time series of every data point within a profile were checked to verify the data quality. To calculate the depth-averaged velocity, Coles wake law was curve fitted over the valid data over the the depth (Equation 3.6).
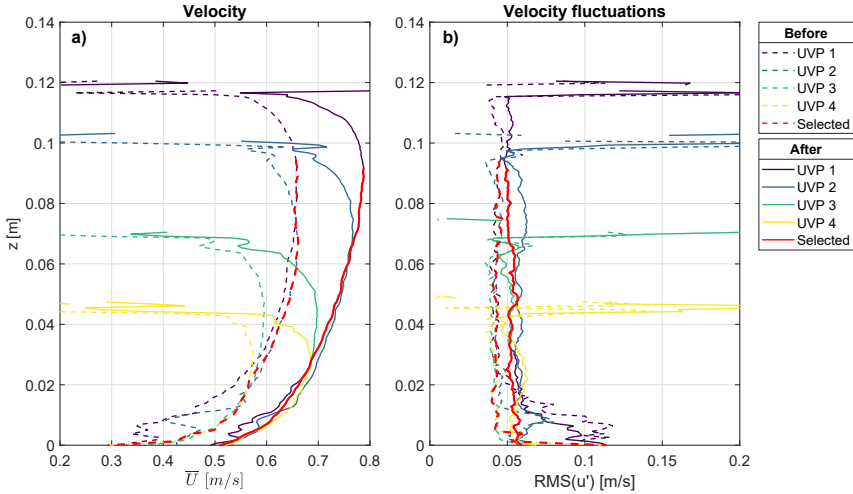
3

Figure 3.5: Selection of vertical profiles included within data analysis from the four staggered UVP probes for a) velocity and b) velocity fluctuations. Example of flow A-C8.7-U67.

3.3. Experimental observations

3.3.1. Suspended sediment concentration

For most experimental runs the suspended sediment was distributed uniformly through the water column (Figures 3.6 to 3.9). Mostly at lower velocities, some increase in clay concentration near the bed can be identified, indicating potential deposition. The concentration measurements during the change of velocity for accelerating flows, show an increase in concentration near the bed, but the concentration is evenly spread over the flow height after the change in velocity. This effect is specifically clear within Condition 03, accelerating flow, experimental run U34 (Figure 3.7a,b,c). Before the velocity change, the clay concentration is uniformly distributed around 8.35%. When the flow increases, an increase in clay concentration is noticeable at the bed and it moves upwards to the surface until afterwards it is equally distributed around 8.6%. The two different velocities within the experiments, before and after the imposed velocity change, have different capacities of keeping sediment in suspension. This redistribution of sediment of the flow depth might influence the adaptation time of the flows. The experimental runs at which this redistribution of sediment might occur are identified by a criteria based upon the relative increase in sediment near the bed: a relative increase in clay concentration of more than 1% in the bottom siphon sample, C_A compared to the median of the 5 other measurement samples, C_{B-F}:

$$\frac{c_A - C_{B-F}}{C_{B-F}} \cdot 100\% > 1\% \tag{3.12}$$

The relative increase in clay concentration correlates with zero velocity measurements and consequently it is identified as potential deposition (Tables 3.9 and 3.10).
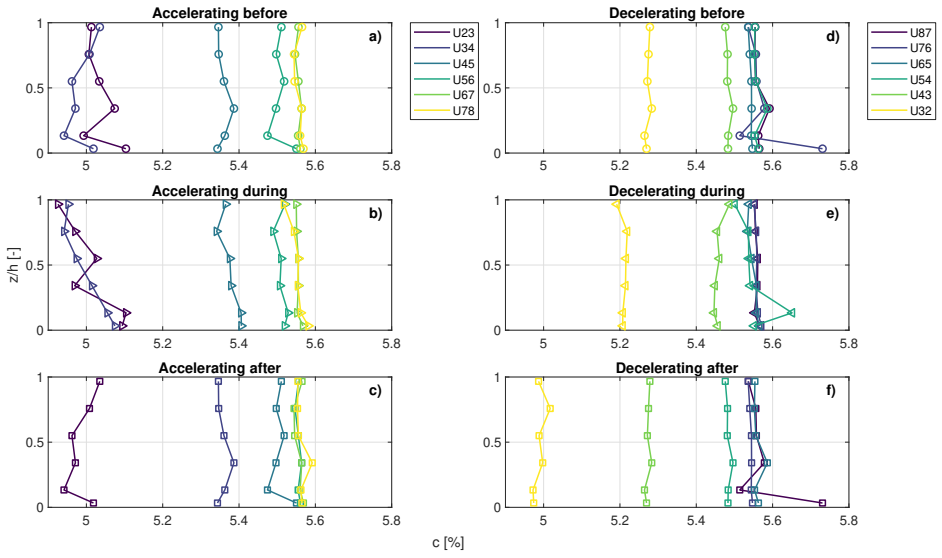
Figure 3.6: Vertical profiles of volumetric sediment concentration of experimental condition C1 (5.0<C<5.6 %) for accelerating flow a) before, b) during, and c) after velocity change and decelerating flows d) before, e) during, and f) after velocity change. Note that U23 indicates a mean flow acceleration from 0.2 to 0.3 m/s and U32 indicates a mean flow deceleration, see Tables 3.1, 3.2 for more details.
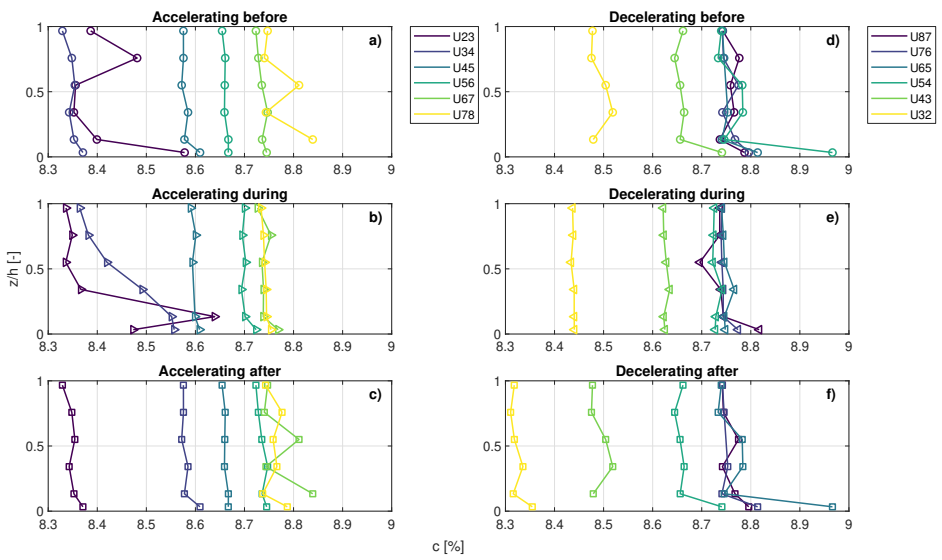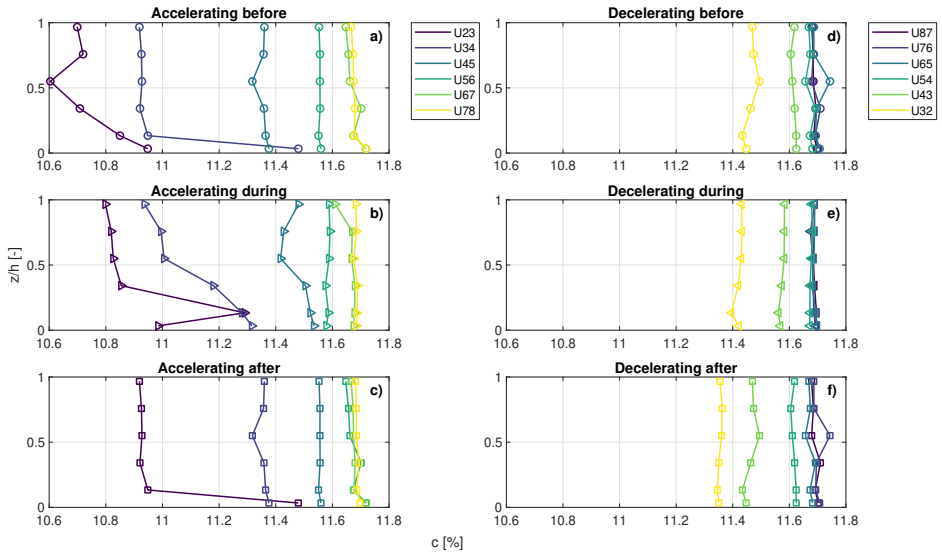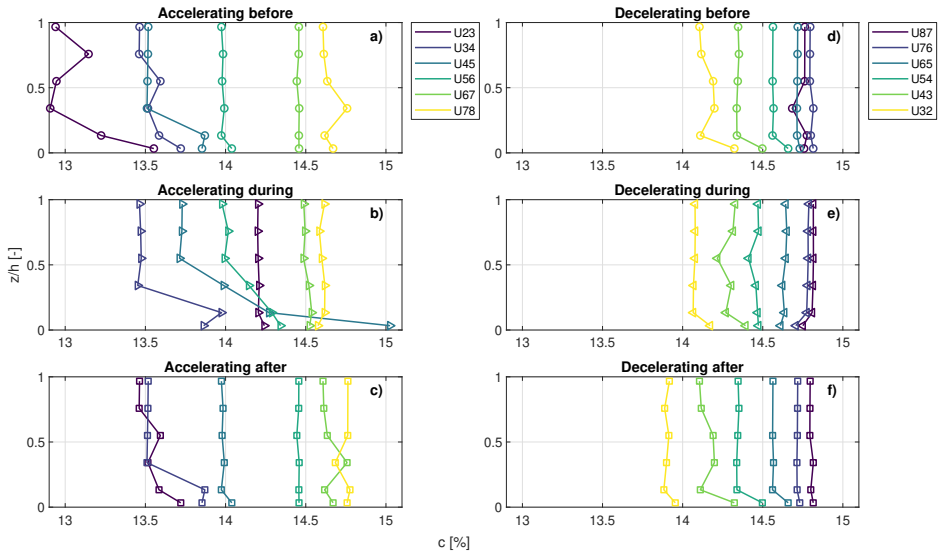

Figure 3.7: Vertical profiles of volumetric sediment concentration of experimental condition C2 (8.3<C<8.8 %) for accelerating flow a) before, b) during, and c) after velocity change and decelerating flows d) before, e) during, and f) after velocity change. Note that U23 indicates a mean flow acceleration from 0.2 to 0.3 m/s and U32 indicates a mean flow deceleration, see Tables 3.1, 3.2 for more details.

Figure 3.8: Vertical profiles of volumetric sediment concentration of experimental condition C3 (10.7<C<11.7 %) accelerating flow a) before, b) during, and c) after velocity change and decelerating flows d) before, e) during, and f) after velocity change. Note that U23 indicates a mean flow acceleration from 0.2 to 0.3 m/s and U32 indicates a mean flow deceleration, see Tables 3.1, 3.2 for more details.

Figure 3.9: Vertical profiles of volumetric sediment concentration of experimental condition C4 (13.1<C<14.8 %) accelerating flow a) before, b) during, and c) after velocity change and decelerating flows d) before, e) during, and f) after velocity change. Note that U23 indicates a mean flow acceleration from 0.2 to 0.3 m/s and U32 indicates a mean flow deceleration, see Tables 3.1, 3.2 for more details.

In Figure 3.10 the depth-averaged clay concentration is plotted on top of the results of (Baas et al., 2009). For all conditions there is a hysteresis effect between the decelerating and accelerating flows. For the same depth-averaged velocity, decelerating flows are able to keep a higher clay concentration within suspension than accelerating flows. This difference in suspended concentration is reduced for higher depth-averaged velocities.
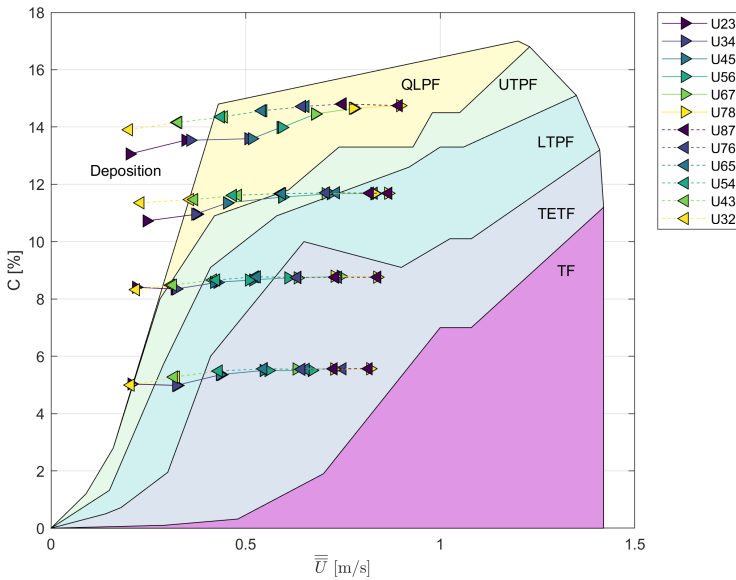
3

Figure 3.10: Experimental runs overlaid on experimental results from Baas et al. (2009). The different colours indicate different experimental with the symbol '>' denoting accelerating flow and '<' denoting decelerating flow. Note that U23 indicates a mean flow acceleration from 0.2 to 0.3 m/s and U32 indicates a mean flow deceleration, see Tables 3.1, 3.2 for more details.

3.3.2. CLAY FLOW TYPES

Figures 3.11 and 3.12 show the normalised time-averaged streamwise velocity profiles ($\overline{U}/\overline{\overline{U}}$) and time-averaged streamwise turbulence intensity profiles ($RMS(u')_0$) for both accelerating and decelerating experimental runs. Rows are associated with clay content (high at the top (C4), low at the bottom (C1)) and columns correspond to depth-averaged flow velocity (slowest at the left ($\overline{\overline{U}} = 0.2\ m/s$) and fastest at the right ($\overline{\overline{U}} = 0.8\ m/s$)). Specific clay concentration values for each row are shown in Tables 3.1 and 3.2. For each experimental run, the flow type is interpreted for the constant time series before and after the imposed velocity change based on the five flow types identified by Baas et al. (2009) (Section 1.3). The controlled velocity changes of 0.1 m/s results in minor variations between clay flow type within an experimental run; i.e. the clay flow type either stays the same before and after the imposed velocity change or the flow passes through one additional adjacent clay flow type (Tables 3.9 and 3.10).
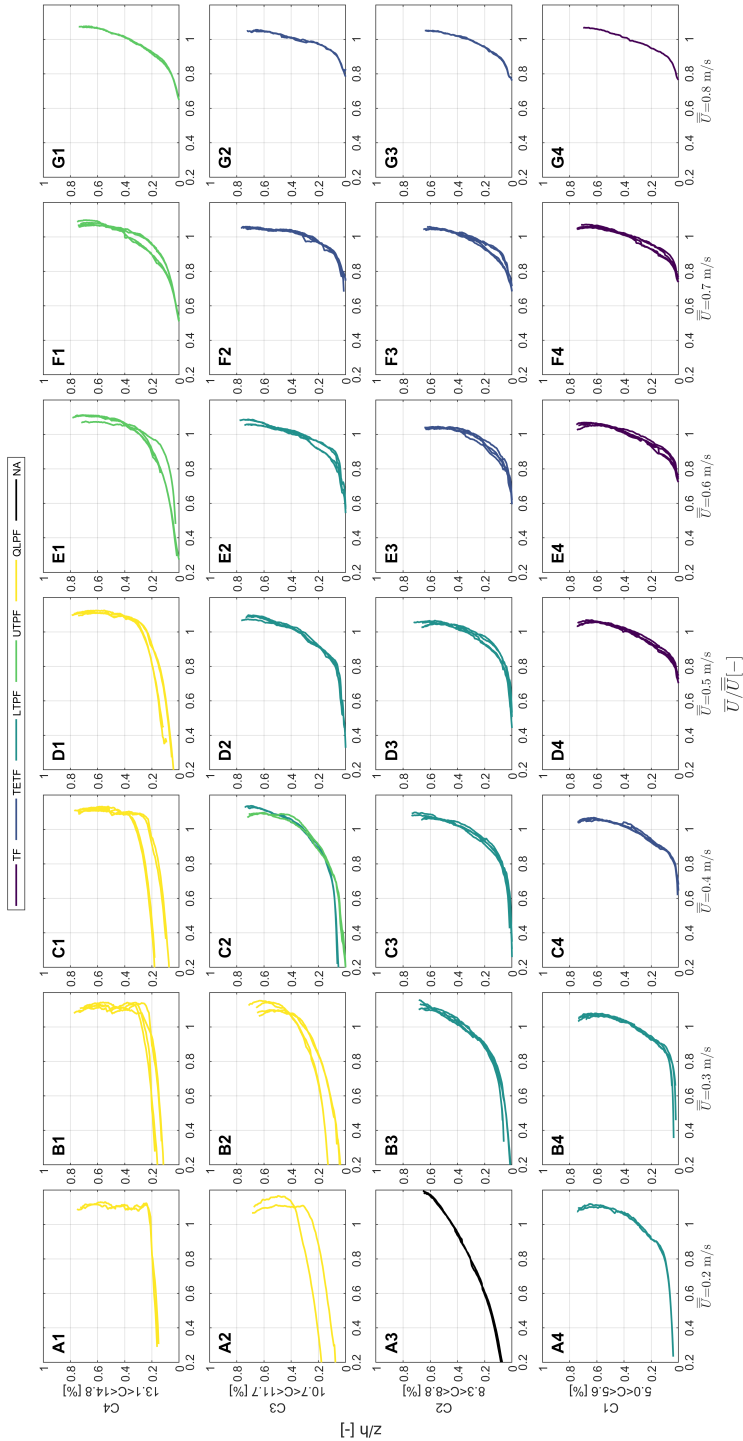
Figure 3.11: Vertical profiles of time-averaged streamwise velocity normalised by depth-averaged velocity ($\overline{U}/\overline{\overline{U}}$) separated into depth-averaged flow velocity and clay concentration (experimental condition C1 to C4, Tables 3.1 and 3.2) for accelerating and decelerating flows.
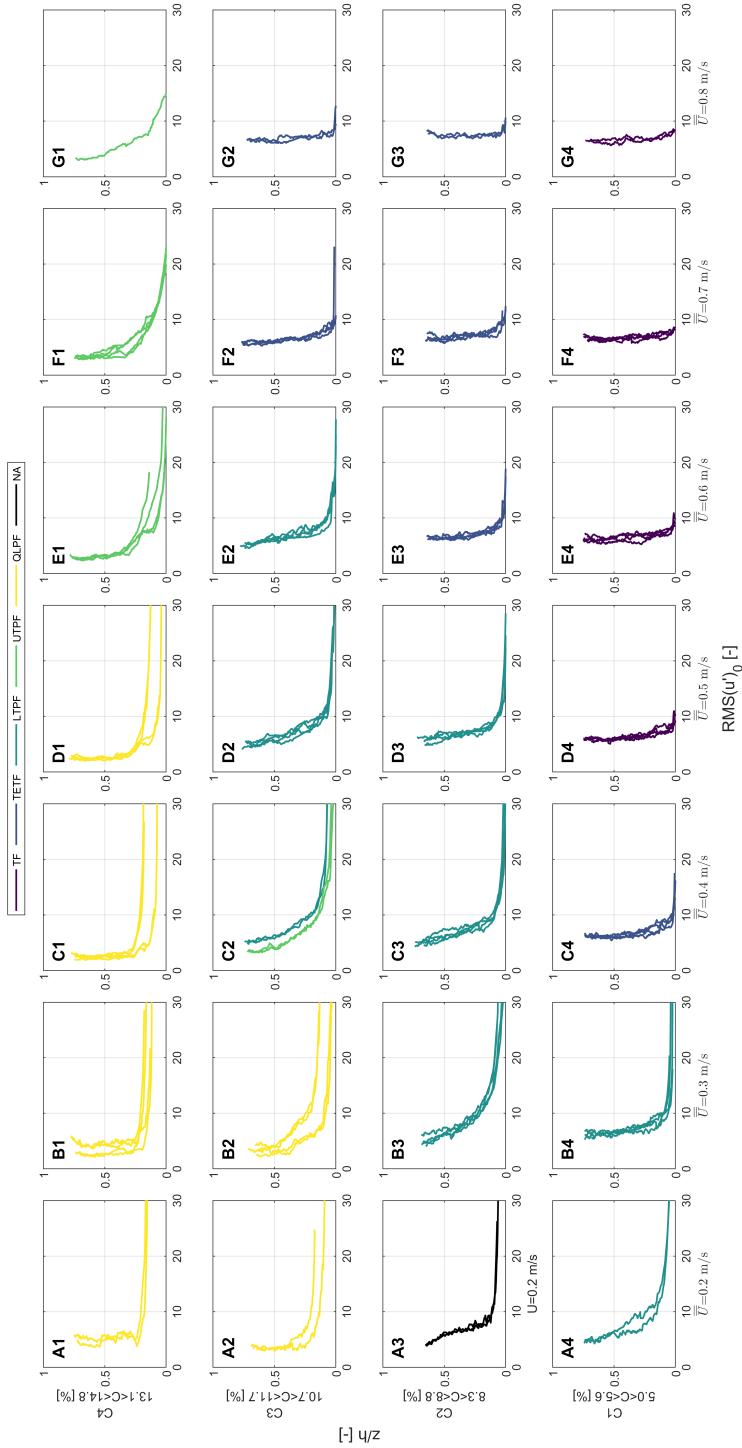
Figure 3.12: Vertical profiles of time-averaged streamwise turbulence intensity ($RMS(u')_0$) separated into depth-averaged flow velocity and clay concentration (experimental condition C1 to C4, Tables 3.1 and 3.2) for accelerating and decelerating flows.

Baas et al. (2009) identified the flow types based on 15 measurement points over the depth, whereas the angled UVPs in these experiments provide an increased amount of points over the depth. To identify the flow types of these experimental runs, additional statistical measurements were identified based upon the five flow types identified by Baas et al. (2009). No single threshold concentration exists for the formation of transitional flows (Section 1.3). However, the different clay flow types contain distinct velocity and turbulence intensity profiles, which can be used for a set of criteria to distinguish between the five flow types. The identification follows several criteria that will be introduced in the following paragraphs. The bottom half of the time-averaged streamwise turbulence intensity profiles ($RMS(u')_0$) were used for the different criteria. The turbulence intensities are normalised values and therefore comparable for different depth-averaged velocities plus it includes both velocity and $RMS(u')$ values. The largest differences within the turbulence intensity profiles is found in the bottom half of the flow and therefore that area was included in the criteria.

Criteria 1 - Differentiation TF & TETF from LTPF, UTPF & QLPF

When a plug flow develops within a clay flow, the near-bed velocity decreases and the turbulence intensity decreases within the plug. This results in a larger variation within the measurements of the turbulence intensity, i.e. the variance of $RMS(u')_0$ across the bottom half of the depth increases. Therefore, the variance of $RMS(u')_0$ is an effective measure to initially distinguish between turbulent flows (TF and TETF) and flows with plug flow development (LTPF, UTPF and QTPF) (Table 3.5; Figure 3.13).

Table 3.5: Criteria 1 - Differentiation between TF & TETF from LTPF, UTPF & QLPF

Criteria	Flow type
$var(RMS(u')_0) < 4$	TF or TETF
$var(RMS(u')_0) > 4$	LTPF, UTPF or QLPF

Criteria 2 - Differentiation TF from TETF

Both turbulent flow (TF) and turbulence-enhanced flow (TETF) exhibit a logarithmic velocity profile. The velocity of turbulence-enhanced transitional flows progressively diminishes, particularly close to the base of the flow, caused by a drag reduction in the boundary layer. This decrease in velocity results in an increase in turbulence intensity near the bed, which can be identified by an increased variance and kurtosis (α_4) of $RMS(u')_0$ across the bottom half of the depth (Table 3.6; Figure 3.13).

Table 3.6: Criteria 2 - Differentiation TF from TETF

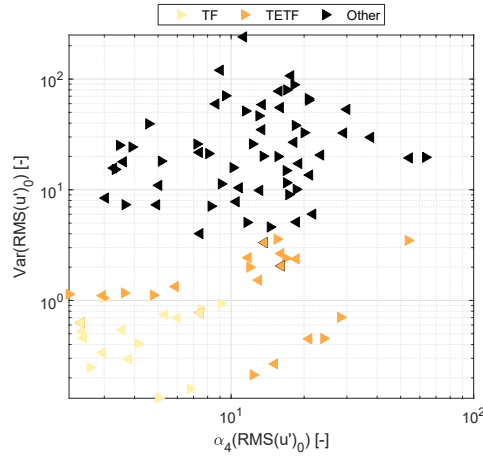| Criteria	Flow type
$var(RMS(u')_0) < 1$ & $\alpha_{4,RMS(u')_0} < 10$	TF
$var(RMS(u')_0) < 4$ & $\alpha_{4,RMS(u')_0} > 10$	TETF
$1 < var(RMS(u')_0) < 4$	TETF

Figure 3.13: Determination of flow types based on the criteria to separate TF and TETF flows.

Criteria 3 - Differentiation LTPF from UTPF & QLPF

The reduced turbulence intensity due to the development of a plug flow is noticeable in the bottom half of UTPF and QLPF flows as the plug flow development reached this height within the flow. The plug flow within LTPF flows only occurs in the top half of the flow and therefore the reduction in $RMS(u')_0$ is not noticeable. Therefore, the following criteria is used for flows that are not yet defined as TF or TETF, i.e. $var(RMS(u')_0) > 4$ (Table 3.7; Figures 3.14a,b):

Table 3.7: Criteria 3 - Differentiation LTPF from UTPF & QLPF

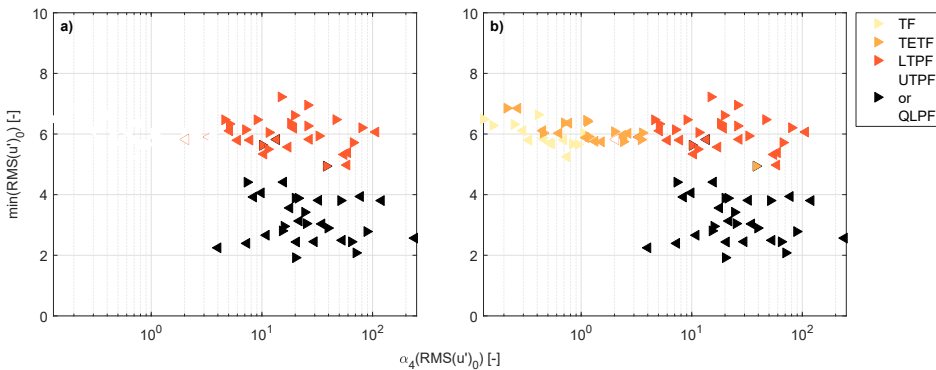| Criteria	Flow type
$min(RMS(u')_0) > 5$	LTPF
$min(RMS(u')_0) < 5$	UTPF or QLPF

Figure 3.14: Determination of flow types based on the criteria to separate LTPF flows from UTPF and QLPF.

Criteria 4 - Differentiation UTPF from QLPF

The increased height of a plug flow within QLPF flows compared to UTPF flows results in an increased correlation between the maximum velocity and depth-averaged velocity (Table 3.8; Figures 3.15a,b).

Table 3.8: Criteria 4 -Differentiation UTPF from QLPF

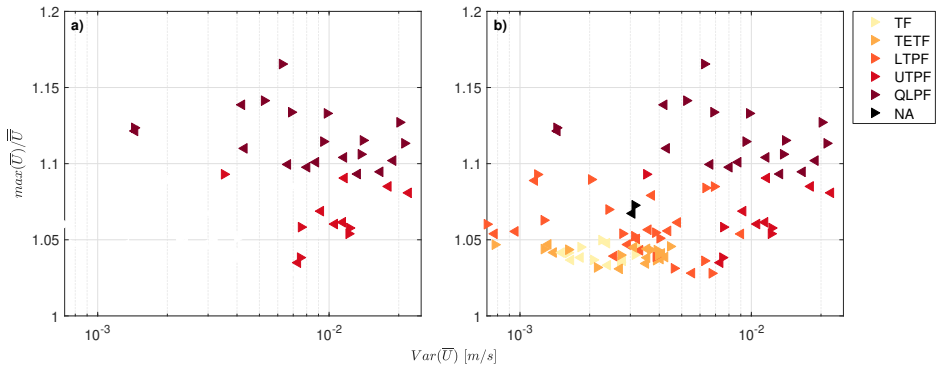| Criteria	Flow type
$max(\overline{U})/\overline{\overline{U}} < 1.1$	UTPF
$max(\overline{U})/\overline{\overline{U}} > 1.1$	QLPF

Figure 3.15: Determination of flow types based on the criteria to separate UTPF and QLPF flows.

To objectively identify the five different flow types within these experiments, a set of statistical criteria are used to separate different flow types based upon the flow types identified by Baas et al. (2009). Initially, the turbulent flows (TF and TETF) are distinguished from flows with plug flow development (LTPF, UTPF and QLPF) by the variance of $RMS(u')_0$ across the bottom half of the depth. Together with the kurtosis, a differentiation can be made between turbulent flows (TF) and turbulence-enhanced transitional flow (TETF). As the plug flow develops further downwards from the surface towards the bed, $RMS(u')_0$ reduces in the bottom half of the flow, separating UTPF and QLPF from LTPF flows. Finally, UTPF and QLPF can be separated by the correlation between the maximum velocity and depth-averaged velocity. Based on these criteria, tables 3.9 and 3.10 show the identified flow types for the experimental runs of the experiments of this research study.

Table 3.9: Overview of flow types defined for the accel- erating experimental runs performed in this study. Flow regime refers to TF = Turbulent flow, TETF= turbulence- enhanced transitional flow, LTPF = lower transitional plug flow, UTPF = upper transitional plug flow, QLPF = quasi-laminar plug flow; (d)=depositional flow.

Experimental run	Flow regime before	after
Experimental condition C1		
A-C5.0-U23	LTPF(d)	LTPF(d)
A-C5.0-U34	LTPF(d)	TETF
A-C5.4-U45	TETF	TF
A-C5.5-U56	TF	TF
A-C5.6-U67	TF	TF
A-C5.6-U78	TF	TF
Experimental condition C2		
A-C8.4-U23	NA(d)	LTPF
A-C8.3-U34	LTPF	LTPF
A-C8.6-U45	LTPF	LTPF
A-C8.7-U56	LTPF	TETF
A-C8.7-U67	TETF	TETF
A-C8.8-U78	TETF	TETF
Experimental condition C3		
A-C10.7-U23	QLPF(d)	QLPF(d)
A-C11.0-U34	QLPF(d)	LTPF
A-C11.4-U45	LTPF	LTPF
A-C11.6-U56	LTPF	LTPF
A-C11.7-U67	LTPF	TETF
A-C11.7-U78	TETF	TETF
Experimental condition C4		
A-C13.1-U23	QLPF(d)	QLPF(d)
A-C13.5-U34	QLPF(d)	QLPF(d)
A-C13.6-U45	QLPF(d)	QLPF
A-C14.0-U56	QLPF	UTPF
A-C14.5-U67	UTPF	UTPF
A-C14.7-U78	UTPF	UTPF

Table 3.10: Overview of flow types defined for the decel- erating experimental runs performed in this study. Flow regime refers to TF = Turbulent flow, TETF= turbulence- enhanced transitional flow, LTPF = lower transitional plug flow, UTPF = upper transitional plug flow, QLPF = quasi-laminar plug flow; (d)=depositional flow.

Experimental run	Flow regime before	after
Experimental condition C1		
D-C5.3-U32	LTPF	LTPF
D-C5.5-U43	TETF	LTPF
D-C5.4-U54	TF	TETF
D-C5.5-U65	TF	TF
D-C5.6-U76	TF	TF
D-C5.6-U87	TF	TF
Experimental condition C2		
D-C8.5-U32	LTPF	NA
D-C8.7-U43	LTPF(d)	LTPF
D-C8.8-U54	LTPF(d)	LTPF(d)
D-C8.8-U65	TETF	LTPF(d)
D-C8.8-U76	TETF	TETF
D-C8.8-U87	TETF	TETF
Experimental condition C3		
D-C11.5-U32	QLPF	QLPF
D-C11.6-U43	UTPF	QLPF
D-C11.7-U54	LTPF	UTPF
D-C11.7-U65	LTPF	LTPF
D-C11.7-U76	TETF	TETF
D-C11.7-U87	TETF	TETF
Experimental condition C4		
D-C14.2-U32	QLPF(d)	QLPF(d)
D-C14.4-U43	QLPF(d)	QLPF(d)
D-C14.6-U54	QLPF	QLPF(d)
D-C14.7-U65	UTPF	QLPF
D-C14.8-U76	UTPF	UTPF
D-C14.7-U87	UTPF	UTPF

3

3.3.3. FLOW ADAPTATION

DETERMINATION OF ADAPTATION OF VELOCITY

To understand the adaptation of different flow types to changes in velocity and the correlation between initial velocity and clay concentration, the adaptation time $\Delta T_{\overline{\overline{U}}}$ is extracted from the velocity data. As no variations in adaptation over the depth are found (Figure 3.16), the depth-averaged velocity is used to identify the adaptation time. The adaptation time is defined as follows:

$$\Delta T_{\overline{\overline{U}}} = T_{adapted\ velocity} - T_{moment\ of\ imposed\ velocity\ change} = T_A - T_M \qquad (3.13)$$

The time of adapted velocity is determined by the time the flow is adjusted to change in velocity, i.e. when the velocity reaches $\overline{\overline{U}}_{after}$. It is important to differentiate between the overall signal change and local variations due to velocity fluctuations. Figure 3.17 shows a time series of the depth-averaged velocity of experimental run A-C0.0-U67, which indicates that due to the high frequency velocity fluctuations it is challenging to accurately determine T_A. In this section, four methods are compared to select the most suitable method for the dataset.
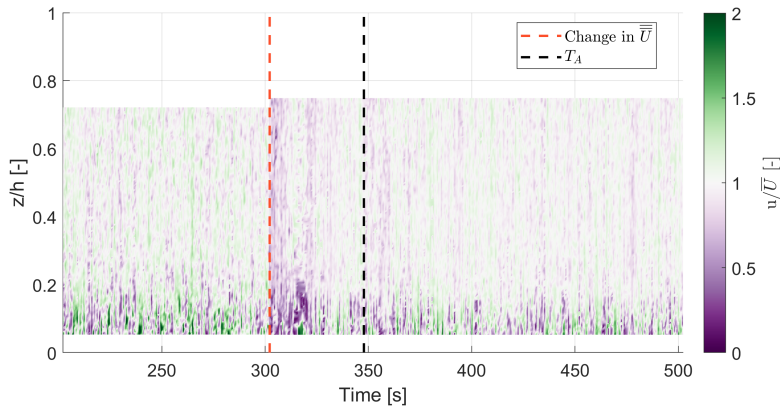

Figure 3.16: Normalised instantaneous velocity ($u/\overline{U}$) of experimental run A-C0.0-U67, where a red dashed line indicates the imposed velocity change and a dashed black line the time of adapted velocity, T_A.

To exclude high frequency variations, the first method uses a moving mean ($\overline{\overline{u}}_m$) through the time series to smooth out the signal (Figure 3.18). The time of adapted velocity, T_A, is determined by the first point when the moving mean is equal to $\overline{\overline{U}}_{after}$. A moving mean smooths out the signal, but the amount of smoothing is dependent on the amount of data points (m) included. Figure 3.18 shows three examples of a moving mean through the time series for different values of m and highlights that $\Delta T_{\overline{\overline{U}}}$ is dependent on the value of m.
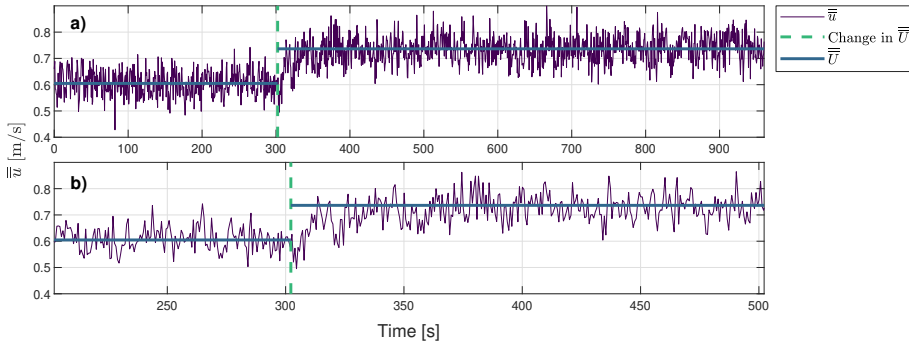
Figure 3.17: a) Full time series of depth-averaged velocity of A-C0.0-U67 overlaid with the moment of imposed velocity change and the depth-averaged velocity before and after the velocity change; b) time series around the velocity change.
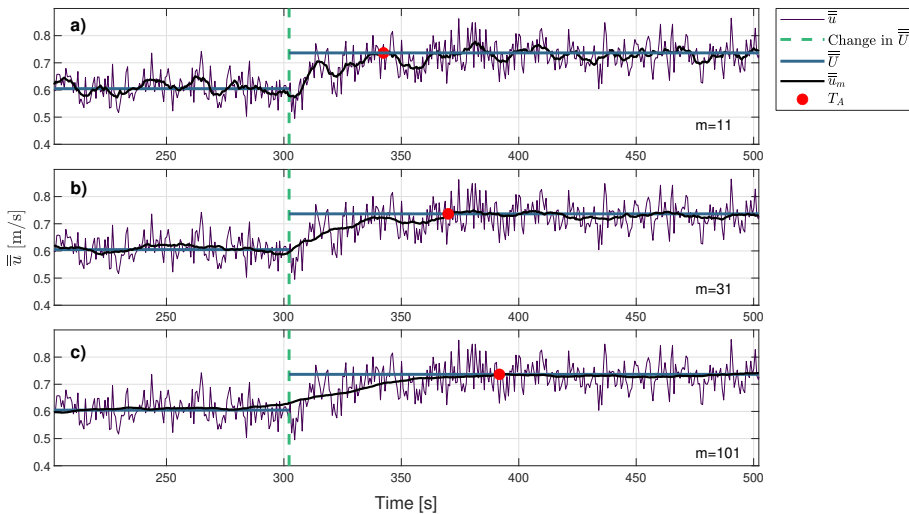
3

Figure 3.18: Moving mean imposed over the time series with different amount of data points included; a) 11 data points; b) 31 data points; c) 101 data points.

A different method is to use the variations in slope within the velocity signal ($d\overline{\overline{U}}/dt$) to determine the time of adapted velocity. T_A is determined by the first time the slope reaches zero after the maximum slope. To smooth out the high frequency variations within the slope, the slope is determined over a moving mean of the signal. Two examples of determining T_A based upon the slope are shown in Figure 3.19 and Figure 3.20, for each example a different amount of data points m is included in the calculation of the moving mean. Determining T_A based upon a slope gives the same challenges as using the original signal, as $\Delta T_{\overline{\overline{U}}}$ depends on the amount of data points m used within determining the slope.
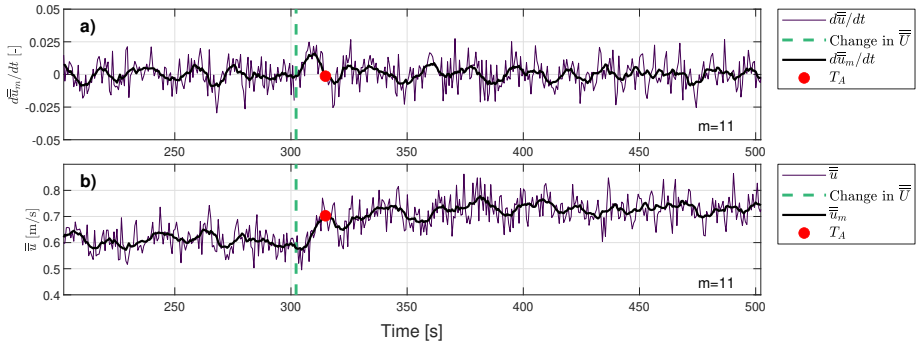
Figure 3.19: a) slope of the depth-averaged velocity time series of experimental run A-C0.0-U67 using 11 data points within the moving mean; b) time series with imposed moving mean and $\Delta T_{\overline{\overline{U}}}$.
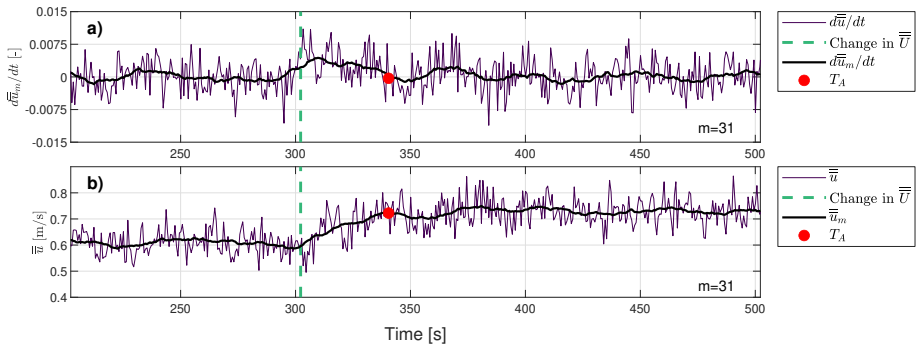

Figure 3.20: a) slope of the depth-averaged velocity time series of experimental run A-C0.0-U67 using 31 data points within the moving mean; b) time series with imposed moving mean and $\Delta T_{\overline{\overline{U}}}$.

To avoid the selection of amount of data points (m) in determination of T_A, the third method calculates the residual error based upon both the mean and the slope of the signal. The time series after the imposed velocity change is divided into two sections, one section where the velocity is still adapting and one section where the velocity is constant. The moment of the division is determined by minimizing the sum of the residual (squared) error of each region from its local mean. Both the mean and slope are included in the calculation of the residual error and for experimental run A-C0.0-U67 the result of this method is shown in Figure 3.21.
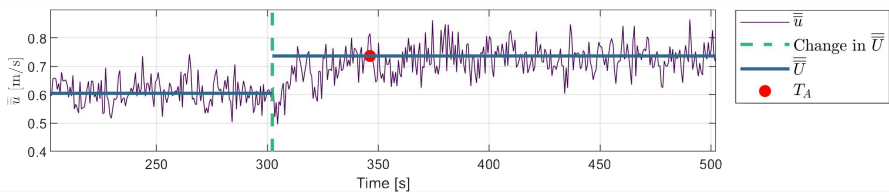

Figure 3.21: Time series of depth-averaged velocity of A-C0.0-U67 overlaid with the moment of imposed velocity change and the depth-averaged velocity before and after the velocity change. T_A is determined by the residual error of both the mean and slope of the signal.

A different method that avoids the selection of m in determination of T_A is fitting a Gaussian function to the time series after the imposed velocity change. The adaptation time is defined as two times the standard deviation of the Gaussian fit (Figure 3.22).
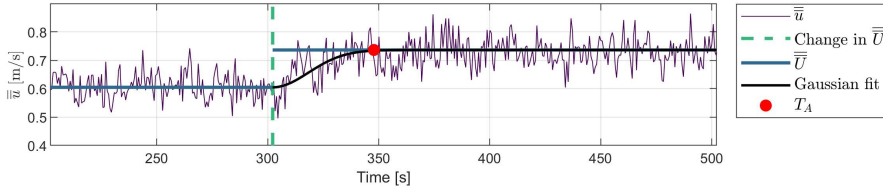

Figure 3.22: Time series of depth-averaged velocity of A-C0.0-U67 overlaid with the moment of imposed velocity change and the depth-averaged velocity before and after the velocity change. T_A is determined by a Gaussian fit to the time series.

The first two methods use a moving mean and highlight that the adaptation time is influenced by the amount of data points included in the moving mean. For experimental run A-C0.0-U67, the correlation between $\Delta T_{\overline{\overline{U}}}$ and amount of data points m is shown in Figure 3.23. The other two methods, residual error and Gaussian fit, are plotted on top of the results and contain a comparable adaptation time for this experimental run. The adaptation time can be different for the various methods, but the patterns between the experimental runs are comparable. To avoid the influence of a moving mean, the Gaussian fit is selected as the most consistent method within the data analysis of this chapter.
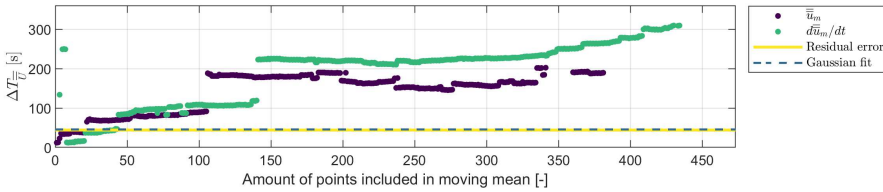

Figure 3.23: Correlation between $\Delta T_{\overline{\overline{U}}}$ of different methods and amount of data points (m) included in determining the moving mean.

DETERMINATION OF ADAPTATION OF TURBULENCE INTENSITY

To understand the adaptation of different flow types to changes in turbulence intensity and the correlation between initial velocity and clay concentration, the adaptation time $\Delta T_{\overline{RMS(u')}}$ is extracted from the UVP data. As no variations in adaptation over the depth are found, the depth-averaged turbulence intensity is used to identify the adaptation time. The adaptation time is defined as follows:

$$\Delta T_{\overline{RMS(u')}_0} = T_{adapted\ turbulence\ intensity} - T_{moment\ of\ imposed\ velocity\ change} = T_R - T_M$$
(3.14)

The time of adapted turbulence intensity is determined by the difference between the imposed velocity change and when the turbulence intensity reaches $\overline{RMS(u')}_{0\,after}$. For the determination of $RMS(u')$, n data points are needed (Equation 3.4) and therefore there is an unavoidable influence of the selection of n in determining $\Delta T_{\overline{RMS(u')}_0}$ (Figure 3.24). To include flow characteristics, the minimum amount of data points should be at least ten times the turbulence kinetic energy time scale, estimated by $h/\overline{\overline{U}}$ (Tennekes and Lumley, 1972; Pope, 2000), which correlates to 2 to 3 datapoints depending on the experimental run. The adaptation time is lengthened with

an increase in data points and therefore higher values of n have a larger influence on the results. Figure 3.25 shows the correlation between the adaptation time minus 0.5 times the time window included in the determination of $RMS(u')$ and amount of points, n, used in the calculation of $RMS(u')$. When the value is below zero, the results are biased by n and when the value is above zero, the values are unbiased. The minimum amount of data points that meet these requirements is n=13, which is chosen for the data analysis.
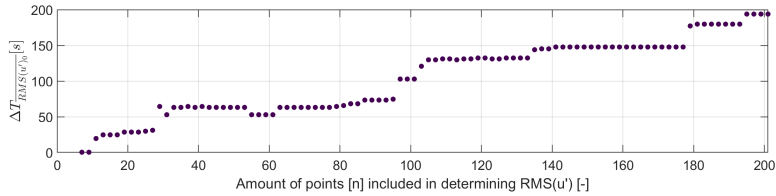

Figure 3.24: Correlation between the adaptation time, $\Delta T_{\overline{RMS(u')_0}}$ and amount of points, n, used in the calculation of $RMS(u')$.
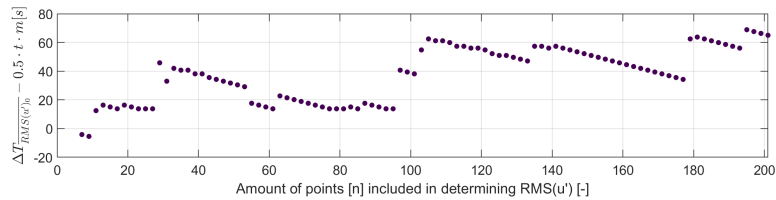

Figure 3.25: Correlation between the adaptation time minus 0.5 times the time window included in the determination of $RMS(u')$ and amount of points, n, used in the calculation of $RMS(u')$.

Similar to the adaptation time of the velocity and for consistency, the adaptation time of the turbulence intensity is determined by a Gaussian fit. The adaptation time is defined as two times the standard deviation of the Gaussian fit (Figure 3.26).
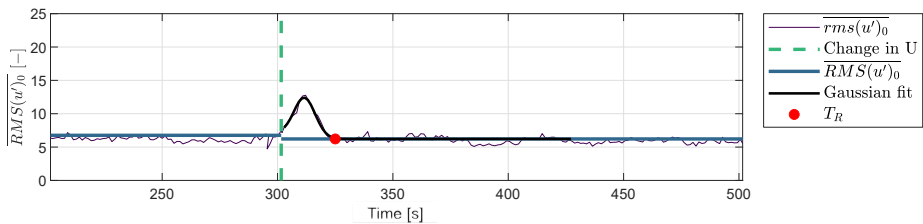

Figure 3.26: Time series of depth-averaged turbulence intensity of D-C11.7-U76 overlaid with the moment of imposed velocity change and the depth-averaged turbulence intensity before and after the velocity change. T_R is determined by a Gaussian fit to the time series.

ADAPTATION TIME

Several aspects can influence the adaptation time of the clay-laden non-uniform flow of these experiments. These include: acceleration or deceleration, clay concentration, deposition, flow velocity before and after, velocity change and clay flow type. To compare different experimental conditions on similar terms, the results are normalised by the velocity step and clay concentration. A larger velocity step results in a longer adaptation time for both accelerating and decelerating flows. The change within the flow is larger and consequently, the flow needs a longer time to adjust to the change. Throughout the experiments, the velocity change is kept as close as possible to 0.1 m/s, but small variations occur due to flume settings, clay concentrations and UVP measurements. To eliminate this effect in the interpretation, the adaptation times are plotted against the normalised velocity, $U_{high}/(U_{high} - U_{low})$. Additionally, the results are normalised with the clay concentration to incorporate the balance between turbulent (velocity) and cohesive (clay concentration) forces, which are the main factors determining the flow type (Baas et al., 2009).

Figures 3.27a and 3.27b show the correlation between velocity normalised by the velocity change and clay concentration, $U_{high}/(U_{high} - U_{low})/C$, and adaptation time of depth-averaged velocity, $\Delta T_{\overline{\overline{U}}}$, for accelerating and decelerating flows, respectively. The colour scheme denotes the identified clay flow types. The accelerating turbulent flows (TF) show comparable adaptation times between 13 and 14 s (Figure 3.27a). Transitional flow types TETF and LTPF show larger variations in adaptation time then TF flows, with adaptation times between 13 and 20 seconds. Overall, the adaptation time of accelerating flows increases as the flow types pass through the transitional flow conditions, with 29 s recorded for the stronger turbulence attenuation flows, UTPF and QLPF. The decelerating flows show a larger range in adaptation time than the accelerating flows (Figure 3.27b). There is no apparent difference in adaptation time between accelerating and decelerating flows. The spread in adaptation time for decelerating flows is particularly large between $0.5 < U_{high}/(U_{high} - U_{low})/C < 1$. Stronger turbulence attenuated flows, UTPF and QLPF, i.e. $U_{high}/(U_{high} - U_{low})/C < 0.5$, show limited scatter in adaptation time.

Figure 3.27: Correlation between velocity normalised by the velocity change and clay concentration, $U_{high}/(U_{high} - U_{low})/C$ and the adaptation time of depth-averaged velocity, $\Delta T_{\overline{\overline{U}}}$, for a) accelerating flow conditions and b) decelerating flow conditions. The colour indicates the clay flow type. A circle denotes the same clay flow type before and after the imposed velocity change and a triangle denotes a transition between clay flow types as the flow accelerates or decelerates.

Figures 3.28a and 3.28b show the correlation between velocity normalised by the velocity change and clay concentration, $U_{high}/(U_{high} - U_{low})/C$, and adaptation time of the depth-averaged turbulence intensity, $\Delta T_{\overline{RMS(u')_0}}$, for accelerating and decelerating flows, respectively. The accelerating flows show varying adaptation times of turbulence intensity between 9 and 77 s (Figure 3.28a). For each clay flow type there is a range of adaptation times, with a suggested increase for adaptation time of the stronger turbulence attenuated flows, QLPF. The decelerating flows indicate an adaptation time dependent on clay flow type. The decelerating turbulent flows (TF) show comparable adaptation times around 30 s (Figure 3.27b). Omitting the two large values ($\Delta T_{\overline{RMS(u')_0}} > 60\ s$), the overall trend suggests that TF flows adapt in 30 s and this time decreases for TETF and LTPF flows. However, it increases again for UTPF and QLPF.
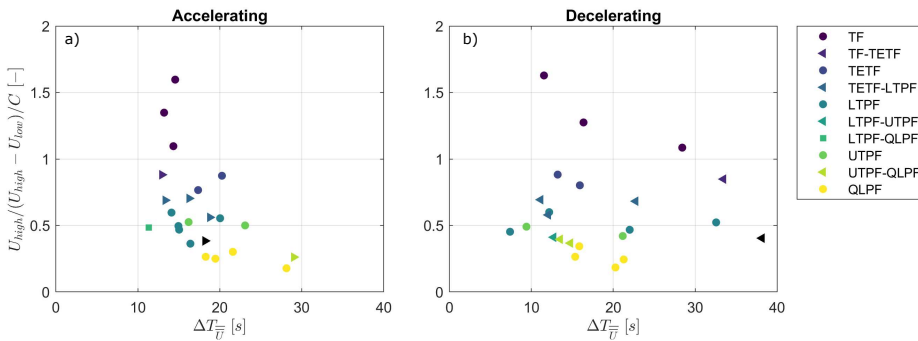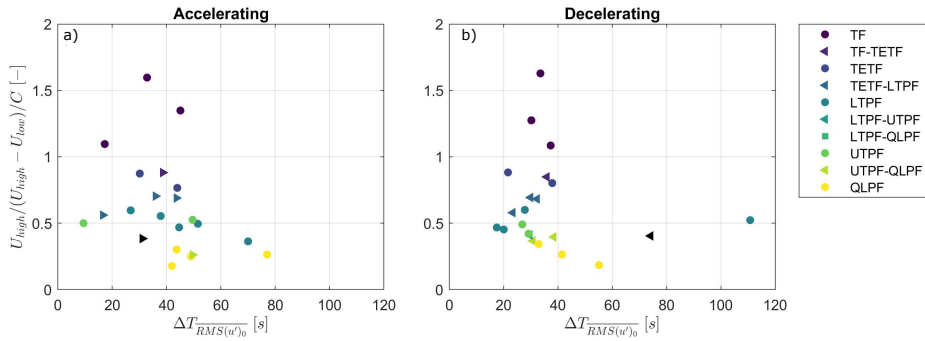
3

Figure 3.28: Correlation between velocity normalised by the velocity change and clay concentration, $U_{high}/(U_{high}-U_{low})/C$ and the adaptation time of depth-averaged turbulence intensity, $\Delta T_{\overline{RMS(u')_0}}$, for a) accelerating flow conditions and b) decelerating flow conditions. The colour indicates the clay flow type. A circle denotes the same clay flow type before and after the imposed velocity change and a triangle denotes a transition between clay flow types as the flow accelerates or decelerates.

3.4. Discussion

3.4.1. Clay concentration

The variations in clay concentrations before, during and after the velocity change for low velocity (U23, U34) accelerating flows, suggests that sediment gets eroded from the bed and afterwards it gets distributed over the full depth (Figures 3.6 to 3.9a,b,c). The distribution of sediment over the full depth after erosion does not occur instantaneously. At the time of the velocity change, sediment gets eroded from the bed and it takes time to distribute this sediment over the full depth. Sediment samples were collected at the same time of the imposed velocity change and consequently at this measurement moment increase in clay concentration is measured (for the experiments experiencing deposition, Table 3.9). After the velocity change, there was sufficient time for the flow to distribute the clay over the depth and the measurements show a constant clay concentration over the depth.

The measured clay concentrations show a hysteresis between the decelerating and accelerating flow conditions, most apparent for the low velocity, high concentration runs A-C10.7-U32 and D-11.5-U32, A-C13.1-U23 and D-C14.2-U32. Decelerating flows were able to keep more sediment in suspension than accelerating flows (Figure 3.10).

A potential reason is the formation of flocs. As flocs grow, their settling velocity might increase (Winterwerp, 2002; Mehta and McAnally, 2008; Spearman and Manning, 2017) and potentially material will deposit, reducing the clay concentration. It is possible that flocs are only able to form or larger flocs can be established at lower flow velocities (Milligan and Hill, 1998; Dyer, 1988;

McAnally and Mehta, 2000; Winterwerp, 2002), resulting in a larger percentage of flocs within accelerating flows as the initial velocity is lower. Potentially the clay flocs might settle and the deposited larger floc size reduces the erosion rate, maintaining a lower clay concentration in the flow until the velocity accelerated enough to erode the larger flocs (Winterwerp and Van Kesteren, 2004; Mehta and McAnally, 2008; Van Maren et al., 2009). The initial velocity in decelerating flows is higher and therefore they might contain a reduced size of flocs in the flow, reducing the settling rate and maintaining a higher concentration. However, this pattern is not observed within the clay suspension measurements. Additionally, a majority of the flows within these experiments contain plug flows with a pervasive network of permanently interlinked clay particles and the influence of floc size would only be noticeable within non-turbulence attenuated flows.

A different potential reason is a difference in the capacity of the flow between eroding sediment and keeping sediment in suspension. The flow at a certain velocity will be able to keep sediment in suspension, but it won't be able to erode sediment (Dyer, 1988; Kostaschuk et al., 1989; Song and Graf, 1996; Schieber et al., 2022). The increase in velocity during acceleration is insufficient to erode sediment from the bed to increase the concentration. If the same velocity is reached by deceleration, the sediment was already in suspension before the flow decelerates and the flow is capable of keeping the sediment in suspension, resulting in a higher concentration for the same flow velocity if the flow decelerates compared to accelerating flows. This hysteresis occurs up until the flow velocity is sufficient to erode sediment from the bed (Kuijper et al., 1990; Portela and Reis, 2005). The hysteresis is found for both cohesive and non-cohesive sediment (Portela and Reis, 2005; Zhang et al., 2009), but the formation of flocs within cohesive sediment might enhance this effect.

One last potential, but unlikely reason, is the total time between the imposed velocity change and the measurement. Breaking flocs with increased turbulence might be easier than forming them within a clay-laden flow. Moreover, establishing a network of flocs and at higher concentrations, a gel, might take even longer. However, the measurements made at the end of the run period of 25 minutes, do not show a reduced clay concentration or further adaptations within the velocity measurements. Consequently, insufficient runtime is an unlikely explanation for the difference in clay concentration between accelerating and decelerating flows.

3.4.2. CLAY FLOW TYPES

The original work on clay-laden flow types by Baas et al. (2009) was conducted under uniform and steady flow conditions, i.e flows that do not change in time nor in space. The phase diagram (Figure 1.11) suggests that there are regions within the clay concentrations versus velocity space where transitions within flow types occur, even though they did not focus on them. In this chapter, the work focused on understanding how flows transition between clay flow types in time. Selected experimental conditions forced changes in velocity while maintaining the clay concentration. Measurements taken, before, during and after the imposed flow velocity changes allowed identification of the different clay flow types. Baas et al. (2009) did not offer quantitative criteria to distinguish between flow types and focused on the near bed measurements and turbulence intensity as well as flow velocity signals. Building upon their framework, this chapter proposed a set of criteria to distinguish between flow types, using statistical measures associated with the flow velocity profiles. The measurements conducted here allowed quantifying flow and turbulence for the full profile, giving a better view of the flow behaviour at each flow type than Baas et al. (2009) who measured at discrete locations within the flow (and like it was done in Chapter 2).

The selected criteria to distinguish between flow types follow the expected pattern between the correlation of turbulent and cohesive forces (Figure 3.29). An increase in depth-averaged velocity results in a shift in boundaries between turbulent, transitional and laminar flow types to higher clay concentrations. Turbulence generated by boundary shear at these higher velocities

becomes greater and the flow is able to prevent flocculation and gelling (McAnally and Mehta, 2000; Winterwerp, 2002; Cuthbertson et al., 2010). The pattern between the different flow types is shifted to higher clay concentrations compared with the data from Baas et al. (2009). This shift can be caused by experimental differences such as flume dimensions, clay material (Section 1.2.4), equipment settings and setup. As clay material is a natural product, differences in chemistry can be identified within various kaolinite samples influencing the clay rheology (Teh et al., 2009; Au and Leong, 2013; Schieber et al., 2022). The methods proposed here include identification of statistical measurements based upon the five flow types identified by Baas et al. (2009) to distinguish between the clay flow types (Section 3.3.2). These methods are more robust than the qualitative interpretation originally proposed by Baas et al. (2009) and they can be adapted to other conditions by following the proposed steps and being flexible with the thresholds recommended.

The balance between turbulent and cohesive forces determines the clay flow type and similar clay flow types are identified depending on flow velocity and clay concentration. Consequently, the identified flow types for the uniform conditions before and after the imposed velocity change are independent of the history of the flow. At the combination of $\overline{\overline{U}} = 0.4$ m/s and $C = 11\%$, two different flow types are identified (Figure 3.29), namely LTPF in accelerating flow A-C11.0-U34 and UTPF in decelerating flow D-C11.7-U43 (Figures 3.11C2, 3.12C2). Due to the hysteresis in clay concentration (Section 3.4.1), the accelerating flow has a slightly lower clay concentration than the decelerating flow and this might cause the difference between UTPF in flow D-C11.7-U43 and LTPF in flow A-C11.0-U34. Lower transitional plug flows are stable across a wider range of concentrations than the upper transitional flows (Baas et al., 2009) and consequently, a small variation in clay concentration or flow velocity can already result in a transition from UTPF to QLPF or LTPF.
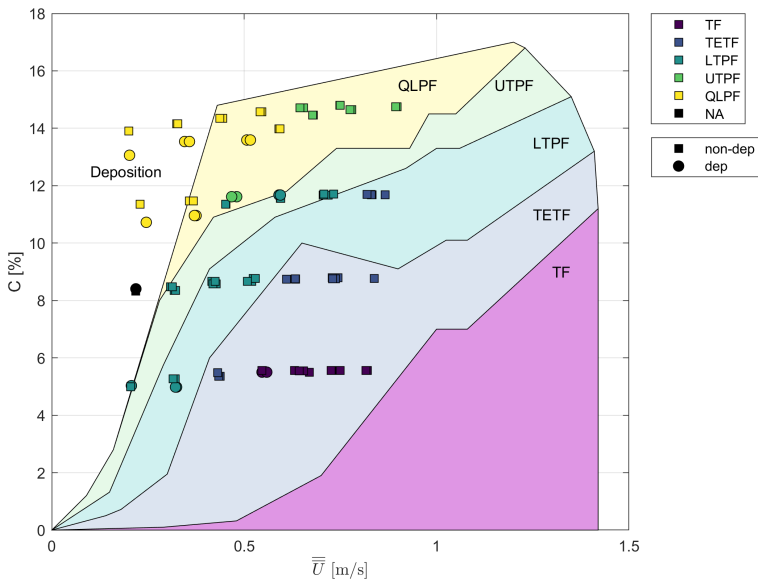

Figure 3.29: Identified flow types overlaid on results from Baas et al. (2009).

The development of a plug flow results in large gradients in downstream velocity and turbulence intensity near the bed and a plug with low or no vertical gradients near the surface (Wang and Plate, 1996; Baas and Best, 2002; Baas et al., 2009). The gradient within the top half of the flow is unable to distinguish between a plug flow and turbulent flow conditions and therefore other criteria are used to differentiate between clay flow types (Section 3.3.2). The average gradient over the top half of the flow might be skewed due to the height of a plug flow or the variations between adjacent measurement points. The criteria selected to distinguish between different uniform flow types are based on the flow properties and therefore the method is suitable to be used in different environments including other flume experiments or field measurements (Baas and Best, 2002; Baas et al., 2009). However, the actual values used to distinguish between flow types could vary between experiments or field data due to various reasons. The statistical values are influenced by the bed location and distance between the bed and the first couple of measurements. Ideally, an exact location of the bed height is known, which is challenging within cohesive sediment flows (Whitehouse et al., 2000; Winterwerp and Van Kesteren, 2004). Additionally, the statistical values are influenced by the amount of measurement points over the depth and correlated with the installation method of the measurement equipment. Moreover, the method is developed for uniform flow conditions as non-uniform flow can influence the turbulence variations within the flow (Cardoso et al., 1991; Kironoto and Graf, 1995; Song and Graf, 1996; Yang et al., 2006; Emadzadeh et al., 2010). To improve the criteria to identify the different flow types, the method should be tested on additional datasets, including but not limited to larger variations in unsteadiness, variations in clay type and combinations of different clay types, i.e. providing an excellent opportunity for future research in non-uniform clay transitional flows (Section 5.3).

3.4.3. Flow adaptation

The accelerating turbulent flows have comparable adaptation times and the adaptation time gradually increases as the clay flow type passes through the transitional flows (Figure 3.27a). This elongated adaptation time correlates with the generation of additional turbulence within TETF flows and the breaking up of clay bonds within a plug flow (LTPF, UTPF and QLPF). Breaking clay bonds between cohesive particles is a time-dependent process (Peterfi, 1927; Freundlich, 1935; Mitchell, 1960; Ren et al., 2021) and, therefore, the turbulence attenuated flows need more time to adjust to the temporal velocity change. In order to break the clay bonds within a plug flow, turbulence needs to penetrate the pervasive, volume filling network of particle bonds (Dyer, 1988; McAnally and Mehta, 2000; Winterwerp, 2002; Cuthbertson et al., 2010), which is increasingly difficult with stronger turbulence attenuated flows. Yield stress of clay suspensions increases exponential with clay concentrations and hence breakage of clay bonds become increasingly difficult (Wan, 1982; Au and Leong, 2013; Yu et al., 2013). Additionally, at the lower velocities, deposition occurs (Section 3.3.1) and when the flow accelerates it picks up sediment from the bed elongating the adaptation time. Erosion from the bed is not an instantaneous response, due to inertia effects, it takes time for the sediment concentration profile to adjust to a new velocity (Dyer, 1988; Whitehouse et al., 2000; Portela and Reis, 2005; Son and Hsu, 2011).

The decelerating flows show a large scatter in adaptation time of turbulent flows (Figure 3.27b). The transitional flow conditions show a comparable trend to the accelerating flows, where stronger turbulence attenuated decelerating flows have a longer adaptation time, due to the formation of clay bonds. The formation of clay bonds is a thixotropic process that is influenced by the balance between inter-particle collision and turbulence (Lick et al., 1993; McAnally and Mehta, 2000; McCave and Hall, 2006; Cuthbertson et al., 2010; Goh et al., 2011; Son and Hsu, 2011). High clay concentrations results in additional inter-particle collision due to increase in clay particles, but results in a reduction due to the turbulence attenuation. The adapation time of the depth-averaged velocity is comparable for the accelerating and decelerating flows apart from the few higher times

of decelerating flows. Especially the stronger turbulence attenuated flows (QLPF) have comparable adaptation times, which suggest there is no apparent difference in time required to establish clay bonds, as in the decelerating flows, compared with breaking clay bonds, as in accelerating flows. Rheology provides insight into the interactions between the particles in a clay suspension (Massey and Ward-Smith, 2012; Nguyen et al., 2018, Section 1.2.5). Yield stress increases exponential with clay concentration (Wan, 1982; Au and Leong, 2013; Yu et al., 2013) and flocculation and the formation of gels is influenced by the thixotropic processes within the kaolinite suspension (Lick et al., 1993; McAnally and Mehta, 2000; McCave and Hall, 2006; Cuthbertson et al., 2010; Goh et al., 2011; Son and Hsu, 2011). To date, there is no suitable scaling available to correlate the yield stress with the development of different clay flow types and the adaptation to velocity changes.

Overall the adaptation time of the depth-averaged turbulence intensity is higher than the adaptation time of the depth-averaged flow velocity (Figure 3.30). The adaptation time of the turbulence intensity will be slightly increased due to the method of calculating $RMS(u')$. However, the difference in adaptation time between the depth-averaged velocity and depth-averaged turbulence intensity is larger than the timespan of the datapoints included in the calculation of $RMS(u')$. Hence, the velocity adapts faster than the turbulence within the clay-laden flows, partly due to the random motion of turbulence (Tennekes and Lumley, 1972; Anderson, 2011; Takeda, 2012). Consequently, reaching a constant velocity might mean that although the velocity has adjusted to the change in velocity, the flow type might not be fully established and clay bonds might still form or break after $\Delta T_{\overline{U}}$.
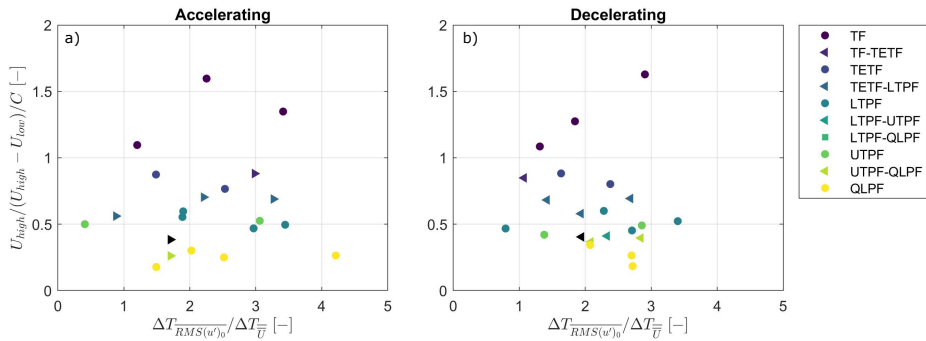

Figure 3.30: Ratio between adaptation time of depth-averaged turbulence intensity, $\Delta T_{\overline{RMS(u')_0}}$, and adaptation time of depth-averaged velocity, $\Delta T_{\overline{U}}$ against velocity normalised by the velocity change and clay concentration, $U_{high}/(U_{high}-U_{low})/C$ for a) accelerating flow conditions and b) decelerating flow conditions. The colour indicates the clay flow type. A circle denotes the same clay flow type before and after the imposed velocity change and a triangle denotes an altering clay flow type as the flow accelerates or decelerates.

The adaptation of the depth-averaged turbulence intensity indicates a similar pattern to the adaptation of depth-averaged velocity for accelerating flows (Figures 3.27a, 3.28a), the adaptation time increases with stronger turbulence attenuation (Au and Leong, 2013; Yu et al., 2013). The time-dependent process of breaking clay bonds elongates the adaptation time of the accelerating flows. The plug flow with a pervasive network of clay bonds prevents the penetration of turbulence making it increasingly difficult to break clay bonds within the flow (Wan, 1982; Ghezzehei and Or, 2001; Nguyen et al., 2018; Safak et al., 2013).

The decelerating flows indicate an adaptation time dependent on clay flow type (Figure 3.28b). Compared to turbulent flows (TF), the adaptation time of LTPF is reduced and increased again for stronger turbulence attenuated flows, UTPF and QLPF. Flocculation occurs when a collision brings

two particles close enough together for attractive forces to overcome repulsive forces (Mehta and McAnally, 2008; Hunter, 2013; Wypych, 2015; Shaikh et al., 2017) and consequently the aggregation rate of cohesive sediment varies over time and per clay flow type (Haralampides et al., 2003; Adamis et al., 2005; Mietta et al., 2009; Yu et al., 2013). If a flow transforms from TETF to LTPF, the enhanced turbulence in TETF allows sufficient inter-particle collision to form the pervasive, volume filling network of particle bonds which is found near the top of the flow in LTPF. Within UTPF flows, cohesive forces become increasingly dominant over turbulent forces, reducing the inter-particle collision and consequently, the formation of clay bonds takes longer. This effect is enhanced for QLPF where a thick rigid plug moves over a thin shear layer. Similar to aggregation theory, where aggregation rate tend to increase with turbulence intensity due to the increased number of inter particle encounters (Lick et al., 1993; van Leussen, 1994; Cuthbertson et al., 2010), TETF flows provides sufficient inter-particle collisions to form clay bonds. Normally, the turbulent motions may generate shear stresses that can limit aggregation rates (Milligan and Hill, 1998; Dyer, 1988; McAnally and Mehta, 2000; Winterwerp, 2002; Son and Hsu, 2011; Safak et al., 2013; Lamb et al., 2020). However, the reduced turbulence in the turbulence attenuated flows prevents this counter effect and the rate of inter-particle collision dominates the adaptation (Tsai et al., 1987; Lick and Lick, 1988; Jiang and Logan, 1991; Barany et al., 2009; Sun et al., 2016).

This variation in adaptation time between flow types does not occur in accelerating flows. The breakage of clay bonds within accelerating flows is not dependent on this inter-particle collision and occurs when the turbulence is strong enough to break the bonds between the clay particles. The increase in turbulence, associated with flow acceleration, occurs throughout the flow, i.e. regardless of the location of the bonded clay particles (Lick and Lick, 1988; Mietta et al., 2009; Safak et al., 2013). Stronger turbulence attenuation, associated with an increase in viscosity, prevents turbulence penetrating the plug flow (Marr et al., 2001; Mohrig and Marr, 2003; Baas et al., 2009; Baker et al., 2017), which elongates the adaptation time.

3.4.4. Wider implications

This study demonstrates that for mud-rich flows flow adaptation time scales to changes in velocity differ between decelerating and accelerating regimes, depending on the balance between turbulent and cohesive forces within a flow. Highlighting both the effect of flow unsteadiness and delay in flow adaptation or relaxation process (Tsujimoto et al., 1990; Tunnicliffe et al., 2018), this difference in adaptation likely impacts sedimentation patterns within muddy rivers. For example, following a typical flood hydrograph with an initial increase in discharge followed by a drop in discharge (Karimaee Tabarestani and Zarrati, 2015; Fielding et al., 2018; Mrokowska and Rowiński, 2019), the increase in discharge and associated turbulence results in breakage of clay bonds. After which clay bonds re-establish as the turbulence reduces with the drop in discharge. Depending on the duration of the flood, accelerating flow is directly followed by decelerating flow and the accelerating flow might experience insufficient time to fully adapt to the change in velocity. Especially in rivers with high suspended sediment concentrations and associated strongly turbulence attenuated flow types as the adaptation of accelerating flows increases with increased turbulence attenuation due to the delay in breakage of clay bonds. Clay bonds might still be established as the falling limb of the flood passes and the flow maintains the cohesive strength throughout the duration of the flood, which allows the flood to maintain the viscous strength to carry debris, imposing potential large damages and changes to river morphology (Di et al., 2008; Brown and Pasternack, 2014; Thiene et al., 2017; Best et al., 2022).

Additionally, within estuaries, the morphology is influenced by tidal currents (Whitehouse et al., 2000; Hoitink et al., 2017), which causes periodic acceleration and deceleration (Leeder, 2011; Uncles and Mitchell, 2017). Under decelerating flows, fluid mud can form (Winterwerp and Van Kesteren, 2004; McAnally et al., 2007; Van Maren et al., 2009; Talling et al., 2012), which is nor-

mally re-entrained by accelerating currents after the intervening slack water (Kirby, 1986), fully during spring tides and partially during neap tides (McAnally et al., 2007). Upon shearing, i.e. accelerating flow, clay bonds between the clay particles break and time is required to restore these clay bonds within the decelerating flow (Ross and Mehta, 1989; Winterwerp and Van Kesteren, 2004). This thixotropic decrease in strength is dependent on the clay flow type and adaptation time available (Winterwerp and Van Kesteren, 2004; McAnally et al., 2007). The bonds within the clay particles are restored faster with lower turbulence attenuation than within strongly turbulent attenuated flow types due to the influence of inter-particle collision on the adaptation time of suspended clay flows. There is not an instantaneous response to variations in changes in velocity and the adaptation time of the clay-laden flows influences the entrainment and erosion rate of the sediment, i.e. a stronger developed network of clay bonds is harder to entrain than separate clay particles or flocs (Winterwerp and Van Kesteren, 2004; Ren et al., 2021). In addition, fully developed turbulence-attenuated flow conditions have reduced turbulence near the bed (Baas et al., 2009), reducing bed friction and consequently the erosion rate. Thus, the adaptation time and if there is sufficient time for the flow to fully develop or not, likely has an influence on the sediment transport and deposition rates within estuaries.

3.5. Conclusion

This research investigated the influence of suspended cohesive clay on changing flow dynamics under unsteady flow conditions, using decelerating and accelerating open-channel flows in a re-circulating flume. These flows may evolve through different clay flow types with different associated degrees of turbulence enhancement and attenuation depending on the clay concentration and whether the flows decelerate or accelerate. The controlled velocity changes within the experiments allowed the clay suspension flows to maintain the flow type or shift to an adjacent flow type, which results in no apparent hysteresis in adaptation between accelerating and decelerating flows. The accelerating flows indicate a continuous increase in adaptation time with stronger turbulence attenuated flows, as the breaking up clay bonds within a stronger plug flow requires more time. The adaptation time of decelerating flows depends on the clay flow type. Initial development of a plug flow within LTPF requires less time than the development of a thick rigid plug found in QLPF, as the inter-particle collisions are reduced with stronger turbulence attenuation. The adaptation time of clay-laden flows to unsteady conditions has a direct influence on the erosion, deposition and sediment transport rates.

4

TURBULENCE MODULATION IN CLAY-LADEN GRAVITY CURRENTS

Subaqueous sediment gravity currents are volumetrically one of the most important sediment transport processes and frequently transport high volumes of cohesive sediment. They can be classified into different flow types, with turbidity currents (turbulent) and debris flows (turbulence-suppressed) as the two end members; transitional flows bridge the gap between turbidity currents and debris flows and exhibit transient turbulent behaviour. Depending on their boundary conditions, gravity currents, can evolve either way along the turbidity current and debris flow spectrum. However, despite commonly carrying high amounts of clay, relative to open-channel flows, the understanding of turbulent dynamics and evolution of cohesive clay-laden sediment gravity currents remains limited. To address this shortcoming, new experiments using constant-flux flows in a submerged flume were conducted. Based on velocity measurements three different flow types were identified with increasing turbulence attenuation: a) turbidity current, b) turbulent plug flow and c) transitional plug flow. Two different types of the gravity current evolution were identified, determined by the balance between turbulent and cohesive forces related to the formation of clay bonds. At low clay concentrations, entrainment of ambient water at the upper interface, plus the turbulence generated at the upper and lower boundaries that penetrated into the gravity current, prevented the formation of clay bonds. Consequently, such gravity currents evolved towards a more turbulent flow condition, i.e. turbidity current. At high clay concentrations, ambient water entrainment and turbulence generation were focused in the outer region allowing the formation of clay bonds in the inner region and hence the development of a plug flow in the inner region. Consequently, such gravity currents evolved towards a less turbulent flow condition, i.e. debris flow. Thus, in addition to the shifting balance between turbulent and cohesive forces, the history and evolution of a flow influence the formation of the type of gravity current.

4.1. INTRODUCTION

Subaqueous sediment gravity currents are volumetrically one of the most important sediment transport processes on our planet (Heezen and Ewing, 1955; Bouma, 1985; Piper et al., 1999; Talling et al., 2012). They can be differentiated into a head, body and tail region (Middleton, 1966a; Pickering and Hiscott, 2015). Experimentally, gravity currents can be divided into the mode of transportation with constant-flux or sustained flows (Ellison and Turner, 1959; Hallworth et al., 1996; Kneller and Buckee, 2000; Gerber et al., 2011) and constant-volume or surge flows (Middleton, 1966a; Hacker et al., 1996; Simpson, 1997; Hallworth and Huppert, 1998; Marino et al., 2005; Nogueira et al., 2014) frequently used methods. Constant-volume type flows, such as lock-exchange experiments, have a more pronounced head region than constant-flux type flows and may not be an accurate representation of constant-flux flows (Peakall et al., 2001; Talling et al., 2015). The structure of the head has been studied extensively (Middleton, 1966a; Kneller et al., 1999; Nogueira et al., 2014; Negretti et al., 2017), whereas the body of the flow often forms the bulk of the flow (Parsons et al., 2007; Peakall and Sumner, 2015; Hage et al., 2019) of which the structure of turbulence remains poorly understood (Wells and Dorrell, 2021).

Sediment-laden gravity currents can be classified into different flow types (Figure 4.1, Haughton et al., 2009; Pickering and Hiscott, 2015). On one side of the spectrum, turbidity currents are relatively dilute flows, in which the particles are supported by the upward component of fluid turbulence (Figure 4.2a,Altinakar et al., 1996; Kneller et al., 1999; Mulder and Alexander, 2001; Leeder, 2011). On the other side of the spectrum, debris or mud flows have limited internal turbulence and cohesive sediment provides the grain support through yield strength (Figure 4.2b, Middleton and Hampton, 1973; Coussot, 1997; Mulder and Alexander, 2001). The cohesive strength resists the admixture of water into the flow, maintaining the coherence of the body (Iverson, 1997; Mulder and Alexander, 2001; Marr et al., 2001; Mohrig and Marr, 2003; Baker et al., 2017). Transitional flows bridge the gap between turbidity currents and debris flows, containing transient turbulent behaviour (Wang and Plate, 1996; Baas et al., 2009; Sumner et al., 2009, Section 1.3).

Figure 4.1: Classification scheme for subaqueous sediment gravity currents with T = turbulent flow and L = laminar flow (Haughton et al., 2009).

Depending on the boundary conditions, subaqueous gravity currents can go through a wide range of transformations both in space and in time (Morgenstern, 1967; Hampton, 1972; Kneller, 1995; Mulder and Alexander, 2001; Felix and Peakall, 2006; Talling et al., 2007; Meiburg and Kneller, 2010; Kane and Pontén, 2012). Gravity currents can accelerate or decelerate, erode sediment from the bed or deposit, entrain water and increase in thickness or dewater and collapse, and contract by the tail approaching the head or stretch. The flow becomes denser, moving towards debris flow, if the combined effects of sediment incorporation, due to erosion, dewatering, and contraction, are higher than dilution, due to deposition, entrainment, and stretching. If clay-bearing, the increasing clay concentration can induce the formation of a plug flow, through clay flocculation and framework development, as found within clay-laden open-channel flows (Baas and Best, 2002; Baas et al., 2009, Section 1.3). On the contrary, the flow becomes more dilute, moving towards turbidity current, if the combined effects of dilution are higher than sediment incorporation (Morgenstern, 1967; Hampton, 1972; Kneller, 1995; Mulder and Alexander, 2001; Felix and Peakall, 2006; Talling et al., 2007; Kane and Pontén, 2012).

4

Turbidity currents are driven by the action of gravity on the density difference between the particle-fluid mixture and the ambient fluid (Kneller and Buckee, 2000; Meiburg and Kneller, 2010). In typical laboratory experiments with a finite-volume (surge flows), the body of the gravity current is rather poorly developed (Middleton, 1993; Kneller and Buckee, 2000; McCaffrey et al., 2003; Cartigny et al., 2013; Azpiroz-Zabala et al., 2017). These turbidity currents have a relatively consistent structure in which the flow maximum occurred almost immediately behind the flow front, followed by a continuous decline in velocity, which is also identified in measured oceanic turbidity current (Xu et al., 2004; Xu, 2010; Khripounoff et al., 2012; Liu et al., 2012; Hughes Clarke, 2016). Turbidity currents measured in the Congo Canyon contains an elongate body that trails behind the frontal-cell (Azpiroz-Zabala et al., 2017), which is more comparable with sustained flows (constant-flux) in physical experiments (Kneller and Buckee, 2000). Within the trailing body, sediment might settle out depending on the sediment properties. Sediment within mud-rich flows settles out slower and consequently, mud-rich flows may have more developed bodies, which become self-sustaining and stretch (Azpiroz-Zabala et al., 2017). In these sustained or constant flux flows, the vertical velocity profile within the body of the gravity current is generally assumed to be quasi-steady and can be divided into an inner and outer region by the height of the velocity maximum (Figure 4.2a, Ellison and Turner, 1959; Kneller and Buckee, 2000; Meiburg and Kneller, 2010; Xu, 2010, Azpiroz-Zabala et al., 2017). The inner region is often a thin dense layer near the base, with a positive velocity gradient, whereas the outer region is often a thicker layer, with a negative velocity gradient (Kneller and Buckee, 2000; Meiburg and Kneller, 2010). The height of the velocity maximum is controlled by the ratio of drag forces at the upper and lower boundaries (Middleton, 1966b; Kneller et al., 2016). The reduced turbulence intensity around the velocity maximum hinders the exchange of sediment between the inner and outer region (Garcia and Parker, 1993; Talling et al., 2007).

The velocity structure below the velocity maximum, i.e. inner region, resembles that of open-channel flow as they are both influenced by bed shear (Kneller et al., 1999; Pope, 2000; Chaudhry, 2008). However, the velocity maximum is often closer to the bed in turbidity currents than in open-channel flows, which enhances shear and near-bed turbulent mixing (Kneller and Buckee, 2000; Buckee et al., 2001; Wells and Dorrell, 2021). Compared with open-channel flow, the outer region of a gravity current can allow additional mixing with the overlying ambient fluid (Altinakar et al., 1996; Kneller and Buckee, 2000; Eggenhuisen et al., 2020).
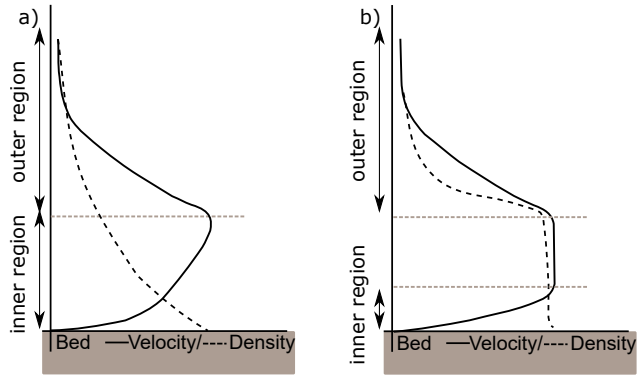
Figure 4.2: Schematic structure of gravity current body velocity and density profiles for a) turbidity currents and b) debris flows (Garcia and Parker, 1993; Hermidas et al., 2018; Kneller and Buckee, 2000; Manica, 2012; Wells and Dorrell, 2021).

Gravity currents may be density stratified, due to vertical gradients in suspended-sediment concentration. Based on experimental results there are three broad groups (Figure 4.3, Kneller and Buckee, 2000; Peakall et al., 2000): a) two-layer model, characterised by a constant density lower region overlaid with a low-concentration plume detrained from the head (Blanchet and Villatte, 1954; Middleton, 1993; Mulder et al., 1997); b) continuous stratification model, commonly seen in low-concentration, weakly depositional currents (Altinakar et al., 1996); c) stepped stratification model, characterised by a distinct inflexion in the concentration profile (García, 1993), which is commonly observed in erosional currents or where the entrainment rate of ambient fluid is high, i.e. gravity currents flowing down steep slopes (García, 1993; Garcia and Parker, 1993; Peakall et al., 2000). Baas et al. (2005) showed that suspended sediment distribution is in fact highly unsteady and considered controlled by the ratio of particle settling velocity to the upward-directed components of local turbulent velocity associated with coherent flow structures, both near-bed ejections and shear instability at the upper part of the flow.
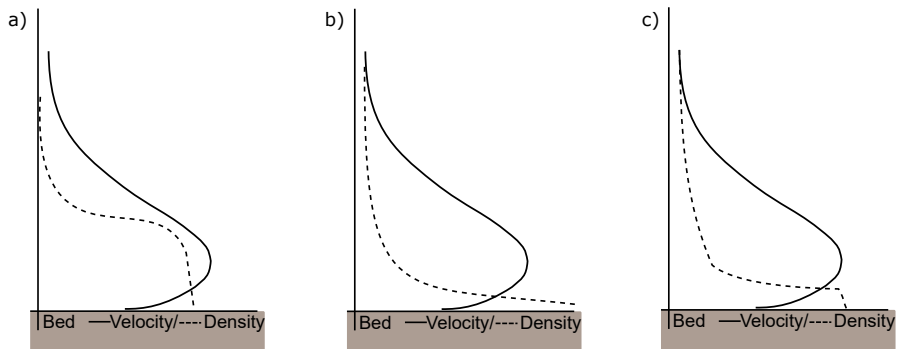

Figure 4.3: Schematic of density profiles in gravity currents; a) two-layer model; b) continuous stratification model; c) stepped stratification model. Modified after (Kneller and Buckee, 2000).

Turbulent mixing at the upper interface of the gravity currents results in entrainment of ambient water, which dilutes the gravity currents and consequently results in an increase in flow thickness (Ellison and Turner, 1959; Parker et al., 1987).

$$\frac{d\overline{\overline{U}}h_0}{dx} = E|\overline{\overline{U}}|$$

(4.1)

where $\overline{\overline{U}}$ is the depth-averaged velocity and h_0 the height of the body of the gravity current, and E the entrainment coefficient, which based on empirical relations can be related to the bulk Richardson number (Ri_b, Equation 4.16) or densimetric Froude number (Fr_d, Ellison and Turner, 1959; Turner, 1986; Parker et al., 1987; Cenedese and Adduce, 2010, Equation 4.14). Flow stability is quantified through the ratio of buoyancy gradient to shear, the gradient Richardson number, Ri_g:

$$Ri_g = -\frac{g}{\rho}\frac{\delta\rho/\delta z}{(\delta u/\delta z)^2}$$

(4.2)

where g is the gravitational acceleration, ρ density, z height above the bed and u streamwise velocity. Time-averaging the numerator and denominator results in the bulk Richardson number (Ri_b), which is the ratio between the inertial force ($\rho u^2/h_0$), i.e. the tendency of the flow to mix or destabilize the stratified fluid, and the buoyancy force ($-\Delta\rho g$), which acts to stabilize the flow (Leeder and Perez-Arlucea, 2006). A smaller value indicates that the flow is more likely to undergo mixing and homogenization. The bulk Richardson number scales inversely with the densimetric Froude number as $Ri = Fr_d^{-2}$. The turbulence within a gravity current is dominated by the bottom drag for subcritical ($Fr < 1$) and dominated by entrainment for supercritical ($Fr > 1$) gravity currents (Parker et al., 1987; Wells and Dorrell, 2021). Instability at the upper interface can result in development of large-amplitude, wave-like, coherent flow structures such as Kelvin-Helmholtz instabilities (Kneller and Buckee, 2000; Venditti et al., 2013).

The transitional flow types of Baas et al. (2009), based on open-channel flow experiments, have been used for interpretation of gravity currents and associated deposits (Sumner et al., 2009; Baker and Baas, 2020; Peakall et al., 2020). However, the dynamic properties of open-channel flow and gravity currents differ significantly, with the main difference being the additional shear effects in the upper surface of the flow for gravity currents (Manica, 2012). The velocity profile of gravity currents tends to go to zero near the upper surface and increase towards the middle (Figure 4.2), whereas open-channel flows have the velocity maximum near the surface (Section 1.1.3, Schlichting and Gersten, 2016). Plug flow development in open-channel flow starts at the free surface, where the shear is the lowest (Baas and Best, 2002; Baas et al., 2009), but gravity currents contain turbulent mixing at the flow-ambient fluid interface. Moreover, open-channel flows are limited by the water surface, whereas gravity currents are not constrained and may expand their depth. Therefore, stability regimes of clay flow types are expected to vary from those of open-channel flows. This may directly influence the sediment transport distances and depositional geometries. Hermidas et al. (2018) aimed to classify transitional flow properties for gravity currents based upon a free shear layer at the top of the flow, a laminar plug layer and a basal boundary layer (Figure 4.4). Based on experiments with sand, silt and clay (maximum volumetric concentration of 7% kaolinite) and viscosity values measured ex-situ by a rheometer, four different flow types were identified, from high concentration to low: a) plug flow, which contained laminar flow in both the boundary and free shear layer; b) top transitional plug flow, where Kelvin Helmholtz instabilities were identified in the top free shear layer on top of a plug flow and laminar boundary layer; c) transitional turbidity current, a turbulent top layer on top of a laminar boundary layer; and d) turbidity current with fully turbulent flow. Turbulence data showed a considerable residual turbulence in the basal boundary layer, higher than in the plug flow itself. However, insufficient turbulence data were provided to ascribe the flows of Hermidas et al. (2018) to a specific transitional flow category of Baas et al. (2009).
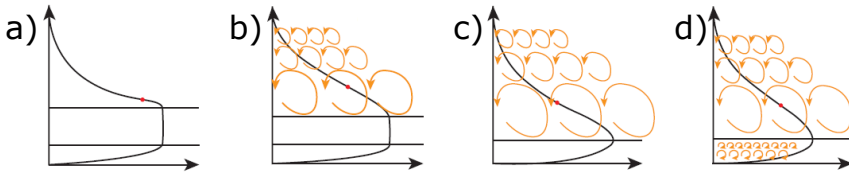
Figure 4.4: Schematic drawing of classification of transitional flow types based upon velocity profiles (Hermidas et al., 2018), with decreasing clay conctration from a) to d). a) plug flow, b) top transitional plug flow, c) transitional turbidity current, d) turbidity current.

Research has focussed frequently on the two end members of the spectrum, turbidity current and debris flow, but it is evident from the work of Baas et al. (2009) that the dynamic structure of transitional clay flows is more complex than the existing conceptual models portray. The transitional flow types that bridge the gap between turbidity current and debris flow are currently poorly understood. The present knowledge of transitional behaviour is based upon the shifting balance between turbulent and cohesive forces of open-channel flows, which are fundamentally different from gravity currents (Kneller et al., 1999; Pope, 2000; Wells and Dorrell, 2021). Hermidas et al. (2018) based transitional flow properties of gravity currents on velocity profiles and viscosity values, whereas Baas et al. (2009) showed that turbulence data is essential for determining transitional flow conditions. Knowing the dynamics of these transitional flow types within gravity currents is pivotal, as erosion, transport and deposition of sediment depend on the magnitude and distribution of flow turbulence (Dorrell et al., 2018). Additionally, gravity currents continuously evolve as they travel downstream and depending on the boundary conditions can shift from turbidity current to debris flow or the opposite. The influence of the shifting balance between turbulent and cohesive forces in combination with the turbulent dynamics of gravity currents on this evolvement downstream is currently poorly understood. An increased understanding of the influence of cohesive sediment on gravity currents is needed. The following research questions are addressed: (1) Which transitional flow types are identifiable in clay-laden gravity currents? (2) How do clay-laden gravity currents evolve between these transitional flow types? Where non-uniformity is defined as the change in velocity along the flume of the quasi-steady body of the gravity current.

4.2. METHODOLOGY

The methodology section is divided into four sections. The experimental setup, involving the description of the flume, equipment location and preparation of the runs is described in Section 4.2.1. The experimental conditions are described in Section 4.2.2. The measurement techniques and instruments used are described in Section 4.2.3 and Section 4.2.4 describes the methods used for the data processing and analysis.

4.2.1. EXPERIMENTAL SETUP

The experiments were conducted at the Total Environment Simulator (TES) at the University of Hull. Fully submerged within the 14 m long and 6 m wide tank, an 8 m long, 0.1 m wide and 0.6 m high channel was placed under a slope of 2.9 degrees, to generate supercritical bypassing, non-depositional gravity currents (Figure 4.5a). The size of the TES allowed the installation of a 8 m long flume, which made it possible to extend the distance between upstream and downstream measurements to 3.75 m. A longer distance between the measurement locations allows further evolvement of the gravity current. During the experiments a pump continuously supplied the channel with mixtures of pure kaolinite (Imerys Polwhite-E, $d_{50} = 9\ \mu m, \rho_s = 2600\ kg/m^3$, Section 2.2.1) and fresh water. For comparison reasons, within these experiments kaolinite is used, similar to flume experiments of Chapters 2 and 3. The use of a mixing tank and pump, allows the

generation of sustained flows (constant-flux), which provides longer detailed measurements of the body of the gravity current. The body forms the bulk of the flow (Parsons et al., 2007) and sustained flows are likely more representative of mud-rich flows with more developed bodies (Azpiroz-Zabala et al., 2017). The flow entered the flume through a diffuser facing upstream and the flow is forced under a 0.96 m long and 0.1 m high gate to control the initial flow height of the gravity current. To ensure uniformly mixed sediment and water samples, a mixer was placed inside a 1.36 m^3 tank with baffles. In addition, a recirculation pump extracted the sediment water mixture from the bottom of the tank to be supplied again at the top. Ahead of the experiments, the sediment and water mixtures were mixed for at least an hour to ensure uniformly mixed input into the flume.
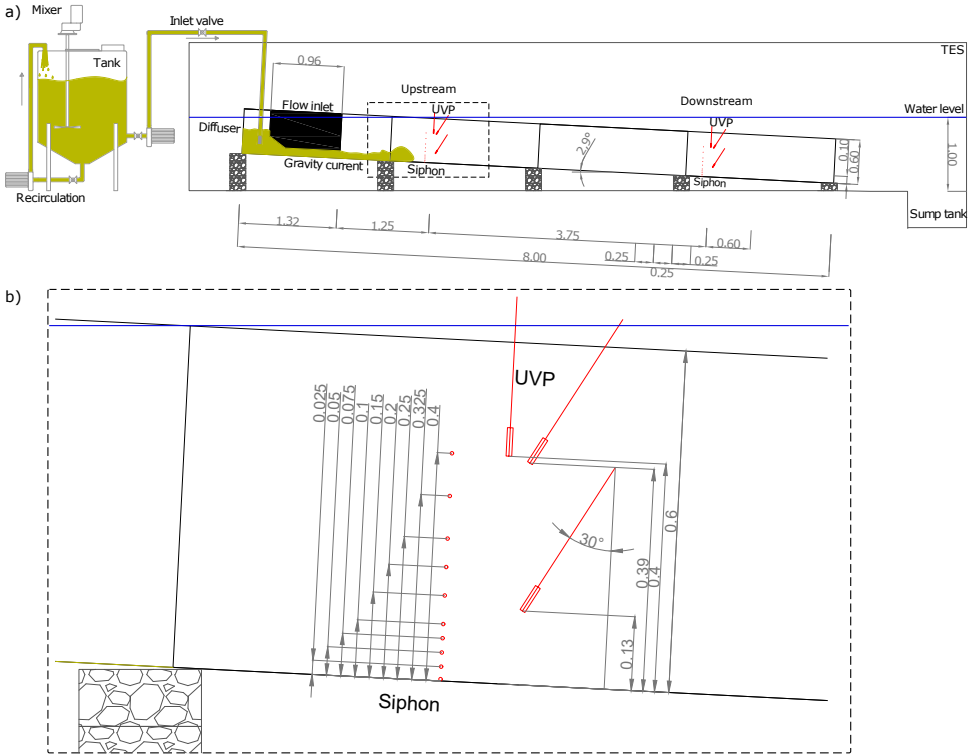

Figure 4.5: a) Side view of experimental setup, b) detailed schematic diagram of installation of equipment. All dimensions in meters.

DISCHARGE

The discharge into the flume was regulated with a valve on the inlet pipe. Closing the valve reduced the discharge into the flume. The correlation between discharge into the flume and settings of the valve had been determined based on clear water tests (Figure 4.6). Based on these clear water tests, two discharges and correlated valve settings were selected for the experiments (Table 4.1). These clear water tests provided information on the limitations of the pump and allowed selection of two valve settings with sufficient difference in discharge. Due to the mechanism of gravity currents, the velocity within the experiments is also influenced by the clay concentration and further analysis therefore focuses on the measured velocity instead of discharge settings For consistency, the valve setting were not changed throughout the experiments of the same flow rate.
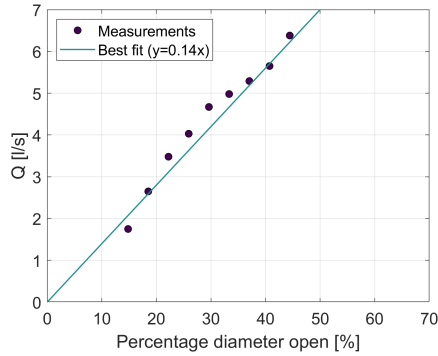
Figure 4.6: Correlation between discharge (Q) into the flume and valve settings correlated to the percentage of the pipe diameter that is not blocked.

4.2.2. EXPERIMENTAL CONDITIONS

To assess the influence of flow velocity and clay concentration on non-uniform clay-laden gravity currents, experiments were conducted with two input discharges and varying clay concentration, resulting in a total of twelve experimental runs (Table 4.1).

Table 4.1: Overview of experimental runs performed in this study. The numbering of experimental runs is defined by the discharge (Q) and the clay concentration in the mixing tank (C); C = volumetric concentration within the mixing tank; C_m = mass concentration within the mixing tank; $T_{ambient}$ = ambient fluid temperature; T_{flow} = fluid temperature flow, measured within the mixing;

Experimental run	Q [l/s]	C [vol %]	C_m [g/L]	$T_{ambient}$ [$°C$]	T_{flow} [$°C$]
		Low discharge			
Q3.5-C2.4	3.5	2.4	61	16.4	16.7
Q3.5-C3.9	3.5	3.9	98	16.2	16.7
Q3.5-C6.3	3.5	6.3	150	15.4	16.7
Q3.5-C8.0	3.5	8.0	186	15.1	17.7
Q3.5-C9.6	3.5	9.6	219	16.4	17.6
Q3.5-C12.2	3.5	12.2	269	15.9	17.6
Q3.5-C14.9	3.5	14.9	317	16.6	19.6
		High discharge			
Q5.0-C1.6	5.0	1.6	42	16.0	16.3
Q5.0-C2.5	5.0	2.5	62	17.0	18.3
Q5.0-C3.1	5.0	3.1	78	16.9	16.5
Q5.0-C7.9	5.0	7.9	185	16.4	18.7
Q5.0-C14.8	5.0	14.8	314	16.9	19.3

4.2.3. DATA ACQUISITION

SUSPENDED SEDIMENT CONCENTRATION

To assess the evolution of the gravity currents downstream, at two locations, upstream (1.25 m downstream of gate) and downstream (5 m downstream of gate), the suspended sediment concentration in the flow was measured by extracting fluid samples from the sidewall of the flume at various heights throughout the flow (Table 4.2, Figure 4.5a,b). The sediment samples were collected twice from the body of the gravity current, at t=80 s (Measurement moment 1=M1) and t=190 s (Measurement moment 2=M2) (Figure 4.7). The samples were collected by flexible plastic tubing of 6 mm diameter in 60 mL sample pots and were weighed after collection, dried at a temperature of $40°C$ until all water had evaporated, and then weighed again to determine their volumetric clay concentration.

Table 4.2: Measurement height (centrepoint) above the bed (z) of siphon samples to measure the clay concentration

Measurement	z [m]
A	0.010
B	0.030
C	0.050
D	0.075
E	0.100
F	0.150
G	0.200
H	0.250
I	0.325
J	0.400

FLOW VELOCITY

To obtain velocity profile measurements two 1 MHz UVPs (Ultrasonic Velocity Profiler, Section 1.4) were placed upstream (1.25 m downstream of the gate) and downstream (5 m downstream of the gate), facing upstream under an angle of $30°$ relative to the vertical (Figure 4.5b) with a distance of 0.26 m between the centres of the probes; at 0.13 m and 0.39 m height above the bed, respectively. The UVPs were directed against the flow direction to measure the streamwise velocity and to reduce the impact of flow obstruction on the measurements. The settings of the UVPs were adjusted to the experimental conditions to increase the data quality (Table 4.3). The measurements were collected for the four UVPs using the multiplexing setting. This multiplexing setting allows measurements to be collected for multiple probes, but it reduces the frequency of the measurements significantly. Instead of switching between probes for each measurement, the measurements were collected for 18.4 to 20.4 s at one probe before switching to the next probe. This increased the temporal resolution of the measurements, providing more detailed turbulence data even if measurements were collected for 25% of the total measurement time (Figure 4.8), i.e. this resulted in high frequency measurements (up to 58.8 Hz) for parts of the body of the gravity current instead of low frequency (∼2Hz) for the full body. Only the UVP at z=0.39 m was used to measure in experimental runs Q3.5-C8.0, Q3.5-C9.6 and downstream Q3.5-C12.2, which was switched in 38.4 to 38.5 s per probe upstream and downstream. Additionally, one 2 MHz probe was located at both the upstream and downstream measurement location facing vertically towards the bed to measure the vertical velocity (Figure 4.5, Table 4.4). The included measurement time points, $N = 650 - 1750$, between the different probes were selected such that the vertical and angled UVP measurements were in line at the upstream and downstream locations.

Table 4.3: Settings for angled UVP measurements. TR = Temporal resolution; ΔD = distance resolution; V_{range}= velocity range; ΔV = velocity resolution; Location in the flume is indicated with U=Upstream and D=Downstream; N = amount of measurement time points before switching probes; ΔT = time length before switching probes.

Condition	TR [Hz]	ΔD [m]	V_{range} [m/s]	ΔV [m/s]	Location	UVP at z=0.39 m		UVP at z=0.13 m	
						N [−]	ΔT [s]	N [−]	ΔT [s]
Low discharge									
Q3.5-C2.4	33.3	0.003	0.446	0.0017	U	650	19.5	650	19.5
					D	650	19.5	650	19.5
Q3.5-C3.9	33.3	0.003	0.470	0.0018	U	650	19.5	650	19.5
					D	650	19.5	650	19.5
Q3.5-C6.3	38.5	0.003	0.555	0.0022	U	750	19.5	750	19.5
					D	750	19.5	750	19.5
Q3.5-C8.0	41.7	0.003	0.594	0.0023	U	1600	38.4	-	-
					D	1600	38.4	-	-
Q3.5-C9.6	45.5	0.003	0.644	0.0025	U	1750	38.5	-	-
					D	1750	38.5	-	-
Q3.5-C12.2	47.6	0.003	0.717	0.0028	U	875	18.8	875	18.8
					D	1750	37.6	-	-
Q3.5-C14.9	52.6	0.003	0.792	0.0031	U	975	18.5	975	18.5
					D	975	18.5	975	18.5
High discharge									
Q5.0-C1.6	47.6	0.003	0.693	0.0027	U	925	19.4	925	19.4
					D	925	19.4	925	19.4
Q5.0-C2.5	45.5	0.003	0.644	0.0025	U	925	20.4	925	20.4
					D	925	20.4	925	20.4
Q5.0-C3.1	55.6	0.003	0.843	0.0033	U	1100	19.8	1100	19.8
					D	1100	19.8	1100	19.8
Q5.0-C7.9	47.6	0.003	0.693	0.0027	U	925	19.4	925	19.4
					D	925	19.4	925	19.4
Q5.0-C14.8	58.8	0.003	0.942	0.0037	U	1150	19.6	1150	19.6
					D	1150	19.6	1150	19.6

Table 4.4: Settings for vertical UVP measurements. TR = Temporal resolution; ΔD = distance resolution; V_{range}= velocity range; ΔV = velocity resolution; Location in the flume is indicated with U=Upstream and D=Downstream; N = amount of measurement time points before switching probes; ΔT = time length before switching probes.

Condition	TR [Hz]	ΔD [m]	V_{range} [m/s]	ΔV [m/s]	Location	N [−]	ΔT [s]
Low discharge							
Q3.5-C2.4	34.5	0.002	0.248	0.0010	U	650	18.9
					D	650	18.9
Q3.5-C3.9	34.5	0.002	0.243	0.0010	U	1300	37.7
					D	1300	37.7
Q3.5-C6.3	31.3	0.002	0.223	0.0009	U	1400	44.8
					D	1400	44.8
Q3.5-C8.0	34.5	0.002	0.243	0.0009	U	1400	40.6
					D	1400	40.6
Q3.5-C9.6	34.5	0.002	0.243	0.0009	U	1400	40.6
					D	1400	40.6
Q3.5-C12.2	34.5	0.002	0.243	0.0009	U	1400	40.6
					D	1400	40.6
Q3.5-C14.9	34.5	0.002	0.248	0.0010	U	1400	40.6
					D	1400	40.6
High discharge							
Q5.0-C1.6	34.5	0.002	0.248	0.0010	U	1400	40.6
					D	1400	40.6
Q5.0-C2.5	34.5	0.002	0.248	0.0010	U	1400	40.6
					D	1400	40.6

Condition	TR [Hz]	ΔD [m]	V_{range} [m/s]	ΔV [m/s]	Location	N [−]	ΔT [s]
Q5.0-C3.1	34.5	0.002	0.248	0.0010	U	1400	40.6
					D	1400	40.6
Q5.0-C7.9	34.5	0.002	0.248	0.0010	U	1400	40.6
					D	1400	40.6
Q5.0-C14.8	34.5	0.002	0.248	0.0010	U	1400	40.6
					D	1400	40.6

4.2.4. DATA PROCESSING

The time series of the velocity was used to determine the arrival of the head, body and tail in the turbidity currents. The velocity within the body is approximately steady and consequently the body is defined as the area of consistent streamwise velocity (Figure 4.7). The area of the body is confirmed by the comparable suspended sediment concentrations at both measurement moments (M1, M2) within the flow (Figure 4.8).

DATA CLEANING

Velocity data collected by UVPs can contain spurious amplitude spikes that are not part of the genuine signal (Met-Flow, 2002; Goring and Nikora, 2002; Wright and Baas, 2013; Dilling and MacVicar, 2017). To clean the UVP data the following steps were followed:

- Removal of outliers - Outliers were removed from the velocity signal by eliminating values 2.5 standard deviations away from the temporal moving mean over 31 data-points

- Deleted measurement bin with 30% or more bad data points - To enhance the accuracy on determination of the mean flow velocity and turbulence intensity, only measurement bins with enough valid data points are included in further data analysis. The full time series at a measurement bin is excluded from the data analysis if more than 30% of the data points within the time series were excluded by previous steps of cleaning the data.
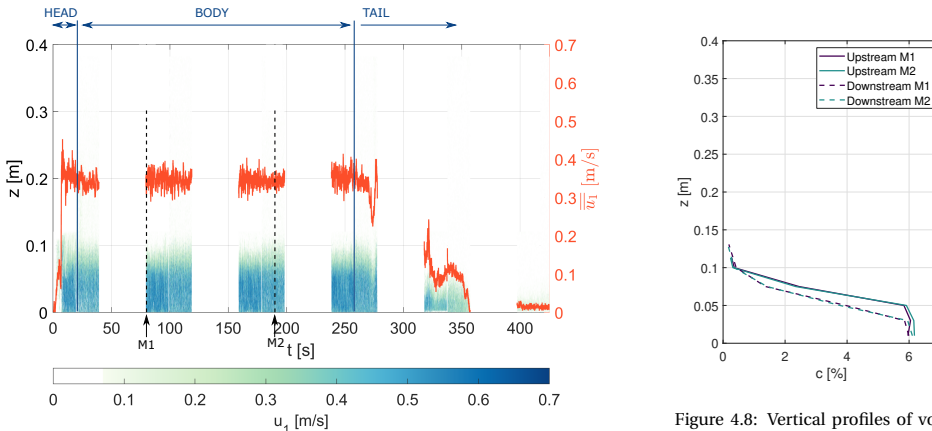

Figure 4.7: Depth-averaged velocity magnitudes ($\overline{\overline{u_1}}$) and streamwise velocity profiles (u_1) upstream in time for flow Q3.5-C6.3. Sediment concentration samples were collected at measurement moments M1 t=80 s and M2 t=190 s.

Figure 4.8: Vertical profiles of volumetric sediment concentration of flow Q3.5-C6.3 for upstream and downstream at measurement moments M1 t=80 s and M2 t=190 s.

DETERMINATION OF FLOW PARAMETERS

To convert the measurements to a streamwise velocity profile (u) and bed-normal velocity profile (v), the streamwise velocity profile was reconstructed from measurements from both the angled UVPs (u_1) and vertical UVP (u_2).

$$u = (u_1 - u_2 cos\alpha)/sin\alpha$$
$$v = u_2 \tag{4.3}$$

The measurement location was the same at the height where the signals of the angled UVP and the vertical UVP cross each other (Figure 4.5b). At the other measurement heights, there was a small shift in the measurements with a maximum shift of 0.25 s depending on the height above the bed and the experimental run. The body of the gravity current was approximately steady (Figure 4.7) and consequently the error imposed by this shift is negligible for the time-averaged results.

Time series of depth-averaged velocity were calculated by integrating the instantaneous velocity data over the depth.

$$\overline{\overline{u_1}} = \frac{1}{h_0} \int_0^{h_0} u_1 \, dz \tag{4.4}$$

where h_0 is flow height and z height above the bed. No deposition was observed within the experiments and the flume bed is defined as z=0. The flow height was defined as the distance from the bed to the height of the flow where the time-averaged velocity is zero (Figure 4.9a).
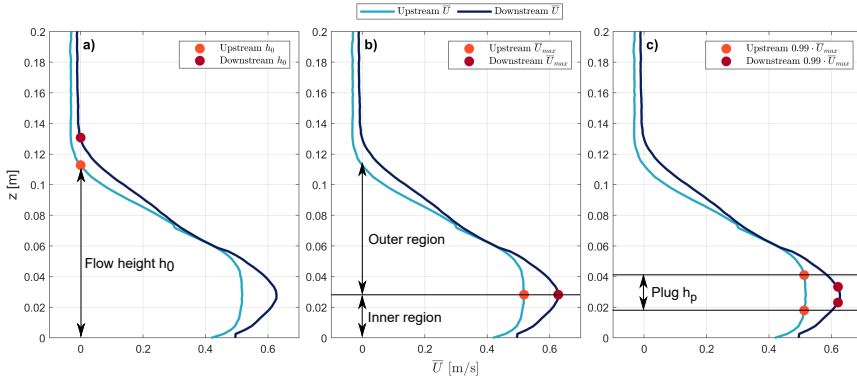

Figure 4.9: a) Flow height, h_0, defined as the distance from the bed to the height of the flow where the time-averaged velocity is zero; b) Maximum velocity separating the inner and outer region of the flow; c) Height of a plug within the gravity current defined by the distance between $0.99\overline{U}_{max}$. Example of experimental run Q3.5-C6.3, with the definitions of flow height, inner and outer region and plug depicted on the upstream measurement location.

The temporal mean flow velocity, $\overline{U}$, $\overline{V}$, and its standard deviation, $RMS(u')$, $RMS(v')$, were calculated from the time series of instantaneous velocity data at each measurement height for the body.

$$\overline{U} = \frac{1}{n} \sum_i^n u_i \tag{4.5}$$

$$\overline{V} = \frac{1}{n} \sum_i^n v_i \tag{4.6}$$

$$RMS(u') = \sqrt{\frac{1}{n} \sum_i^n (u_i - \overline{U})^2} \tag{4.7}$$

$$RMS(v') = \sqrt{\frac{1}{n}\sum_{i}^{n}\overline{(v_i - \overline{V})^2}} \tag{4.8}$$

where n is the number of velocity measurements. A dimensionless measure for turbulence intensity proposed by Baas and Best (2002) is used herein:

$$RMS(u')_0 = \frac{RMS(u')}{\overline{U}} \cdot 100 \tag{4.9}$$

The vertical concentration, velocity and turbulence intensity profiles were plotted with normalised heights adjusted to the height of the velocity maximum (z_{max}) to separate the inner region from the outer region.

$$z_{inner} = z/z_{max} \tag{4.10}$$

such that $z_{inner} = 1$ at the height of the velocity maximum, z_{max}.

$$z_{outer} = (z - z_{max})/(h_0 - z_{max}) \tag{4.11}$$

such that $z_{outer} = 1$ at the depth of the flow, h_0.

Depth-averaged flow parameters were calculated for both the full flow height, h_0, and for the inner region, z_{inner}. The results of the inner region were used for comparison with open-channel flow results of Baas et al. (2009) and Chapters 2, 3.

Depth-averaged velocity for the full flow depth was calculated by integrating the time-averaged velocities over the depth (Figure 4.9a). Depth-averaged velocity of the inner region was calculated by integrating the time-averaged velocities from the bed ($z = 0$) to the height of the velocity maximum (z_{max}, Figure 4.9b).

$$\overline{\overline{U}} = \frac{1}{h_0}\int_0^{h_0}\overline{U}dz \qquad\qquad \overline{\overline{U}}_{inner} = \frac{1}{z_{max}}\int_0^{z_{max}}\overline{U}dz \tag{4.12}$$

The depth-averaged clay concentration was calculated by integrating the suspended sediment samples (c) over the depth, from the lowest measurement at $z_A = 0.010\ m$ to the flow height (h_0). The vertical profiles of volumetric sediment concentration were constant over the body of the flow (Figure 4.8) and throughout the analysis the measurements at M2 (t=190 s) were used. The clay concentration within the inner region was calculated by integrating the suspended sediment samples (c) over the depth, from the lowest measurement at $z_A = 0.010\ m$ to the height of the velocity maximum (z_{max}).

$$C_f = \frac{1}{h_0 - z_A}\int_{z_A}^{h_0}cdz \qquad\qquad C_{inner} = \frac{1}{z_{max} - z_A}\int_{z_A}^{z_{max}}cdz \tag{4.13}$$

The densimetric Froude number was calculated as:

$$Fr_d = \frac{\overline{\overline{U}}}{\sqrt{g'h_0}} \qquad\qquad Fr_{d,inner} = \frac{\overline{\overline{U}}_{inner}}{\sqrt{g'_{inner}z_{max}}} \tag{4.14}$$

where the reduced gravity is:

$$g' = g\frac{\rho_s - \rho_w}{\rho_w}C_f \qquad\qquad g'_{inner} = g\frac{\rho_s - \rho_w}{\rho_w}C_{f,inner} \tag{4.15}$$

where $\frac{\rho_s - \rho_w}{\rho_w}$ is the submerged specific density of sediment particles, C_f the depth-averaged volumetric clay concentration within the flow and $C_{f,inner}$ the depth-averaged volumetric clay concentration of the inner region .

The Richardson number was calculated as:

$$Ri = \frac{g' h_0}{\overline{\overline{U}}} \qquad\qquad Ri_{inner} = \frac{g'_{inner} z_{max}}{\overline{\overline{U}}_{inner}} \qquad\qquad (4.16)$$

Reynolds number was calculated as:

$$Re = \frac{\overline{\overline{U}} h_0}{\nu_e} \qquad\qquad Re_{inner} = \frac{\overline{\overline{U}}_{inner} z_{max}}{\nu_{e,inner}} \qquad\qquad (4.17)$$

where ν_e and $\nu_{e,inner}$ is the effective viscosity with the influence of clay suspension approximated based upon Wan (1982) (Equation 2.8).

As the data were approximately steady ($dt = 0$), the entrainment ratio was calculated as:

$$\frac{d\overline{\overline{U}} h_0}{dx} = E|\overline{\overline{U}}| \qquad\qquad (4.18)$$

A plug flow was characterised by a zone of low velocity gradient. The height of a plug, h_p, within the streamwise velocity profile was defined as the height between $0.99\overline{U}_{max}$ (Figure 4.9c). To classify as a plug, the height of plug needed to be minimal 10% of the flow height ($h_p/h_0 * 100\% > 10\%$).

SELECTION OF PROFILES

Distant particles gave weaker echoes than particles close to the transducer and depending on the concentration within the flow, the signal could be attenuated, reducing the measurement window. To measure the full velocity profile, two 1 MHz probes were installed in a staggered array (Figure 4.5b). The UVPs were directed against the flow direction to measure the streamwise velocity and to reduce the impact of flow obstruction on the measurements. For further data analysis, one profile was selected from the two staggered UVP probes; the highest UVP capturing the top half of the flow and the lower UVP capturing the bottom half of the flow (Figure 4.10).
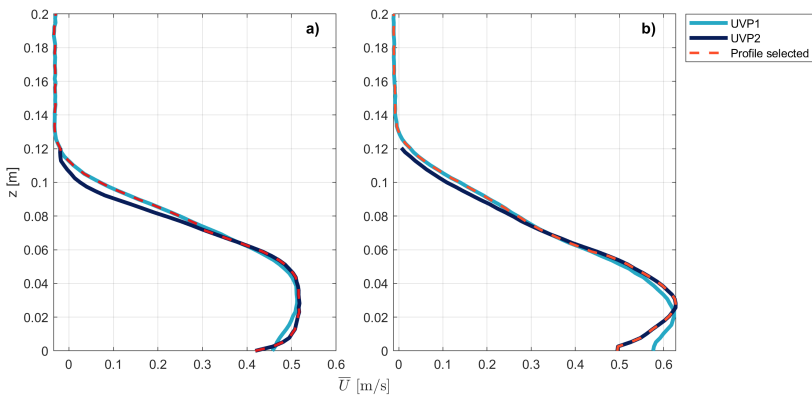

Figure 4.10: Selection of vertical velocity profiles included within data analysis from the two staggered angled 1 MHz UVP probes at measurement locations a) upstream and b) downstream. Example of experimental run Q3.5-C6.3.

4.3. EXPERIMENTAL OBSERVATIONS

4.3.1. SUSPENDED SEDIMENT CONCENTRATION

Figure 4.11a,c shows the vertical profiles of suspended sediment concentration normalised for the inner region ($z_{inner} = z/z_{max}$) for the experimental runs with a discharge of Q=3.5 l/s for upstream and downstream locations, respectively and Figure 4.11b,d shows the vertical profiles of suspended sediment concentration normalised for the inner region ($z_{inner} = z/z_{max}$) for the experimental runs with a discharge of Q=5.0 l/s for upstream and downstream locations, respectively. Figure 4.12a,c shows the vertical profiles of suspended sediment concentration normalised for the outer region ($z_{outer} = (z-z_{max})/(h_0-z_{max})$) for the experimental runs with a discharge of Q=3.5 l/s for upstream and downstream, respectively and Figure 4.12b,d shows the vertical profiles of suspended sediment concentration normalised for the outer region ($z_{outer} = (z-z_{max})/(h_0-z_{max})$) for the experimental runs with a discharge of Q=5.0 l/s for upstream and downstream, respectively. The suspended sediment concentration measurements of the experimental runs are shown in Figure 4.11 normalised for the inner region and Figure 4.12 normalised for the outer region.

As expected the clay concentration in the body of the gravity current increases with a higher input of clay concentration within the mixing tank. The suspended sediment concentrations shows a consistent increase in concentration apart from experimental run Q3.5-C14.9 (Figure 4.13), where the concentration might have been too high for the measurement method used within these experiments. A comparison of the depth-averaged clay concentration in flows with the initial concentration in the mixing tank shows the same reduction in clay concentration for run Q3.5-C14.9 (Figure 4.13). For all experimental runs, the clay concentration in the inner region is maintained between the upstream and downstream location, but the outer region shows a reduction in clay concentration at the downstream location.
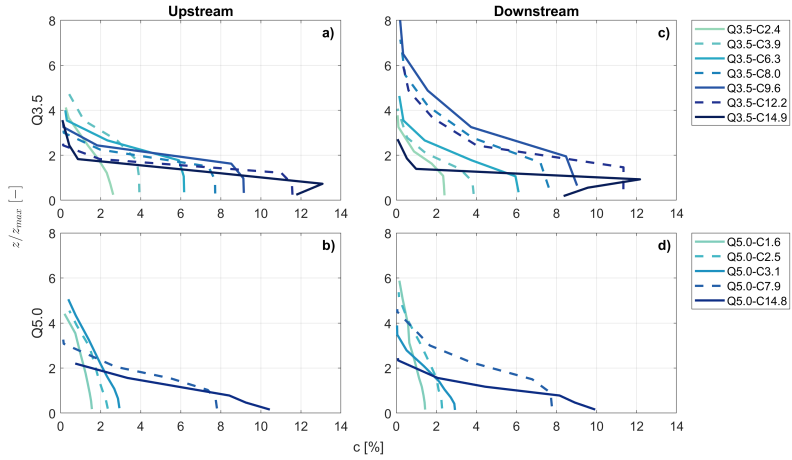
4

Figure 4.11: Vertical profiles $z_{inner} = z/z_{max}$ of volumetric sediment concentration (c [%]) for discharge rate Q=3.5 l/s a) upstream and c) downstream, and for discharge rate Q=5.0 l/s b) upstream and d) downstream.
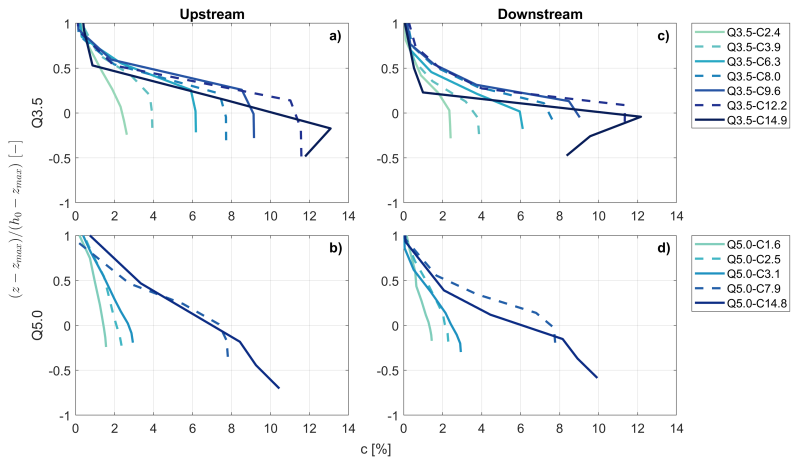

Figure 4.12: Vertical profiles $z_{outer} = (z - z_{max})/(h_0 - z_{max})$ of volumetric sediment concentration (c [%]) for discharge rate Q=3.5 l/s a) upstream and c) downstream, and for discharge rate Q=5.0 l/s b) upstream and d) downstream.
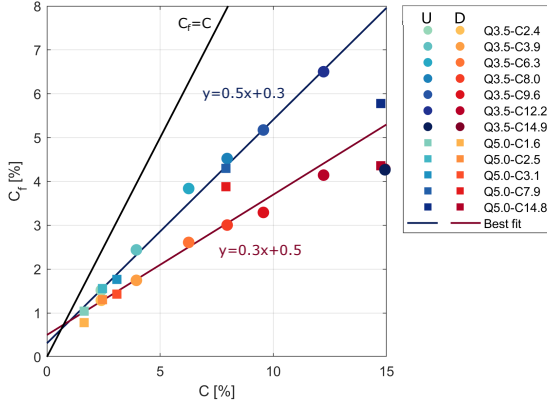
Figure 4.13: Correlation between depth-averaged clay concentration within the body of the gravity current (C_f) and volumetric concentration within the mixing tank (C). Location in the flume is indicated with U=Upstream and D=Downstream.

4.3.2. Vertical velocity

Inner region

Figure 4.14a,c shows the time-averaged vertical velocity profiles ($\overline{V}$) normalised for the inner region ($z_{inner} = z/z_{max}$) for the experimental runs with a discharge of Q=3.5 l/s for upstream and downstream locations, respectively and Figure 4.14b,d shows the time-averaged streamwise vertical velocity profiles ($\overline{V}$) for the experimental runs with a discharge of Q=5.0 l/s for upstream and downstream locations, respectively. Upstream, most experimental runs with a discharge of Q=3.5 l/s indicates a stronger downwards velocity around the streamwise velocity maximum ($z/z_{max} = 1$), which varies depending on the clay concentration. Experimental runs Q3.5-C2.4, Q3.5-C12.2 and Q3.5-C14.9 contains positive velocities upwards at the height of the streamwise velocity maximum. The vertical velocity is positive upwards near the bed for all experimental runs at the upstream location. Downstream, the vertical velocity is more uniform than upstream with a fairly consistent positive velocity upwards over the full flow height. The vertical velocity of experimental run Q3.5-C14.9 is close to zero in the inner region. Upstream, for the experimental runs with a discharge of Q=5.0 l/s (Figure 4.15b), experimental runs Q5.0-C7.9 and Q5.0-C14.8 show a similar pattern as the lower discharge runs; downwards vertical velocity around the velocity maximum and upwards near the bed. Experimental runs Q5.0-C1.6 and Q5.0-C2.5 indicate an opposite pattern with a stronger downwards velocity around the streamwise velocity maximum ($z/z_{max} = 1$). Downstream, the inner region shows a consistent low vertical velocity for all runs with a higher discharge (Figure 4.15d).

Outer region

Figure 4.15a,c shows the time-averaged vertical velocity profiles ($\overline{V}$) normalised for the outer region ($z_{outer} = (z - z_{max})/(h_0 - z_{max})$) for the experimental runs with a discharge of Q=3.5 l/s for upstream and downstream locations, respectively and Figure 4.15b,d shows the time-averaged streamwise vertical velocity profiles ($\overline{V}$) for the experimental runs with a discharge of Q=5.0 l/s for upstream and downstream locations, respectively. Upstream, experimental runs with a discharge of Q=3.5 l/s contain a positive upwards velocity at the upper interface. A similar pattern is identified for experimental runs Q5.0-C7.9 and Q5.0-C14.8. Downstream, for experimental runs with a discharge of Q=3.5 l/s and Q5.0-C7.9 and Q5.0-C14.8, the vertical velocity is more uniform than upstream with a fairly consistent positive velocity upwards. Experimental runs Q5.0-C1.6, Q5.0-C2.5 and Q5.0-C3.1 show a larger positive upwards velocity in the outer region (Figure 4.15d).

4

Figure 4.14: Vertical profiles $z_{inner} = z/z_{max}$ of vertical temporal mean velocity ($\overline{V}$) for discharge rate Q=3.5 l/s a) upstream and c) downstream, and for discharge rate Q=5.0 l/s b) upstream and d) downstream, where a positive value represents upwards velocity and a negative value represents downwards velocity.

Figure 4.15: Vertical profiles $z_{outer} = (z - z_{max})/(h_0 - z_{max})$ of vertical temporal mean velocity ($\overline{V}$) for discharge rate Q=3.5 l/s a) upstream and c) downstream, and for discharge rate Q=5.0 l/s b) upstream and d) downstream, where a positive value represents upwards velocity and a negative value represents downwards velocity.

4.3.3. Streamwise velocity

Inner region

Figure 4.16a,c shows the time-averaged streamwise velocity profiles ($\overline{U}$) normalised for the inner region ($z_{inner} = z/z_{max}$) for the experimental runs with a discharge of Q=3.5 l/s for upstream and downstream, respectively and Figure 4.16b,d shows the time-averaged streamwise velocity profiles ($\overline{U}$) normalised for the inner region ($z_{inner} = z/z_{max}$) for the experimental runs with a discharge of Q=5.0 l/s for upstream and downstream, respectively. For all experimental runs, the streamwise maximum velocity ($z/z_{max} = 1$) of the gravity current increases with increasing clay concentration. Except for experimental run Q3.5-C14.9, which shows a reduced maximum velocity compared with experimental run Q3.5-C12.2 at both the upstream and downstream measurement locations (Figure 4.16a,c). Experimental run Q3.5-C14.9 shows a more constant velocity around the velocity maximum (Section 4.3.3 - Plug flow). Experimental run Q3.5-C14.9 contained invalid data at the bottom of the flow and therefore near bed data is excluded for this experimental run. Compared to the upstream measurement location, the velocity maximum increases downstream, except for the experimental runs Q5.0-C1.6, Q5.0-C2.5, Q5.0-C3.1, which show a decrease in maximum velocity downstream (Figure 4.16b,d). The higher discharge runs (Q=5.0 l/s) tend to have a higher maximum velocity than the lower discharge runs (Q=3.5 l/s) for comparable clay concentrations.

Figure 4.17a,c shows the vertical profiles of the standard deviation of the streamwise temporal mean velocity ($RMS(u')$) normalised for the inner region ($z_{inner} = z/z_{max}$) for the experimental runs with a discharge of Q=3.5 l/s for upstream and downstream locations, respectively. Upstream, $RMS(u')$ shows a reduction around the height of the velocity maximum and $RMS(u')$ increases in the inner region towards the bed. At the height of the velocity maximum, $RMS(u')$ shows an increase with increasing clay concentration, and consequently an increase with increasing velocity (Figure 4.16a). Downstream, $RMS(u')$ shows a similar pattern as upstream with a reduced $RMS(u')$ around the velocity maximum and increasing values towards the bed. Experimental run Q3.5-C14.9 shows an increase in $RMS(u')$ at the velocity maximum, which decreases towards the bed after which it increases again closer to the bed. Figure 4.17b,d shows the vertical profiles of the standard deviation of the streamwise temporal mean velocity ($RMS(u')$) normalised for the inner region ($z_{inner} = z/z_{max}$) for the experimental runs with a discharge of Q=5.0 l/s for upstream and downstream locations, respectively. Upstream, $RMS(u')$ decreases at the height of the velocity maximum ($z/z_{max} = 1$) with increasing clay concentration for the experimental runs Q5.0-C1.6, Q5.0-C2.5, Q5.0-C3.1, Q5.0-C7.9. Relative to Q5.0-C7.9, experimental run Q5.0-C14.8 shows an increase in $RMS(u')$. Upstream, experimental runs Q5.0-C1.6 and Q5.0-C2.5 show a decrease in $RMS(u')$ towards the bed and experimental run Q5.0-C3.1 shows an increase in $RMS(u')$ towards the bed. Experimental runs Q5.0-C7.9 and Q5.0-C14.8 show a decrease below the velocity maximum, but an increase in $RMS(u')$ closer to the bed. $RMS(u')$ values at the downstream location are constant over the inner region with an increase towards the bed for experimental runs Q5.0-C1.6, Q5.0-C2.5, Q5.0-C3.1, Q5.0-C7.9. $RMS(u')$ values of experimental run Q5.0-C14.8 reduce below the velocity maximum and increase again towards the bed.

Figure 4.18a,c shows the vertical profiles of the time-averaged streamwise turbulence intensity profiles ($RMS(u')_0$) normalised for the inner region ($z_{inner} = z/z_{max}$) for the experimental runs with a discharge of Q=3.5 l/s for upstream and downstream locations, respectively and Figure 4.18b,d shows the vertical profiles of the time-averaged streamwise turbulence intensity profiles ($RMS(u')_0$) normalised for the inner region ($z_{inner} = z/z_{max}$) for the experimental runs with a discharge of Q=5.0 l/s for upstream and downstream locations, respectively. Due to normalisation with the time-averaged streamwise velocity, the turbulence intensity values are high near the bed where the streamwise velocity tends to go to zero. At the height of the velocity maximum ($z/z_{max} = 1$), the turbulence intensity values are comparable for the experimental runs with a
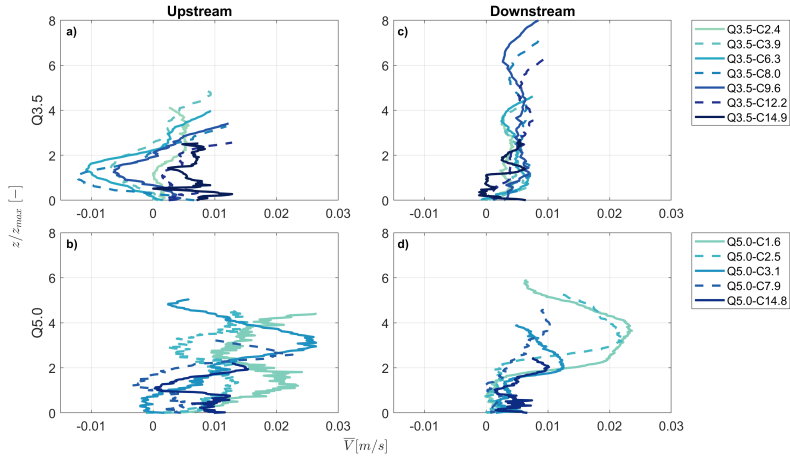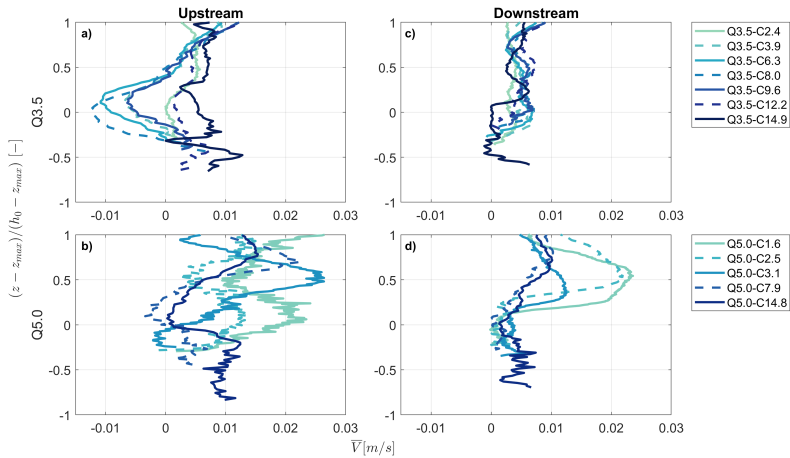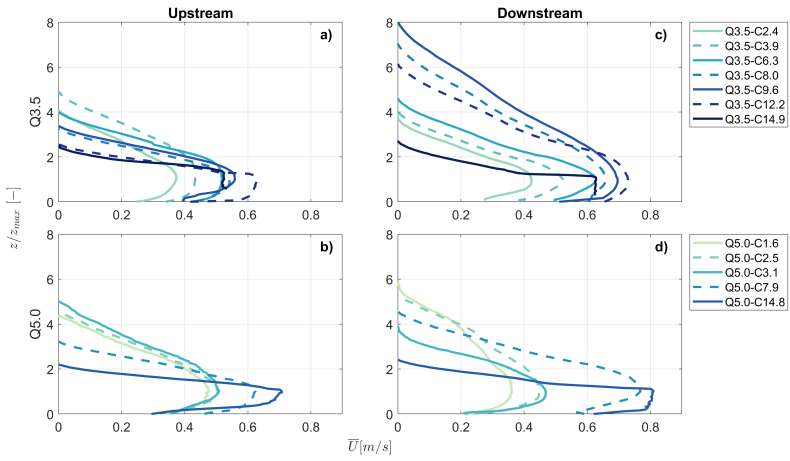
Figure 4.16: Vertical profiles $z_{inner} = z/z_{max}$ of streamwise temporal mean velocity $(\overline{U})$ for discharge rate Q=3.5 l/s a) upstream and c) downstream and for discharge rate Q=5.0 l/s b) upstream and d) downstream.

Figure 4.17: Vertical profiles $z_{inner} = z/z_{max}$ of standard deviation of the streamwise temporal mean velocity $(RMS(u'))$ for discharge rate Q=3.5 l/s a) upstream and c) downstream, and for discharge rate Q=5.0 l/s b) upstream and d) downstream.
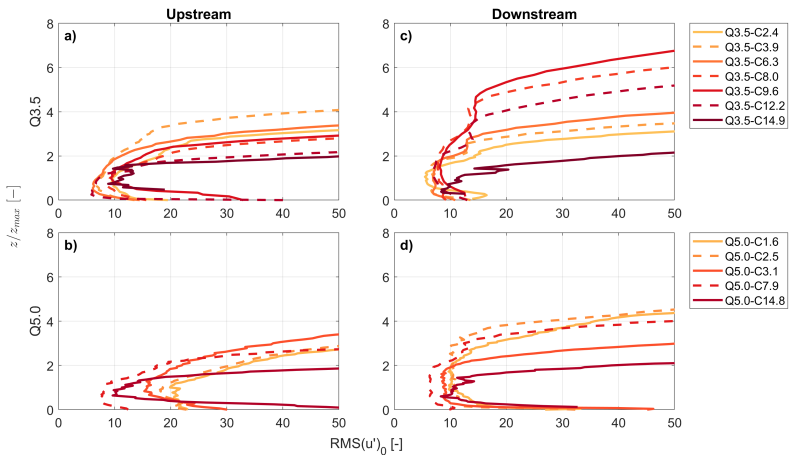
Figure 4.18: Vertical profiles $z_{inner} = z/z_{max}$ of time-averaged streamwise turbulence intensity $(RMS(u')_0)$ for discharge rate Q=3.5 l/s a) upstream and c) downstream, and for discharge rate Q=5.0 l/s b) upstream and d) downstream.
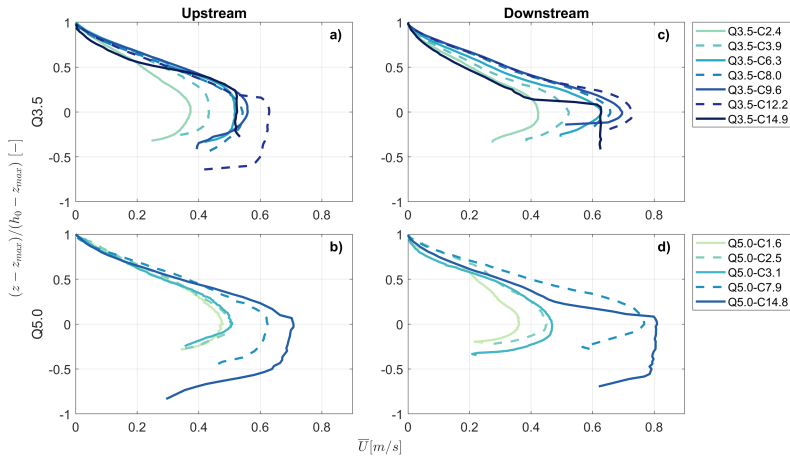
Figure 4.19: Vertical profiles $z_{outer} = (z - z_{max})/(h_0 - z_{max})$ of streamwise temporal mean velocity ($\overline{U}$) for discharge rate Q=3.5 l/s a) upstream and c) downstream and for discharge rate Q=5.0 l/s b) upstream and d) downstream.

Figure 4.20: Vertical profiles $z_{outer} = (z - z_{max})/(h_0 - z_{max})$ of standard deviation of the streamwise temporal mean velocity ($RMS(u')$) for discharge rate Q=3.5 l/s a) upstream and c) downstream, and for discharge rate Q=5.0 l/s b) upstream and d) downstream.
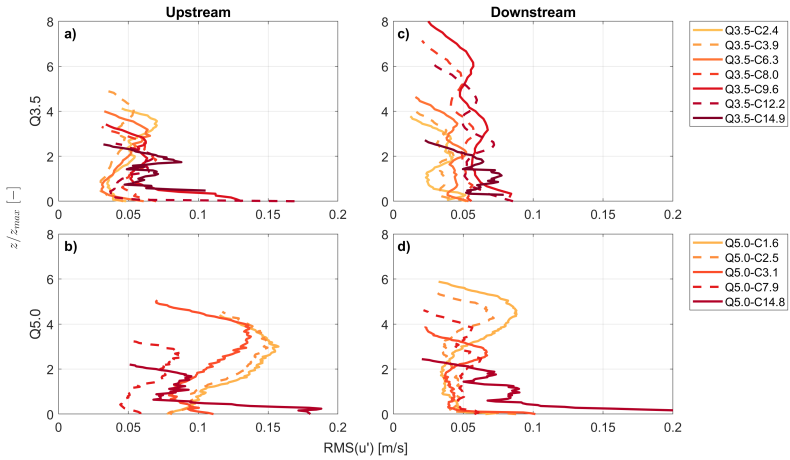

Figure 4.21: Vertical profiles $z_{outer} = (z - z_{max})/(h_0 - z_{max})$ of time-averaged streamwise turbulence intensity ($RMS(u')_0$) for discharge rate Q=3.5 l/s a) upstream and c) downstream, and for discharge rate Q=5.0 l/s b) upstream and d) downstream.
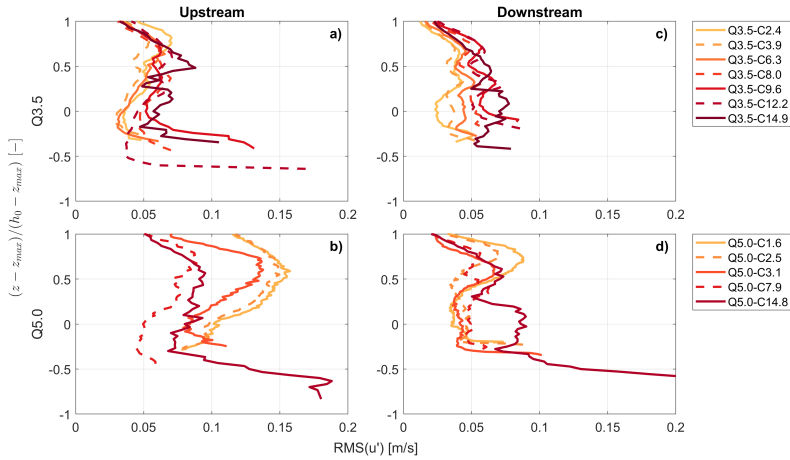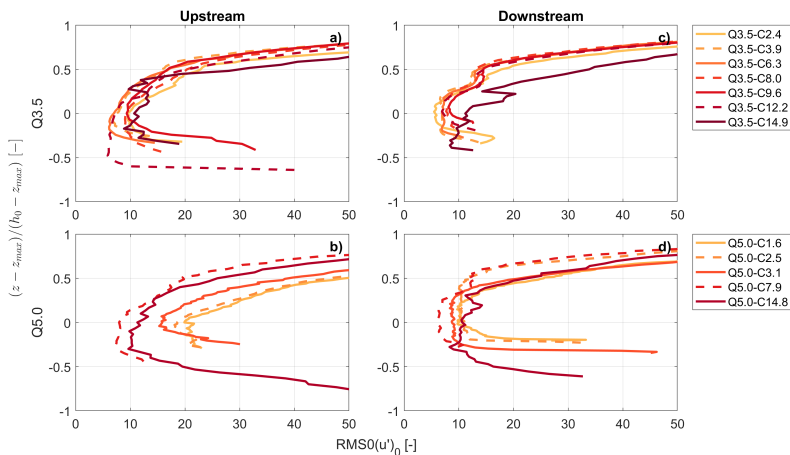
discharge of Q=3.5 l/s. Upstream, there is a small deviation between the runs Q3.5-C3.9, Q3.5-C6.3, Q3.5-C12.2, which have slightly lower turbulence intensity than the runs Q3.5-C2.4, Q3.5-C8.0, Q3.5-C9.6 and Q3.5-C14.9. Downstream a small increase with increasing clay concentration can be identified (Figure 4.18c). For the experimental runs with a high discharge of Q=5.0 l/s, a decrease in turbulence intensity with increasing clay concentration up until run Q5.0-C7.9 can be identified, after which there is an increase in turbulence intensity for Q5.0-C14.8, both upstream and downstream (Figure 4.18b,d). The higher discharge runs (Q=5.0 l/s) tend to have higher turbulence intensity values than the lower discharge runs (Q=3.5 l/s).

OUTER REGION

Figure 4.19a,c shows the time-averaged streamwise velocity profiles ($\overline{U}$) normalised for the outer region ($z_{outer} = (z - z_{max})/(h_0 - z_{max})$) for the experimental runs with a discharge of Q=3.5 l/s for upstream and downstream, respectively and Figure 4.19b,d shows the time-averaged streamwise velocity profiles ($\overline{U}$) normalised for the outer region ($z_{outer} = (z - z_{max})/(h_0 - z_{max})$) for the experimental runs with a discharge of Q=5.0 l/s for upstream and downstream, respectively. The velocity gradually decreases towards zero in the outer region of the flow. At the downstream location, experimental runs Q3.5-C14.9 and Q5.0-C14.8 contain a strong gradient of reduction in flow velocity directly above the plug flow (Section 4.3.3 - Plug flow).

Figure 4.20a,c shows the vertical profiles of the standard deviation of the streamwise temporal mean velocity ($RMS(u')$) normalised for the outer region ($z_{outer} = (z - z_{max})/(h_0 - z_{max})$) for the experimental runs with a discharge of Q=3.5 l/s for upstream and downstream locations, respectively. Figure 4.20b,d shows the vertical profiles of the standard deviation of the streamwise temporal mean velocity ($RMS(u')$) normalised for the outer region ($z_{outer} = (z - z_{max})/(h_0 - z_{max})$) for the experimental runs with a discharge of Q=5.0 l/s for upstream and downstream locations, respectively. In the outer region, $RMS(u')$ shows an increase above the velocity maximum but decreases again towards the top of the gravity current at the upstream location. Experimental runs with a low discharge of Q=3.5 l/s show lower $RMS(u')$ values at the upstream location than experimental runs with a high discharge of Q=5.0 l/s. $RMS(u')$ decreases with increasing clay concentration for the experimental runs Q5.0-C1.6, Q5.0-C2.5, Q5.0-C3.1, Q5.0-C7.9 and relative to Q5.0-C7.9, experimental run Q5.0-C14.8 shows an increase in $RMS(u')$ in the outer region. Downstream, $RMS(u')$ shows a similar pattern as upstream, increasing $RMS(u')$ above the velocity maximum and reducing again near the top of the flow, apart from an additional local decrease in $RMS(u')$ at $z_{outer} = 0.5$. Experimental runs Q3.5-C14.9 and Q5.0-C14.8 initially maintain higher $RMS(u')$ values above the velocity maximum before it follows the trend of the other conditions.

Figure 4.21a,c shows the vertical profiles of the time-averaged streamwise turbulence intensity profiles ($RMS(u')_0$) normalised for the outer region ($z_{outer} = (z - z_{max})/(h_0 - z_{max})$) for the experimental runs with a discharge of Q=3.5 l/s for upstream and downstream locations, respectively and Figure 4.21b,d shows the vertical profiles of the time-averaged streamwise turbulence intensity profiles ($RMS(u')_0$) normalised for the outer region ($z_{outer} = (z - z_{max})/(h_0 - z_{max})$) for the experimental runs with a discharge of Q=5.0 l/s for upstream and downstream locations, respectively. Due to normalisation with the time-averaged streamwise velocity, the turbulence intensity values are high near the upper interface of the gravity currents where the streamwise velocity tends to go to zero. Above the velocity maximum, the turbulence intensity gradually increases at the upstream location. The turbulence intensity values of experimental run Q3.5-C14.9 vary around 12 up to $z_{outer} = 0.4$ after which they gradually increase. Experimental runs with a discharge of Q=3.5 l/s contain comparable turbulence intensity values, whereas the turbulence intensity values of experimental runs with a discharge of Q=5.0 l/s decrease with increasing clay concentration up until run Q5.0-C7.9 after which there is a relative increase in turbulence intensity for experimental run Q5.0-C14.8. Turbulence intensity values of experimental runs with a discharge of Q=3.5 l/s at the downstream location increase upwards in the outer region, with fairly constant values between

$z_{outer} = 0.25 - 0.5$. Turbulence intensity of experimental run Q3.5-C14.9 increases in the outer region as well but contains larger variations directly above the velocity maximum. Experimental runs with a discharge of Q=5.0 l/s contain constant turbulence intensity values above the velocity maximum, which increase from $z_{outer} = 0.3$ upwards.

PLUG FLOW

Figure 4.22 shows the correlation between clay concentration in the inner region and plug height of the velocity profile. The experimental runs Q5.0-C1.6 and Q5.0-C2.5 show no plug flow at either the upstream or downstream location. The low concentration experimental runs Q3.5-C2.4 and Q5.0-C3.1 and the high concentration experimental run Q5.0-C14.8 show a plug flow at the down-stream location. The experimental runs Q3.5-C3.9, Q3.5-C6.3, Q3.5-C8.0, Q3.5-C9.6 and Q5.0-C7.9 show a plug flow at the upstream location. The two high concentration, low discharge runs Q3.5-C12.2 and Q3.5-C14.9 show a plug flow at both the upstream and downstream location, where the plug flow is decreasing in height for run Q3.5-C12.2 and increasing in height for run Q3.5-C14.9 as the flow moves downstream.
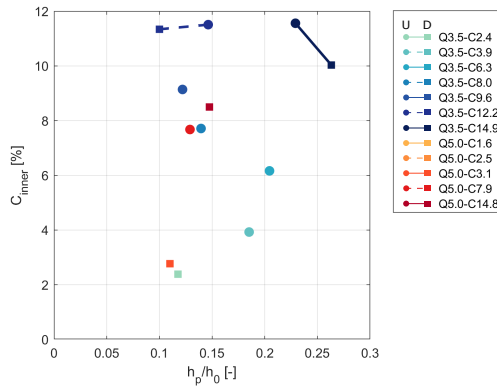
Figure 4.22: Correlation between depth-averaged concentration of the inner region and plug height (h_p) normalised by flow height (h_0). Location in the flume is indicated with U=Upstream and D=Downstream.

Table 4.5: Plug height identified within the experimental runs

Experimental run	Upstream h_p/h_0 [-]	Downstream h_p/h_0 [-]
Low discharge		
Q3.5-C2.4	-	0.12
Q3.5-C3.9	0.19	-
Q3.5-C6.3	0.20	-
Q3.5-C8.0	0.14	-
Q3.5-C9.6	0.12	-
Q3.5-C12.2	0.15	0.10
Q3.5-C14.9	0.23	0.26
High discharge		
Q5.0-C1.6	-	-
Q5.0-C2.5	-	-
Q5.0-C3.1	-	0.11
Q5.0-C7.9	0.13	-
Q5.0-C14.8	-	0.15

4.3.4. DIMENSIONLESS PARAMETERS

Tables 4.6, 4.7 and 4.8 show an overview of velocity and clay concentration measurements and the dimensionless parameters of the experimental runs, which have been calculated for the full flow depth as well as the inner region.

Table 4.6: Overview of variables of experimental runs within this study. E = entrainment; Location in the flume is indicated with U=Upstream and D=Downstream; h_0 = flow height; $\overline{\overline{U}}$ = depth-averaged velocity; $\overline{U}_{max}$ = maximum velocity; $\overline{\overline{U}}_{inner}$ = depth-averaged velocity of the inner region; z_{max}/h_0 = relative height of velocity maximum.

Experimental run	E [-]	Location	h_0 [m]	$\overline{\overline{U}}$ [m/s]	$\overline{U}_{max}$ [m/s]	$\overline{\overline{U}}_{inner}$ [m/s]	z_{max}/h_0 [-]
Low discharge							
Q3.5-C2.4	0.0027	U	0.169	0.24	0.37	0.34	0.24
		D	0.174	0.25	0.42	0.37	0.26
Q3.5-C3.9	0.0038	U	0.138	0.29	0.43	0.41	0.20
		D	0.146	0.31	0.52	0.47	0.25
Q3.5-C6.3	0.0049	U	0.113	0.35	0.52	0.50	0.25
		D	0.131	0.36	0.63	0.57	0.22
Q3.5-C8.0	0.0023	U	0.115	0.33	0.51	0.51	0.30
		D	0.126	0.32	0.61	0.63	0.14
Q3.5-C9.6	0.0057	U	0.110	0.36	0.54	0.49	0.29
		D	0.128	0.37	0.66	0.66	0.12
Q3.5-C12.2	0.0050	U	0.105	0.42	0.63	0.60	0.39
		D	0.128	0.41	0.73	0.71	0.16
Q3.5-C14.9	0.0122	U	0.123	0.26	0.52	0.52	0.40
		D	0.146	0.30	0.63	0.63	0.37
High discharge							
Q5.0-C1.6	0.0074	U	0.249	0.46	0.48	0.44	0.23
		D	0.377	0.51	0.36	0.32	0.17
Q5.0-C2.5	0.0000	U	0.233	0.32	0.51	0.45	0.22
		D	0.262	0.29	0.45	0.40	0.19
Q5.0-C3.1	0.0058	U	0.233	0.31	0.51	0.44	0.20
		D	0.279	0.28	0.47	0.41	0.26
Q5.0-C7.9	0.0035	U	0.159	0.41	0.62	0.58	0.31
		D	0.154	0.47	0.77	0.68	0.22
Q5.0-C14.8	0.0085	U	0.141	0.46	0.71	0.59	0.45
		D	0.156	0.51	0.81	0.78	0.41

Table 4.7: Overview of variables of experimental runs within this study. Location in the flume is indicated with U=Upstream and D=Downstream; C_f = depth-averaged volumetric concentration; $C_{f,m}$ = depth-averaged mass concentration; ν_e= effective kinematic viscosity, based upon (Wan, 1982) (Equation 2.8); Re = Reynolds number; Fr_d = densimetric Froude number; Ri = Richardson number.

Experimental run	Location	C_f [vol %]	$C_{f,m}$ [g/L]	ν_e [$m^2/s \cdot 10^{-6}$]	Re [$- \cdot 10^4$]	Fr_d [-]	Ri [-]
Low discharge							
Q3.5-C2.4	U	1.5	39	1.15	3.5	1.17	0.73
	D	1.3	33	1.12	3.8	1.29	0.60
Q3.5-C3.9	U	2.4	62	1.35	3.0	1.24	0.65
	D	1.8	45	1.20	3.7	1.50	0.44
Q3.5-C6.3	U	3.8	97	1.75	2.8	1.34	0.56
	D	2.6	66	1.39	3.3	1.51	0.44
Q3.5-C8.0	U	4.1	112	1.99	2.0	1.18	0.72
	D	3.0	76	1.50	3.2	1.30	0.59
Q3.5-C9.6	U	5.1	126	2.23	1.7	1.27	0.62
	D	3.3	83	1.58	3.0	1.48	0.46
Q3.5-C12.2	U	6.5	156	2.79	1.6	1.28	0.61
	D	4.1	103	1.86	2.8	1.40	0.51
Q3.5-C14.9	U	4.3	106	1.90	1.7	0.88	1.29
	D	4.3	107	1.90	2.3	0.96	1.10

Experimental run	Location	C_f [vol %]	$C_{f,m}$ [g/L]	ν_e [$m^2/s\cdot10^{-6}$]	Re [$-\cdot10^4$]	Fr_d [-]	Ri [-]
			High discharge				
Q5.0-C1.6	U	1.0	28	1.08	6.5	1.51	0.44
	D	0.8	20	1.05	6.8	1.03	0.95
Q5.0-C2.5	U	1.6	40	1.16	3.4	1.33	0.56
	D	1.3	34	1.12	4.1	1.23	0.66
Q5.0-C3.1	U	1.8	46	1.20	7.1	1.21	0.68
	D	1.4	37	1.14	8.1	1.12	0.80
Q5.0-C7.9	U	4.3	106	1.91	2.6	1.25	0.64
	D	3.9	96	1.77	4.2	1.50	0.45
Q5.0-C14.8	U	5.8	139	2.48	6.7	1.26	0.63
	D	4.4	107	1.93	7.0	1.54	0.42

Table 4.8: Overview of variables of the inner region of experimental runs within this study. Location in the flume is indicated with U=Upstream and D=Downstream; C_{inner} = depth-averaged volumetric concentration of the inner region; $C_{inner,m}$ depth-averaged mass concentration of the inner region; $\nu_{e,inner}$= effective kinematic viscosity of the inner region, based upon (Wan, 1982) (Equation 2.8); Re_{inner} = Reynolds number of the inner region; $Fr_{d,inner}$ = densimetric Froude number of the inner region; Ri_{inner} = Richardson number of the inner region.

Experimental run	Location	C_{inner} [vol %]	$C_{inner,m}$ [g/L]	$\nu_{e,inner}$ [$m^2/s\cdot10^{-6}$]	Re_{inner} [$-\cdot10^4$]	$Fr_{d,inner}$ [-]	Ri_{inner} [-]
			Low discharge				
Q3.5-C2.4	U	2.5	68	1.37	1.0	2.63	0.14
	D	2.4	65	1.34	1.2	2.63	0.14
Q3.5-C3.9	U	3.9	108	1.78	0.7	3.08	0.11
	D	3.8	105	1.74	1.0	3.18	0.10
Q3.5-C6.3	U	6.2	174	2.64	0.5	2.97	0.11
	D	6.0	170	2.59	0.6	3.46	0.08
Q3.5-C8.0	U	7.7	221	3.36	0.5	2.50	0.16
	D	7.5	216	3.27	0.3	4.28	0.05
Q3.5-C9.6	U	9.1	267	4.09	0.4	2.29	0.19
	D	9.0	261	3.99	0.3	4.45	0.05
Q3.5-C12.2	U	11.5	345	5.43	0.5	2.19	0.21
	D	11.3	339	5.33	0.3	3.65	0.08
Q3.5-C14.9	U	11.6	346	5.46	0.2	0.73	1.89
	D	10.0	296	4.58	0.5	1.51	0.44
			High discharge				
Q5.0-C1.6	U	1.5	41	1.15	2.1	3.72	0.07
	D	1.4	37	1.13	1.8	2.69	0.14
Q5.0-C2.5	U	2.2	61	1.30	1.8	3.33	0.09
	D	2.2	60	1.30	1.5	2.99	0.11
Q5.0-C3.1	U	2.9	78	1.46	1.4	3.05	0.11
	D	2.8	75	1.43	2.0	2.27	0.19
Q5.0-C7.9	U	7.7	220	3.34	0.9	2.37	0.18
	D	7.7	222	3.36	0.7	3.32	0.09
Q5.0-C14.8	U	9.3	273	4.20	0.9	1.89	0.28
	D	8.5	246	3.75	1.3	2.63	0.14

4

The entrainment of ambient fluid into the body of the gravity body within the experimental results, following Equation 4.18, corresponds with correlations found in literature (Parker et al., 1987, Figure 4.23).

$$E = 0.075/(1 + 718Ri^{2.4})^{0.5} \qquad (4.19)$$

Experimental run Q3.5-C14.9 deviates from the correlation between entrainment and densimetric Froude number to the lower clay concentration measurements (Section 4.3.1). Experimental run Q5.0-C2.5 contains a lower entrainment rate compared to the other experimental runs as the product of depth-averaged flow velocity and flow height is very similar between the upstream and downstream measurements.
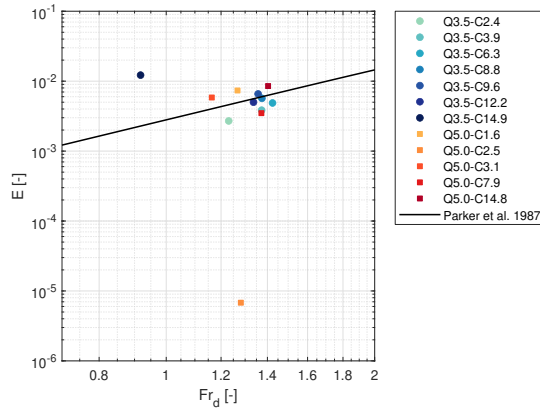

Figure 4.23: Entrainment ratio (E) as a function of densimetric Froude number (Fr_d).

4.3.5. TIME SERIES

Characteristics of the time series of the streamwise velocity measurements can support the identification of turbulence enhancement and attenuation within a clay suspension flow (Baas et al., 2009). To further assess the turbulence, a fast Fourier transform is conducted on the time series. The results are shown for selective heights, near the bed within the inner region ($z_{inner} = 0.35$), in the outer region ($z_{outer} = 0.5$) and at the height of the velocity maximum (z_{max}). The results are shown for four different experimental runs, including a low (Q3.5-C2.4), medium (Q3.5-C6.3) and high (Q3.5-C14.9) clay concentration run for the low discharge and the high clay concentration, high discharge run (Q5.0-C14.8) for both upstream and downstream locations. The time series are not influenced by the frequency of the mixer or any of the pumps, which have frequencies of 50Hz, greater than the range of frequencies from the fast Fourier transforms (Figure 4.5).

INNER REGION

Figure 4.25 shows the velocity fluctuations of time series of streamwise velocity at $z_{inner} = 0.35$ (Figure 4.24) for experimental run Q3.5-C2.4 (Figure 4.25a,e), Q3.5-C6.3 (Figure 4.25b,f), Q3.5-C14.9 (Figure 4.25c,g) and Q5.0-C14.8 (Figure 4.25d,h) for both upstream and downstream locations, respectively. Figure 4.26 shows the outcome of the fast Fourier transform for experimental run Q3.5-C2.4 (Figure 4.26a,e), Q3.5-C6.3 (Figure 4.26b,f), Q3.5-C14.9 (Figure 4.26c,g) and Q5.0-C14.8 (Figure 4.26d,h) for both upstream and downstream locations, respectively. The time series and Fourier transform of experimental run Q3.5-C14.9 are excluded at $z_{inner} = 0.35$ as there is no valid velocity data available.

The velocity fluctuations are constant around the mean and are characterized by quasi-random velocity fluctuations due to the turbulent fluid motion. Experimental run Q3.5-C2.4 shows larger velocity fluctuations than experimental run Q3.5-C6.3. Experimental runs Q3.5-C2.4 and Q3.5-C6.3 show a similar range of velocity fluctuations at the upstream and downstream locations, whereas experimental run Q5.0-C14.9 shows larger velocity fluctuations upstream than at the downstream location.

The fast Fourier transform indicates relatively consistent importance of frequency ranges for experimental runs Q3.5-C2.4 and Q3.5-C6.3 both at the upstream and downstream locations. A few higher spikes and a small averaged increase from 0 to around 1 Hz can be identified. At the downstream location, experimental run Q3.5-C14.9 shows increased energy for frequencies up to 2 Hz. The frequencies between 2 and 4 Hz show a gradually decreasing importance and a consistent but reduced energy for frequencies upwards from 4 Hz. A similar pattern of difference in importance between lower and higher frequencies can be identified in experimental run Q5.0-C14.8 at both upstream and downstream locations. Upstream, the energy within the spectrum is consistent up to 1 Hz, after which it reduces between 1 and 2 Hz and it is reduced but fairly consistent from 2 Hz upwards. Downstream, the energy is consistent up to 1 Hz, after which it reduces more gradually between 1 and 4 Hz to end up consistently lower from 4 Hz upwards.

OUTER REGION

Figure 4.28 shows the velocity fluctuations of time series of streamwise velocity at $z_{outer} = 0.5$ (Figure 4.27) for experimental run Q3.5-C2.4 (Figure 4.28a,e), Q3.5-C6.3 (Figure 4.28b,f), Q3.5-C14.9 (Figure 4.28c,g) and Q5.0-C14.8 (Figure 4.28d,h) for both upstream and downstream locations, respectively. Figure 4.29 shows the outcome of the fast Fourier transform for experimental run Q3.5-C2.4 (Figure 4.29a,e), Q3.5-C6.3 (Figure 4.29b,f), Q3.5-C14.9 (Figure 4.29c,g) and Q5.0-C14.8 (Figure 4.29d,h) for both upstream and downstream locations, respectively.

The velocity fluctuations are constant around the mean and are characterized by quasi-random velocity fluctuations due to the turbulent fluid motion. The velocity fluctuations are larger than found within the inner region (Figure 4.25). The high clay concentration runs, Q3.5-C14.9 and Q5.0-C14.8, show larger velocity fluctuations at $z_{outer} = 0.5$ than the experimental runs Q3.5-C2.4 and Q3.5-C6.3 at both upstream and downstream locations.

The fast Fourier transform shows increased energy for frequencies up to 0.4 Hz and reduced energy for frequencies higher than 0.4 Hz for experimental run Q3.5-C2.4. At the upstream location, there is more variation in the height of the spikes and at the downstream location, the energy of frequencies gradually reduces from 0 to 0.4 Hz. Higher spikes can be identified between 0.4 to 1.5 Hz at the upstream location for experimental run Q3.5-C6.3. The importance of the rest of the frequencies is more equally distributed within experimental run Q3.5-C6.3 at the upstream and downstream locations. The high concentration runs Q3.5-C14.9 and Q3.5-C14.8 contain higher spikes at lower frequencies, which gradually decrease towards the higher frequencies. The reduction in importance is more gradual than identified in the inner region (Figure 4.26).

VELOCITY MAXIMUM

Figure 4.31 shows the velocity fluctuations of time series of streamwise velocity at the height of the velocity maximum (Figure 4.30) for experimental run Q3.5-C2.4 (Figure 4.31a,e), Q3.5-C6.3 (Figure 4.31b,f), Q3.5-C14.9 (Figure 4.31c,g) and Q5.0-C14.8 (Figure 4.31d,h) for both upstream and downstream locations, respectively. Figure 4.32 shows the outcome of the fast Fourier transform for experimental run Q3.5-C2.4 (Figure 4.32a,e), Q3.5-C6.3 (Figure 4.32b,f), Q3.5-C14.9 (Figure 4.32c,g) and Q5.0-C14.8 (Figure 4.32d,h) for both upstream and downstream locations, respectively.

The velocity fluctuations are constant around the mean and are characterized by quasi-random velocity fluctuations due to the turbulent fluid motion. The velocity fluctuations at the velocity maximum are similar in range or on average smaller than in the inner region (Figure 4.25) and are significantly smaller than the velocity fluctuations in the outer region (Figure 4.28). The velocity fluctuations at the velocity maximum show no clear difference between the upstream and downstream measurement locations.

The fast Fourier transform indicates higher spikes at the lower frequencies, which gradually decrease up to around 1 Hz and from 1 Hz upwards there is a fairly consistent distribution in height of spikes at the upstream location for experimental runs Q3.5-C2.4 and Q3.5-C6.3. At the downstream location for these experimental runs, the time series contains the full range of frequencies with relatively equal distribution. The high clay concentration runs Q3.5-C14.9 and Q3.5-C14.8 show increased energy in frequencies up to around 2 Hz at the upstream location. The energy in frequencies reduces from 2 to 4 Hz and it is reduced, but fairly consistent from 4 Hz upwards. A similar pattern of difference in importance between lower and higher frequencies can be identified at the downstream location for experimental runs Q3.5-C14.9 and Q5.0-C14.8. This difference in importance between lower and higher frequencies is more distinct at the downstream location than at the upstream location. The energy within the spectrum is consistently high up to 1 Hz, after which it gradually reduces between 1 and 2 Hz and it is reduced but fairly consistent from 2 Hz upwards.
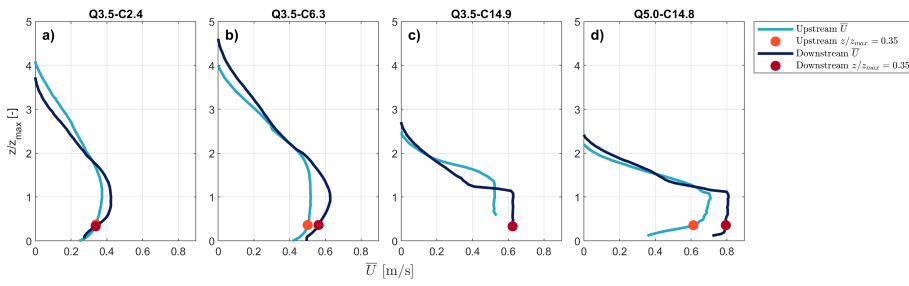
Figure 4.24: Upstream and downstream vertical profiles ($z_{inner} = z/z_{max}$) of temporal mean velocity ($\overline{U}$) with indicated $z_{inner} = 0.35$ for experimental run a) Q3.5-C2.4; b) Q3.5-C6.3; c) Q3.5-C14.9; d) Q5.0-C14.8.

Figure 4.25: Velocity fluctuations of time series of streamwise velocity at $z_{inner} = 0.35$ (Figure 4.24) normalised with time-averaged velocity $((u-\overline{U})/\overline{U})$, for experimental runs a,e) Q3.5-C2.4; b,d) Q3.5-C6.3; c,g) Q3.5-C14.9; d,h) Q5.0-C14.8, upstream and downstream, respectively.

Figure 4.26: Single sided fast Fourier transform on time series of streamwise velocity at $z_{inner} = 0.35$ (Figure 4.24), for experimental runs a,e) Q3.5-C2.4; b,f) Q3.5-C6.3; c,g) Q3.5-C14.9; d,h) Q5.0-C14.8, upstream and downstream, respectively.

Figure 4.27: Upstream and downstream vertical profiles ($z_{outer} = (z - z_{max})/(h_0 - z_{max})$) of temporal mean velocity ($\overline{U}$) with indicated $z_{outer} = 0.5$ for experimental run a) Q3.5-C2.4; b) Q3.5-C6.3; c) Q3.5-C14.9; d) Q5.0-C14.8.
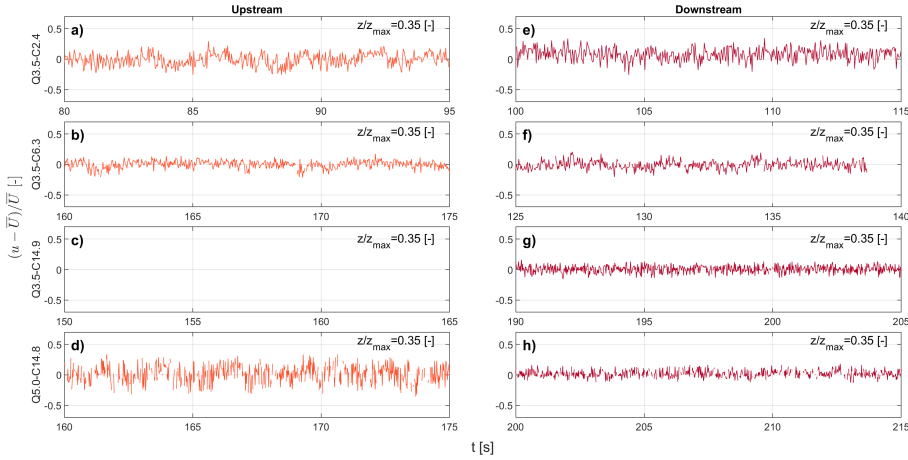

Figure 4.28: Velocity fluctuations of time series of streamwise velocity at $z_{outer} = 0.5$ (Figure 4.27) normalised with time-averaged velocity ($(u - \overline{U})/\overline{U}$), for experimental runs a,e) Q3.5-C2.4; b,d) Q3.5-C6.3; c,g) Q3.5-C14.9; d,h) Q5.0-C14.8, upstream and downstream, respectively.
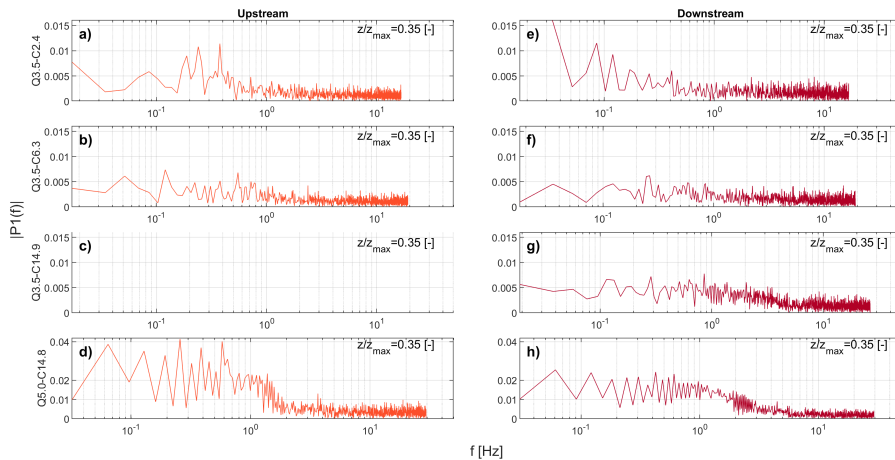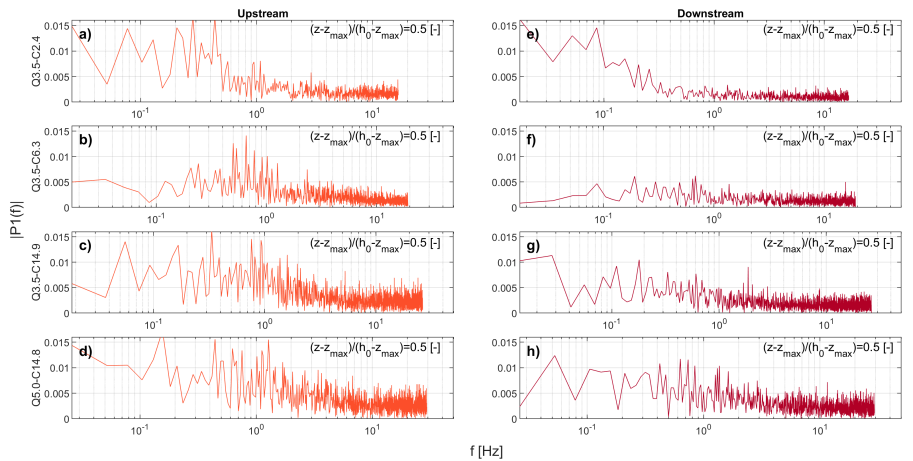

Figure 4.29: Single sided fast Fourier transform on time series of streamwise velocity at $z_{outer} = 0.5$ (Figure 4.27), for experimental runs a,e) Q3.5-C2.4; b,f) Q3.5-C6.3; c,g) Q3.5-C14.9; d,h) Q5.0-C14.8, upstream and downstream, respectively.
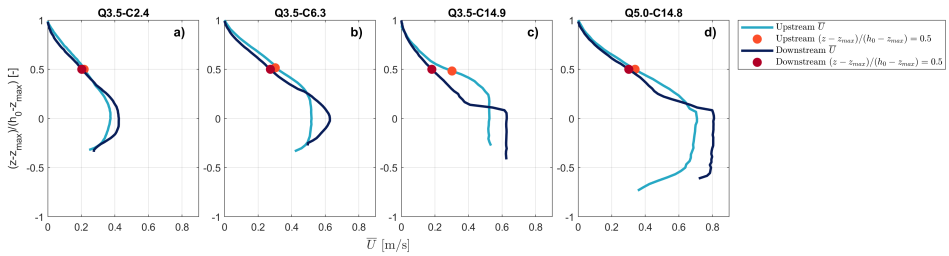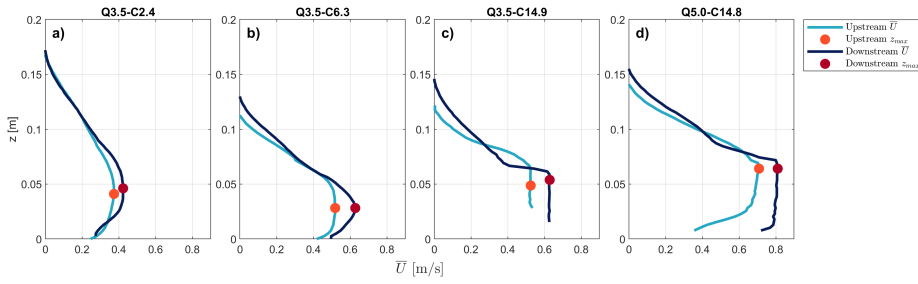
Figure 4.30: Upstream and downstream vertical profiles of temporal mean velocity ($\overline{U}$) with indicated velocity maximum for experimental run a) Q3.5-C2.4; b) Q3.5-C6.3; c) Q3.5-C14.9; d) Q5.0-C14.8.
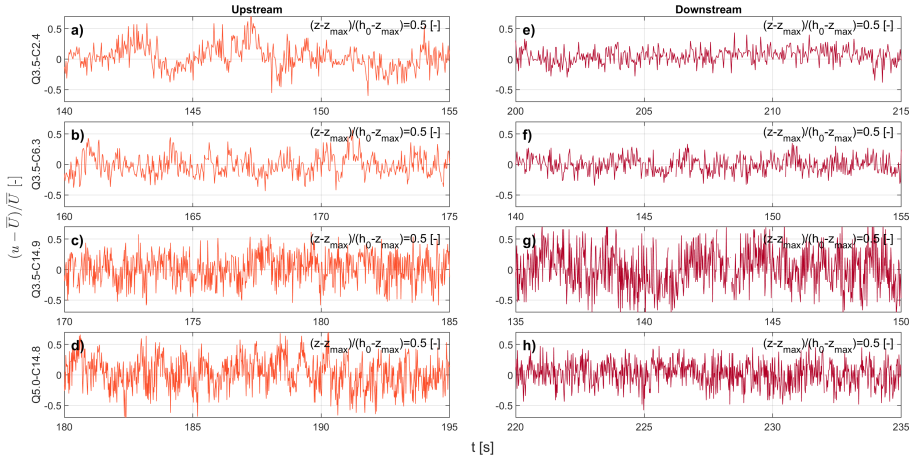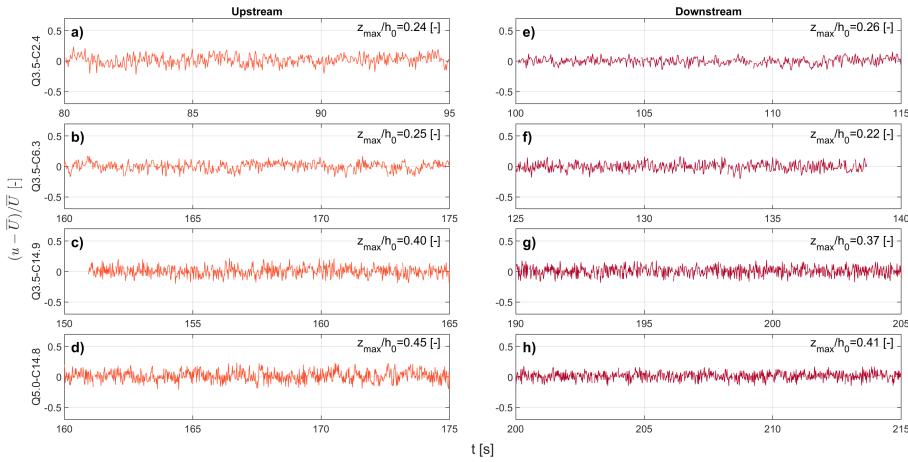

Figure 4.31: Velocity fluctuations of time series of streamwise velocity at the height of the velocity maximum (z_{max}, Figure 4.30) normalised with time-averaged velocity ($(u - \overline{U})/\overline{U}$), for experimental runs a,e) Q3.5-C2.4; b,d) Q3.5-C6.3; c,g) Q3.5-C14.9; d,h) Q5.0-C14.8, upstream and downstream, respectively.

Figure 4.32: Single sided fast Fourier transform on time series of streamwise velocity at the height of the velocity maximum (z_{max}, Figure 4.30), for experimental runs a,e) Q3.5-C2.4; b,f) Q3.5-C6.3; c,g) Q3.5-C14.9; d,h) Q5.0-C14.8, upstream and downstream, respectively.

4.4. DISCUSSION

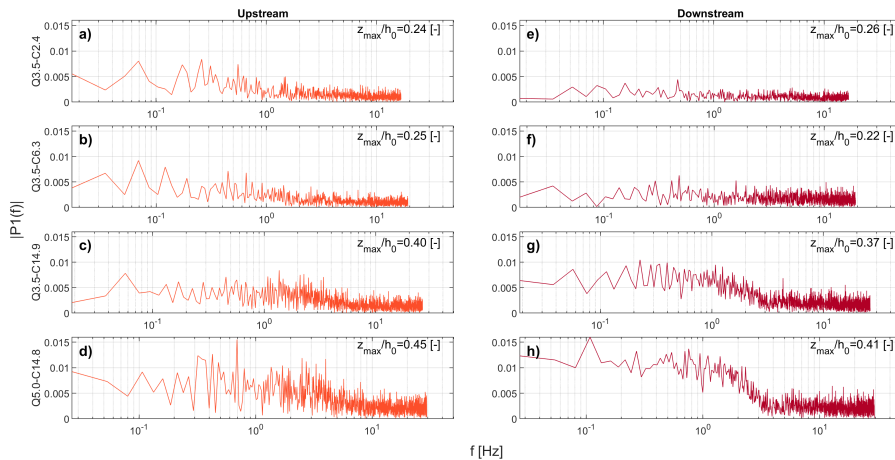On one side of the spectrum, turbidity currents are relatively dilute flows (Mulder and Alexander, 2001; Leeder, 2011); correlated to TF flows based on the classification of Baas et al. (2009). On the other side of the spectrum, debris or mud flows have limited internal turbulence and cohesive sediment provides the grain support through yield strength (Middleton and Hampton, 1973; Mulder and Alexander, 2001); correlated to QLPF flows based on the classification of Baas et al. (2009). Transitional flows bridge the gap between turbidity currents, i.e. turbulent flows, and debris flows, i.e. quasi-laminar plug flow, containing transient turbulent behaviour (Wang and Plate, 1996; Baas et al., 2009; Sumner et al., 2009). Transitional flow properties of gravity currents are expected to differ from those of open-channel flows. To understand these differences, a comparison between the different experimental runs is made for the velocity and turbulence intensity at different regions within the flow, including the inner region, outer region and plug flow (Section 4.4.1). Once the different flow properties are identified at both the upstream and downstream location, the evolvement of the gravity current is assessed by comparing the velocity and turbulence intensity between the upstream and downstream location (Section 4.4.2).

4.4.1. CLAY FLOW TYPES

INNER REGION

Near the base of the flow an increase in turbulence intensity can be identified as being generated due to the friction with the bed of the flow (Nezu and Nakagawa, 1993; Altinakar et al., 1996; Pope, 2000; Schlichting and Gersten, 2016). Near the bed the velocity fluctuations might be influenced by the passage of intermittent turbulent flow structures produced by shear at the bed of the flume (Best and Leeder, 1993; Kneller and Buckee, 2000; Buckee et al., 2001; Baas et al., 2005), which potentially could explain the intensified frequencies between 0.1 and 0.4 Hz at the upstream location. The velocity profile of experimental runs Q3.5-C2.4 and Q3.5-C6.3 is characteristic of a turbidity current, i.e consisting of jet region on top of a wall region (Altinakar et al., 1996; Kneller et al., 1999; Wells and Dorrell, 2021, Figure 4.2). The time series show a similar randomised pattern around the mean at both the upstream and downstream locations and the fast Fourier transform indicates an equal distribution of frequencies within the time series. Overall, this suggests turbulent flows within the inner region for experimental runs Q3.5-C2.4 and Q3.5-C6.3. The plug flow identified in the velocity profiles of experimental runs Q3.5-C14.9 and Q5.0-C14.8 extends far into the inner region at the downstream location (Section 4.3.3). The fast Fourier transform of these runs indicates a differentiation between low and high frequencies, which might suggest the initial stages of turbulence attenuation (Section 4.4.1 Plug flow).

OUTER REGION

In the outer region, velocity fluctuations are stronger than at the height of the velocity maximum. The boundary shear with the ambient fluid at the top of the turbidity current results in an increase in turbulence intensity (Altinakar et al., 1996; Kneller and Buckee, 2000; Gray et al., 2006; Eggenhuisen et al., 2020). The lower frequency variations or coherent flow structures identified in the time series (Figure 4.28) in the outer region might be related to turbulent mixing or Kelvin-Helmholtz vortices at the top of the turbidity current (Goldfarb et al., 2002; Hacker et al., 1996; Kneller and Buckee, 2000; Venditti et al., 2013). The degree of turbulence in the outer region of experimental runs Q3.5-C2.4, Q3.5-C3.9, Q3.5-C6.3, Q3.5-C8.0 and Q5.0-C7.9 has similar values as the turbulence in the inner region. Turbulence near the bed is higher for experimental runs Q3.5-C9.6, Q3.5-C12.2, Q3.5-C14.9 and Q5.0-C14.8, which is consistent with the supercritical nature of the flow (Parker et al., 1987; García, 1993; Garcia, 1994; Wells and Dorrell, 2021). In experimental runs Q5.0-C1.6, Q5.0-C2.5 and Q5.0-C3.1 the degree of turbulence in the outer region is larger than in the inner region (Figures 4.17, 4.20). Experiments have shown that as the flow viscosity increases, the amount of mixing in the outer region reduces (Marr et al., 2001; Mohrig and Marr,

2003; Baker et al., 2017). This reduction in turbulence intensity is not identified in the outer region for the clay concentrations included within the experimental runs of this study. In combination with viscosity measurements, Hermidas et al. (2018) suggest turbulence attenuated free shear layer for velocity profiles with the inflexion point above the velocity maximum close to the plug flow, like in experimental runs Q3.5-C14.9 and Q5.0-C14.8. However, the turbulence intensity data and time series (Figures 4.21, 4.28) show no indication of turbulence attenuation in the outer region for these high concentration runs Q3.5-C14.9 and Q5.0-C14.8.

Velocity maximum
The turbulence intensity profiles show typical reduced turbulence intensity at the height of the velocity maximum (z_{max}) with enhanced turbulence intensity maxima above (outer region) and below (inner region) the velocity maximum, where the velocity gradients are largest (Kneller et al., 1999; Best et al., 2001; Buckee et al., 2001; Choux et al., 2005; Gray et al., 2006; Cartigny et al., 2013; Eggenhuisen et al., 2020). Locally, a reduction in turbulence intensity is found possibly due to the reduced shear production of turbulence around the velocity maximum (Kneller et al., 1999; Buckee et al., 2001). The gradually increasing turbulence intensity with increasing clay concentration (Section 4.3.3), suggests turbulent flow conditions. Based on visualisation, the time series indicates turbulent flow conditions at the velocity maximum for all experimental runs (Figure 4.31). However, a more detailed analysis of the plug flow region suggests a more complex pattern of turbulence dynamics (Section 4.4.1 Plug flow).

Plug flow
Within the velocity profiles, a plug flow can be identified for some experimental runs, based only upon a zone of low velocity gradient (Section 4.3.3). In open-channel flows, a plug flow region is characterised by a low velocity gradient and a reduction in turbulence intensity (Wang and Plate, 1996; Baas and Best, 2002; Baas et al., 2009). However, this reduction in turbulence intensity is not identified within the flows of these experiments (Figures 4.18, 4.21). For example, the high clay concentration run Q3.5-C14.9, which shows a clear plug flow region within the velocity profile, has comparable turbulence intensity values at the upstream location and higher turbulence intensity values at the downstream location than the other experimental runs with a discharge of Q=3.5 l/s. The frequently used measure of turbulence intensity, standard deviation around the mean velocity (Best et al., 2001; Baas et al., 2009; Eggenhuisen and McCaffrey, 2012), might not be the most suitable criteria to determine turbulence attenuation within a flow. Turbulence is characterised by random motion around the mean with a range of frequencies (Pope, 2000; Kaneda et al., 2003; Iyer et al., 2020, Section 1.1.1). If turbulence attenuation occurs due to the presence of clay, high-frequency velocity fluctuations may be gradually suppressed with increasing clay concentration as the viscous flow quickly attenuates the (high-frequency) fluctuations (Harker and Temple, 1988; Pope, 2000; Baas et al., 2009). The fast Fourier transform indicates this turbulence attenuation of high-frequency velocity fluctuations downstream in experimental run Q3.5-C14.9 (Figure 4.32g) and Q5.0-C14.8 (Figure 4.32h). The low, Q3.5-C2.4, and medium, Q3.5-C6.3, clay concentration runs show consistent importance of the full range of frequencies within the time series (Figure 4.32e,f), whereas the high clay concentration runs Q3.5-C14.8 and Q5.0-C14.9 show that the higher frequencies above 4 Hz are suppressed relative to the lower frequencies below 2 Hz (Figure 4.32g,h). This reduction in the importance of higher frequencies within the time series suggests early stages of turbulence attenuation within the flow. The standard deviation, $RMS(u')$, captures an average of velocity fluctuations around the mean (Glüer et al., 1995; Pope, 2000) and is, therefore, unable to pick up this differentiation in the distribution of frequencies within the time series. Open-channel flow experiments indicated that increase in clay concentration or reduction in velocity can result in full turbulence attenuation, detectable by reduced $RMS(u')$ values (Baas and Best, 2002; Baas and Best, 2008; Baas et al., 2009, Chapters 2, 3). Additional gravity current

experiments with increased clay concentration should be conducted to assess if this turbulence attenuation can occur within gravity currents. The stronger cohesive forces with increased clay concentration might result in turbulence attenuation, but the additional turbulence generated in the outer region due to the ambient flow, which does not occur in open-channel flows (Chaudhry, 2008; Leeder, 2011; Dorrell et al., 2019), might prevent the turbulence attenuation.

This differentiation in the importance of lower and higher frequencies has been identified within the plug flow of the high clay concentration runs Q3.5-C14.9 and Q5.0-C14.8. However, the differentiation is not observed within all plug flows identified within the velocity profile (Section 4.3.3). For example, at the upstream location, in experimental run Q3.5-C6.3 a plug flow was identified in the velocity profile (Table 4.5), but the fast Fourier transform indicates a relatively equal distribution of frequencies (Figure 4.32b). The differentiation in the importance of lower and higher frequencies is particularly clear in the high clay concentration runs Q3.5-C14.9 and Q5.0-C14.8 (Figure 4.32). This suggests that a plug flow within the velocity profile develops already at lower clay concentrations and the attenuation of higher frequencies occurs at higher clay concentrations due to the increased viscosity within the flow.

CLAY FLOW TYPES

Three clay flow types for gravity currents are proposed for the experimental runs (Figure 4.33, Table 4.9), based on the velocity and turbulence profiles in combination with the analysis of the time series of the inner region, outer region and plug flow development. For all experimental runs, enhanced turbulence intensity is found below the velocity maximum, in the inner region due to bed shear stress (Altinakar et al., 1996; Kneller et al., 1999; Choux et al., 2005; Cartigny et al., 2013). In the outer region, additional turbulence is present due to shear with the ambient fluid, which causes turbulent mixing or Kelvin-Helmholtz vortices (Goldfarb et al., 2002; Hacker et al., 1996; Kneller and Buckee, 2000; Venditti et al., 2013; Eggenhuisen et al., 2020). The gravity currents can be divided into velocity profiles with and without a plug flow (Section 4.3.3). Additional analysis of the velocity time series suggests that gravity currents with a plug flow in the velocity profile can be further subdivided into velocity signals with or without differentiation in the importance of lower and higher frequencies.

Table 4.9: Overview of identified flow types (Figure 4.33)

| Experimental run	Upstream	Downstream
	Low discharge	
Q3.5-C2.4	turbidity current	turbidity current
Q3.5-C3.9	turbulent plug flow	turbidity current
Q3.5-C6.3	turbulent plug flow	turbidity current
Q3.5-C8.0	turbulent plug flow	turbidity current
Q3.5-C9.6	turbulent plug flow	turbidity current
Q3.5-C12.2	turbulent plug flow	turbidity current
Q3.5-C14.9	turbulent plug flow	transitional plug flow
	High discharge	
Q5.0-C1.6	turbidity current	turbidity current
Q5.0-C2.5	turbidity current	turbidity current
Q5.0-C3.1	turbidity current	turbidity current
Q5.0-C7.9	turbulent plug flow	turbidity current
Q5.0-C14.8	turbulent plug flow	transitional plug flow
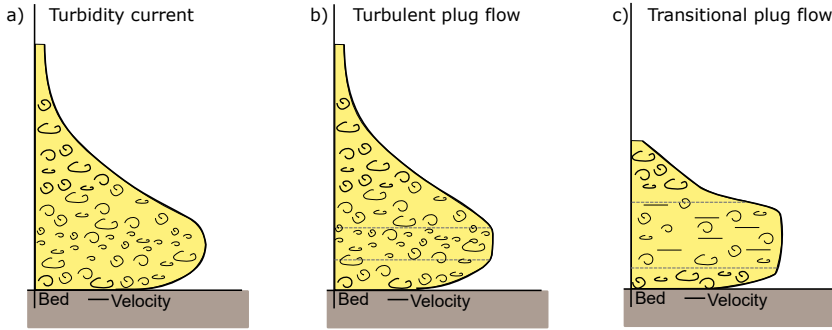
Figure 4.33: Schematics of velocity profile and flow structure for the three flow types identified in this paper: a) turbidity current, b) turbulent plug flow, c) transitional plug flow.

The gravity currents without a plug flow are fully turbulent and are classified as 'turbidity current' (Figure 4.33a). These turbidity currents contain reduced turbulence around the velocity maximum with two peaks of maximum shear on either side of the velocity maximum, i.e. the typical turbulence intensity profile for turbidity currents. Fast Fourier analysis on the time series of velocity measurements shows equal distribution among the full frequency range at the velocity maximum, in the inner region and the outer region.

The gravity currents with a plug flow within the velocity profile, but without any differentiation in the energy of lower or higher frequencies are classified as 'turbulent plug flow' (Figure 4.33b). These turbulent plug flows contain a region of low velocity gradient, defined as plug flow (Figure 4.9) around the velocity maximum. The turbulence intensity profiles or analysis of time series of velocity measurements show no signs of turbulence attenuation.

The gravity currents with a plug flow in the velocity profile together with differentiation in the energy of lower and higher frequencies in the fast Fourier analysis on the velocity time series are classified as 'transitional plug flow' (Figure 4.33c). These transitional plug flows contain a plug flow within the velocity profile, i.e. a region in the velocity profile with low velocity gradient. The turbulence intensity profiles show the typical shape with reduced turbulence intensity around the velocity maximum and two peaks of maximum shear on either side of the velocity maximum. Initial signs of turbulence attenuation are identified in the velocity time series at the velocity maximum and within the plug flow. The higher frequencies are attenuated relative to the lower frequencies, possibly due to the increasing viscous forces within the flow. These transitional plug flows contain a differentiation in lower and higher frequencies within the turbulence.

Hermidas et al. (2018) based his classification of transitional flow properties for gravity currents on the velocity profile and viscosity values measured ex-situ by a rheometer. Hermidas et al. (2018) identified four flow types, from low to high clay concentration: turbidity current, transitional turbidity current, top transitional plug flow and plug flow (Figure 4.4). Viscosity measurements are not available within this study and turbulence intensity measurements are not available within the study of Hermidas et al. (2018), but similarities can be identified if a comparison is made based solely on the vertical profiles of the streamwise temporal mean velocity. Turbidity current identified within this study is separated into two flow types by Hermidas et al. (2018): turbidity current and transitional turbidity current. The laminar boundary layer of transitional turbidity current is not identified within the experimental results of this study as bed shear resulted in enhanced turbulence intensity in the inner region. In open-channel flow, transitional clay flow types initially show an increase in near-bed turbulence in TETF and LTPF flows (Baas et al., 2009). However, the combination of decreased near-bed velocity and increased near-bed turbulence with turbu-

lence decrease in the upper part of the flow as identified in LTPF flows in open-channel flow is not identified within the experimental results of the gravity currents. The top transitional plug flow of Hermidas et al. (2018) can be associated with turbulent plug flow and the plug flow of Hermidas et al. (2018) can be associated with transitional plug flow. However, the laminar flow, i.e. turbulence attenuation within these flow types of Hermidas et al. (2018) is not identified within the experimental results of this study.

With increasing clay concentration, the gravity current moves from a fully turbulent turbidity current to a turbulent plug flow, where the development of a plug flow within the velocity profile starts. With further increasing clay concentration, the gravity current develops towards a transitional plug flow, where the higher frequencies within the plug flow start to get attenuated by the increasingly viscous forces in the flow. The transitional flows within these experiments range from turbidity current up to transitional plug flow, excluding the development of a debris flow. Additional research should be conducted to explore if stronger turbulence attenuation is able to develop or if the additional turbulence generated in the outer region due to mixing with the ambient flow prevents the turbulence attenuation (Leeder, 2011; Dorrell et al., 2019). It might be expected that additional flow types can be identified with stronger turbulence attenuation with higher clay concentrations (Marr et al., 2001; Baker et al., 2017). Figure 4.34 shows the identified flow types in correlation with depth-averaged clay concentration and depth-averaged flow velocity in the inner region. Clay concentration, i.e. cohesive forces and velocity, i.e. turbulent forces control the dynamics of clay flows (Baas et al., 2009; Baker et al., 2017; Craig et al., 2020; Sobocinska and Baas, 2022). The boundaries between turbidity current and turbulent plug flow move to higher clay concentrations as the depth-averaged velocity increases. The turbulence generated is greater at a higher velocity and consequently, the turbulence is able to prevent flocculation at higher concentrations (McAnally and Mehta, 2000; Partheniades, 2009; Cuthbertson et al., 2010). Transitional plug flows are expected to occur at higher clay concentrations than turbidity current or turbulent plug flow, but Figure 4.34 indicates a different pattern. Transitional plug flow is identified at relatively high concentrations, but lower than in certain turbidity currents or turbulent plug flows. For the transitional plug flow identified in experimental run Q3.5-C14.9, the clay concentration could be higher than measured (Section 4.3.1). However, it is expected that the thixotropic processes of the formation of clay bonds also influence the clay flow type (Skempton and Northey, 1952; Yu et al., 2013; Ren et al., 2021, Section 4.4.2).
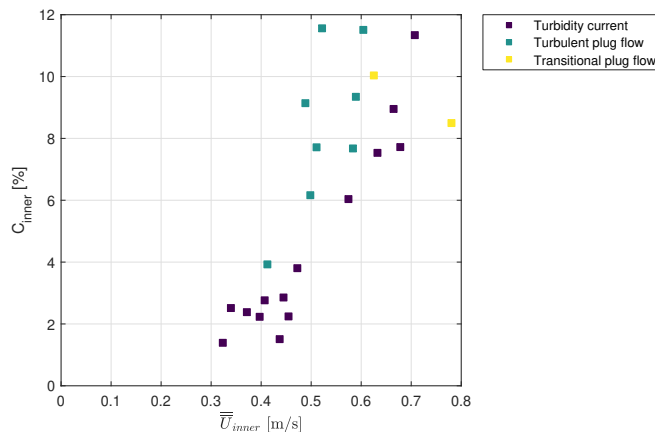

Figure 4.34: Phase space of transitional flow types identified for gravity currents as a function of depth-averaged velocity in the inner region, $\overline{\overline{U}}_{inner}$, and depth-averaged clay concentration in the inner region, C_{inner}.

OPEN-CHANNEL FLOW COMPARISON

The velocity structure below the velocity maximum mostly resembles that of open-channel flow (Altinakar et al., 1996; Kneller et al., 1999; Kneller, 2003; Dorrell et al., 2019). Hence, for the comparison of clay flow types between open-channel flows and gravity currents, the results of the inner region are used for the gravity currents. Figure 4.35 shows the depth-averaged results of the inner region from the experimental runs overlaid on the identified flow types for open-channel flows by Baas et al. (2009). A direct comparison would suggest that most experimental runs fit within the TETF regime and higher clay concentration runs fit in either LTPF, UTPF or QLPF. The plug flow regions of clay flow types in open-channel flows are defined by a low velocity gradient and low turbulence intensity (Wang and Plate, 1996; Baas and Best, 2002; Baas et al., 2009). The gravity currents in this experimental study do show a low velocity gradient, but the associated reduction in turbulence intensity is not identified (Section 4.4.1). However, differences between open-channel flows and gravity currents need to be taken into account in the comparison.

The shifting balance between turbulent and cohesive forces regulates the dynamic structure of cohesive flows. Maintaining the turbulence forces, turbulence attenuation occurs with increasing clay concentration (Baas and Best, 2002; Baas et al., 2009). Hence, a higher clay concentration in open-channel flow results in either turbulence enhancement or turbulence attenuation. However, the main driving mechanism for turbidity currents is the density contrast between sediment-laden and ambient fluid (Simpson, 1997; Mulder and Alexander, 2001; Leeder, 2011). Consequently, increasing the clay concentration within gravity currents results in enhancement of flow speed and associated turbulence. Therefore, a further increase in sediment concentrations is required to counterbalance the turbulent forces. As flow velocity increases, the shear between the gravity current and ambient fluid increases. The intensified mixing at the upper interface leads to more homogenous suspension of sediment and reduced concentrations due to enhanced entrainment of ambient water (Ellison and Turner, 1959; Altinakar et al., 1996; Kneller and Buckee, 2000; Eggenhuisen et al., 2020). These additional processes in gravity currents mean that 'simply' an increase in clay concentration does not have to result in turbulence attenuation as like in open-channel flows.

Figure 4.35 compares the inner region of gravity currents with open-channel flows, which are both influenced by bottom shear (Altinakar et al., 1996; Chaudhry, 2008; Wells and Dorrell, 2021). In open-channel flow, the development of a plug layer starts at the free surface where the shear is lowest (Baas and Best, 2002; Baas et al., 2009). Subaqueous gravity currents experience additional shear at the upper interface due to the ambient fluid and consequently, the shear at the upper boundary of gravity currents is higher than that of open-channel flows (Chaudhry, 2008; Leeder, 2011). The minimum shear at the velocity maximum can result in a reduction of mixing between the inner and outer region, allowing sediment to be trapped within the inner region near the bed (Buckee et al., 2001; Talling et al., 2007; Kane and Pontén, 2012). If the clay concentration is high enough, the viscous forces might prevent penetration of the additional turbulence and the turbulent mixing at the upper interface could be reduced with increasing viscosity (Marr et al., 2001; Mohrig and Marr, 2003; Baker et al., 2017). However, it is also a possibility that the additional turbulence generated at the upper interface penetrates into the flow, towards the bed (Islam and Imran, 2010; Eggenhuisen and McCaffrey, 2012; Krug et al., 2015). The flow thickness in the experimental runs is between 0.1 and 0.4 m (Table 4.6). The additional turbulence generated at the upper interface in these experiments has relatively more influence on the flow turbulence than within naturally thicker flows. In natural flows, potentially, turbulence attenuation might occur easier within the flow as turbulence might not penetrate from the upper interface over the full flow height. Although, full-scale turbidity currents are often more turbulent than experimental ones (Meiburg and Kneller, 2010; Talling et al., 2013), which might prevent turbulence attenua-

tion up to higher clay concentrations. The additional source of turbulence at the upper interface of gravity currents might shift the balance of transitional clay flows towards higher clay concentrations, i.e. higher clay concentrations are required to attenuate the turbulence within a gravity current compared with open-channel flows, for comparable flow thickness and flow depth.
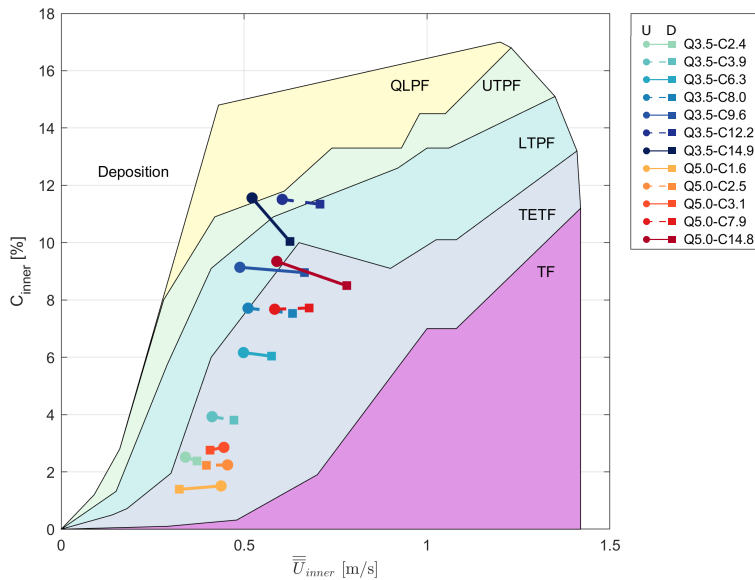

Figure 4.35: Depth-averaged results of the inner region of streamwise velocity ($\overline{\overline{U}}$) and volumetric clay concentration ($C_{f,inner}$) overlaid on results form Baas et al. (2009). Location in the flume is indicated with U=Upstream and D=Downstream.

4.4.2. FLOW EVOLUTION

A gravity current is naturally non-uniform and consistently evolves while moving downstream. The transformation in space depends on the boundary conditions, which determines the balance between sediment incorporation and dilution (Felix and Peakall, 2006; Talling et al., 2007; Kane and Pontén, 2012). No deposition of sediment occurred during the experiments and there was no initial sediment on the bed of the flume, hence the gravity current was unable to erode sediment. Therefore, the balance of sediment incorporation and dilution within the experiments depends on the velocity change between upstream and downstream and the entrainment of ambient water at the upper interface of the gravity current. Additionally, the formation of bonds between cohesive sediment particles is a time-dependent (thixotropic) process (Peterfi, 1927; Freundlich, 1935; Mitchell, 1960; Ren et al., 2021). The evolvement of a cohesive gravity current is influenced by the balance of entrainment and the existence or formation of clay bonds as the gravity current evolves. Based on the experimental results, three different trends can be identified (Table 4.10; Figure 4.36). For low clay concentrated gravity currents ($C \leq 3.1$), the gravity current remains within the turbidity current regime, both upstream and downstream (Flow evolution type III). A turbulent plug flow can be identified at the upstream location for higher clay concentration within the experimental runs ($C \geq 3.9$). Depending on the clay concentration, these gravity currents evolve towards a turbidity current downstream (Flow evolution type I, $3.9 \leq C \leq 12.2$) or a transitional plug flow (Flow evolution type II, $C \geq 14.8$).

Table 4.10: Identified flow evolution types of the experimental runs

| Experimental run	Flow evolution type	Flow evolution
	Low discharge	
Q3.5-C2.4	III	remain Turbidity current
Q3.5-C3.9	I	Turbulent plug flow to Turbidity current
Q3.5-C6.3	I	Turbulent plug flow to Turbidity current
Q3.5-C8.0	I	Turbulent plug flow to Turbidity current
Q3.5-C9.6	I	Turbulent plug flow to Turbidity current
Q3.5-C12.2	I	Turbulent plug flow to Turbidity current
Q3.5-C14.9	II	Turbulent plug flow to Transitional plug flow
	High discharge	
Q5.0-C1.6	III	remain Turbidity current
Q5.0-C2.5	III	remain Turbidity current
Q5.0-C3.1	III	remain Turbidity current
Q5.0-C7.9	I	Turbulent plug flow to Turbidity current
Q5.0-C14.8	II	Turbulent plug flow to Transitional plug flow
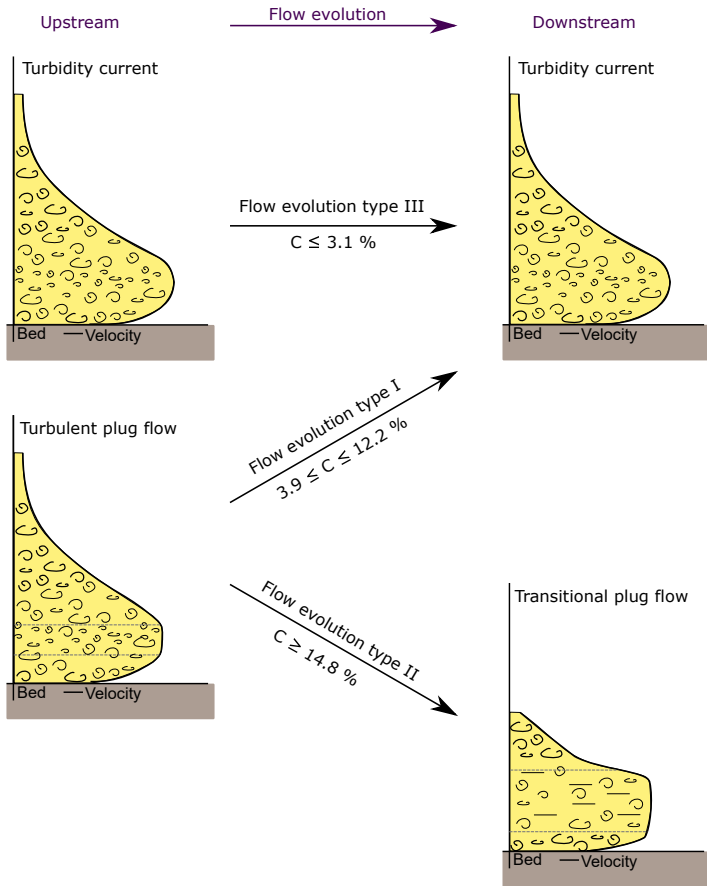
Figure 4.36: Schematics of flow evolution between the upstream and downstream measurement locations, where the evolution depends on the initial clay concentration.

FLOW EVOLUTION TYPE I: TURBULENT PLUG FLOW TO TURBIDITY CURRENT

The supercritical gravity currents are dominated by entrainment (Parker et al., 1987; Wells and Dorrell, 2021, Table 4.7). Entrainment of ambient water dilutes the gravity current as it evolves downstream, resulting in lower clay concentrations in the outer region at the downstream location (Ellison and Turner, 1959; Morgenstern, 1967; Allen, 1971; Hallworth et al., 1996; Marr et al., 2001, Figure 4.12), but the inner region at the downstream location maintained the clay concentration (Figure 4.11, Table 4.8). Interface instability can be related to the Richardson number, which expresses the size of velocity gradient across the boundary relative to the density gradient across the boundary (Kneller et al., 1999; Leeder and Perez-Arlucea, 2006). A critical Richardson number (Ri<0.25) suggests that density stratification in these flows (Table 4.7) is insufficiently stable to suppress vertical mixing (Kneller and Buckee, 2000; Buckee et al., 2001; Waltham, 2004). The dilution of the gravity current at the upper interface results in flow thickening (Ellison and Turner, 1959; Waltham, 2004, Wells and Dorrell, 2021; Table 4.6). The combination of an increase in flow height and a reduction of clay concentration in the outer region of the flow results downstream in a decreased depth-averaged clay concentration (Table 4.7). The bed slope allows the gravity currents to accelerate downstream (Figure 4.16) and the relative height of the velocity maximum (z_{max}/h_0) decreases downstream for the higher concentration runs (>=C6.3). The reduction in height of the velocity maximum correlates with increasingly higher shear at the ambient interface than at the bed (Middleton, 1966b; Talling et al., 2007; Islam and Imran, 2010; Wells and Dorrell, 2021). A plug flow was identified at the upstream location for the majority of experimental runs of flow evolution type I. This plug flow is not identified at the downstream location (Figure 4.22). The plug flow within the velocity profile at the upstream location indicates initial signs of turbulence attenuation, but the $RMS(u')$ values and fast Fourier transform suggest mostly turbulent flows. Consequently, the flows at the upstream location have been identified as turbulent plug flow (Figure 4.34, Table 4.9). In the inner region, $RMS(u')$ values are comparable between the upstream and downstream locations or slightly higher at the downstream location (Figure 4.17). The increase in $RMS(u')$ values in combination with no plug flow in the velocity profile at the downstream location suggest fully turbulent flows, classified as turbidity current (Figure 4.34, Table 4.9). The evolvement of the gravity current is dominated by entrainment at the upper interface and acceleration downslope. Combining all effects of entrainment of ambient water, acceleration, plug flow development, flow evolution type I flows move towards a more turbulent turbidity current downstream, i.e. the flow develops from turbulent plug flow to turbidity current (Figure 4.36).

FLOW EVOLUTION TYPE II: TURBULENT PLUG FLOW TO TRANSITIONAL PLUG FLOW

Flow evolution type II flows also experience entrainment of ambient water, which dilutes the flow and results in flow thickening. This results mostly in a reduction in clay concentration in the outer region (Ellison and Turner, 1959; Wells and Dorrell, 2021, Figures 4.11, 4.12). The bed slope within the experiments allows the gravity currents to accelerate downstream (Figure 4.16) and the relative height of the velocity maximum (z_{max}/h_0) decreases downstream, as the supercritical flows are dominated by entrainment and shear with the ambient fluid in the outer region (Parker et al., 1987; Islam and Imran, 2010; Wells and Dorrell, 2021). Experimental run Q3.5-C14.9 contains a plug flow at both the upstream and downstream locations, where the plug grows in height mostly towards the bed at the downstream location (Figure 4.16a,c). Experimental run Q5.0-C14.8 only contains a plug flow at the downstream and not at the upstream location (Figure 4.22). Similar to experimental run Q3.5-C14.9, the constant streamwise velocity profile over the flow depth of experimental run Q5.0-C14.8, i.e. the plug flow develops from the velocity maximum towards the bed as the flow moves from upstream to downstream (Figure 4.16b,d). In the inner region, turbulence intensity values ($RMS(u')_0$) of flow evolution type II are lower at the downstream location than at the

upstream location (Figure 4.18), especially over the development height of the plug flow. This is also noticeable in the fast Fourier transform where the turbulence attenuation of high-frequency velocity fluctuations downstream is more distinct than at the upstream location (Figure 4.32). In addition to the balance of velocity change and entrainment between the upstream and downstream locations, which affects the evolvement of the gravity current downstream, the evolvement is also influenced by the formation and breakage of clay bonds. The formation of bonds between cohesive sediment particles is a time-dependent (thixotropic) process (Peterfi, 1927; Freundlich, 1935; Mitchell, 1960; Ren et al., 2021, Section 1.2.3) and, therefore, at the downstream location, the clay particles had more time to form cohesive bonds than at the upstream location. Consequently, the viscous forces within the clay suspensions are able to start suppressing the turbulence at the downstream location (Harker and Temple, 1988; Pope, 2000; Baas et al., 2009). Combining the effects of evolvement downstream and the development of clay bonds, flow evolution type II flows move towards a less turbulent debris flow downstream, i.e. the flow develops from turbulent plug flow to transitional plug flow (Figure 4.36). Within these higher concentration gravity currents, it seems that the development of clay bonds within the flow is stronger than the entrainment and mixing of ambient water, which results in initial signs of turbulence attenuation. In both flow evolution types I and II, the same clay type is used and consequently this is an effect of increased clay concentrations, which enhances the inter-particle collision between clay particles allowing formation of clay bonds (Lick et al., 1993; McAnally and Mehta, 2000; McCave and Hall, 2006; Cuthbertson et al., 2010; Goh et al., 2011; Son and Hsu, 2011). Opposite to flow evolution type I where the entrainment and mixing of ambient water prevent the formation of clay bonds, resulting in the development of a more turbulent turbidity current at the downstream location (Figure 4.36).

FLOW EVOLUTION TYPE III: TURBIDITY CURRENT

Entrainment of ambient water dilutes the gravity current as it evolves downstream, resulting in flow thickening (Ellison and Turner, 1959; Wells and Dorrell, 2021, Table 4.6). The clay concentration of these gravity currents gradually increases towards the bed and does not contain a lutocline or large increase in clay concentration in the bottom half of the gravity current. Clay is spread over a larger height as the flow thickens downstream with a small reduction in clay concentration over the full flow depth compared with upstream (Figures 4.11, 4.12). Entrainment and mixing at the upper interface are reduced by increased density stratification (Parker et al., 1987; Marr et al., 2001; Winterwerp and Van Kesteren, 2004; Cenedese and Adduce, 2010; Krug et al., 2015). The density stratification within flow evolution type III flows is small and as a result, the entrainment rates are high, which is also noticeable by the increased vertical velocity in the outer region (Section 4.15). In contrast with flow evolution types I and II, which both accelerate downstream, flow evolution type III flows decelerate (Figure 4.16). The relative height of the velocity maximum (z_{max}/h_0) decreases downstream, as the supercritical flows are dominated by entrainment and shear with the ambient fluid in the outer region (Parker et al., 1987; Islam and Imran, 2010; Wells and Dorrell, 2021). Turbulence intensity values ($RMS(u')_0$) decrease downstream for flow evolution type III, except close to the bed where the turbulence intensity increases. The turbulence intensity values of the flow evolution type III flows are higher at the upstream location than other flow evolution types, which could suggest turbulence-enhanced flows at the upstream location. The flow type is classified as turbidity current upstream (Figure 4.34, Table 4.9), because it fits the characteristics of this flow type. Ideally, for the identification of turbulence-enhanced transitional flow (TETF), a reference levels, such as clear water or a lower clay concentration, is used. However, since a gravity current moves due to the density difference between the suspended sediment and ambient water there is a minimum required concentration. The time series of these flows show no obvious changes in frequency distribution and the sub-second-scale velocity fluctuations superimposed on rising and falling limbs of second-scale fluctuations identified by Baas et al. (2009) in TETF

flows are not identified here. At the downstream location, the gravity current contains similar velocity profiles and turbulence intensity values as flow evolution type I, which suggests turbulent flow at the downstream location. Combining all the effects of flow evolvement, flow evolution type III flows maintains a turbulent turbidity current downstream, i.e. the flow remains within the turbidity current regime.

The flow evolution types indicate that the flow evolvement downstream is a complex interplay of cohesive and turbulent forces. Although, both the low and high clay concentration runs accelerate downstream, the low concentration runs move towards a more turbulent turbidity current (flow evolution type I) and the high concentration runs move towards a less turbulent debris flow (flow evolution type II). At the downstream location, clay particles had more time to form cohesive bonds than at the upstream location. If the formation of clay bonds occurs at the downstream location is determined by the relative influence of cohesive and turbulent forces. Below a threshold concentration, entrainment and mixing at the upper interface dominate the evolvement. The dilution and flow thickening results in stronger turbulent forces, which prevent the formation of clay bonds (Dyer, 1988; McAnally and Mehta, 2000; Winterwerp, 2002; Partheniades, 2009; Cuthbertson et al., 2010). In this scenario, the turbulent forces are dominant over the cohesive forces and flows remain in or evolve to the regime of a turbidity current. Shear with the ambient fluid increases as the flow accelerates, leading to further intensified mixing at the upper interface and a more homogenous suspension of sediment and reduced concentration due to enhanced entrainment of ambient water (Ellison and Turner, 1959; Altinakar et al., 1996; Kneller and Buckee, 2000; Eggenhuisen et al., 2020). The reduction in density stratification then further enhances the entrainment rate (Parker et al., 1987; Marr et al., 2001; Winterwerp and Van Kesteren, 2004; Cenedese and Adduce, 2010; Krug et al., 2015). As the flow would develop further downstream, the turbulent forces remain dominant and the gravity current remains within the turbidity current regime.

Above a threshold concentration, the formation of clay bonds in the inner region can dominate the flow evolution. The higher clay concentration intensifies the inter-collision between clay particles allowing the formation of clay bonds and enhancing the viscosity in the flow (Wan, 1982; Mehta and McAnally, 2008; Laxton and Berg, 2006; Au and Leong, 2013). The stronger cohesive forces consequently outbalance the turbulent forces and turbulence attenuation can start to develop in the plug flow. As the flow would develop further downstream, it can develop in two directions. Either the acceleration with an associated increase in turbulent mixing and entrainment of ambient water can start to penetrate into the inner region, allowing the turbulence to increase and breakage of clay bonds over time. In this scenario, the gravity current would develop towards a turbulent plug flow or turbidity current. A different option is that the formation of clay bonds enhances the viscosity significantly, which can reduce the mixing at the upper interface (Parker et al., 1987; Marr et al., 2001; Mohrig and Marr, 2003; Winterwerp and Van Kesteren, 2004; Cenedese and Adduce, 2010; Krug et al., 2015; Baker et al., 2017). The reduction in turbulent mixing would prevent entrainment of ambient water and allow the cohesive forces to be maintained and the gravity current either remains in the transitional plug flow regime or could potentially develop further towards a debris flow (Waltham, 2004; Felix and Peakall, 2006). Interface instability is expected with a low Richardson number (Ri<0.25) and above a critical value, density stratification is sufficiently stable to dissipate energy generated through shear and to suppress vertical mixing (Kneller and Buckee, 2000; Buckee et al., 2001; Waltham, 2004; Wells and Dorrell, 2021). A higher initial sediment concentration, might results in stronger density stratification that could reduce the mixing in the flow, allowing for stronger turbulence attenuation due to the viscous forces and further development towards a debris flow. These scenarios assess flow acceleration as occurred within the experimental results, whereas deceleration could lead to a reduction in turbulence intensity due to a reduced velocity and reduced mixing at the upper interface. Consequently, flow deceleration and / or detrainment of water could allow the development of a transitional plug flow

or further progressed turbulence attenuation (Meiburg and Kneller, 2010). However, if the flow develops towards a debris flow or if sediment starts to settle depends on the boundary conditions (Lowe, 1982; Sumner et al., 2009; Baas et al., 2011). However, settling of sediment out of a gravity current might dilute the flow, but it might also result in a denser inner layer where sediment is trapped (Felix and Peakall, 2006; Postma et al., 1988 Sylvester and Lowe, 2004; Talling et al., 2007; Kane and Pontén, 2012). Additional work is needed to research this interplay of velocity and sediment concentration variations on the turbulence dynamics of gravity currents.

OPEN-CHANNEL FLOW COMPARISON

The shifting balance between turbulent and cohesive forces regulates the dynamic structure of cohesive flows (Baas et al., 2009; Baker et al., 2017; Craig et al., 2020). In open-channel flows, this correlates to the clay concentration in the flow and the depth-averaged velocity (Section 1.3). Deceleration of open-channel flows results in a decrease in turbulent forces and consequently, the flow shifts towards the left in the phase diagram (Figure 4.35). Depending on the relative decrease in velocity, the flow either maintains the clay flow type or moves towards a less turbulent one (Chapter 3). On the other hand, acceleration of open-channel flows results in an increase in turbulent forces and consequently the flow shifts towards the right in the phase diagram (Figure 4.35). Depending on the relative increase in velocity, the flow either maintains the clay flow type or moves towards a more turbulent one (Chapter 3). The continuous evolvement of gravity currents, influenced by the balance between turbulent and cohesive forces in the flow, regulates the turbulence dynamics of gravity currents. Depending on the balance between the generation of additional turbulence at the upper interface and the formation of clay bonds within the flow, an accelerating gravity current can either shift towards a more turbulent turbidity current or a less turbulent transitional plug flow. This means that the flow type within a gravity current is influenced by the history of the flow and consequently it is not possible to generate a phase diagram with fixed boundaries like for open-channel flows. The sediment concentration and the slope determined the acceleration of the gravity currents within these experiments. Additional experiments with different slopes would give more insight into the rate of acceleration or deceleration on the evolvement of the gravity current. If the slope is steeper, the flow accelerates faster and the entrainment of ambient water increases according to Equation 4.18 (Ellison and Turner, 1959; Parker et al., 1987; Altinakar et al., 1996; Kneller and Buckee, 2000), which enhances the increase in turbulence within the flow. A flatter slope, might reduce the friction at the upper interface with the ambient fluid and allow for more dominant cohesive forces and the formation of clay bonds (Dyer, 1988; Mietta et al., 2009; Baas et al., 2009; Safak et al., 2013). A longer flume would give more insight into the further development of these gravity currents (Section 4.4.1) and if further development allows for a phase diagram with more defined boundaries. Potentially, a phase diagram can be identified for the two end members of the spectrum, turbidity current and debris flow, but not for the transitional flow conditions as the gravity current continues to evolve.

4.4.3. WIDER IMPLICATIONS

This study demonstrates that turbulent-laminar transitions in gravity currents are more complex than in open-channel flows. In addition to the balance between turbulent and cohesive forces that determine clay flow types in open-channel flows (Wang and Plate, 1996; Baas and Best, 2002; Baas et al., 2009), evolvement of gravity currents is also influenced by the balance between generation of additional turbulence at the upper interface (Kneller and Buckee, 2000; Marr et al., 2001; Mohrig and Marr, 2003; Eggenhuisen et al., 2020; Wells and Dorrell, 2021) and the thixotropic process of the formation of clay bonds (Peterfi, 1927; Mitchell, 1960; Ren et al., 2021). This study demonstrates that for mud-rich flows the history of the flow (e.g. decelerating or accelerating) influences the flow dynamics, due to the time required to form and break down cohesive bonds between

particles, whose presence affects the flow dynamics. The supercritical flows in these experiments are dominated by entrainment at the upper interface and consequently, the maintained clay concentration and turbulence in the inner region allowed the formation of clay bonds, depending on the height of the clay concentration, correlated to the inter-particle collision rate (Lick et al., 1993; McAnally and Mehta, 2000; McCave and Hall, 2006; Cuthbertson et al., 2010; Goh et al., 2011; Son and Hsu, 2011).

Previous research has shown that transitional flow properties influence bedform type (Baas et al., 2011; Baas et al., 2016b; Schindler et al., 2015), depositional structures (Sumner et al., 2009; Haughton et al., 2009; Hermidas et al., 2018) and sole marks commonly observed in sedimentary structures (Peakall et al., 2020; Baas et al., 2021). Depositional features under transitional open-channel flow or transitional gravity currents might differ due to the different turbulence dynamics. Depositional features are strongly influenced by near-bed turbulence, which can result in stronger development in height or migration of bedforms in clay flow types with enhanced near-bed turbulence and no bedform development in strongly turbulence attenuated flows (Baas and Best, 2008; Baas et al., 2011; Baas et al., 2016b). The increase in near-bed turbulence found in TF to TETF and LTPF flows is not identified in the transitional flow conditions in this research on gravity currents, which might be reflected in the deposits under gravity currents by a reduction in variation in heights of bedforms. The depositional features under gravity currents are expected to vary gradually over a distance due to the continuous evolvement and adaptation to cohesive forces.

Moreover, due to the additional friction at the upper interface of gravity currents, higher clay concentrations are needed in gravity currents to attenuate the turbulence than in open-channel flows, for comparable flow thickness and flow depth. Consequently, the separation in deposits of mud, sand or mixed mud-sand under gravity currents might occur at higher concentrations than experimental research of open-channel flows suggest (Sumner et al., 2009; Baas et al., 2011; Baas et al., 2016b).

4.5. CONCLUSION

This research investigated the influence of suspended cohesive clay on changing flow dynamics within non-uniform gravity currents, using constant-flux flows in a submerged flume. Within the experimental flows, three different flow types were identified: a) turbidity current, fully turbulent flow; b) turbulent plug flow, where the velocity profile contains a plug flow, but turbulence intensity remains high; c) transitional plug flow, where the velocity profile contains a plug flow and fast Fourier transform shows attenuation of higher frequencies within the time series. Similar to the clay flow type in open-channel flows, the balance between turbulent and cohesive forces influences the flow type, but due to the additional source of turbulence at the upper interface, higher clay concentrations are needed to result in turbulence enhancement or attenuation than in open-channel flows. In addition to this balance between turbulent and cohesive forces, the evolution of a gravity current influences the clay flow type. The balance between entrainment plus additional mixing at the upper interface and the existence or formation of clay bonds determines the evolution. If the entrainment of ambient water is faster than the formation of clay bonds, the gravity current evolves towards a more turbulent flow condition. If the formation of clay bonds is faster than the entrainment, the gravity current evolves towards a less turbulent flow condition. Maintaining other boundary conditions, the deviation in development is influenced by a threshold clay concentration. Therefore, in addition to shifting balance between turbulent and cohesive forces, the history and evolvement of a flow influences the formation of a clay flow type within a gravity current.

5

CONCLUSION

The main objective of this thesis has been to better understand turbulence modulation in non-uniform and unsteady clay suspension flows. Cohesive sediment particles are subjected to a set of attractive and repulsive forces as a result of the mineralogical properties of the sediment and the adsorption of ions on the particle surfaces (Coussot, 1997; Partheniades, 2009; Shaikh et al., 2017). Agglomerations, known as flocs, form when the attractive forces exceed the repulsive forces, which continues as the flocs grow in size until the number of particles is reduced up to a negligible probability of particles collision (van Olphen, 1977; Hogg, 2000; Mehta, 2013). As clay concentration increases, flocs grow in size up to the "gelling" point, which is characterised by a pervasive, volume-filling network of particle bonds (van Olphen, 1977; Winterwerp and Van Kesteren, 2004; Genovese, 2012). Turbulent energy within the gel is dissipated by the high effective viscosity, and the flow becomes laminar. Conversely, de-flocculation, i.e. breakage of bonds between clay particles in flocs and gels, can occur if the turbulence within the flow is sufficiently strong. Thus, an increase in turbulence generation in the flows by, for example, an increasing flow velocity has the potential to break up bonds between the clay particles and reduce the flow viscosity Partheniades, 2009. The cohesive forces within a flow are influenced by the suspended clay concentration and rheology. This interplay between turbulent and cohesive forces regulates the flow dynamics of clay suspension flows (Wang and Plate, 1996; Baas and Best, 2002; Baas et al., 2009).

Previous research has been conducted on this interplay of forces within uniform open-channel flows developing a phase diagram based on flow velocity and clay concentration (Baas and Best, 2002; Baas et al., 2009, Section 1.3). The transitional flow properties of open-channel flows, have been linked to bedform types (Baas et al., 2011; Baas et al., 2016a), sedimentary sequences (Sumner et al., 2009; Baker and Baas, 2020) and sedimentary sole structures (Peakall et al., 2020; Baas et al., 2021). Experimental research on decelerating flows has identified different deposit types, either separated deposits of mud and sand or mixed mud-sand, which can be correlated to different transitional flow properties (Sumner et al., 2009; Hermidas et al., 2018). The mixed mud-sand deposits can be graded into different regimes depending on relative clay content or laminae within the deposit (Amy et al., 2006; Haughton et al., 2009). In addition to clay flow types, the yield strength is used within previous research to examine flow properties of high clay concentration flows, such as debris flows (Middleton and Hampton, 1973; Lowe, 1979; Talling et al., 2012; Manica, 2012; Talling et al., 2013). Clay concentration or yield strength is sometimes used within the classification of gravity currents (Middleton, 1993; Pickering and Hiscott, 2015), whereas the exact composition and size of the sediment in combination with the flow shear velocity determine the flow properties (Baas et al., 2009). Lock-exchange experiments provided insight into hydrodynamic, de-

positional and rheological processes, including run-out distance, of subaqueous clay-laden gravity currents (Felix and Peakall, 2006; Manica, 2012; Baker et al., 2017). However, constant-volume experiments, such as lock-exchange, provide limited insight into the body of a gravity current, the bulk of the flow (Peakall et al., 2001; Parsons et al., 2007; Talling et al., 2015; Hage et al., 2019). Furthermore, visual observations are frequently used (Kneller and Buckee, 2000; Mohrig and Marr, 2003; Nogueira et al., 2013; Baker et al., 2017), whereas turbulence measurements would provide more insight into the flow dynamics of transitional flow properties. Consequently, the flow structure of subaqueous clay-laden gravity currents remains poorly understood.

The phase diagram based on flow velocity and clay concentration (Figure 1.11), which provides insight into transitional flow properties of clay-laden flow is based on steady, uniform open-channel flow, i.e flows that do not change in time nor in space. The phase diagram suggests that there are regions within the clay concentrations versus velocity space where transitions within flow types occur. Non-uniform and unsteady flows would cross those regions and the turbulent-laminar transitions within these clay flow types remain unknown. Despite flows naturally being non-uniform and/or unsteady, there is limited understanding of how clay suspension flows adapt to these changes in velocity, whereas it has significant influence on the sediment transport patterns within a flow and the sedimentary deposits (Baas et al., 2011; Dorrell and Hogg, 2012; Moody et al., 2013). Especially due to the thixotropic process of clay flows and the potential hysteresis in the formation and breakage of clay bonds (Peterfi, 1927; Freundlich, 1935; Mitchell, 1960; Ren et al., 2021). This research investigates the influence of suspended cohesive sediment on non-uniform (Chapter 2) and unsteady (Chapter 3) open-channel flows. Moreover, to date, the phase diagram for uniform clay suspension open-channel flows is used to understand turbulent-laminar transitions in gravity currents (Talling et al., 2012; Hermidas et al., 2018; Baker and Baas, 2020). However, clear differences between open-channel flows and gravity currents can be identified, which are expected to influence the interplay between cohesive and turbulent forces within the flow. The research in this thesis is extended to experimental constant-flux gravity currents to investigate the difference in the influence of suspended clay on open-channel flows and gravity currents (Chapter 4).

This concluding chapter discusses the difference between non-uniform and unsteady clay suspension flows, after which a comparison is made between open-channel flows and gravity currents. The limitations of the research and experimental setups are discussed, with suggestions for future research. The discussion introduces a broader perspective of different aspects influencing turbulence modulation in non-uniform and unsteady clay suspension flows.

5.1. NON-UNIFORM VERSUS UNSTEADY OPEN-CHANNEL FLOW

Experiments presented in Chapter 2 looked at the transitions between clay flow types induced by a change in channel geometry, i.e. spatial varying flow. Experiments presented in Chapter 3 looked at the adaptation of clay flow types to changes in flow velocity, i.e. temporal varying flow. In both experimental sets, the flows were accelerated and decelerated by imposing a change in conditions. Figure 5.1 combines the identified adaptation times of both sets of experiments after the velocity change.

The inset in the flume in Chapter 2 forced the flow through a narrow to wide transition (decelerating flows) or through a wide to narrow transition (accelerating flows) depending on the flow direction (Figure 2.3b). The depth-averaged velocity follows the changes in width of the flume and will vary with a factor of 2.5 between the narrow section (0.2 m) and wide section (0.5 m), with minor adjustments for variations in flow depth. The results showed a difference in adaptation between decelerating and accelerating flows due to the fact that establishing cohesive clay bonds between clay particles, as in decelerating flows, requires more time than breaking up these bonds, as in the accelerating flows.

The controlled velocity changes of 0.1 m/s in Chapter 3 results in relatively minor variations between clay flow type within an experimental run; i.e. the clay flow type either stays the same before and after the imposed velocity change or the flow passes through one additional adjacent clay flow type. The accelerating flows indicate a continuous increase in adaptation time with stronger turbulence attenuated flows, as the breaking up clay bonds within a stronger plug flow requires more time. The adaptation time of decelerating flows depends on the clay flow type. Initial development of a plug flow within LTPF requires less time than the development of a thick rigid plug found in QLPF, as the inter-particle collisions are reduced with stronger turbulence attenuation.

The velocity changes within the tapering experiments with non-uniform flow (Chapter 2) are larger (Table 2.1, Figure 2.5) and consequently, the flow passes through a larger variety of clay flow types than the unsteady flows in Chapter 3 (Tables 3.9, 3.10, Figure 3.10). When a flow passes through several flow types, especially if it includes both turbulent and attenuated flow types, the development of turbulence attenuated flow types requires more time. This could be associated with the formation of clay bonds that influences the adaptation time for decelerating flows. Non-uniform flow conditions showed that accelerating flows are able to adapt faster than decelerating flows, which is potentially correlated to the breakage of clay bonds requiring less time than the formation. On the contrary, the adaptation time of the depth-averaged velocity in the unsteady flows (Chapter 3) is comparable for accelerating and decelerating flow, suggesting no hysteresis effect between the breakage and formation of clay bonds. The controlled velocity changes in Chapter 3 result in the clay flow type either staying the same before and after the imposed velocity change or the flow passing through one additional adjacent clay flow type, whereas the flow passes through several clay flow types in Chapter 2. When there are minor variations between flow types (Chapter 3), the flow is able to adjust faster as a reduced amount of clay bonds need to establish themselves or break and the adaptation of decelerating and accelerating flows is more comparable without hysteresis.

Within the spatial resolution of the experiments, the adaptation length of the non-uniform accelerating flows was close to zero within the narrow section, i.e. after the narrowing section where the flow continuously adapted associated with the gradual velocity change. The formation of clay flow type adapted without significant delay (Chapter 2). On the contrary, the unsteady accelerating flows (Chapter 3) indicate an increase in adaptation with stronger turbulence attenuated flows. The experiments with unsteady flows contain a larger range of clay concentrations and velocities than the experiments with non-uniform flows and consequently a larger range of clay flow types and stronger turbulence attenuation. In order to break clay bonds within a plug flow, turbulence needs to penetrate the pervasive, volume-filling network of particle bonds, which is increasingly difficult with stronger turbulence attenuated flows. Due to lower clay concentrations in the non-uniform flow experiments, the turbulence attenuation was weaker and it was easier to break up the clay bonds within the flow resulting in adaptation without significant delay. However, the higher clay concentration in the unsteady flow experiments showed stronger turbulence attenuation, making it harder to break the clay bonds and consequently extending the adaptation time.

For a better comparison between the experiments and an increased understanding of the influence of varying velocity on flow adaptation, additional experiments are proposed. Experiments with temporal varying flow conditions passing through a larger variety of clay flow types should provide a more detailed understanding of the formation of different clay flow types. If the flow passes through several clay flow types, does the flow still adapt instantly after a temporal velocity change or is it possible to identify the different flow types the flow passes through and would this enhance the adaptation time? Would passing through several clay flow types, indicate a hysteresis in adaptation of decelerating and accelerating flows? The non-instantaneous response of clay-laden flows has significant influence on sediment transport rates within an environment. However, the range of non-uniformity and unsteadiness in clay-laden flows is countless and consequently

5

expanding knowledge on turbulent-laminar transitions would allow a stronger link between experimental results and scenario's in natural environments.

The experimental research allows comparison between adaptation of non-uniform and unsteady clay suspension flows. In the non-uniform flow experiments (Chapter 2), the adaptation time is determined based on the difference between clay flows and clear water flows. This relative adaptation time captures the influence of clay concentration on non-uniform flows, excluding the adaptation to the change in velocity. In the unsteady flow experiments (Chapter 3), the adaptation time is determined by reaching a quasi-steady turbulence intensity within the clay flow after the imposed velocity change, which correlates with a constant depth-averaged velocity. The poor quality turbulence measurements in the clear water flows of the unsteady flow experiments do not allow for determining a relative adaptation time. Hence, a comparison is done with the absolute adaptation time, with some assumptions for the tapering experiments. Assuming the start of adaptation at the start of the velocity change, i.e. at the start of the tapering section, the absolute adaptation time for the accelerating flows is throughout the tapering section (P7 to P3; 2.4 m; Table 5.1). The decelerating flows developed throughout the wide section and therefore, here the absolute adaptation time for the decelerating flows is throughout the tapering and wide section (P3 to P9; 3.9 m; Table 5.1). For decelerating flows, the turbulence intensities at the end of the wide section, at P9 (Figure 2.3b), remained non-uniform in Chapter 2, suggesting that the length of the flume was insufficient to establish equilibrium after the widening section. Consequently, the full adaptation time of these flows might be longer than suggested in Figure 5.1. Overall, comparison of the absolute adaptation time, suggests that a flow adapts faster to spatial varying flow than temporal varying flow (Figure 5.1). The inset in the flume forced the flow velocity to change gradually, whereas a sudden velocity change is imposed in Chapter 3. The gradual change in velocity allowed the flow to adjust continuously reducing the overall adaptation time. Clay bonds can already be broken or formed while the velocity is gradually changing within the tapering section. These experiments encountered for one ratio of change in width and additional experiments conducted with a variety of ratios provides more insight in the influence of the rate of change in velocity on the formation of clay flow types. Ideally conducted in a longer flume, where the full adaptation time can be measured after the tapering section.

Table 5.1: Absolute adaptation time, T, and length, L, scales

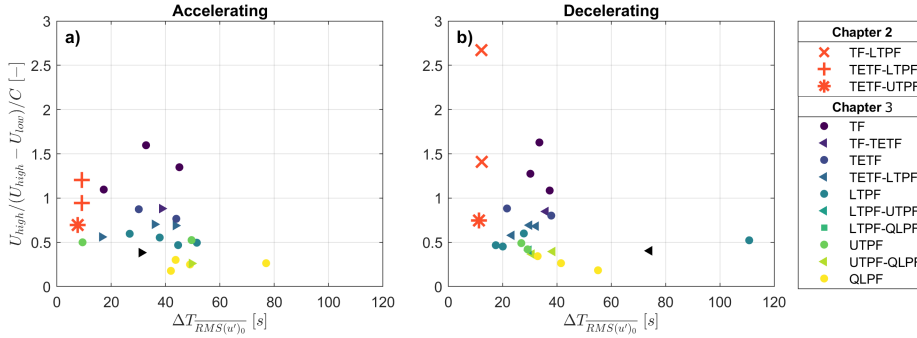| Experimental run	Points	Flow regimes	L [m]	T [s]
Decelerating flow				
D3-C0.9	P3 to P9	TF to LTPF	≥3.9	≥12.2
D5-C2.7	P3 to P9	TETF to UTPF	≥3.9	≥11.3
Accelerating flow				
A2-C1.4	P7 to P3	LTPF to TETF	2.4	9.2
A4-C2.8	P7 to P3	UTPF to TETF	2.4	7.7

Figure 5.1: Correlation between velocity normalised by the velocity change and clay concentration, $U_{high}/(U_{high} - U_{low})/C$ and the adaptation time of depth-averaged turbulence intensity, $\Delta T_{\overline{RMS(u')_0}}$, for the experimental runs of Chapter 2 and Chapter 3 for a) accelerating flow conditions and b) decelerating flow conditions. The results of Chapter 2 are indicated with different symbols correlating to the clay flow types the flow evolves through within the flume. For the results of Chapter 3, the colour indicates the clay flow type. A circle denotes the same clay flow type before and after the imposed velocity change and a triangle denotes a transition between clay flow types as the flow accelerates or decelerates.

5.2. OPEN-CHANNEL FLOW VERSUS GRAVITY CURRENTS

The experiments conducted at the Total Environment Simulator at the University of Hull included gravity currents, using constant-flux flows in a submerged flume (Chapter 4). Various experimental runs were conducted with varying initial clay concentration and inlet discharge. The gravity current evolved as it moved downstream and at two locations, upstream and downstream, velocity measurements and sediment samples were collected to assess the flow dynamics. Three different clay flow types have been identified based on the velocity and turbulence dynamics.

5.2.1. CLAY FLOW TYPES

Open-channel flows are influenced by bottom shear (Tennekes and Lumley, 1972; Chaudhry, 2008; Massey and Ward-Smith, 2012) and gravity currents are influenced by both bottom shear and friction at the upper interface as the flow moves under an ambient fluid (Altinakar et al., 1996; Kneller and Buckee, 2000; Leeder, 2011). In order to make a more proportionate comparison, Figure 5.2 compares the minimum turbulence intensity of open-channel flow results of Chapter 3 and gravity currents of Chapter 4 for the different identified flow types in open-channel flows and gravity currents. The results of the open-channel flows (Chapter 3) include the depth-averaged clay concentration against the minimum turbulence intensity found over the flow depth. The results of the gravity currents (Chapter 4) include the depth-averaged clay concentration of the inner region, which is most comparable with open-channel flows (Altinakar et al., 1996; Kneller et al., 1999; Kneller, 2003; Dorrell et al., 2019) against the turbulence intensity at the velocity maximum, which is typically the height at which the minimum turbulence intensity is found (Kneller et al., 1999; Best et al., 2001; Buckee et al., 2001; Choux et al., 2005; Gray et al., 2006; Cartigny et al., 2013; Eggenhuisen et al., 2020). The open-channel flows indicate stronger turbulence attenuated flow conditions with increasing clay concentration and the stronger turbulence attenuated clay flow types coincide with lower turbulence intensity values. The increasing clay concentration allows the formation of networks of flocs in the flow, i.e. clay gels, which enhances the viscosity and yield stress (Wan, 1982; Adamis et al., 2005; Yu et al., 2013). Enhancing the viscosity results in progressively attenuation of turbulence in the flow (Au and Leong, 2013; Lin et al., 2016; Baker et al., 2017). In the region where cohesive forces outbalance the turbulent forces, a plug flow develops, which is characterised by a low velocity gradient and low turbulence intensity (Wang and Plate, 1996; Baas and Best, 2002; Baas et al., 2009).

The results of the gravity currents show a larger variation in turbulence intensity with increasing clay concentration. Out of the three flow types identified, transitional plug flow is defined as the transitional clay flow type in gravity currents with the strongest signs of turbulence attenuation (Section 4.4.1). Figure 5.2 shows that the transitional plug flows contain relatively high turbulence intensity values. At the lower clay concentrations ($C_{inner} < 3.5\%$) only turbidity currents are identified. Otherwise, the turbulence intensities of turbidity currents and turbulent plug flows show no obvious trend based on the correlation of clay concentration in the inner region and minimum turbulence intensity within the flow. This confirms the finding that $RMS(u')_0$ might not be the most suitable parameter to assess the turbulence dynamics within the gravity currents. The body of gravity currents is approximately steady, but gravity currents are naturally non-uniform. Therefore, the flow is constantly evolving and consequently there is continuous clay particle aggregation and aggregate breakup due to the interplay of varying fluid shear and suspended sediment concentration (Lick et al., 1993; Manning and Dyer, 1999; Mietta et al., 2009; Safak et al., 2013). A network of clay bonds, associated with an enhanced viscosity is required to result in full turbulence attenuation (Baas et al., 2009; Au and Leong, 2013; Yu et al., 2013; Lin et al., 2016; Baker et al., 2017) and the continuous evolvement of gravity currents might prevent this. At least within the boundary conditions of these experiments, such as the length of the flume, bed slope, initial discharge and clay concentration, the clay bonds don't have the required time to fully develop to establish further turbulence attenuation.

With the same boundary conditions, i.e. clay type, concentration and flow depth, then generally, the turbulence intensity of the gravity currents is higher than that of open-channel flows. At clay concentrations where in open-channel flows turbulence attenuation occurs, the turbulence intensity in gravity currents remains high and no full development of a turbulence attenuated plug flow is identified. The additional source of turbulence at the upper interface of gravity currents might shift the balance of transitional clay flows towards higher clay concentrations, i.e. higher clay concentrations are required to attenuate the turbulence within a gravity current compared with open-channel flows. The clay concentrations within these gravity currents allowed initial stages of turbulence attenuation (Chapter 4), but further experiments should be conducted with higher clay concentrations to assess if additional transitional flow types can be identified or if the entrainment of ambient water prevents the development towards a debris flow.

Research into open-channel clay suspension flows (Chapters 2, 3) and gravity currents (Chapter 4), have highlighted differences in the turbulent dynamics of clay suspension flows. The standard deviation of the velocity fluctuations, $RMS(u')$ and a dimensionless turbulence intensity measure, $RMS(u')_0$, are proven to be efficient measures to use to identify different levels of turbulence attenuation, i.e. clay flow types, in open-channel flows (Baas and Best, 2002; Baas et al., 2009; Baas et al., 2016a). However, research into transitional flow properties in clay-laden gravity currents indicates that the use of standard deviation, $RMS(u')$, might not be a suitable measure to assess turbulence attenuation within a flow as it represents one averaged value of velocity fluctuations dominated by lower frequencies, whereas fast Fourier transform provides a distribution of the full range of frequencies within the velocity time series (Tennekes and Lumley, 1972; Glüer et al., 1995; Anderson, 2011; Takeda, 2012). Initial signs of turbulence attenuation are identified in the plug flow in the velocity profile where the higher frequencies are less important as they are attenuated by the viscous forces in the flow (Harker and Temple, 1988; Pope, 2000; Baas et al., 2009). To further understand the turbulence dynamics of clay suspension flows, it would be interesting to conduct fast Fourier transforms on velocity time series from clay-laden open-channel flows. This has been excluded in this research as the open-channel flow measurements are collected in multiplexing mode (Section 2.2.3; Section 3.2.3). This multiplexing setting allows measurements to be collected for multiple probes, but it reduces the frequency of the measurements significantly. Therefore, the frequency range in the measurements of open-channel flows in Chapters 2 and 3 is reduced compared with the frequency range included in the

measurements of the gravity currents (Chapter 4). Fast Fourier transforms on the velocity time series of Chapters 2 and 3 are therefore not able to capture the differentiation in the importance of lower and higher frequencies in the same amount of detail as in Chapter 4. This additional analysis is recommended for future research as it might provide more detailed insight into the turbulence dynamics of clay suspension flows.
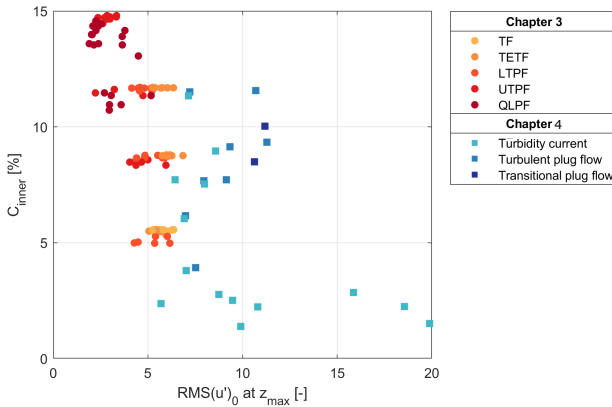

Figure 5.2: Turbulence intensity values of Chapter 3 and Chapter 4 against clay concentration. The results of Chapter 3 include the depth-averaged clay concentration, C, and the minimal turbulence intensity found over the depth $min(RMS(u')_0)$, which correlates to the height of the velocity maximum. The different red colour scale denotes the different flow types identified in the flow. The result of Chapter 4 include the depth-averaged clay concentration in the inner region, C_{inner} and the turbulence intensity at the height of the velocity maximum, z_{max}. The different blue colour scale denotes the different flow types identified in the flow.

5.2.2. FLOW EVOLUTION AND ADAPTATION

For both sets of open-channel flow experiments, the adaptation time of the development of the clay flow type is determined, which is defined as the time when uniform conditions are reached in Chapter 2 and steady conditions in Chapter 3. Due to the nature of gravity currents, they continuously evolve as they flow downstream. Gravity currents may alter its velocity, deposit or erode sediment, incorporate water and increase in flow height or dewater and reduce in flow height, depending on the boundary conditions (Mulder and Alexander, 2001; Felix and Peakall, 2006; Talling et al., 2007; Meiburg and Kneller, 2010; Kane and Pontén, 2012; Sequeiros et al., 2018). Therefore, the steady flow is non-uniform at the upstream and downstream measurement locations in Chapter 4 and the gravity current continues to evolve further downstream. To assess the adaptation time of gravity currents as they evolve between the upstream and downstream location and in order to compare with the open-channel flow results of Chapters 2 and 3, the adaptation times for the experimental runs in Chapter 4 are defined by the travel time of the gravity current between the upstream and downstream measurement location.

$$\Delta T_{GC} = \frac{D}{(\overline{\overline{U}}_{inner,upstream} + \overline{\overline{U}}_{inner,downstream})/2} \tag{5.1}$$

where ΔT_{GC} is the adaptation time, or travel time between the upstream and downstream location of the gravity current, D is the distance between the upstream and downstream measurements, $D = 3.75m$ (Figure 4.5a) and $\overline{\overline{U}}_{inner}$ is depth-averaged velocity within the inner region (Equation 4.12).

The adaptation times, ΔT_{GC}, are overlaid on the open-channel flow results in Figure 5.3. The gravity currents are more comparable with the non-uniform flow results of Chapter 2 than the unsteady flow results of Chapter 3. The gravity currents are non-uniform as well and the gradual change in velocity allowed them to adjust continuously, reducing the adaptation time (Section 5.1). The adaptation time is influenced by the travel time between the measurement locations and the gravity current will evolve further downstream.
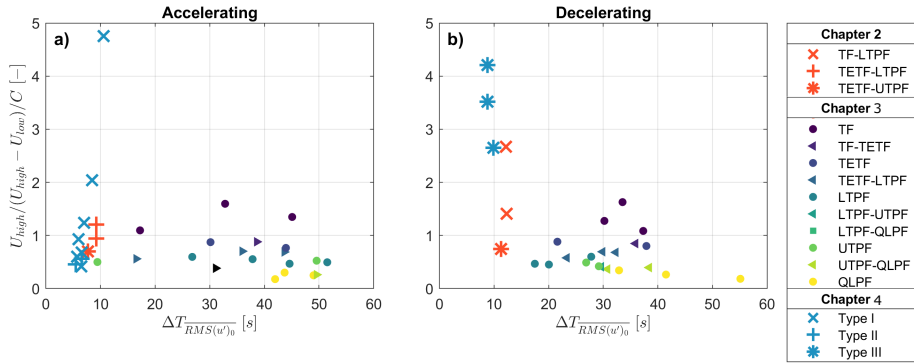

Figure 5.3: Correlation between velocity normalised by the velocity change and clay concentration, $U_{high}/(U_{high} - U_{low})/C$ and the adaptation time of depth-averaged turbulence intensity, $\Delta T_{\overline{RMS(u')_0}}$, for the experimental runs of Chapter 2, Chapter 3 and adaptation time, or travel time between the upstream and downstream location of the gravity current, ΔT_{GC} of Chapter 4 for a) accelerating flow conditions and b) decelerating flow conditions. The results of Chapter 2 are indicated with different symbols correlating to the clay flow types the flow evolves through within the flume. For the results of Chapter 3, the colour indicates the clay flow type. A circle denotes the same clay flow type before and after the imposed velocity change and a triangle denotes a transition between clay flow types as the flow accelerates or decelerates. The results of Chapter 4 are indicated with different symbols correlating to the identified flow evolution types.

The further evolvement of the gravity currents will be influenced by the shifting balance between turbulent and cohesive forces, where the cohesive forces are influenced by the time clay bonds require to establish themselves. Flow evolution type I flows developed from turbulent plug flow to turbidity current. Entrainment of ambient water and mixing at the upper interface, in combination with flow acceleration, results in a shift towards more turbulent flow conditions. As the flow would develop further downstream, the continuous dilution and flow thickening results in consistently dominant turbulent forces over cohesive forces. Flow evolution type III flows remained within the turbulent current regime and are expected to remain in this regime as the flow develops further downstream. Due to the limited density stratification in these flows, the entrainment rates remain high and further mixing with ambient fluid will occur (Ellison and Turner, 1959; Parker et al., 1987; Cenedese and Adduce, 2010; Krug et al., 2015).

Flow evolution type II flows developed from turbulent plug flow to transitional plug flow. The further evolvement of these flows downstream can move in two directions. Either the continuous entrainment of ambient fluid and flow thickening results in the enhancement of turbulent mixing in the flow, which eventually penetrates into the inner region to break the established clay bonds. Or additional clay bonds in the inner region establish, enhancing the viscosity in the flow, which might prevent turbulent mixing to penetrate into the inner region. The reduced turbulence intensity around the velocity maximum might hinder the exchange of sediment between the inner and outer region (Garcia and Parker, 1993; Buckee et al., 2001; Talling et al., 2007), allowing the concentration and associated viscosity to remain high in the inner region. The second scenario is more likely with a higher initial clay concentration or a flatter slope, where the flow acceleration is reduced and the associated mixing at the upper interface (Ellison and Turner, 1959; Altinakar

et al., 1996; Kneller and Buckee, 2000; Marr et al., 2001; Mohrig and Marr, 2003; Eggenhuisen et al., 2020). Decelerating gravity currents on the other hand and detrainment of water can result in denser flows at the downstream location if sediment remains in suspension and does not settle out. Instead of settling out, sediment can also be trapped in the inner region due to the turbulence profile of gravity currents (Sylvester and Lowe, 2004; Talling et al., 2007; Kane and Pontén, 2012) To further assess the evolvement of clay-laden gravity currents, additional research is required with a larger variety of clay concentrations, discharges and bed slopes.

5.3. WIDER IMPLICATIONS

Transitional flow conditions can be expected in a wide range of flows (Whitehouse et al., 2000; Baas et al., 2009; Talling et al., 2012; Hermidas et al., 2018), but the precise conditions at which each flow type is reached depends on the balance between cohesive and turbulent forces and the adaptation to non-uniform or unsteady conditions. The experiments conducted within this thesis are based on laboratory experiments conducted with fresh water flows transporting pure kaolinite clay, moving over a fixed, smooth bed. Although the experiments provide new insights into the adaptation of non-uniform and unsteady clay suspension flows, there are several limitations within the experimental setup and differences compared with natural flows.

5.3.1. RHEOLOGICAL PROPERTIES OF CLAY

Kaolinite has weaker cohesive strength than most other clay minerals, such as montmorillonite, illite or chlorite (Section 1.2.4), and is thus likely to show transitional flow behaviour at higher concentrations (van Olphen, 1977; Baas et al., 2016a). It is increasingly difficult to break bonds between clay particles of clay types with stronger cohesive properties than kaolinite and consequently, stronger turbulence is required for disaggregation (van Olphen, 1977; Adamis et al., 2005; Yu et al., 2013; Ren et al., 2021). The boundaries between the transitional clay flow types within the phase diagram (Baas et al., 2009) are therefore shifted to lower volumetric suspended clay concentrations compared with kaolinite suspension flows (Baas et al., 2016a; Baker et al., 2017); i.e. for stronger clay types, transitional flow properties can already be observed at lower clay concentrations than for kaolinite suspensions. This affects the adaptation times for turbulent-laminar transitions. The differentiation in adaptation time due to breakage and formation of clay bonds is then already noticeable at lower clay concentrations for stronger clay types. Moreover, higher shear or stronger turbulent forces are required to break the clay bonds in clay-laden flows with intensified cohesive strength. Therefore, the adaptation time of accelerating flows might be elongated for comparable clay concentrations, since the cohesive forces are stronger in the stronger clay type preventing the turbulent forces to penetrate into the plug flow to break the clay bonds. However, the adaptation time of decelerating flows might be reduced as clay bonds are established easier with stronger attractive forces between the clay particles. This might also affect the evolvement of gravity currents. If the gravity current experiments were conducted with bentonite instead of kaolinite, the stronger attractive forces between clay particles might result in stronger turbulence attenuation in the inner region of flow evolution type II flows. Entrainment and additional mixing in the outer region could be unable to penetrate into the inner region due to the enhanced viscosity in the inner region.

Furthermore, in addition to the variations in cohesion between clay types, the thixotropic processes of formation and breakage of clay bonds vary between different clay types (Skempton and Northey, 1952; Lunne and Andersen, 2007; Hogg, 2000; Shahriar et al., 2018; Ren et al., 2021). After an applied shear stress (i.e. accelerating flow), bonds between clay particles get broken and the flow attempts to adjust itself to the new situation and local ions in the double layer (Section 1.2.2) will redistribute (Hogg, 2000; Zhang et al., 2017). The flow also attempts to adjust itself with a reduction in shear (i.e. decelerating flow). In both situations, after enough time a new equilib-

rium is formed with a balance between attractive and repulsive forces and an established amount of clay bonds (Skempton and Northey, 1952; Ren et al., 2021). The chemical structure varies between clay types and consequently, the adaptation time of the double layer varies, i.e. the rate of thixotropy varies between clay types. For example, swelling clay types, such as bentonite, tend to need longer to rearrange the ions of clay particles than kaolinite (Skempton and Northey, 1952; Abdou and Ahmed, 2013; Shahriar et al., 2018). These elongated thixotropic processes can result in higher adaptation times for flows with different clay types, depending on their chemistry. The balance between cohesive strength and thixotropic processes determines the effect on adaptation to non-uniform or unsteady flow conditions. For example, bentonite is a stronger clay type than kaolinite but takes longer to adapt to changes in shear stress as it is a swelling clay. In accelerating flows, clay bonds in bentonite suspensions flows might take longer to break due to the stronger attractive forces between clay particles. In addition, the adaptation to accelerating flow might be longer due to the increased thixotropic processes in bentonite suspension flows than kaolinite suspension flows. However, in decelerating flows, bentonite suspension flows might establish clay bonds faster due to the stronger attractive forces between clay particles. On the other hand, the adaptation to decelerating flow might be longer due to increased thixotropic processes. Further research is required to assess the relative influence of both aspects and if there is a stronger hysteresis in adaptation to accelerating and decelerating flows in suspension flows with stronger clay types than kaolinite.

Other factors influencing the rheological properties, next to clay type or minerals are salinity (Section 5.3.2), the solid fraction or water content, pH (Palomino and Santamarina, 2005; Kelessidis et al., 2007; Shoaib and Bobicki, 2021), temperature (Lin et al., 2016) and shear rate history (Mietta et al., 2009; Jeong, 2010; Shakeel et al., 2019), on top of mixtures of different sediment types and organic matter (Section 5.3.3). All these variations could result in different adaptation times in natural flows than measured within the experiments conducted in this research and further research is required to assess the exact influence.

5.3.2. Salinity

Throughout the experiments within this thesis, fresh water is used, whereas salt water is common in natural environments, such as estuaries and oceans (Dyer, 1988; Telesh and Khlebovich, 2010; Leeder, 2011). Salinity of water in marine basins promotes cohesion by aiding flocculation (Li and Gust, 2000; Laxton and Berg, 2006). Salinity may encourage the formation of larger flocs and gels in a shorter time compared to fresh water flows as the salt concentration shrinks the double layer thickness and increases the attraction forces of particles (Di Maio, 1996; Winterwerp and Van Kesteren, 2004; Rinaldi and Clariá Jr, 2016, Section 1.2). The influence of salinity is also dependent on the clay type and might be non-linear with changing salinity (Gorakhki and Bareither, 2015). In addition to the cohesive strength, it influences the thixotropic process as well (Ren et al., 2021).

5.3.3. Combination of sediments

Natural flows typically transport mixtures of cohesive, non-cohesive, and organic material. Different clay types have different material properties (Section 1.2.4), which also influences the thixotropic behaviour (Abend and Lagaly, 2000; Goh et al., 2011). For example, kaolinite is a non-swelling clay hence particles do not delaminate and their surface area remains low, leading to limited particle-particle interactions (Teh et al., 2009). Bentonite on the other hand already shows thixotropic behaviour at low volume concentrations due to the swelling nature of the clay (Laird, 2006, Section 1.2.4). Delamination due to the hydration of sodium ions results in increased particle concentration, decreased clay platelet size and increased particles' specific surface area with enhanced particle-particle interaction and high yield stress values (Leong et al., 1995; Laird, 2006).

Therefore, small concentrations of bentonite in kaolinite suspensions can already significantly change the rheological properties (Keren, 1989; Lagaly, 1989; Shakeel et al., 2021). In general, the yield stress is an important control on the flow mobility of clay-laden flows (Au and Leong, 2013; Lin et al., 2016), but accurate determination of the yield stress is required, which include the mixture of natural sediments and not only the relative clay concentration (Wan, 1982; Van Kessel and Blom, 1998; Au and Leong, 2013; Lin et al., 2016). The relative fraction of clay can significantly influence the flow behaviour (Takahashi, 2014). Rheological tests indicate shear-thickening or Bingham behaviour for low amounts of clay relative to non-cohesive sediment, but shear-thinning behaviour for large amounts of clay (Nguyen et al., 2018). Moreover, the yield stress of natural muddy sediments is influenced by the pre-shearing and time of recovery (Shakeel et al., 2020).

The combination of cohesive and non-cohesive sediment can either increase the concentration of the suspension allowing turbulence attenuation or the presence of non-cohesive can increase the distance between clay particles, making aggregation increasingly difficult (Ancey and Jorrot, 2001; Ilstad et al., 2004). Flocculation rate and the maximal floc size decrease with sand-to-mud concentration ratios above 50% due to the reduction in collisions between clay particles as sand particles result in an obstruction and indirect due to the additional shear generated by sand particles (Elghobashi, 1994; Cuthbertson et al., 2010). However, the sand particles can also result in an increase in concentration allowing to damp turbulence. Non-cohesive particles surrounded by clay particles could interact with each other as colloidal particles, i.e. non-cohesive particles get incorporated into the floc structure and enhance the yield stress (Sumner et al., 2000; Ancey and Jorrot, 2001). The influence of non-cohesive sediment also depends on the flow properties already in flow. For example, the addition of non-cohesive sediment in a turbidity current can enhance the density difference within the flow, which is the main driving mechanism of turbidity currents and consequently the increase in concentration might result in enhancing the turbulence within the flow (Ilstad et al., 2004; Baas et al., 2011). On the other hand, addition of non-cohesive sediment in a debris flow can further enhance the yield stress in the flow (Ilstad et al., 2004) if the gel, i.e. space-filling network of particle bonds, is already strong enough to support larger grains (Hampton, 1975; Torfs et al., 1996; Marr et al., 2001; Amy et al., 2006; Sumner et al., 2009; Baas et al., 2011; Schindler et al., 2015). Due to the different physical properties of cohesive and non-cohesive sediment, segregation of sediment type can occur due to the different settling behaviour, depending on the relative concentration (Amy et al., 2006; Mehta and McAnally, 2008; Spearman and Manning, 2017). The complex interaction between different sediment materials influences the adaptation time within non-uniform and unsteady flows and the evolvement of gravity currents downstream. Additional research is required to assess the relative influence of different volume fractions. If the non-cohesive sediment prevents clay bonds to form, the adaptation time of decelerating flows might reduce as the non-cohesive sediment can result in additional turbulence breaking clay bonds (Elghobashi, 1994). If the non-cohesive sediment enhances the yield strength in the flow, the adaptation time might reduce as well in decelerating flows as thixotropic processes are reduced in sand-mud mixtures. Gravity currents might evolve to turbulence attenuated flow type if the additional non-cohesive sediment increases the yield stress in the flow, but if it prevents the formation of clay bonds, the gravity current might evolve to a turbidity current instead.

Moreover, biological cohesion occurs naturally in sedimentary environments and is caused by extracellular polymeric substances (EPS) which result from the life cycles of microorganisms. EPS binds directly to sand grains rather than acting as discrete particles or particle clusters as muds do in sand-mud mixtures (Jacobs et al., 2011; Schindler et al., 2015), which can enhance the cohesive forces within a flow already with small amounts (Paterson et al., 1990; Malarkey et al., 2015; Parsons et al., 2016; Shakeel et al., 2019; Craig et al., 2020; Sobocinska and Baas, 2022).

5.3.4. Topographic interaction

Within the experiments conducted, a fixed, smooth bed is used, which can be regarded as an analogue for erosion-resistant muddy surfaces for which the erosion resistance is strongly dependent on the cohesion of the sediment, the history of erosional forces and the timescale of flocculation and consolidation (Mitchener and Torfs, 1996; Crooks and Pye, 2000; Winterwerp and Van Kesteren, 2004; Zhang et al., 2022). However, surface roughness is a ubiquitous part of morphology in natural environments. Surface roughness, e.g. gravel bed (Baas and Best, 2009; Roy et al., 2004; Reidenbach et al., 2010; Stoesser et al., 2015, Section 1.1.3) or bedforms, e.g. ripples or dunes (Leeder, 2011; Baas et al., 2011; Baas et al., 2013; Schindler et al., 2015) or topography on top of deposits of gravity currents such as debrites (Talling et al., 2012; Fonnesu et al., 2015) or hybrid event beds (Haughton et al., 2009; Baas et al., 2011; Kane and Pontén, 2012), can generate additional turbulence, which may cause a shift in the phase boundaries to higher concentrations (Baas and Best, 2009), as the additional turbulence may break clay bonds within the flow (Lick and Lick, 1988; Mietta et al., 2009; Cuthbertson et al., 2010; Safak et al., 2013; Lamb et al., 2020). Additionally, an erodible surface can enhance the sediment concentration in the flow (Partheniades, 1965; Winterwerp and Van Kesteren, 2004; Van Prooijen and Winterwerp, 2010; Stoesser et al., 2015), in contrast to the non-erodible bed used in the experiments. On the other hand, settling or deposition of sediment from the flows can reduce the sediment concentration in the flow (McAnally et al., 2007; Mehta and McAnally, 2008; Spearman and Manning, 2017; Schieber et al., 2022). However, settling of sediment out of a gravity current might dilute the flow, but it might also result in a denser inner layer where sediment is trapped (Felix and Peakall, 2006; Postma et al., 1988 Sylvester and Lowe, 2004; Talling et al., 2007; Kane and Pontén, 2012). Additional work is needed to research this interplay of velocity and sediment concentration variations on the turbulence dynamics of open-channel flows and gravity currents.

5.3.5. Rate of non-uniformity or unsteadiness

Within the experiments, the rate of non-uniformity of the open-channel flows was confined by the ratio in flume width (Figure 2.3) and the unsteadiness by the imposed velocity change of 0.1 m/s (Chapter 3). The non-uniformity of the gravity currents was constrained by the fixed bed slope and the measurement distance between the upstream and downstream locations (Chapter 4). However, a large range in non-uniformity or unsteadiness of natural flows exists (Yang et al., 2006; Leeder, 2011; Karimaee Tabarestani and Zarrati, 2015; Talling et al., 2012). Within the experiments, the range of non-uniformity or unsteadiness can be expanded by varying the ratio in change of width, including a range of imposed velocity changes and a variety of bed slopes. This would already give more insight into the adaptation of turbulence dynamics in clay-laden flows, but not yet cover the full range of non-uniformity or unsteadiness found in natural environments. There are for example various topographic variations that can alter the flow speed. For example, Coriolis forces which can alter the flow direction of a gravity current (Persson, 2005; Cossu et al., 2010), meandering rivers (Van Maren, 2007; Li et al., 2007) or sinuosity of submarine channels (Clark and Pickering, 1996; Gee et al., 2007; Peakall et al., 2012), industrial settings including narrowing waterways under bridges or within sewers (Ackers et al., 2001) and flood hydrographs with varying discharge rates (Karimaee Tabarestani and Zarrati, 2015; Fielding et al., 2018; Mrokowska and Rowiński, 2019). The adaptation of the clay-laden flows will depend on the boundary conditions, among other things the (cohesive) sediment concentration in the flow and the rate of velocity changes. In general, larger changes in velocity results in increased adaptation length and time scales, especially if the clay flow passes through several clay flow types.

In addition to the rate of non-uniformity or unsteadiness, the experiments were conducted in a confined channel, whereas natural gravity currents experience additional 3D influences (La Rocca and Bateman, 2010; Soutter et al., 2021). As a current leaves the confined channel, the sediment is

able to spread in multiple directions. Consequently, gravity currents often rapidly spread resulting in deposition after deceleration of the current as it loses its driving force. Topography has crucial influences on gravity current pathways and deposit character (Kneller and Buckee, 2000; Soutter et al., 2021). Additional research on the influence on the rate of non-uniformity or unsteadiness would give more insight into the adaptation time and length scales, which could provide more detailed predictions for different scenarios. However, the exact adaptation and consequently the transport of sediment is a complex system influenced by several aspects and boundary conditions. Especially as Chapter 4 showed that depending on the clay concentration with the same bed slope, i.e. rate of non-uniformity, the flow can either adapt to a more turbulent turbidity current or a less turbulent debris flow, influenced by the thixotropic cohesive forces in the flow. Therefore, additional research into specific scenarios is needed to research the local sediment transport rates and adaptation of turbulent dynamics in clay-laden flows.

5.3.6. SCALING EFFECTS

Within physical experiments, Froude scaling is commonly used, where Froude number is maintained and Reynolds number is relaxed under the assumption that inertia dominates over viscous effects (Struiksma et al., 1985; Peakall et al., 1996; Kneller and Buckee, 2000). Generally, the Reynolds number requires to be above the laminar-turbulent threshold (Section 1.1), but the Reynolds number and turbulence levels have a significant influence on the turbulence attenuation due to the presence of clay. The scaling of sediment is another limitation of scaling flume experiments. Solely, non-cohesive sediment can be scaled down up to the extent of silt sizes, but the cohesive forces of clay are scale-independent (Paola et al., 2009; Scheeres et al., 2010; Thakur et al., 2016). De Leeuw et al. (2016) emphasizes the importance of scalable turbulent-sediment interactions for turbidity currents using the relationship between Shield's number (Shields, 1936) and particle Reynolds number (Van Rijn, 1984). Shields scaling includes scaling of sediment transport relative to turbulence levels (Pohl et al., 2020a; Ferguson et al., 2020; Fernandes et al., 2020), however it still excludes the influence of cohesive sediment. Hermidas et al. (2018) suggest different scaling regimes for the boundary shear layer, the free shear layer and the plug layer to overcome the influence of apparent viscosity on scaling effects. The threshold concentration for turbulence attenuation might be higher for natural flows since full-scale turbidity currents are often more turbulent (Meiburg and Kneller, 2010; Talling et al., 2013), and therefore more likely to break the bonds between clay particles than laboratory-scale turbidity currents. However, the turbulence attenuation that is likely to occur in decelerating flow conditions, is frequently found within the distal fringe of the system and possibly more comparable in size with physical experiments as turbidity currents thin distally (Sturm and Matter, 1978; Lowe, 1982; Kane et al., 2017; Soutter et al., 2021). The restriction of cohesion versus turbulence limits the extrapolation to natural environments. The most efficient way, although challenging, of correlating the experimental results to natural flows is by direct monitoring of clay-laden flows and comparing them with physical experimental results (Xu et al., 2004; Talling et al., 2015; Azpiroz-Zabala et al., 2017; Hage et al., 2019; Heijnen et al., 2020). However, the trends of turbulent-laminar transitions observed in the physical experiments are expected to hold for flows in natural environments.

5.3.7. LIMITATIONS OF UVP MEASUREMENTS

Generally, research on the internal structure of clay-laden flows is limited due to the challenges of data acquisition in opaque, high-concentration flows. Frequently used measurement equipment in physical experiments, for example, acoustic doppler velocimeter (ADV) or particle image velocimetry (PIV) measurements, are unable to measure in clay-laden flows (Poelma et al., 2006; Tropea et al., 2007; Linne et al., 2009; Aberle et al., 2017) and consequently, previous research has focused on conceptual models based on visualisation with a lack of quantitative support (Kneller

and Buckee, 2000; Mohrig and Marr, 2003; Nogueira et al., 2013; Baker et al., 2017). Velocity measurements can be obtained by UVP measurements, which allows the determination of velocity profile and turbulence structure of clay-laden flows (Takeda, 1991; Best et al., 1997; Best et al., 2001; Baas et al., 2009), but are limited to one direction. Additionally, fast Fourier transforms on the gravity current measurements (Chapter 4) suggest the turbulence attenuation within clay-laden flows is more complex than suggested by Baas et al. (2009). Full three directional high-frequency measurements would further advance the understanding of turbulence dynamics within clay-laden flows. Advances are made using Ultrasound Imaging Velocimetry (UIV) or echo-particle image velocimetry (echo-PIV) (Crapper et al., 2000; Poelma, 2017; Discetti and Coletti, 2018), which can provide instantaneous two-component velocity fields on the order of several centimeters squared (Poelma et al., 2011; Aberle et al., 2017), topography measurements in sediment-laden flows (Zou et al., 2015) or concentration measurements (Toorman et al., 2002; Zou et al., 2016). The rate of successive videos limits the allowed velocity speeds within the flow (Crapper et al., 2000; Fraser et al., 2017; Aberle et al., 2017), measured up to 0.7 m/s (Zhang et al., 2011; Poelma et al., 2012). Developments in hardware and processing algorithms, currently hindered by the demand outside medical needs, might rapidly enhance allowing a paradigm shift in experimental fluid dynamics (Discetti and Coletti, 2018).

5

Abdou, M. I. and Ahmed, H. E. (2013), 'A study on the thixotropy of egyptian bentonite suspensions', *Petroleum Science and Technology* **31**(19), 1980–1991.

Abend, S. and Lagaly, G. (2000), 'Sol–gel transitions of sodium montmorillonite dispersions', *Applied Clay Science* **16**(3-4), 201–227.

Aberle, J., Rennie, C. D., Admiraal, D. M. and Muste, M. (2017), *Experimental Hydraulics: Methods, Instrumentation, Data Processing and Management: Volume II: Instrumentation and Measurement Techniques*, CRC Press. 1.4, 5.3.7

Ackers, J., Butler, D., Leggett, D. and May, R. (2001), Designing sewers to control sediment problems, *in* 'Urban Drainage Modeling', pp. 818–823. 1, 2.1, 5.3.5

Adamis, Z., Williams, R. B. and Fodor, J. (2005), *Bentonite, kaolin, and selected clay minerals*, World health organization. 1.2.1, 1.2.2, 1.2.3, 1.2.4, 1.2.5, 1.2.5, 3.4.3, 5.2.1, 5.3.1

Allen, J. (1971), 'Mixing at turbidity current heads, and its geological implications', *Journal of Sedimentary Research* **41**(1), 97–113.

Altinakar, M. S., Graf, W. H. and Hopfinger, E. J. (1996), 'Flow structure in turbidity currents', *Journal of Hydraulic Research* **34**(5), 713–718.

Amy, L. A., Talling, P. J., Edmonds, V. O., Sumner, E. J. and Lesueur, A. (2006), 'An experimental investigation of sand–mud suspension settling behaviour: implications for bimodal mud contents of submarine flow deposits', *Sedimentology* **53**(6), 1411–1434. 1.2.3, 5, 5.3.3

Ancey, C. and Jorrot, H. (2001), 'Yield stress for particle suspensions within a clay dispersion', *Journal of Rheology* **45**(2), 297–319.

Anderson, T. W. (2011), *The statistical analysis of time series*, John Wiley & Sons.

Andersson, B., Andersson, R., Håkansson, L., Mortensen, M., Sudiyo, R. and Van Wachem, B. (2011), *Computational fluid dynamics for engineers*, Cambridge university press. 1.1.1, 1.1, 1.1.2

Antoine, G., Camenen, B., Jodeau, M., Némery, J. and Esteves, M. (2020), 'Downstream erosion and deposition dynamics of fine suspended sediments due to dam flushing', *Journal of Hydrology* **585**, 124763.

Asmala, E., Bowers, D. G., Autio, R., Kaartokallio, H. and Thomas, D. N. (2014), 'Qualitative changes of riverine dissolved organic matter at low salinities due to flocculation', *Journal of Geophysical Research: Biogeosciences* **119**(10), 1919–1933. 1.2.2

Au, P. and Leong, Y. (2013), 'Rheological and zeta potential behaviour of kaolin and bentonite composite slurries', *Colloids and Surfaces A: Physicochemical and Engineering Aspects* **436**, 530–541. 1.2.5, 3.4.2, 3.4.3, 3.4.3, 4.4.2, 5.2.1, 5.3.3

Azpiroz-Zabala, M., Cartigny, M. J., Talling, P. J., Parsons, D. R., Sumner, E. J., Clare, M. A., Simmons, S. M., Cooper, C. and Pope, E. L. (2017), 'Newly recognized turbidity current structure can explain prolonged flushing of submarine canyons', *Science Advances* **3**(10), e1700200. 1.4, 4.1, 4.2.1, 5.3.6

Baas, J. H. and Best, J. L. (2002), 'Turbulence modulation in clay-rich sediment-laden flows and some implications for sediment deposition', *Journal of Sedimentary Research* **72**(3), 336–340. 1, 1.10, 1.3, 1.3, 1.4, 1.5, 2.1, 2.2.1, 2.2.4, 2.4.1, 3.1, 3.2.4, 3.4.2, 4.1, 4.1, 4.2.4, 4.4.1, 4.4.1, 4.4.3, 5, 5.2.1

Baas, J. H. and Best, J. L. (2008), 'The dynamics of turbulent, transitional and laminar clay-laden flow over a fixed current ripple', *Sedimentology* **55**(3), 635–666. 1, 4.4.1, 4.4.3

Baas, J. H. and Best, J. L. (2009), 'On the flow of natural clay suspensions over smooth and rough beds', *European Research Community on Flow, Turbulence and Combustion (ERCOFTAC) Bulletin* **78**, 58–63. 1.3, 5.3.4

Baas, J. H., Best, J. L. and Peakall, J. (2011), 'Depositional processes, bedform development and hybrid bed formation in rapidly decelerated cohesive (mud–sand) sediment flows', *Sedimentology* **58**(7), 1953–1987. 1.2.3, 1.3, 4.4.2, 4.4.3, 5, 5.3.3, 5.3.4

Baas, J. H., Best, J. L. and Peakall, J. (2016*a*), 'Comparing the transitional behaviour of kaolinite and bentonite suspension flows', *Earth Surface Processes and Landforms* **41**(13), 1911–1921. 1.3, 5, 5.2.1, 5.3.1

Baas, J. H., Best, J. L. and Peakall, J. (2016*b*), 'Predicting bedforms and primary current stratification in cohesive mixtures of mud and sand', *Journal of the Geological Society* **173**(1), 12–45. 1, 4.4.3

Baas, J. H., Best, J. L., Peakall, J. and Wang, M. (2009), 'A phase diagram for turbulent, transitional, and laminar clay suspension flows', *Journal of Sedimentary Research* **79**(4), 162–183. 1, 1.1.3, 1.2, 1.2.3, 1.2.5, 1.3, 1.10, 1.3, 1.11, 1.3, 1.4, 1.5, 1.5, 2.1, 2.2.1, 2.2.1, 2.2.2, 2.5, 2.4.1, 2.4.1, 3.1, 3.3.1, 3.10, 3.3.2, 3.3.2, 3.3.2, 3.3.3, 3.4.2, 3.29, 3.4.2, 3.4.3, 3.4.4, 4.1, 4.1, 4.1, 4.1, 4.2.4, 4.3.5, 4.4, 4.4.1, 4.4.1, 4.4.1, 4.35, 4.4.2, 4.4.3, 5, 5.2.1, 5.3, 5.3.1, 5.3.7

Baas, J. H., Davies, A. G. and Malarkey, J. (2013), 'Bedform development in mixed sand–mud: The contrasting role of cohesive forces in flow and bed', *Geomorphology* **182**, 19–32.

Baas, J. H., McCaffrey, W. D., Haughton, P. D. W. and Choux, C. (2005), 'Coupling between suspended sediment distribution and turbulence structure in a laboratory turbidity current', *Journal of Geophysical Research: Oceans* **110**(C11).

Baas, J. H., Tracey, N. D. and Peakall, J. (2021), 'Sole marks reveal deep-marine depositional process and environment: Implications for flow transformation and hybrid-event-bed models', *Journal of Sedimentary Research* **91**(9), 986–1009. 1.3, 4.4.3, 5

Bagnold, R. A. (1954), 'Experiments on a gravity-free dispersion of large, solid spheres in a Newtonian fluid under shear', *Proceedings of the Royal Society of London. Series A. Mathematical and Physical Sciences* **225**(1160), 49–63. 1, 2.1

Baker, M. L. and Baas, J. H. (2020), 'Mixed sand–mud bedforms produced by transient turbulent flows in the fringe of submarine fans: Indicators of flow transformation', *Sedimentology* **67**(5), 2645–2671. 1.3, 4.1, 5

Baker, M. L., Baas, J. H., Malarkey, J., Jacinto, R. S., Craig, M. J., Kane, I. A. and Barker, S. (2017), 'The effect of clay type on the properties of cohesive sediment gravity flows and their deposits', *Journal of Sedimentary Research* **87**(11), 1176–1195. 1.3, 1.4, 3.4.3, 4.1, 4.4.1, 4.4.1, 4.4.1, 4.4.2, 5, 5.2.1, 5.3.1, 5.3.7

Barany, S., Meszaros, R., Kozakova, I. and Skvarla, I. (2009), 'Kinetics and mechanism of flocculation of bentonite and kaolin suspensions with polyelectrolytes and the strength of floccs', *Colloid Journal* **71**(3), 285–292. 1.2.3, 3.4.3

Barbero, R., Abatzoglou, J. T., Larkin, N. K., Kolden, C. A. and Stocks, B. (2015), 'Climate change presents increased potential for very large fires in the contiguous United States', *International Journal of Wildland Fire* **24**(7), 892–899. 1, 1.5, 2.1, 3.1

Barnes, H. A. (1997), 'Thixotropy: a review', *Journal of Non-Newtonian Fluid Mechanics* **70**(1-2), 1–33. 1.2.5

Batchelor, G. K. (1972), 'The determination of the bulk stress in a suspension of spherical particles to order c2', *Journal of Fluid Mechanics* **56**(3), 401–427. 1.2.5

Beazley, K. M. (1972), 'Viscosity-concentration relations in deflocculated kaolin suspensions', *Journal of Colloid and Interface Science* **41**(1), 105–115. 1.2.5

Bergaya, F. and Lagaly, G. (2013*a*), General introduction: clays, clay minerals, and clay science, *in* 'Developments in clay science', Vol. 5, Elsevier, pp. 1–19. 1.2.1, 1.2.2

Bergaya, F. and Lagaly, G. (2013*b*), *Handbook of clay science*, Newnes. 1.2.1, 1.2.2, 1.2.4

Best, J., Ashmore, P. and Darby, S. E. (2022), 'Beyond just floodwater', *Nature Sustainability* pp. 1–3. 1, 3.4.4

Best, J., Bennett, S., Bridge, J. and Leeder, M. (1997), 'Turbulence modulation and particle velocities over flat sand beds at low transport rates', *Journal of Hydraulic Engineering* **123**(12), 1118–1129. 1, 2.1, 5.3.7

Best, J. L., Kirkbride, A. D. and Peakall, J. (2001), 'Mean flow and turbulence structure of sediment-laden gravity currents: new insights using ultrasonic doppler velocity profiling', *Particulate Gravity Currents* pp. 157–172. 1.4, 1.5, 2.2.3, 4.4.1, 5.2.1, 5.3.7

Best, J. L. and Leeder, M. R. (1993), 'Drag reduction in turbulent muddy seawater flows and some sedimentary consequences', *Sedimentology* **40**(6), 1129–1137. 1.3, 2.4.1, 4.4.1

Biferale, L. and Procaccia, I. (2005), 'Anisotropy in turbulent flows and in turbulent transport', *Physics Reports* **414**(2-3), 43–164. 1.1.1

Bilotta, G. S. and Brazier, R. E. (2008), 'Understanding the influence of suspended solids on water quality and aquatic biota', *Water Research* **42**(12), 2849–2861. 1

Blanchet, C. and Villatte, H. (1954), 'Experimental studies of density currents in a glass sided ume', *UN Econ. Comm. for Asian and Far East, Water Res. Ser., Flood Control Ser* .

Bouma, A. H. (1985), Introduction to submarine fans and related turbidite systems, *in* 'Submarine fans and related turbidite systems', Springer, pp. 3–5.

Brown, R. A. and Pasternack, G. B. (2014), 'Hydrologic and topographic variability modulate channel change in mountain rivers', *Journal of Hydrology* **510**, 551–564.

Buaria, D., Pumir, A., Bodenschatz, E. and Yeung, P. (2019), 'Extreme velocity gradients in turbulent flows', *New Journal of Physics* **21**(4), 043004. 1.1.1

Buckee, C., Kneller, B. and Peakall, J. (2001), 'Turbulence structure in steady, solute-driven gravity currents', *Particulate Gravity Currents* pp. 173–187.

Cardoso, A. H., Graf, W. H. and Gust, G. (1991), 'Steady gradually accelerating flow in a smooth open channel', *Journal of Hydraulic Research* **29**(4), 525–543.

Cartigny, M. J., Eggenhuisen, J. T., Hansen, E. W. and Postma, G. (2013), 'Concentration-dependent flow stratification in experimental high-density turbidity currents and their relevance to turbidite facies models', *Journal of Sedimentary Research* **83**(12), 1047–1065.

Cenedese, C. and Adduce, C. (2010), 'A new parameterization for entrainment in overflows', *Journal of Physical Oceanography* **40**(8), 1835–1850.

Chaudhry, M. H. (2008), *Open-channel flow*, 2nd edn, Springer Science & Business Media. 1.1, 1.1, 2.1, 4.1, 4.4.1, 4.4.1, 5.2.1

Chauhan, K., Nagib, H. and Monkewitz, P. (2007), On the composite logarithmic profile in zero pressure gradient turbulent boundary layers, *in* '45th AIAA Aerospace Sciences Meeting and Exhibit', p. 532. 1.1.3, 1.1.3, 1.1.3

Choux, C., Baas, J., McCaffrey, W. and Haughton, P. (2005), 'Comparison of spatio–temporal evolution of experimental particulate gravity flows at two different initial concentrations, based on velocity, grain size and density data', *Sedimentary Geology* **179**(1-2), 49–69.

Chovet, C., Lippert, M., Foucaut, J. and Keirsbulck, L. (2017), 'Dynamical aspects of a backward-facing step flow at large reynolds numbers', *Experiments in Fluids* **58**(11), 1–15.

Chow, V. T. (1959), *Open-channel hydraulics*, McGraw-Hill book company, inc. 1.1

Clark, J. D. and Pickering, K. T. (1996), *Submarine channels: Processes and architecture*, Vallis Press.

Clauser, F. H. (1954), 'Turbulent boundary layers in adverse pressure gradients', *Journal of the Aeronautical Sciences* **21**(2), 91–108. 1.1.3

Coles, D. (1956), 'The law of the wake in the turbulent boundary layer', *Journal of Fluid Mechanics* **1**(2), 191–226. 1.1.3, 1.1.3

Cossu, R., Wells, M. G. and Wåhlin, A. (2010), 'Influence of the coriolis force on the velocity structure of gravity currents in straight submarine channel systems', *Journal of Geophysical Research: Oceans* **115**(C11).

Coussot, P. (1997), *Mudflow rheology and dynamics*, IAHR Monograph, Balkema, Rotterdam. 1.2.2, 1.2.3, 1.2.5, 1.2.5, 4.1, 5

Craig, M. J., Baas, J. H., Amos, K. J., Strachan, L. J., Manning, A. J., Paterson, D. M., Hope, J. A., Nodder, S. D. and Baker, M. L. (2020), 'Biomediation of submarine sediment gravity flow dynamics', *Geology* **48**(1), 72–76.

Crapper, M., Bruce, T. and Gouble, C. (2000), 'Flow field visualization of sediment-laden flow using ultrasonic imaging', *Dynamics of Atmospheres and Oceans* **31**(1-4), 233–245.

Crooks, S. and Pye, K. (2000), 'Sedimentological controls on the erosion and morphology of saltmarshes: implications for flood defence and habitat recreation', *Geological Society, London, Special Publications* **175**(1), 207–222.

Cuthbertson, A. J., Dong, P. and Davies, P. A. (2010), 'Non-equilibrium flocculation characteristics of fine-grained sediments in grid-generated turbulent flow', *Coastal Engineering* **57**(4), 447–460. 1.2.3, 1.2.3, 2.4.2, 3.4.2, 3.4.3, 3.4.3, 4.4.1, 4.4.2, 4.4.3, 5.3.3, 5.3.4

Davidson, P. A. (2015), *Turbulence: an introduction for scientists and engineers*, Oxford university press. 1.1.1, 1.1.2

Davis, C., Haughton, P., McCaffrey, W., Scott, E., Hogg, N. and Kitching, D. (2009), 'Character and distribution of hybrid sediment gravity flow deposits from the outer forties fan, palaeocene central north sea, ukcs', *Marine and Petroleum Geology* **26**(10), 1919–1939.

De Leeuw, J., Eggenhuisen, J. T. and Cartigny, M. J. (2016), 'Morphodynamics of submarine channel inception revealed by new experimental approach', *Nature Communications* **7**(1), 1–7.

Delgado, Á. V., González-Caballero, F., Hunter, R., Koopal, L. and Lyklema, J. (2007), 'Measurement and interpretation of electrokinetic phenomena', *Journal of Colloid and Interface Science* **309**(2), 194–224. 1.2.2

Derjaguin, B. and Landau, L. (1941), 'Theory of the stability of strongly charged lyophobic sols and of the adhesion of strongly charged particles in solutions of electrolytes', *Acta Physicochimica* **14**, 633–662. 1.2.2

Di, B. F., Chen, N. S., Cui, P., Li, Z. L., He, Y. P. and Gao, Y. C. (2008), 'Gis-based risk analysis of debris flow: an application in sichuan, southwest china', *International Journal of Sediment Research* **23**(2), 138–148.

Di Maio, C. (1996), 'Exposure of bentonite to salt solution: osmotic and mechanical effects', *Geotechnique* **46**(4), 695–707. 1.3, 5.3.2

Dilling, S. and MacVicar, B. (2017), 'Cleaning high-frequency velocity profile data with autoregressive moving average (arma) models', *Flow Measurement and Instrumentation* **54**, 68–81.

Discetti, S. and Coletti, F. (2018), 'Volumetric velocimetry for fluid flows', *Measurement Science and Technology* **29**(4), 042001.

Dorrell, R. M., Amy, L. A., Peakall, J. and McCaffrey, W. D. (2018), 'Particle size distribution controls the threshold between net sediment erosion and deposition in suspended load dominated flows', *Geophysical Research Letters* **45**(3), 1443–1452. 1, 1.5, 2.1, 3.1, 4.1

Dorrell, R. M. and Hogg, A. J. (2012), 'Length and time scales of response of sediment suspensions to changing flow conditions', *Journal of Hydraulic Engineering* **138**(5), 430–439. 1, 1.5, 2.1, 2.4.3, 3.1, 5

Dorrell, R. M., Peakall, J., Darby, S. E., Parsons, D. R., Johnson, J., Sumner, E. J., Wynn, R. B., Özsoy, E. and Tezcan, D. (2019), 'Selfsharpening induces jetlike structure in seafloor gravity currents', *Nature Communications* **10**(1), 1–10.

Dyer, K. R. (1988), Fine sediment particle transport in estuaries, *in* 'Physical Processes in Estuaries', Springer, pp. 295–310. 1.2.3, 2.4.2, 3.4.1, 3.4.3, 3.4.3, 4.4.2, 5.3.2

Dyer, K. R. and Manning, A. J. (1999), 'Observation of the size, settling velocity and effective density of flocs, and their fractal dimensions', *Journal of Sea Research* **41**(1-2), 87–95. 1.2.3

Eggenhuisen, J. T. and McCaffrey, W. D. (2012), 'The vertical turbulence structure of experimental turbidity currents encountering basal obstructions: implications for vertical suspended sediment distribution in non-equilibrium currents', *Sedimentology* **59**(3), 1101–1120.

Eggenhuisen, J. T., Tilston, M. C., de Leeuw, J., Pohl, F. and Cartigny, M. J. (2020), 'Turbulent diffusion modelling of sediment in turbidity currents: An experimental validation of the rouse approach', *The Depositional Record* **6**(1), 203–216.

Einstein, A. (1906), 'Eine neue bestimmung der moleküldimensionen', *Annalen der Physik* **324**(2), 289–306. 1.2.5, 1.2.5

Elghobashi, S. (1994), 'On predicting particle-laden turbulent flows', *Applied Scientific Research* **52**(4), 309–329.

Ellison, T. H. and Turner, J. S. (1959), 'Turbulent entrainment in stratified flows', *Journal of Fluid Mechanics* **6**(3), 423–448.

Emadzadeh, A., Chiew, Y. M. and Afzalimehr, H. (2010), 'Effect of accelerating and decelerating flows on incipient motion in sand bed streams', *Advances in Water Resources* **33**(9), 1094–1104. 1, 2.1, 3.4.2

Evans, J. C. and Ryan, C. (2005), Time-dependent strength behavior of soil-bentonite slurry wall backfill, *in* 'Waste Containment and Remediation: Proceedings of the Geo-Frontiers 2005 Congress'. 1.2.5

Felix, M. and Peakall, J. (2006), 'Transformation of debris flows into turbidity currents: mechanisms inferred from laboratory experiments', *Sedimentology* **53**(1), 107–123. 1, 1.3, 4.1, 4.4.2, 4.4.2, 5, 5.2.2, 5.3.4

Ferguson, R. A., Kane, I. A., Eggenhuisen, J. T., Pohl, F., Tilston, M., Spychala, Y. T. and Brunt, R. L. (2020), 'Entangled external and internal controls on submarine fan evolution: an experimental perspective', *The Depositional Record* **6**(3), 605–624.

Fernandes, A. M., Buttles, J. and Mohrig, D. (2020), 'Flow substrate interactions in aggrading and degrading submarine channels', *Journal of Sedimentary Research* **90**(6), 573–583.

Fielding, C. R., Alexander, J. and Allen, J. P. (2018), 'The role of discharge variability in the formation and preservation of alluvial sediment bodies', *Sedimentary Geology* **365**, 1–20. 1, 3.1, 3.4.4, 5.3.5

Finley, P. J., Phoe, K. C. and Poh, J. (1966), 'Velocity measurments in a thin turbulent water layer', *La Houille Blanche* **6**, 713–721. 1.1.3

Flemming, B. W. (2002), Chapter six geographic distribution of muddy coasts, *in* 'Proceedings in marine science', Vol. 4, Elsevier, pp. 99–201. 1

Fonnesu, M., Haughton, P., Felletti, F. and McCaffrey, W. (2015), 'Short length-scale variability of hybrid event beds and its applied significance', *Marine and Petroleum Geology* **67**, 583–603.

Fraser, K. H., Poelma, C., Zhou, B., Bazigou, E., Tang, M.-X. and Weinberg, P. D. (2017), 'Ultrasound imaging velocimetry with interleaved images for improved pulsatile arterial flow measurements: a new correction method, experimental and in vivo validation', *Journal of The Royal Society Interface* **14**(127), 20160761.

Freundlich, H. (1935), *Thixotropy (Vol. 1)*, Hermann & cie. 1.2.3, 1.2.5, 3.4.3, 4.4.2, 4.4.2, 5

Furukawa, Y., Reed, A. H. and Zhang, G. (2014), 'Effect of organic matter on estuarine flocculation: a laboratory study using montmorillonite, humic acid, xanthan gum, guar gum and natural estuarine flocs', *Geochemical Transactions* **15**(1), 1–9. 1.2.2

García, M. H. (1993), 'Hydraulic jumps in sediment-driven bottom currents', *Journal of Hydraulic Engineering* **119**(10), 1094–1117.

Garcia, M. H. (1994), 'Depositional turbidity currents laden with poorly sorted sediment', *Journal of Hydraulic Engineering* **120**(11), 1240–1263.

Garcia, M. and Parker, G. (1993), 'Experiments on the entrainment of sediment into suspension by a dense bottom current', *Journal of Geophysical Research: Oceans* **98**(C3), 4793–4807.

Gee, M., Gawthorpe, R., Bakke, K. and Friedmann, S. (2007), 'Seismic geomorphology and evolution of submarine channels from the angolan continental margin', *Journal of Sedimentary Research* **77**(5), 433–446.

Geertsema, M., Clague, J. J., Schwab, J. W. and Evans, S. G. (2006), 'An overview of recent large catastrophic landslides in northern British Columbia, Canada', *Engineering Geology* **83**(1-3), 120–143. 1, 2.1, 3.1

Gelardi, G. and Flatt, R. J. (2016), Working mechanisms of water reducers and superplasticizers, *in* 'Science and Technology of concrete Admixtures', Elsevier, pp. 257–278. 1.5

Genovese, D. B. (2012), 'Shear rheology of hard-sphere, dispersed, and aggregated suspensions, and filler-matrix composites', *Advances in Colloid and Interface Science* **171**, 1–16. 1.2.3, 5

Gerber, G., Diedericks, G. and Basson, G. R. (2011), 'Particle image velocimetry measurements and numerical modeling of a saline density current', *Journal of Hydraulic Engineering* **137**(3), 333–342.

Ghezzehei, T. A. and Or, D. (2001), 'Rheological properties of wet soils and clays under steady and oscillatory stresses', *Soil Science Society of America Journal* **65**(3), 624–637. 1.2.5, 3.4.3

Glüer, C.-C., Blake, G., Lu, Y., Blunt, B. A., Jergas, M. and Genant, H. K. (1995), 'Accurate assessment of precision errors: how to measure the reproducibility of bone densitometry techniques', *Osteoporosis International* **5**(4), 262–270.

Goh, R., Leong, Y.-K. and Lehane, B. (2011), 'Bentonite slurrieszeta potential, yield stress, adsorbed additive and time-dependent behaviour', *Rheologica Acta* **50**(1), 29–38.

Goldfarb, D. J., Glasser, B. J. and Shinbrot, T. (2002), 'Shear instabilities in granular flows', *Nature* **415**(6869), 302–305.

Gorakhki, M. H. and Bareither, C. A. (2015), 'Salinity effects on sedimentation behavior of kaolin, bentonite, and soda ash mine tailings', *Applied Clay Science* **114**, 593–602.

Goring, D. G. and Nikora, V. I. (2002), 'Despiking acoustic doppler velocimeter data', *Journal of Hydraulic Engineering* **128**(1), 117–126.

Gratiot, N. and Manning, A. (2004), 'An experimental investigation of floc characteristics in a diffusive turbulent flow', *Journal of Coastal Research* pp. 105–113. 1.2.3

Gray, T., Alexander, J. and Leeder, M. R. (2006), 'Longitudinal flow evolution and turbulence structure of dynamically similar, sustained, saline density and turbidity currents', *Journal of Geophysical Research: Oceans* **111**(C8).

Gregorova, E., Pabst, W. and Bouchet, J. (2009), 'Influence of particle shape on the viscosity of kaolin suspensions', *Acta Geodynamic Geomater* **672**(45.1), 45–1. 1.2.5

Gust, G. (1976), 'Observations on turbulent-drag reduction in a dilute suspension of clay in sea-water', *Journal of Fluid Mechanics* **75**(1), 29–47. 1.3

Hacker, J., Linden, P. F. and Dalziel, S. B. (1996), 'Mixing in lock-release gravity currents', *Dynamics of Atmospheres and Oceans* **24**(1-4), 183–195.

Hage, S., Cartigny, M. J. B., Sumner, E. J., Clare, M. A., Hughes Clarke, J. E., Talling, P. J., Lintern, D. G., Simmons, S. M., Silva Jacinto, R., Vellinga, A. J. et al. (2019), 'Direct monitoring reveals initiation of turbidity currents from extremely dilute river plumes', *Geophysical Research Letters* **46**(20), 11310–11320.

Hallworth, M. A. and Huppert, H. E. (1998), 'Abrupt transitions in high-concentration, particle-driven gravity currents', *Physics of Fluids* **10**(5), 1083–1087.

Hallworth, M. A., Huppert, H. E., Phillips, J. C. and Sparks, R. S. J. (1996), 'Entrainment into two-dimensional and axisymmetric turbulent gravity currents', *Journal of Fluid Mechanics* **308**, 289–311.

Hampton, M. (1975), 'Competence of fine-grained debris flows', *Journal of Sedimentary Research* **45**(4), 834–844. 1.2.3, 5.3.3

Hampton, M. A. (1972), 'The role of subaqueous debris flow in generating turbidity currents', *Journal of Sedimentary Research* **42**(4).

Hansen, L., LHEUREUX, J. S. and Longva, O. (2011), 'Turbiditic, clay-rich event beds in fjord-marine deposits caused by landslides in emerging clay deposits–palaeoenvironmental interpretation and role for submarine mass-wasting', *Sedimentology* **58**(4), 890–915. 1.5

Haralampides, K., McCorquodale, J. A. and Krishnappan, B. (2003), 'Deposition properties of fine sediment', *Journal of Hydraulic Engineering* **129**(3), 230–234.

Harker, A. and Temple, J. (1988), 'Velocity and attenuation of ultrasound in suspensions of particles in fluids', *Journal of Physics D: Applied Physics* **21**(11), 1576.

Haughton, P., Davis, C., McCaffrey, W. and Barker, S. (2009), 'Hybrid sediment gravity flow deposits–classification, origin and significance', *Marine and Petroleum Geology* **26**(10), 1900–1918. 1, 1.3, 1.3, 4.1, 4.1, 4.4.3, 5, 5.3.4

Heezen, B. C. and Ewing, M. (1955), 'Orleansville earthquake and turbidity currents', *AAPG Bulletin* **39**(12), 2505–2514.

Heijnen, M. S., Clare, M. A., Cartigny, M. J., Talling, P. J., Hage, S., Lintern, D. G., Stacey, C., Parsons, D. R., Simmons, S. M., Chen, Y. et al. (2020), 'Rapidly-migrating and internally-generated knickpoints can control submarine channel evolution', *Nature Communications* **11**(1), 1–15. 1.3, 1.5, 5.3.6

Hermidas, N., Eggenhuisen, J. T., Jacinto, R. S., Luthi, S. M., Toth, F. and Pohl, F. (2018), 'A classification of clay-rich subaqueous density flow structures', *Journal of Geophysical Research: Earth Surface* **123**(5), 945–966. 1.3, 1.3, 4.2, 4.1, 4.4, 4.1, 4.4.1, 4.4.1, 4.4.3, 5, 5.3, 5.3.6

Hogg, R. (2000), 'Flocculation and dewatering', *International Journal of Mineral Processing* **58**(1-4), 223–236.

Hoitink, A. J. F., Wang, Z. B., Vermeulen, B., Huismans, Y. and Kästner, K. (2017), 'Tidal controls on river delta morphology', *Nature Geoscience* **10**(9), 637–645.

Hu, W., Xu, Q., Wang, G., Scaringi, G., Mcsaveney, M. and Hicher, P. (2017), 'Shear resistance variations in experimentally sheared mudstone granules: A possible shear-thinning and thixotropic mechanism', *Geophysical Research Letters* **44**(21), 11040–11050. 1.2.5

Huang, H. (1993), 'Porosity-size relationship of drilling mud flocs: fractal structure', *Clays and Clay Minerals* **41**(3), 373–379. 1.2.3

Huber, M. L., Perkins, R. A., Laesecke, A., Friend, D. G., Sengers, J. V., Assael, M. J., Metaxa, I. N., Vogel, E., Mareš, R. and Miyagawa, K. (2009), 'New international formulation for the viscosity of H2O', *Journal of Physical and Chemical Reference Data* **38**(2), 101–125.

Hughes Clarke, J. E. (2016), 'First wide-angle view of channelized turbidity currents links migrating cyclic steps to flow characteristics', *Nature Communications* **7**(1), 1–13.

Hunter, R. J. (2013), *Zeta potential in colloid science: principles and applications*, Vol. 2, Academic press. 1.2.2, 3.4.3

Hutchins, N. and Choi, K.-S. (2002), 'Accurate measurements of local skin friction coefficient using hot-wire anemometry', *Progress in Aerospace Sciences* **38**(4-5), 421–446. 1.1.3

Ilstad, T., Elverhøi, A., Issler, D. and Marr, J. G. (2004), 'Subaqueous debris flow behaviour and its dependence on the sand/clay ratio: a laboratory study using particle tracking', *Marine Geology* **213**(1-4), 415–438.

Islam, M. A. and Imran, J. (2010), 'Vertical structure of continuous release saline and turbidity currents', *Journal of Geophysical Research: Oceans* **115**(C8).

Iverson, R. M. (1997), 'The physics of debris flows', *Reviews of Geophysics* **35**(3), 245–296.

Iyer, K. P., Sreenivasan, K. R. and Yeung, P. K. (2020), 'Scaling exponents saturate in three-dimensional isotropic turbulence', *Physical Review Fluids* **5**(5), 054605. 1.1.1, 4.4.1

Jacobs, W., Le Hir, P., Van Kesteren, W. and Cann, P. (2011), 'Erosion threshold of sand–mud mixtures', *Continental Shelf Research* **31**(10), S14–S25.

Jeong, S. W. (2010), 'Grain size dependent rheology on the mobility of debris flows', *Geosciences Journal* **14**(4), 359–369.

Ji, Z. (2017), *Hydrodynamics and water quality: modeling rivers, lakes, and estuaries*, John Wiley & Sons. 1

Jiang, Q. and Logan, B. E. (1991), 'Fractal dimensions of aggregates determined from steady-state size distributions', *Environmental Science & Technology* **25**(12), 2031–2038. 1.2.3, 3.4.3

Kane, I. A. and Pontén, A. S. M. (2012), 'Submarine transitional flow deposits in the paleogene gulf of mexico', *Geology* **40**(12), 1119–1122. 1, 4.1, 4.4.1, 4.4.2, 4.4.2, 5.2.2, 5.2.2, 5.3.4

Kane, I. A., Pontén, A. S., Vangdal, B., Eggenhuisen, J. T., Hodgson, D. M. and Spychala, Y. T. (2017), 'The stratigraphic record and processes of turbidity current transformation across deep-marine lobes', *Sedimentology* **64**(5), 1236–1273.

Kaneda, Y., Ishihara, T., Yokokawa, M., Itakura, K. and Uno, A. (2003), 'Energy dissipation rate and energy spectrum in high resolution direct numerical simulations of turbulence in a periodic box', *Physics of Fluids* **15**(2), L21–L24. 1.1.1, 4.4.1

Karimaee Tabarestani, M. and Zarrati, A. R. (2015), 'Sediment transport during flood event: a review', *International Journal of Environmental Science and Technology* **12**(2), 775–788. 1, 3.1, 3.4.4, 5.3.5

Karimi, L. and Salem, A. (2011), 'The role of bentonite particle size distribution on kinetic of cation exchange capacity', *Journal of Industrial and Engineering Chemistry* **17**(1), 90–95. 1.2.4

Kaszuba, M., Corbett, J., Watson, F. M. and Jones, A. (2010), 'High-concentration zeta potential measurements using light-scattering techniques', *Philosophical Transactions of the Royal Society: Mathematical, Physical and Engineering Sciences* **368**(1927), 4439–4451. 1.2.2

Kelessidis, V. C., Tsamantaki, C. and Dalamarinis, P. (2007), 'Effect of ph and electrolyte on the rheology of aqueous wyoming bentonite dispersions', *Applied Clay Science* **38**(1-2), 86–96.

Keren, R. (1989), 'Rheology of mixed kaolinite-montmorillonite suspensions', *Soil Science Society of America Journal* **53**(3), 725–730.

Khelifa, A. and Hill, P. S. (2006), 'Models for effective density and settling velocity of flocs', *Journal of Hydraulic Research* **44**(3), 390–401. 1.2.3

Khripounoff, A., Crassous, P., Bue, N. L., Dennielou, B. and Jacinto, R. S. (2012), 'Different types of sediment gravity flows detected in the var submarine canyon (northwestern mediterranean sea)', *Progress in Oceanography* **106**, 138–153.

Kirby, R. (1986), 'Suspended fine cohesive sediment in the severn estuary and inner bristol channel, uk'.

Kironoto, B. A. and Graf, W. H. (1995), 'Turbulence characteristics in rough non-uniform open-channel flow.', *Proceedings of the Institution of Civil Engineers-Water Maritime and Energy* **112**(4), 336–348.

Kleinhans, M. G. and Grasmeijer, B. T. (2006), 'Bed load transport on the shoreface by currents and waves', *Coastal Engineering* **53**(12), 983–996. 1.5

Klimpel, R. C. and Hogg, R. (1986), 'Effects of flocculation conditions on agglomerate structure', *Journal of Colloid and Interface Science* **113**(1), 121–131. 1.2.3

Kneller, B. (1995), 'Beyond the turbidite paradigm: physical models for deposition of turbidites and their implications for reservoir prediction', *Geological Society, London, Special Publications* **94**(1), 31–49. 1, 4.1

Kneller, B. (2003), 'The influence of flow parameters on turbidite slope channel architecture', *Marine and Petroleum Geology* **20**(6-8), 901–910. 1.1.3, 4.4.1, 5.2.1

Kneller, B. and Buckee, C. (2000), 'The structure and fluid mechanics of turbidity currents: a review of some recent studies and their geological implications', *Sedimentology* **47**, 62–94. 1, 1.3, 1.4, 4.1, 4.1, 4.2, 4.1, 4.3, 4.1, 4.4.1, 4.4.1, 4.4.2, 4.4.3, 5, 5.2.1, 5.2.2, 5.3.5, 5.3.6, 5.3.7

Kneller, B. C., Bennett, S. J. and McCaffrey, W. D. (1999), 'Velocity structure, turbulence and fluid stresses in experimental gravity currents', *Journal of Geophysical Research: Oceans* **104**(C3), 5381–5391.

Kneller, B., Nasr-Azadani, M. M., Radhakrishnan, S. and Meiburg, E. (2016), 'Long-range sediment transport in the world's oceans by stably stratified turbidity currents', *Journal of Geophysical Research: Oceans* **121**(12), 8608–8620.

Kostaschuk, R. A., Luternauer, J. L. and Church, M. A. (1989), 'Suspended sediment hysteresis in a salt-wedge estuary: Fraser river, canada', *Marine Geology* **87**(2-4), 273–285.

Krieger, I. M. (1972), 'Rheology of monodisperse latices', *Advances in Colloid and Interface Science* **3**(2), 111–136. 1.2.5

Krone, R. B. (1962), 'Flume studies of transport of sediment in estrarial shoaling processes.', *Final Report, Hydraulic Engineering and Sanitary Engineering Research Laboratory, University of California* . 1.2.3

Krone, R. B. (1963), A study of rheologic properties of estuarial sediments, Technical report, California University Berkeley Sanitary Engineering Research lab. 1.2.3

Krug, D., Holzner, M., Lüthi, B., Wolf, M., Kinzelbach, W. and Tsinober, A. (2015), 'The turbulent/non-turbulent interface in an inclined dense gravity current', *Journal of Fluid Mechanics* **765**, 303–324.

Kuenen, P. H. (1950), Turbidity currents of high density, *in* '18th International Geological Congress (1948), London, Reports, pt', Vol. 8, pp. 44–52. 1.3

Kuenen, P. H. (1951), 'Properties of turbidity currents of high density'. 1.3

Kuenen, P. H. and Migliorini, C. (1950), 'Turbidity currents as a cause of graded bedding', *The Journal of Geology* **58**(2), 91–127. 1.3

Kuijper, C., Cornelisse, J. and Winterwerp, J. (1990), 'Erosion and deposition characteristics of natural muds: sediments from the westerschelde (near breskens)'.

La Rocca, M. and Bateman, P. (2010), *Experimental and theoretical modelling of 3D gravity currents*, In Tech publishing. Rijeka.

Lagaly, G. (1989), 'Principles of flow of kaolin and bentonite dispersions', *Applied Clay Science* **4**(2), 105–123.

Laird, D. A. (2006), 'Influence of layer charge on swelling of smectites', *Applied Clay Science* **34**(1-4), 74–87.

Lamb, M. P., de Leeuw, J., Fischer, W. W., Moodie, A. J., Venditti, J. G., Nittrouer, J. A., Haught, D. and Parker, G. (2020), 'Mud in rivers transported as flocculated and suspended bed material', *Nature Geoscience* **13**(8), 566–570. 1.2.3, 2.4.2, 2.4.3, 3.4.3, 5.3.4

Laxton, P. B. and Berg, J. C. (2006), 'Relating clay yield stress to colloidal parameters', *Journal of Colloid and Interface Science* **296**(2), 749–755. 1.2.5, 1.3, 4.4.2, 5.3.2

Leeder, M. and Perez-Arlucea, M. (2006), *Physical Processes in Earth and Environmental Sciences*, Blackwell publishing.

Leeder, M. R. (2011), *Sedimentology and sedimentary basins: from turbulence to tectonics*, 2nd edn, John Wiley & Sons. 1, 1.1, 1.3, 1.3, 3.1, 3.4.4, 4.1, 4.4, 4.4.1, 4.4.1, 4.4.1, 5.2.1, 5.3.2, 5.3.4, 5.3.5

Leong, Y., Scales, P. J., Healy, T. W. and Boger, D. V. (1995), 'Effect of particle size on colloidal zirconia rheology at the isoelectric point', *Journal of the American Ceramic Society* **78**(8), 2209–2212.

Levich, V. G. (1962), 'Physicochemical hydrodynamics'. 1.2.3

Lewkowicz, A. K. (1982), 'An improved universal wake function for turbulent boundary layers and some of its consequences', *Z. Flugwiss. Weltraumforsch* **6**(4), 261–266. 1.1.3

Lhermitte, R. and Lemmin, U. (1994), 'Open-channel flow and turbulence measurement by high-resolution doppler sonar', *Journal of Atmospheric and Oceanic Technology* **11**(5), 1295–1308. 1.4

Li, L., Lu, X. and Chen, Z. (2007), 'River channel change during the last 50 years in the middle yangtze river, the jianli reach', *Geomorphology* **85**(3-4), 185–196.

Li, M. Z. and Gust, G. (2000), 'Boundary layer dynamics and drag reduction in flows of high cohesive sediment suspensions', *Sedimentology* **47**(1), 71–86. 1.3, 1.3, 2.4.1, 5.3.2

Lick, W., Huang, H. and Jepsen, R. (1993), 'Flocculation of fine-grained sediments due to differential settling', *Journal of Geophysical Research: Oceans* **98**(C6), 10279–10288. 1.2.3, 2.4.2, 3.4.3, 3.4.3, 4.4.2, 4.4.3, 5.2.1

Lick, W. and Lick, J. (1988), 'Aggregation and disaggregation of fine-grained lake sediments', *Journal of Great Lakes Research* **14**(4), 514–523.

Lin, Y., Cheah, L. K., Phan-Thien, N. and Khoo, B. C. (2016), 'Effect of temperature on rheological behavior of kaolinite and bentonite suspensions', *Colloids and Surfaces A: Physicochemical and Engineering Aspects* **506**, 1–5. 1.2.5, 5.2.1, 5.3.1, 5.3.3

Linne, M. A., Paciaroni, M., Berrocal, E. and Sedarsky, D. (2009), 'Ballistic imaging of liquid breakup processes in dense sprays', *Proceedings of the Combustion Institute* **32**(2), 2147–2161. 1.4, 5.3.7

Liu, J. T., Wang, Y.-H., Yang, R. J., Hsu, R. T., Kao, S.-J., Lin, H.-L. and Kuo, F. H. (2012), 'Cyclone-induced hyper-pycnal turbidity currents in a submarine canyon', *Journal of Geophysical Research: Oceans* **117**(C4).

Lowe, D. R. (1979), Sediment gravity flows: their classification and some problems of application to natural flows and deposits, *in* 'Geology of Continental Slopes', Vol. 27, SEPM Special publication, pp. 75–82.

Lowe, D. R. (1982), 'Sediment gravity flows; ii, depositional models with special reference to the deposits of high-density turbidity currents', *Journal of Sedimentary Research* **52**(1), 279–297. 1.3, 1.3, 4.4.2, 5.3.6

Lowe, D. R. and Guy, M. (2000), 'Slurry-flow deposits in the britannia formation (lower cretaceous), north sea: a new perspective on the turbidity current and debris flow problem', *Sedimentology* **47**(1), 31–70. 1.5

Lunne, T. and Andersen, K. H. (2007), Soft clay shear strength parameters for deepwater geotechnical design, *in* 'Offshore site investigation and geotechnics: confronting new challenges and sharing knowledge', OnePetro.

Malarkey, J., Baas, J. H., Hope, J. A., Aspden, R. J., Parsons, D. R., Peakall, J., Paterson, D. M., Schindler, R. J., Ye, L., Lichtman, I. D., Bass, S. J., Davies, A. G., Manning, A. J. and Thorne, P. D. (2015), 'The pervasive role of biological cohesion in bedform development', *Nature Communications* **6**(1), 1–6. 1.3, 5.3.3

Manica, R. (2012), 'Sediment gravity flows: Study based on experimental simulations', *Hydrodynamics-Natural Water Bodies* **1**, 263–286.

Manning, A. and Dyer, K. (1999), 'A laboratory examination of floc characteristics with regard to turbulent shearing', *Marine Geology* **160**(1-2), 147–170. 1.2.3, 1.2.3, 1.2.3, 2.4.2, 5.2.1

Marino, B. M., Thomas, L. P. and Linden, P. F. (2005), 'The front condition for gravity currents', *Journal of Fluid Mechanics* **536**, 49–78.

Marr, J. G., Harff, P. A., Shanmugam, G. and Parker, G. (2001), 'Experiments on subaqueous sandy gravity flows: the role of clay and water content in flow dynamics and depositional structures', *Geological Society of America Bulletin* **113**(11), 1377–1386. 1.2.3, 3.4.3, 4.1, 4.4.1, 4.4.1, 4.4.1, 4.4.2, 4.4.3, 5.2.2, 5.3.3

Massey, B. S. and Ward-Smith, J. (2012), *Mechanics of fluids*, 9th edn, Taylor & Francis Group. 1.1, 1.1.2, 1.2.5, 1.9, 3.4.3, 5.2.1

McAnally, W. H., Friedrichs, C., Hamilton, D., Hayter, E., Shrestha, P., Rodriguez, H., Sheremet, A. and Teeter, A. (2007), 'Management of fluid mud in estuaries, bays, and lakes. i: Present state of understanding on character and behavior', *Journal of Hydraulic Engineering* **133**(1), 9–22. 1.2.3, 3.4.4, 5.3.4

McAnally, W. H. and Mehta, A. J. (2000), 'Aggregation rate of fine sediment', *Journal of Hydraulic Engineering* **126**(12), 883–892. 1.2.3, 1.2.3, 2.4.2, 3.4.1, 3.4.2, 3.4.3, 3.4.3, 4.4.1, 4.4.2, 4.4.3

McCaffrey, W. D., Choux, C. M., Baas, J. H. and Haughton, P. D. W. (2003), 'Spatio-temporal evolution of velocity structure, concentration and grain-size stratification within experimental particulate gravity currents', *Marine and Petroleum Geology* **20**(6-8), 851–860.

McCave, I. (1984), 'Size spectra and aggregation of suspended particles in the deep ocean', *Deep Sea Research Part A. Oceanographic Research Papers* **31**(4), 329–352. 1.2.3

McCave, I. and Hall, I. R. (2006), 'Size sorting in marine muds: Processes, pitfalls, and prospects for paleoflow-speed proxies', *Geochemistry, Geophysics, Geosystems* **7**(10). 1.2.3, 3.4.3, 4.4.2, 4.4.3

McDowell, D. M. and O'connor, B. (1977), *Hydraulic behaviour of estuaries*, Macmillan International Higher Education. 1.6

Mehta, A. J. (2013), *An introduction to hydraulics of fine sediment transport*, Vol. 38, World Scientific Publishing Company. 1, 5

Mehta, A. J., McAnally Jr, W. H., Hayter, E. J., Teeter, A. M., Schoellhamer, D., Heltzel, S. B. and Carey, W. P. (1989), 'Cohesive sediment transport. ii: Application', *Journal of Hydraulic Engineering* **115**(8), 1094–1112. 1, 2.1

Mehta, A. J. and McAnally, W. H. (2008), Fine grained sediment transport, *in* 'Sedimentation engineering: Processes, measurements, modeling, and practice', pp. 253–306. 1.2.2, 1.2.3, 1.7, 1.8, 1.2.3, 1.1, 2.4.2, 3.4.1, 3.4.3, 4.4.2, 5.3.3, 5.3.4

Meiburg, E. and Kneller, B. (2010), 'Turbidity currents and their deposits', *Annual Review of Fluid Mechanics* **42**, 135–156.

Met-Flow (2002), Ultrasound Velocity Profiler, UVP-DUO Monitor, User's Guide, Version 5.4, Technical report, Met-Flow, Lausanne, Switserland. 1.4, 2.2.3, 3.2.4, 4.2.4

Meunier, A. and Velde, B. (2004), The mineralogy of illite. what is illite?, *in* 'Illite', Springer, pp. 3–62. 1.2.4

Middleton, G. V. (1966a), 'Experiments on density and turbidity currents: I. motion of the head', *Canadian Journal of Earth Sciences* **3**(4), 523–546.

Middleton, G. V. (1966b), 'Experiments on density and turbidity currents: II. uniform flow of density currents', *Canadian Journal of Earth Sciences* **3**(5), 627–637.

Middleton, G. V. (1993), 'Sediment deposition from turbidity currents', *Annual Review of Earth and Planetary Sciences* **21**, 89–114. 1.3, 4.1, 4.1, 5

Middleton, G. V. and Hampton, M. A. (1973), 'Part i. sediment gravity flows: mechanics of flow and deposition'. 1.3, 4.1, 4.4, 5

Mietta, F., Chassagne, C., Manning, A. J. and Winterwerp, J. C. (2009), 'Influence of shear rate, organic matter content, ph and salinity on mud flocculation', *Ocean Dynamics* **59**(5), 751–763. 1.2.3, 1.2.3, 2.4.2, 3.4.3, 4.4.2, 5.2.1, 5.3.1, 5.3.4

Milligan, T. G. and Hill, P. (1998), 'A laboratory assessment of the relative importance of turbulence, particle composition, and concentration in limiting maximal floc size and settling behaviour', *Journal of Sea Research* **39**(3-4), 227–241.

Mitchell, J. K. (1960), 'Fundamental aspects of thixotropy in soils', *Journal of the Soil Mechanics and Foundations Division* **86**(3), 19–52. 1.2.3, 1.2.5, 3.4.3, 4.4.2, 4.4.2, 4.4.3, 5

Mitchell, J. K., Soga, K. et al. (2005), *Fundamentals of soil behavior*, Vol. 3, John Wiley & Sons New York. 1.2.2, 1.4

Mitchener, H. and Torfs, H. (1996), 'Erosion of mud/sand mixtures', *Coastal Engineering* **29**(1-2), 1–25.

Mohrig, D. and Marr, J. G. (2003), 'Constraining the efficiency of turbidity current generation from submarine debris flows and slides using laboratory experiments', *Marine and Petroleum Geology* **20**(6-8), 883–899. 1.3, 1.4, 3.4.3, 4.1, 4.4.1, 4.4.1, 4.4.2, 4.4.3, 5, 5.2.2, 5.3.7

Monin, A. S. and Yaglom, A. M. (2013), *Statistical fluid mechanics, volume II: mechanics of turbulence*, Vol. 2, Courier Corporation. 1.1.1, 1.1.1

Moody, J. A., Shakesby, R. A., Robichaud, P. R., Cannon, S. H. and Martin, D. A. (2013), 'Current research issues related to post-wildfire runoff and erosion processes', *Earth-Science Reviews* **122**, 10–37. 1, 1.5, 2.1, 3.1, 5

Morgenstern, N. (1967), 'Submarine slumping and the initiation of turbidity currents', *Marine Geotechnique* **3**, 189–220.

Mrokowska, M. M. and Rowiński, P. M. (2019), 'Impact of unsteady flow events on bedload transport: A review of laboratory experiments', *Water* **11**(5), 907. 1, 3.1, 3.4.4, 5.3.5

Mueller, S., Llewellin, E. W. and Mader, H. M. (2010), 'The rheology of suspensions of solid particles', *Proceedings of the Royal Society A: Mathematical, Physical and Engineering Sciences* **466**(2116), 1201–1228. 1.2.5

Mulder, T. and Alexander, J. (2001), 'The physical character of subaqueous sedimentary density flows and their deposits', *Sedimentology* **48**(2), 269–299. 1, 1.2, 1.3, 1.3, 1.3, 4.1, 4.1, 4.4, 4.4.1, 5.2.2

Mulder, T., Savoye, B. and Syvitski, J. P. M. (1997), 'Numerical modelling of a mid-sized gravity flow: the 1979 nice turbidity current (dynamics, processes, sediment budget and seafloor impact)', *Sedimentology* **44**(2), 305–326.

Nasser, M. and James, A. (2006), 'The effect of polyacrylamide charge density and molecular weight on the flocculation and sedimentation behaviour of kaolinite suspensions', *Separation and Purification Technology* **52**(2), 241–252. 1.2.2

Negretti, M., Flòr, J. and Hopfinger, E. J. (2017), 'Development of gravity currents on rapidly changing slopes', *Journal of Fluid Mechanics* **833**, 70–97.

Nezu, I., Kadota, A. and Nakagawa, H. (1997), 'Turbulent structure in unsteady depth-varying open-channel flows', *Journal of Hydraulic Engineering* **123**(9), 752–763. 1.1.3, 2.1, 2.1

Nezu, I. and Nakagawa, H. (1993), *Turbulence in Open-Channel Flows: Delft Hydraulics*, International Association for Hydraulic Research, Monograph. 1.1.3, 1.1.3, 1.3, 4.4.1

Nghiem, J. A., Fischer, W. W., Li, G. K. and Lamb, M. P. (2022), 'A mechanistic model for mud flocculation in freshwater rivers', *Journal of Geophysical Research: Earth Surface* p. e2021JF006392.

Nguyen, V. B. Q., Kang, H. and Kim, Y. (2018), 'Effect of clay fraction and water content on rheological properties of sand–clay mixtures', *Environmental Earth Sciences* **77**(16), 1–9. 1.2.5, 1.2.5, 3.4.3, 3.4.3, 5.3.3

Nogueira, H. I., Adduce, C., Alves, E. and Franca, M. J. (2013), 'Analysis of lock-exchange gravity currents over smooth and rough beds', *Journal of Hydraulic Research* **51**(4), 417–431. 1.4, 5, 5.3.7

Nogueira, H. I. S., Adduce, C., Alves, E. and Franca, M. J. (2014), 'Dynamics of the head of gravity currents', *Environmental Fluid Mechanics* **14**(2), 519–540.

Novopashin, S. and Muriel, A. (2002), 'Is the critical reynolds number universal?', *Journal of Experimental and Theoretical Physics* **95**(2), 262–265. 1.1

Nyman, P., Box, W. A. C., Stout, J. C., Sheridan, G. J., Keesstra, S. D., Lane, P. N. J. and Langhans, C. (2020), 'Debris-flow-dominated sediment transport through a channel network after wildfire', *Earth Surface Processes and Landforms* **45**(5), 1155–1167.

Pabst, W. (2004), 'Fundamental considerations on suspension rheology', *Ceramics Silikaty* **48**(1), 6–13. 1.2.5

Palomino, A. M. and Santamarina, J. C. (2005), 'Fabric map for kaolinite: effects of ph and ionic concentration on behavior', *Clays and Clay Minerals* **53**(3), 211–223.

Paola, C., Straub, K., Mohrig, D. and Reinhardt, L. (2009), 'The unreasonable effectiveness of stratigraphic and geomorphic experiments', *Earth-Science Reviews* **97**(1-4), 1–43.

Parker, G., Garcia, M., Fukushima, Y. and Yu, W. (1987), 'Experiments on turbidity currents over an erodible bed', *Journal of Hydraulic Research* **25**(1), 123–147.

Parsapour-Moghaddam, P., Brennan, C. P., Rennie, C. D., Elvidge, C. K. and Cooke, S. J. (2019), 'Impacts of channel morphodynamics on fish habitat utilization', *Environmental Management* **64**(3), 272–286. 1

Parsons, D. R., Schindler, R. J., Hope, J. A., Malarkey, J., Baas, J. H., Peakall, J., Manning, A. J., Ye, L., Simmons, S., Paterson, D. M., Aspden, R. J., Bass, S. J., Davies, A. G., Lichtman, I. D. and Thorne, P. D. (2016), 'The role of biophysical cohesion on subaqueous bed form size', *Geophysical Research Letters* **43**(4), 1566–1573. 1.3, 5.3.3

Parsons, J. D., Friedrichs, C. T., Traykovski, P. A., Mohrig, D., Imran, J., Syvitski, J. P., Parker, G., Puig, P., Buttles, J. L. and García, M. H. (2007), 'The mechanics of marine sediment gravity flows', *Continental Margin Sedimentation: from sediment transport to sequence stratigraphy* **37**, 275–334.

Partheniades, E. (1965), 'Erosion and deposition of cohesive soils', *Journal of the Hydraulics Division* **91**(1), 105–139. 1, 2.1, 5.3.4

Partheniades, E. (2009), *Cohesive sediments in open channels: erosion, transport and deposition*, Butterworth-Heinemann. 1.2, 1.2.1, 1.2.2, 1.2.3, 1.2.3, 1.1, 1.5, 2.4.2, 4.4.1, 4.4.2, 5

Patacci, M., Haughton, P. D. W. and McCaffrey, W. D. (2014), 'Rheological complexity in sediment gravity flows forced to decelerate against a confining slope, braux, se francecurrent ripples', *Journal of Sedimentary Research* **84**(4), 270–277.

Paterson, D., Crawford, R. and Little, C. (1990), 'Subaerial exposure and changes in the stability of intertidal estuarine sediments', *Estuarine, Coastal and Shelf Science* **30**(6), 541–556. 1.3, 5.3.3

Peakall, J., Ashworth, P. and Best, J. (1996), 'Physical modelling in fluvial geomorphology: principles, applications and unresolved issues', *The Scientific Nature of Geomorphology* pp. 221–253.

Peakall, J., Best, J., Baas, J. H., Hodgson, D. M., Clare, M. A., Talling, P. J., Dorrell, R. M. and Lee, D. R. (2020), 'An integrated process-based model of flutes and tool marks in deep-water environments: Implications for palaeohydraulics, the bouma sequence and hybrid event beds', *Sedimentology* **67**(4), 1601–1666. 1.3, 4.1, 4.4.3, 5

Peakall, J., Felix, M., McCaffrey, B. and Kneller, B. (2001), 'Particulate gravity currents: Perspectives', *Particulate Gravity Currents* pp. 1–8.

Peakall, J., Kane, I. A., Masson, D. G., Keevil, G., McCaffrey, W. and Corney, R. (2012), 'Global (latitudinal) variation in submarine channel sinuosity', *Geology* **40**(1), 11–14.

Peakall, J., McCaffrey, B. and Kneller, B. (2000), 'A process model for the evolution, morphology, and architecture of sinuous submarine channels', *Journal of Sedimentary Research* **70**(3), 434–448.

Peakall, J. and Sumner, E. J. (2015), 'Submarine channel flow processes and deposits: A process-product perspective', *Geomorphology* **244**, 95–120.

Pedocchi, F. and García, M. H. (2012), 'Acoustic measurement of suspended sediment concentration profiles in an oscillatory boundary layer', *Continental Shelf Research* **46**, 87–95. 1.4

Persson, A. (2005), 'The coriolis effect', *History of Meteorology* **2**, 1–24.

Peterfi, T. (1927), 'Arch entwicklungsmech', *Organ* **112**, 680–695. 1.2.3, 1.2.5, 3.4.3, 4.4.2, 4.4.2, 4.4.3, 5

Pickering, K. T. and Hiscott, R. N. (2015), *Deep marine systems: processes, deposits, environments, tectonics and sedimentation*, John Wiley & Sons. 1.3, 1.3, 4.1, 5

Piper, D. J., Cochonat, P. and Morrison, M. L. (1999), 'The sequence of events around the epicentre of the 1929 grand banks earthquake: initiation of debris flows and turbidity current inferred from sidescan sonar', *Sedimentology* **46**(1), 79–97.

Poelma, C. (2017), 'Ultrasound imaging velocimetry: a review', *Experiments in Fluids* **58**(1), 1–28.

Poelma, C., Mari, J. M., Foin, N., Tang, M., Krams, R., Caro, C. G., Weinberg, P. D. and Westerweel, J. (2011), '3d flow reconstruction using ultrasound piv', *Experiments in Fluids* **50**(4), 777–785.

Poelma, C., Van Der Mijle, R., Mari, J., Tang, M., Weinberg, P. D. and Westerweel, J. (2012), 'Ultrasound imaging velocimetry: Toward reliable wall shear stress measurements', *European Journal of Mechanics-B/Fluids* **35**, 70–75.

Poelma, C., Westerweel, J. and Ooms, G. (2006), 'Turbulence statistics from optical whole-field measurements in particle-laden turbulence', *Experiments in Fluids* **40**(3), 347–363. 1.4, 5.3.7

Pohl, F., Eggenhuisen, J. T., Cartigny, M. J. B., Tilston, M. C., de Leeuw, J. and Hermidas, N. (2020a), 'The influence of a slope break on turbidite deposits: An experimental investigation', *Marine Geology* **424**, 106160.

Pohl, F., Eggenhuisen, J. T., Kane, I. A. and Clare, M. A. (2020b), 'Transport and burial of microplastics in deep-marine sediments by turbidity currents', *Environmental Science & Technology* **54**(7), 4180–4189. 1

Pope, S. B. (2000), *Turbulent flows*, Cambridge university press. 1.1, 1.1.1, 1.1.1, 1.1.1, 1.1.2, 1.2, 1.1.3, 3.3.3, 4.1, 4.1, 4.4.1, 4.4.2, 5.2.1

Portela, L. I. and Reis, M. M. (2005), Analysis of cohesive sediment transport in decelerating and accelerating flow, *in* 'Coastal Engineering 2004: (In 4 Volumes)', World Scientific, pp. 1818–1829.

Postma, G., Nemec, W. and Kleinspehn, K. L. (1988), 'Large floating clasts in turbidites: a mechanism for their emplacement', *Sedimentary Geology* **58**(1), 47–61.

Qingyang, S. (2009), 'Velocity distribution and wake-law in gradually decelerating flows', *Journal of Hydraulic Research* **47**(2), 177–184.

R. Lowe, D., Guy, M. and Palfrey, A. (2003), 'Facies of slurry-flow deposits, britannia formation (lower cretaceous), north sea: implications for flow evolution and deposit geometry', *Sedimentology* **50**(1), 45–80. 1.5

Reidenbach, M., Limm, M., Hondzo, M. and Stacey, M. (2010), 'Effects of bed roughness on boundary layer mixing and mass flux across the sediment-water interface', *Water Resources Research* **46**(7).

Ren, Y., Yang, S., Andersen, K. H., Yang, Q. and Wang, Y. (2021), 'Thixotropy of soft clay: A review', *Engineering Geology* **287**, 106097. 1.2.3, 1.2.3, 1.2.5, 3.4.3, 3.4.4, 4.4.1, 4.4.2, 4.4.2, 4.4.3, 5, 5.3.1, 5.3.2

Reneau, S. L., Katzman, D., Kuyumjian, G. A., Lavine, A. and Malmon, D. V. (2007), 'Sediment delivery after a wildfire', *Geology* **35**(2), 151–154. 1, 2.1, 2.4.3, 3.1

Richardson, J. and Zaki, W. (1954), 'The sedimentation of a suspension of uniform spheres under conditions of viscous flow', *Chemical Engineering Science* **3**(2), 65–73. 1.2.5

Rinaldi, V. A. and Clariá Jr, J. J. (2016), 'Time dependent stress–strain behavior of bentonite slurries; effect of thixotropy', *Powder Technology* **291**, 311–321. 1.3, 5.3.2

Ross, M. A. and Mehta, A. J. (1989), 'On the mechanics of lutoclines and fluid mud', *Journal of Coastal Research* pp. 51–62.

Roy, A. G., Buffin-Belanger, T., Lamarre, H. and Kirkbride, A. D. (2004), 'Size, shape and dynamics of large-scale turbulent flow structures in a gravel-bed river', *Journal of Fluid Mechanics* **500**, 1–27.

Russel, W., Saville, D. and Schowalter, W. (1989), *Collodial Dispersions*, Cambridge University Press. 1.2.5

Safak, I., Allison, M. and Sheremet, A. (2013), 'Floc variability under changing turbulent stresses and sediment availability on a wave energetic muddy shelf', *Continental Shelf Research* **53**, 1–10. 1.2.3, 1.2.3, 2.4.2, 3.4.3, 4.4.2, 5.2.1, 5.3.4

Sandham, N. (1991), 'An alternative formulation of the outer law of the turbulent boundary layer'. 1.1.3

Sankey, J. B., Kreitler, J., Hawbaker, T. J., McVay, J. L., Miller, M. E., Mueller, E. R., Vaillant, N. M., Lowe, S. E. and Sankey, T. T. (2017), 'Climate, wildfire, and erosion ensemble foretells more sediment in western USA watersheds', *Geophysical Research Letters* **44**(17), 8884–8892. 1, 2.1, 2.4.3, 3.1

Scheeres, D. J., Hartzell, C. M., Sanchez, P. and Swift, M. (2010), 'Scaling forces to asteroid surfaces: The role of cohesion', *Icarus* **210**(2), 968–984.

Schieber, J., Li, Z., Yawar, Z., Cao, X., Ashley, T. and Wilson, R. (2022), 'Kaolinite deposition from moving suspensions: The roles of flocculation, salinity, suspended sediment concentration and flow velocity/bed shear', *Sedimentology* .

Schindler, R. J., Parsons, D. R., Ye, L., Hope, J. A., Baas, J. H., Peakall, J., Manning, A. J., Aspden, R. J., Malarkey, J., Simmons, S., Paterson, D. M., Lichtman, I. D., Davies, A. G., Thorne, P. D. and Bass, S. J. (2015), 'Sticky stuff: Redefining bedform prediction in modern and ancient environments', *Geology* **43**(5), 399–402. 1, 4.4.3, 5.3.3, 5.3.4

Schlichting, H. and Gersten, K. (2016), *Boundary-layer theory*, Springer Berlin Heidelberg. 1.1.2, 1.2, 1.1.3, 1.1.3, 1.2.3, 2.2.1, 4.1, 4.4.1

Segalini, A., Örlü, R. and Alfredsson, P. H. (2013), 'Uncertainty analysis of the von kármán constant', *Experiments in Fluids* **54**(2), 1–9. 1.1.3

Sequeiros, O. E., Mosquera, R. and Pedocchi, F. (2018), 'Internal structure of a self-accelerating turbidity current', *Journal of Geophysical Research: Oceans* **123**(9), 6260–6276.

Shahriar, A. R., Abedin, M. Z. and Jadid, R. (2018), 'Thixotropic aging and its effect on 1-d compression behavior of soft reconstituted clays', *Applied Clay Science* **153**, 217–227.

Shaikh, S. M. R., Nasser, M. S., Hussein, I., Benamor, A., Onaizi, S. A. and Qiblawey, H. (2017), 'Influence of polyelectrolytes and other polymer complexes on the flocculation and rheological behaviors of clay minerals: A comprehensive review', *Separation and Purification Technology* **187**, 137–161. 1.2.1, 1.2.2, 1.2.4, 3.4.3, 5

Shakeel, A., Kirichek, A. and Chassagne, C. (2019), 'Is density enough to predict the rheology of natural sediments?', *Geo-Marine Letters* **39**(5), 427–434. 1.3, 5.3.1, 5.3.3

Shakeel, A., Kirichek, A. and Chassagne, C. (2020), 'Effect of pre-shearing on the steady and dynamic rheological properties of mud sediments', *Marine and Petroleum Geology* **116**, 104338.

Shakeel, A., Kirichek, A. and Chassagne, C. (2021), 'Rheology and yielding transitions in mixed kaolinite/bentonite suspensions', *Applied Clay Science* **211**, 106206.

Shanmugam, G. (2000), '50 years of the turbidite paradigm (1950s 1990s): deep-water processes and facies modelsa critical perspective', *Marine and Petroleum Geology* **17**(2), 285–342. 1.3

Shields, A. (1936), 'Anwendung der aehnlichkeitsmechanik und der turbulenzforschung auf die geschiebebewegung', *PhD Thesis Technical University Berlin* .

Shoaib, M. and Bobicki, E. R. (2021), 'Rheological implications of ph induced particle–particle association in aqueous suspension of an anisotropic charged clay', *Soft Matter* **17**(34), 7822–7834.

Simpson, J. E. (1997), *Gravity currents: In the environment and the laboratory*, Cambridge university press. 1.4, 4.1, 4.4.1

Skempton, A. and Northey, R. (1952), 'The sensitivity of clays', *Geotechnique* **3**(1), 30–53. 1.2.3, 1.2.5, 4.4.1, 5.3.1

Smith, H. G., Sheridan, G. J., Lane, P. N., Nyman, P. and Haydon, S. (2011), 'Wildfire effects on water quality in forest catchments: a review with implications for water supply', *Journal of Hydrology* **396**(1-2), 170–192. 1, 2.1

Sobocinska, A. and Baas, J. H. (2022), 'Effect of biological polymers on mobility and run-out distance of cohesive and non-cohesive sediment gravity flows', *Marine Geology* p. 106904.

Son, M. and Hsu, T. (2011), 'The effects of flocculation and bed erodibility on modeling cohesive sediment resuspension', *Journal of Geophysical Research: Oceans* **116**(C3).

Song, T. and Chiew, Y. M. (2001), 'Turbulence measurement in nonuniform open-channel flow using acoustic doppler velocimeter (adv)', *Journal of Engineering Mechanics* **127**(3), 219–232.

Song, T. and Graf, W. H. (1996), 'Velocity and turbulence distribution in unsteady open-channel flows', *Journal of Hydraulic Engineering* **122**(3), 141–154.

Soulsby, R. (1997), *Dynamics of marine sands*, Thomas Telford London, UK. 1.1.3, 1.2.3, 1.4

Soutter, E. L., Bell, D., Cumberpatch, Z. A., Ferguson, R. A., Spychala, Y. T., Kane, I. A. and Eggenhuisen, J. T. (2021), 'The influence of confining topography orientation on experimental turbidity currents and geological implications', *Frontiers in Earth Science* **8**, 540633.

Spazzini, P. G., Iuso, G., Onorato, M., Zurlo, N. and Di Cicca, G. M. (2001), 'Unsteady behavior of back-facing step flow', *Experiments in Fluids* **30**(5), 551–561.

Spearman, J. (2017), 'An examination of the rheology of flocculated clay suspensions', *Ocean Dynamics* **67**(3), 485–497. 1.2.5

Spearman, J. and Manning, A. J. (2017), 'On the hindered settling of sand-mud suspensions', *Ocean Dynamics* **67**(3), 465–483. 1.2.3, 1.2.3, 3.4.1, 5.3.3, 5.3.4

Spencer, K. L., Wheatland, J. A., Bushby, A. J., Carr, S. J., Droppo, I. G. and Manning, A. J. (2021), 'A structure–function based approach to floc hierarchy and evidence for the non-fractal nature of natural sediment flocs', *Scientific Reports* **11**(1), 1–10. 1.2.3

Spencer, K., Wheatland, J., Carr, S., Manning, A., Bushby, A., Gu, C., Botto, L. and Lawrence, T. (2022), 'Quantification of 3-dimensional structure and properties of flocculated natural suspended sediment', *Water Research* **222**, 118835. 1.2.3

Spychala, Y. T., Hodgson, D. M., Prélat, A., Kane, I. A., Flint, S. S. and Mountney, N. P. (2017), 'Frontal and lateral submarine lobe fringes: comparing sedimentary facies, architecture and flow processes', *Journal of Sedimentary Research* **87**(1), 75–96.

Stoesser, T., McSherry, R. and Fraga, B. (2015), 'Secondary currents and turbulence over a non-uniformly roughened open-channel bed', *Water* **7**(9), 4896–4913.

Struiksma, N., Olesen, K., Flokstra, C. and De Vriend, H. (1985), 'Bed deformation in curved alluvial channels', *Journal of Hydraulic Research* **23**(1), 57–79.

Sturm, M. and Matter, A. (1978), 'Turbidites and varves in lake brienz (switzerland): deposition of clastic detritus by density currents', *Modern and Ancient Lake Sediments* pp. 147–168.

Sumner, E. J., Talling, P. J. and Amy, L. A. (2009), 'Deposits of flows transitional between turbidity current and debris flow', *Geology* **37**(11), 991–994. 1.2.3, 1.3, 1.3, 4.1, 4.1, 4.4, 4.4.2, 4.4.3, 5, 5.3.3

Sumner, R., Munkler, J., Carriere, S. and Shook, C. (2000), 'Rheology of kaolin slurries containing large silica particles', *Journal of Hydrology and Hydromechanics/Vodohospodarsky Casopis* **48**(2), 110–124.

Sun, S., Weber-Shirk, M. and Lion, L. W. (2016), 'Characterization of flocs and floc size distributions using image analysis', *Environmental Engineering Science* **33**(1), 25–34. 1.2.3, 3.4.3

Sun, Y. and Huang, H. (2015), Effect of rheology on drilling mud loss in a natural fracture, *in* '49th US Rock Mechanics/Geomechanics Symposium', OnePetro. 1.2.5

Swanson, F. J. (1981), 'Fire and geomorphic processes', *in: Mooney, H.A., et al., eds., Fire Regimes and Ecosystem Properties: U.S. Department of Agriculture Forest Service General Technical Report WO-26* pp. 401–444. 1, 2.1, 3.1

Sylvester, Z. and Lowe, D. R. (2004), 'Textural trends in turbidites and slurry beds from the oligocene flysch of the east carpathians, romania', *Sedimentology* **51**(5), 945–972. 1.5, 4.4.2, 5.2.2, 5.3.4

Syvitski, J. P., Asprey, K. and Leblanc, K. (1995), 'In-situ characteristics of particles settling within a deep-water estuary', *Deep Sea Research Part II: Topical Studies in Oceanography* **42**(1), 223–256. 1.2.2

Takahashi, T. (2014), *Debris flow: mechanics, prediction and countermeasures*, 2nd edn, CRC Press. 1.2.5, 1.3, 5.3.3

Takeda, Y. (1991), 'Development of an ultrasound velocity profile monitor', *Nuclear Engineering and Design* **126**(2), 277–284. 1.4, 2.2.3, 5.3.7

Takeda, Y. (2012), *Ultrasonic Doppler velocity profiler for fluid flow*, Vol. 101, Springer Science & Business Media.

Talling, P. J., Allin, J., Armitage, D. A., Arnott, R. W. C., Cartigny, M. J. B., Clare, M. A., Felletti, F., Covault, J. A., Girardclos, S., Hansen, E., Hill, P. R., Hiscott, R. N., Hogg, A. J., Clarke, J. H., Jobe, Z. R., Malgesini, G., Mozzato, A., Naruse, H., Parkinson, S., Peel, F. J., Piper, D. J. W., Pope, E., Postma, G., Rowley, P., Sguazzini, A., Stevenson, C. J., Sumner, E. J., Sylvester, Z., Watts, C. and Xu, J. (2015), 'Key future directions for research on turbidity currents and their deposits', *Journal of Sedimentary Research* **85**(2), 153–169. 1.3, 1.5, 4.1, 5, 5.3.6

Talling, P. J., Masson, D. G., Sumner, E. J. and Malgesini, G. (2012), 'Subaqueous sediment density flows: Depositional processes and deposit types', *Sedimentology* **59**(7), 1937–2003. 1, 1.2, 1.3, 2.1, 3.1, 3.4.4, 4.1, 5, 5.3, 5.3.4, 5.3.5

Talling, P. J., Paull, C. K. and Piper, D. J. W. (2013), 'How are subaqueous sediment density flows triggered, what is their internal structure and how does it evolve? direct observations from monitoring of active flows', *Earth-Science Reviews* **125**, 244–287. 1.2.5, 1.4, 4.4.1, 5, 5.3.6

Talling, P. J., Wynn, R. B., Masson, D. G., Frenz, M., Cronin, B. T., Schiebel, R., Akhmetzhanov, A. M., Dallmeier-Tiessen, S., Benetti, S., Weaver, P. P. E., Georgiopoulou, A., Zuhlsdorff, C. and Amy, L. A. (2007), 'Onset of submarine debris flow deposition far from original giant landslide', *Nature* **450**(7169), 541–544. 1, 4.1, 4.4.1, 4.4.2, 4.4.2, 5.2.2, 5.2.2, 5.3.4

Teh, E.-J., Leong, Y.-K., Liu, Y., Fourie, A. and Fahey, M. (2009), 'Differences in the rheology and surface chemistry of kaolin clay slurries: The source of the variations', *Chemical Engineering Science* **64**(17), 3817–3825.

Telesh, I. V. and Khlebovich, V. V. (2010), 'Principal processes within the estuarine salinity gradient: a review', *Marine Pollution Bulletin* **61**(4-6), 149–155.

Tennekes, H. and Lumley, J. L. (1972), *A first course in turbulence*, MIT press. 1.1, 1.1, 1.1.1, 1.1.1, 1.1.2, 1.1.2, 1.1.3, 1.1.3, 3.3.3, 3.4.3, 5.2.1

Thakur, S. C., Ooi, J. Y. and Ahmadian, H. (2016), 'Scaling of discrete element model parameters for cohesionless and cohesive solid', *Powder Technology* **293**, 130–137.

Thiene, M., Shaw, W. D. and Scarpa, R. (2017), 'Perceived risks of mountain landslides in italy: stated choices for subjective risk reductions', *Landslides* **14**(3), 1077–1089.

Thomas, R., Schindfessel, L., McLelland, S., Creëlle, S. and De Mulder, T. (2017), 'Bias in mean velocities and noise in variances and covariances measured using a multistatic acoustic profiler: The nortek vectrino profiler', *Measurement Science and Technology* **28**(7), 075302. 1.4, 2.2.3

Tihon, J., Pěnkavová, V., Havlica, J. and Šimčík, M. (2012), 'The transitional backward-facing step flow in a water channel with variable expansion geometry', *Experimental Thermal and Fluid Science* **40**, 112–125.

Toms, B. A. (1949), 'Some observations on the flow of linear polymer solutions through straight tubes at large reynolds numbers', *Proc. First Int. Conger. on Rheology* **2**, 135–141. 1.3

Toorman, E. A. (1997), 'Modelling the thixotropic behaviour of dense cohesive sediment suspensions', *Rheologica Acta* **36**(1), 56–65. 1.2.3

Toorman, E., Bruens, A., Kranenburg, C. and Winterwerp, J. (2002), Interaction of suspended cohesive sediment and turbulence, *in* 'Proceedings in Marine Science', Vol. 5, Elsevier, pp. 7–23.

Torfs, H., Mitchener, H., Huysentruyt, H. and Toorman, E. (1996), 'Settling and consolidation of mud/sand mixtures', *Coastal Engineering* **29**(1-2), 27–45. 1.2.3, 5.3.3

Tropea, C. (1983), 'A note concerning the use of a one-component lda to measure shear stress terms', *Experiments in Fluids* **1**(4), 209–210. 1.4, 3.2.3

Tropea, C., Yarin, A. L., Foss, J. F. et al. (2007), *Springer handbook of experimental fluid mechanics*, Vol. 1, Springer. 1.4, 5.3.7

Tsai, C., Iacobellis, S. and Lick, W. (1987), 'Flocculation of fine-grained lake sediments due to a uniform shear stress', *Journal of Great Lakes Research* **13**(2), 135–146.

Tsujimoto, T., Mori, A., Okabe, T. and Ohmoto, T. (1990), 'Nonequilibrium sediment transport: A generalized model', *Journal Hydroscience Hydraulic Engineering* **7**(2), 1–25.

Tunnicliffe, J., Brierley, G., Fuller, I. C., Leenman, A., Marden, M. and Peacock, D. (2018), 'Reaction and relaxation in a coarse-grained fluvial system following catchment-wide disturbance', *Geomorphology* **307**, 50–64.

Turner, J. S. (1986), 'Turbulent entrainment: the development of the entrainment assumption, and its application to geophysical flows', *Journal of Fluid Mechanics* **173**, 431–471.

Uncles, R. J. and Mitchell, S. B. (2017), *Estuarine and coastal hydrography and sediment transport*, Cambridge University Press. 1, 3.1, 3.4.4

Van Kessel, T. and Blom, C. (1998), 'Rheology of cohesive sediments: comparison between a natural and an artificial mud', *Journal of Hydraulic Research* **36**(4), 591–612.

van Leussen, W. (1994), 'Estuarine macroflocs and their role in fine-grained sediment transport', *Ph. D. Thesis, University of Utrecht* . 1.2.3, 3.4.3

Van Maren, D. (2007), 'Grain size and sediment concentration effects on channel patterns of silt-laden rivers', *Sedimentary Geology* **202**(1-2), 297–316.

Van Maren, D. S., Winterwerp, J. C., Wang, Z. Y. and Pu, Q. (2009), 'Suspended sediment dynamics and morphodynamics in the yellow river, china', *Sedimentology* **56**(3), 785–806.

van Olphen, H. (1977), *An introduction to clay colloid chemistry: for clay technologists, geologists, and soil scientists*, Wiley. 1, 1.2, 1.2.1, 1.2.2, 1.2.3, 1.2.3, 1.2.4, 1.5, 5, 5.3.1

Van Prooijen, B. C. and Winterwerp, J. C. (2010), 'A stochastic formulation for erosion of cohesive sediments', *Journal of Geophysical Research: Oceans* **115**(C1).

Van Rijn, L. C. (1984), 'Sediment transport, part i: bed load transport', *Journal of Hydraulic Engineering* **110**(10), 1431–1456.

Van Rijn, L. C. (2011), 'Coastal erosion and control', *Ocean & Coastal Management* **54**(12), 867–887. 1.1.3

Venditti, J. G., Best, J. L., Church, M. and Hardy, R. J. (2013), *Coherent Flow Structures at Earth's Surface*, John Wiley & Sons.

Verwey, E. J., Overbeek, J. T. G. and van Nes, K. (1948), 'Theory of the stability of lyophobic colloids: the interaction of sol particles having an electric double layer'. 1.2.2

Virk, P. S. (1975), 'Drag reduction fundamentals', *AIChE Journal* **21**(4), 625–656. 1.3

Waltham, D. (2004), 'Flow transformations in particulate gravity currents', *Journal of Sedimentary Research* **74**(1), 129–134.

Wan, Z. (1982), *Bed Material Movement in Hyperconcentrated Flow*, Series paper 31, Institute of Hydrodynamics and Hydraulic Engineering, Technical University of Denmark. 1.2.5, 1.2.5, 2.2.4, 3.2.4, 3.4.3, 3.4.3, 4.2.4, 4.7, 4.8, 4.4.2, 5.2.1, 5.3.3

Wan, Z. and Wang, Z. (1994), *Hyperconcentrated Flow*, CRC press. 1.2.5, 2.1

Wang, Z. and Larsen, P. (1994), 'Turbulent structure of water and clay suspensions with bed load', *Journal of Hydraulic Engineering* **120**(5), 577–600. 1, 2.1

Wang, Z. and Plate, E. C. J. (1996), 'A preliminary study on the turbulence structure of flows of non-newtonian fluid', *Journal of Hydraulic Research* **34**(3), 345–361. 1, 1.2, 1.3, 2.2.1, 3.4.2, 4.1, 4.4, 4.4.1, 4.4.1, 4.4.3, 5, 5.2.1

Wells, M. G. and Dorrell, R. M. (2021), 'Turbulence processes within turbidity currents', *Annual Review of Fluid Mechanics* **53**, 59–83. 1.3, 4.1, 4.1, 4.2, 4.1, 4.1, 4.4.1, 4.4.1, 4.4.2, 4.4.3

White, F. M. (2016), *Fluid Mechanics*, McGraw-Hill New York. 1.1, 1.2.5, 1.9, 2.2.1, 2.4, 2.2.1

Whitehouse, R. J. S., Soulsby, R. L., Roberts, W. and Mitchener, H. J. (2000), *Dynamics of estuarine muds*, Thomas Telford. 1, 1.2, 1.2.2, 1.2.3, 1.3, 1.4, 2.1, 3.4.2, 3.4.3, 3.4.4, 5.3

Winterwerp, J. C. (2002), 'On the flocculation and settling velocity of estuarine mud', *Continental Shelf Research* **22**(9), 1339–1360. 1.2.3, 1.2.3, 2.4.2, 3.4.1, 3.4.2, 3.4.3, 3.4.3, 4.4.2

Winterwerp, J. C. and Van Kesteren, W. G. M. (2004), *Introduction to the physics of cohesive sediment dynamics in the marine environment*, Elsevier. 1, 1.3, 1.2.2, 1.2.3, 1.2.3, 1.2.4, 1.1, 1.3, 1.5, 2.1, 3.1, 3.4.1, 3.4.2, 3.4.4, 4.4.2, 5, 5.3.2, 5.3.4

Wright, J. D. and Baas, J. H. (2013), 'Despiking ultrasonic doppler velocity-profiling data', *Journal of Sedimentary Research* **83**(11), 955–962.

Wypych, F. (2015), Clay surfaces: Chemical modification, *in* 'Encyclopedia of Surface and Colloid Science, Third Edition', CRC Press, pp. 1160–1176. 1.2.1, 1.2.2, 3.4.3

Xu, C. and Dong, P. (2017), 'A dynamic model for coastal mud flocs with distributed fractal dimension', *Journal of Coastal Research* **33**(1), 218–225. 1.2.3

Xu, J., Noble, M. and Rosenfeld, L. K. (2004), 'In-situ measurements of velocity structure within turbidity currents', *Geophysical Research Letters* **31**(9). 1.3, 1.5, 4.1, 5.3.6

Xu, J. P. (2010), 'Normalized velocity profiles of field-measured turbidity currents', *Geology* **38**(6), 563–566.

Yang, S., Xu, W. and Yu, G. (2006), 'Velocity distribution in a gradually accelerating free surface flow', *Advances in Water Resources* **29**(12), 1969–1980. 1, 2.1, 3.4.2, 5.3.5

Ye, L., Manning, A. J. and Hsu, T. (2020), 'Oil-mineral flocculation and settling velocity in saline water', *Water Research* **173**, 115569. 1.2.2

Yong, R. H. and Warkentin, B. P. (1975), *Soil properties and behaviour*, Elsevier, Amsterdam. 1.2, 1.2.2, 1.2.4

Yu, B., Ma, Y. and Qi, X. (2013), 'Experimental study on the influence of clay minerals on the yield stress of debris flows', *Journal of Hydraulic Engineering* **139**(4), 364–373. 1.2.3, 1.2.5, 1.2.5, 3.4.3, 3.4.3, 4.4.1, 5.2.1, 5.3.1

Zhang, F., Lanning, C., Mazzaro, L., Barker, A. J., Gates, P. E., Strain, W. D., Fulford, J., Gosling, O. E., Shore, A. C., Bellenger, N. G., Rech, B., Chen, J., Chen, J. and Shandas, R. (2011), 'In vitro and preliminary in vivo validation of echo particle image velocimetry in carotid vascular imaging', *Ultrasound in Medicine & Biology* **37**(3), 450–464.

Zhang, Q., Bing, Y. and Onyx, W. H. (2009), 'Fine sediment carrying capacity of combined wave and current flows', *International Journal of Sediment Research* **24**(4), 425–438.

Zhang, X., Liu, X., Wu, H., Liu, S., Zhu, Y., Bi, Z. and Xu, Z. (2022), 'Experimental study on the incipient movement of muddy clay under different salinity conditions', *The Scientific World Journal* **2022**.

Zhang, X. W., Kong, L. W., Yang, A. W. and Sayem, H. M. (2017), 'Thixotropic mechanism of clay: A microstructural investigation', *Soils and Foundations* **57**(1), 23–35. 1.2.3, 5.3.1

Zhong, G. and Peng, X. (2021), 'Transport and accumulation of plastic litter in submarine canyonsthe role of gravity flows', *Geology* **49**(5), 581–586. 1

Zhu, Z., Wang, H. and Peng, D. (2017), 'Dependence of sediment suspension viscosity on solid concentration: A simple general equation', *Water* **9**(7), 474. 1.2.5

Zou, X., Ma, Z., Hu, W., Wang, J., Song, H., Hu, X. and Tao, W. (2015), 'B-mode ultrasound imaging measurement and 3d reconstruction of submerged topography in sediment-laden flow', *Measurement* **72**, 20–31.

Zou, X., Song, H., Wang, C. and Ma, Z. (2016), 'Relationships between b-mode ultrasound imaging signals and suspended sediment concentrations', *Measurement* **92**, 34–41.

ACKNOWLEDGEMENTS

At the start of my PhD journey, I decided to let my hair grow and only cut it off after my viva to be able to donate a minimum of 16" (41 cm). The hair donation will be used to provide real hair wigs to children and young people, who have lost their own hair through cancer treatment or other conditions. A PhD journey, including my own, always comes with ups and downs; opportunities and challenges; a process of experiences, emotions and times you don't believe in yourself; personal growth and obtained "transferable" skills. Over the duration of my PhD, my hair has slowly grown in length and provided me with a constant reminder that the challenges I faced are only relative. Throughout my career so far, I have been privileged by being healthy, privileged by having healthy loving parents who are able to and have supported me throughout my degree, but I also have been privileged by being Dutch and had opportunities that others didn't have. Having taught at deprived secondary schools in Hull as a PhD student, showed even more clearly that being intelligent and hard-working is not always enough to obtain a higher degree. There are so many more aspects involved, such as but not limited to (cultural) background, home environment, and health, but also simply already due to the challenging system of stipends that frequently does not cover a full degree. I can only say I am grateful for all the privileges I had in life, and that I was able to do this, especially during a global pandemic. Along this journey, many people have supported me, looked out for me and kept believing in me. I dedicate this thesis to all the women in my life, who have been role models for me and paved the way within the engineering world of mud. I hope the girl who gets a wig from my donated hair can wear it with pride!
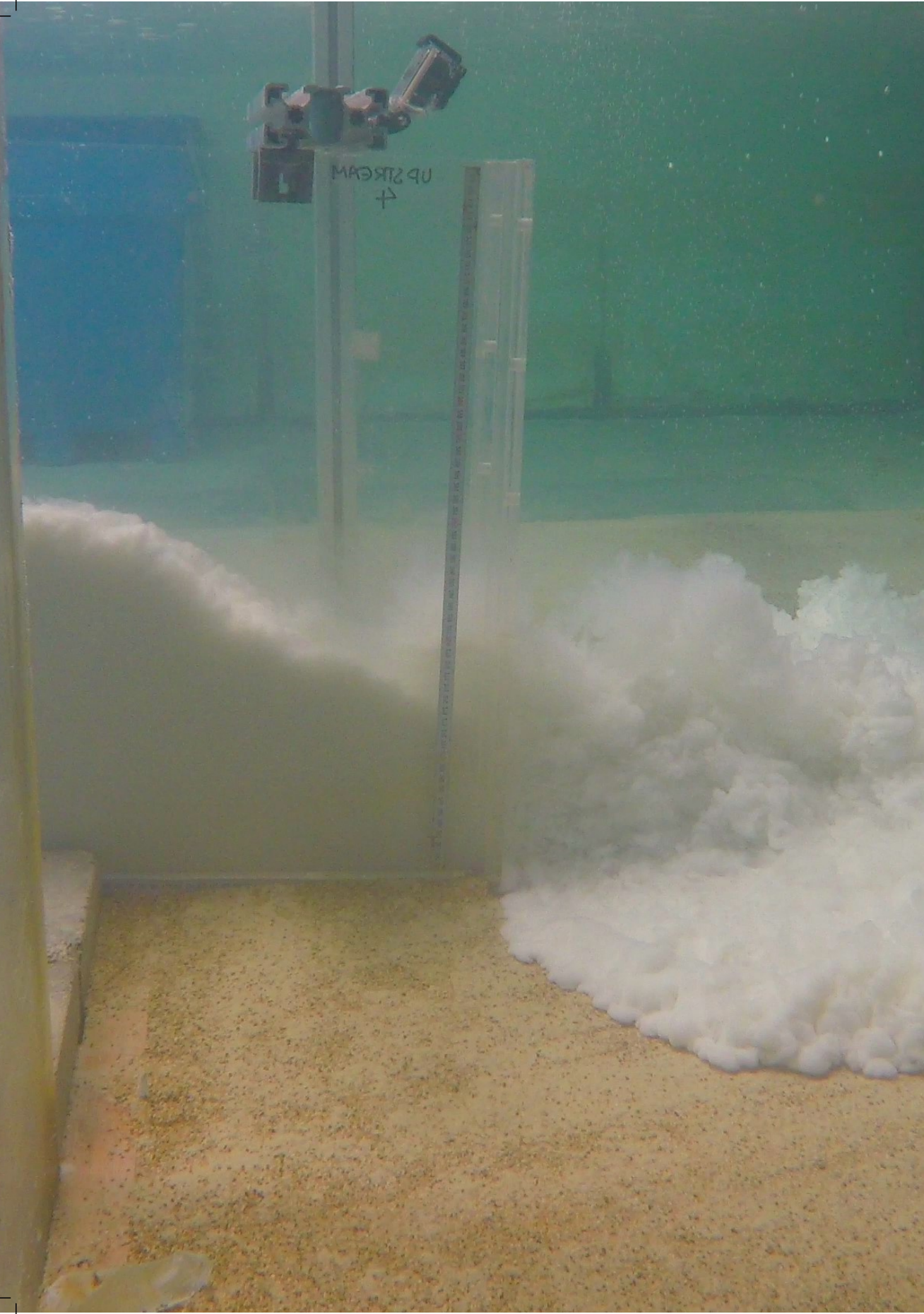
M.G.W. (Marijke) de Vet
Hull, September 2022

a) before   b) after

157